FERMILAB-THESIS-1998-11

A SEARCH FOR CHARGED HIGGS BOSON DECAYS OF THE TOP QUARK USING HADRONIC DECAYS OF THE TAU LEPTON IN PROTON–ANTIPROTON COLLISIONS AT $\sqrt{s} = 1.8$ TEV AT CDF

BY LESLIE STEVAN GROER

A Dissertation submitted to the

Graduate School—New Brunswick

Rutgers, The State University of New Jersey

in partial fulfillment of the requirements

for the degree of

Doctor of Philosophy

Graduate Program in Physics and Astronomy

Written under the direction of

Professor Terence Watts

and approved by

_____

_____

_____

_____

_____

New Brunswick, New Jersey

October, 1998

ABSTRACT OF THE DISSERTATION

A Search for Charged Higgs Boson Decays of the Top Quark using Hadronic Decays of the Tau Lepton in Proton–Antiproton Collisions at $\sqrt{s} = 1.8$ TeV at CDF

by Leslie Stevan Groer

Dissertation Director: Professor Terence Watts

The Standard Model predicts the existence of one neutral scalar Higgs boson, which is a remnant of the mechanism that breaks the $\mathrm{SU}(2)_L \times \mathrm{U}(1)_Y$ electroweak symmetry and generates masses for the heavy vector bosons and fermions. Many extensions to the Standard Model predict two or more Higgs doublets, resulting in a larger spectrum of Higgs bosons including a charged Higgs boson ($H^{\pm}$). For a light charged Higgs boson mass, the top quark decay into a charged Higgs boson and bottom quark might occur.

This thesis presents results of a direct search for this top quark decay mode via the charged Higgs decay to a tau lepton and tau-neutrino, using the hadronic decays of the tau leptons. The search data consist of 100 pb^{-1} of Run 1 data collected between 1992–1995 at the CDF detector, from $p\overline{p}$ collisions at a center-of-mass energy of 1.8 TeV produced at Fermilab's Tevatron accelerator.

A total of seven events are observed in two search channels with an expected background contribution of 7.4 ± 2.0 events coming from fake taus (5.4 ± 1.5), heavy vector boson decays with jets (1.9 ± 1.3) and dibosons (0.08 ± 0.06). Lacking evidence for a signal, we set limits on charged Higgs production at the 95% confidence level

in the charged Higgs mass plane versus $\tan\beta$ (a parameter of the theory) for a top quark mass of 175 GeV/c^2 and for top production cross sections ($\sigma_{t\bar{t}}$) of 5.0 and 7.5 pb, assuming the Type-II Two-Higgs-Doublet-Model. For large $\tan\beta$, this analysis excludes a charged Higgs boson of mass below 147 (158) GeV/c^2 for $\sigma_{t\bar{t}}$ = 5.0 (7.5) pb. Using the Standard Model measured top quark cross section from CDF, this limit increases to 168 GeV/c^2 and we also exclude a branching fraction of top decays via this charged Higgs mode of greater than 43% for charged Higgs masses below 168 GeV/c^2.

Acknowledgements

Success in the scientific enterprise at the end of this century is very often the result of the efforts of hundreds or even thousands of people. This is particularly true in the field of Experimental High Energy Physics. I am forever indebted and grateful for the resolute and stalwart efforts of all the CDF collaborators and Fermilab staff for the construction and extremely successful operation of such wonderful and fun tools with which to explore the Universe, such as the Tevatron and the CDF detector! The multitude of extremely competent and knowledgeable CDF collaborators, listed in Appendix G, have served as my University.

I would like to thank my advisor, Terry Watts, for introducing me to the field and for bringing me on board at CDF and providing constant and unflagging support throughout all these years.

This analysis was conducted in the Tau Working Group at CDF, consisting mostly of collaborators from Rutgers University. I would especially like to thank John Conway, Cal Loomis, Eddie Kuns and Terry Watts for being such wonderful colleagues and always providing helpful advice and encouragement. This analysis would not have been possible without them.

In particular, John and Cal, my true "partners in crime" on the charged Higgs analysis have always been encouraging and leading by example. Thank you for guiding me, teaching me, helping me learn physics and withstanding my constant badgering with patience and good humor. Thank you John, for being my mentor and for providing me with tremendous exposure and opportunities in the field.

Eddie and Carol Hawk, my fellow graduate students, I will never forget being in the trenches with you. Thanks for the friendship, fun times, and cheerful assistance along the way. The other members of the Rutgers team, Tom Devlin, Robert

Kennedy, Liz Buckley-Geer and Michael Walsh, have also always been extremely generous in offering help and advice over the years.

I am grateful for the invaluable advice and counsel I have received from the many members and conveners of the CDF Exotics group. Thank you all.

Thanks to the members of my thesis committee over the years — Tom Devlin, Jolie Cizewski, David Harrington, Nathan Seiberg, Willem Kloet and Anwar Bhatti — for their overview of my progress and for the many useful comments and suggestions along the way that have helped me develop my presentation style and have improved the thesis.

To all my friends at Fermilab, colleagues and roommates, thanks for making life in the Midwest enjoyable. The Potluck Crowd and Lunch Group — Joe, Randy, Leila, Carol H., Mike, Carol AW, Kara, Steve P., Todd, Noreen, Alma, Dong, Steve D., Maggie, and Kyoko — enlivened many a lunchtime, evening or midnight chat session with warmth, humor and commiseration when needed. My roommates, Dirk N., Dirk J., Lisa, Anton, Rich, Brian and Gerhard, with whom I enjoyed many a fun trip to Chicago, nights out on the town or quiet dinner parties at home, deserve many accolades.

It has been a pleasure to be associated with the members of the Fermilab Graduate Student Association. I think we have accomplished a lot and have improved the lives and careers of our fellow students. Roy Thatcher of the Computing Division also deserves special kudos for his sterling efforts in arranging computing classes that have benefited many of the students.

Particular mention must be made of the motley crew I met at Rutgers University who, over the years, have kept me sane and provided hours of entertainment, warm friendship and have aided in my intellectual and spiritual growth. They made my arrival and transition into the Northern Hemisphere so much more comfortable and enjoyable. Therefore, to my family away from home — Anil, Sue, Johnny, Andreas (sorry, no Andreon yet — the search continues ...), Kevin, Andy, Joe, Peter, Tony, Cettina, Bill, Remco, Donna, Lucia and Hlynur — Thanks for being there (and providing a buffer to all those Americans).

To my fellow countrymen, Elisa and Mark, thanks for the many hours of intellectual and philosophical debate. Tui, especially, thank you for being such a great sounding board, a great listener and a true friend.

This thesis is dedicated in loving memory to my father, Hymie, and to my mother, Ellen. Thank you for providing a safe, enriching and loving environment; for always encouraging my career, supporting my endeavors, and never standing in the way of my ambitions though it took me half-way across the world and wouldn't earn me much money! Joanne, thanks for being the best sister a brother could want and also a best friend. I'm glad you could join me on this continent. I think I have the best family in the whole world and I love and cherish you dearly.

And finally to Lee Robbins, my personal cattle-prod! Thanks for being a constant source of love, encouragement, comfort, joy, fun, steadfastness, stability and faith. Thank you for sharing your life with me and filling each day with love, warmth and friendship. I know I am a lucky guy. Thank you also to your family that has been so accepting of me.

This work was supported in part by United States National Science Foundation Grant PHY-94-17820.

Table of Contents

List of Tables

List of Figures

List of Abbreviations

2HDM	Two Higgs Doublet Model
BBC	Beam-Beam Counter
BFM	BuFfer Manager
BMX	Buffer MultipleXor
CDF	Collider Detector at Fermilab
CEM	Central ElectroMagnetic calorimeter
CERN	Centre Européen pour la Recherche Nucléaire (European Laboratory for Particle Physics)
CES	Central Electron Strip chamber
CESR	Cornell Electron Storage Ring
CFT	Central Fast Tracker
CHA	Central HAdronic calorimeter
CKM	Cabibbo-Kobayashi-Maskawa matrix
CMP	Central Muon uPgrade tracking chambers
CMU	Central MUon tracking chambers
CMX	Central Muon eXtension tracking chambers
CPR	Central PReradiator
CPU	Central Processing Unit
CS	Consumer Server
CTC	Central Tracking Chamber
DAQ	Data AcQuisition system
DST	Data Summary Tape
EM	ElectroMagnetic energy
$\not\!\!E_T$	missing transverse Energy
EVB	EVent Builder

FCNC	Flavor Changing Neutral Current
FEM	Forward ElectroMagnetic calorimeter
FMU	Forward MUon tracking chambers
FHA	Forward HAdron calorimeter
FRED	Front-end REadout and Decision
FRC	Fastbus Readout Controller
GMSB	Gauge Mediated Supersymmetry Breaking
GUT	Grand Unified Theory
HAD	HADronic energy
LEP	Large Electron–Positron collider at CERN
MSSM	Minimal SuperSymmetric Model
MX	MultipleXing fast electronic scanner
PAD	Physics Analysis Dataset
PEM	Plug ElectroMagnetic calorimeter
PLJ	Photon-Lepton-Jets software package
PHA	Plug HAdron calorimeter
QED	Quantum ElectroDynamics
QCD	Quantum ChromoDynamics
RGE	Renormalization Group Equation
SCPU	Scanner CPU
SECVTX	SECondary VerTeX algorithm
SLAC	Stanford Linear ACcelerator
SM	Standard Model of particle physics
SSP	SLAC Scanner Processors
SUGRA	SUperGRAvity theory
SUSY	SUperSYmmetry theory
SVX	Silicon VerteX detector
TAUO	TAU Object
TS	Trigger Supervisor

VEV	Vacuum Expectation Value
VTX	VerTeX time projection chamber
WHA	Wall HAdronic calorimeter

ODE TO THE CHARGED HIGGS

The top exists, no doubt of that,
A partner to the b;
Theorists are also sure the world
Has supersymmetry.

If Higgs is how we get our mass
The spectrum gets enlarged.
Not only is there one H-nought,
There's more than one H-charged.

If top is heavier than H,
It radiates this field.
The t becomes a b, you see,
With lower W yield.

If we have H's on our tapes,
How can we know they're there?
Well, H's like to go to taus,
While W don't care.

Ev'n in our gold mine, CDF,
The taus are hard to see,
But imagine if we found the H
AND Supersymmetry!

Mike Albrow
March 1997

Introduction

This thesis describes a search for top quarks decaying to charged Higgs bosons ($t \to H^+ b$) where the charged Higgs bosons decay to tau leptons ($H^+ \to \tau^+ \nu$) and the tau decays into hadronic decay products. The analysis is based on proton-antiproton ($p\overline{p}$) collisions at a center-of-mass energy of $\sqrt{s} = 1.8$ TeV produced at the Tevatron at Fermilab, which currently has the highest energy proton-antiproton collisions in the world, and measured with the Collider Detector at Fermilab (CDF). The data set used in the analysis is based on the Run 1 data sample of 118 pb^{-1} of integrated luminosity collected by CDF from August 1992 to December 1995.

This analysis was begun after the initial evidence of the top quark was observed at CDF, but before its confirmed discovery. Hence, the analysis and limit extractions are done independently of the CDF top analyses which were concurrently underway. This analysis was done in collaboration with Dr. Charles Loomis and Prof. John Conway, under the supervision of Prof. Terence Watts. The tools and data sets used in this analysis were developed in conjunction with the CDF Tau Working Group, under the auspices of the CDF Exotics Physics Group.

The results from this analysis were published in the July 21, 1997 issue of Physical Review Letters [1] and have been presented at numerous conferences (e.g. see Reference [2]).

Organization of the Thesis

The theoretical and experimental frameworks for the analysis and current status of measurements of the top quark and searches for the charged Higgs bosons are reviewed in Chapter 1. The multi-purpose CDF detector which studies the interactions of collisions of protons and antiprotons provided by the Fermilab Tevatron Collider

is described in Chapter 2. Chapter 3 discusses the strategy for the charged Higgs boson search using the hadronic decays of the tau lepton. Chapter 4 describes the reprocessing and the selection of the initial analysis data sets. Chapter 5 describes the further reduction and analysis of these data. Chapter 6 describes the predictions for a charged Higgs signal and Chapter 7 describes the backgrounds to the search. Chapter 8 presents the null results for the search and derives limits based on the observed data and the estimates of the signal and backgrounds.

The various appendices describe some ancillary details to the analysis. Appendix A shows the calculations for the branching fractions for top quark decays to charged Higgs bosons and Standard Model W bosons and the branching fractions for the charged Higgs decays. These calculations are used to extract the limits in Chapter 8. Appendix B describes the operations and production of proton-antiproton collisions at the Tevatron. Appendix C describes the data acquisition system used at CDF in Run 1. Appendix D discusses the measurement of the missing E_T trigger efficiency which was crucial to the analysis. Similarly, Appendix E describes the measurement of the fake rates for the hadronically decaying tau leptons which was critical in understanding the backgrounds to the analysis. Appendix F describes the algorithm used to identify secondary vertices from the decays of long-lived particles, such as hadrons containing bottom quarks.

Appendix G contains the CDF author list from the publication in Reference [1].

Chapter 1

Theoretical and Experimental Framework

I begin this chapter with an overview of the Standard Model of particle physics, including the Higgs mechanism which breaks the electroweak symmetry of the model. Section 1.2 reviews some of the limitations of this model and describes the most theoretically attractive replacement — supersymmetry. The more general extension of the Standard Model Higgs sector to include two Higgs doublets is presented in Section 1.2.2. One of the predictions of this extended Higgs sector is a pair of charged Higgs scalar bosons, the subject of this thesis.

Section 1.3.1 reviews the original motivations and eventual discovery of the top quark. The top quark production mechanisms and calculations are discussed in Section 1.3.2 and the top quark decay properties in the Standard Model are discussed in Section 1.3.3. The current status of top quark measurements at the Tevatron are presented in Section 1.3.4.

Section 1.4 reviews the theoretical constraints and current experimental limits, both direct and indirect, on the production of charged Higgs bosons.

1.1 The Standard Model

Over the last few decades, what is known as the "Standard Model" (SM) of particle physics has become the foundation and touchstone of high-energy particle experiments and theories. The SM is described in numerous text-books, a few of which are to be found in References [3, 4, 5, 6, 7]. I will summarize some of the salient features below.

There are four known forces that govern the interactions of matter in the universe.

The SM describes three of these interactions: the electromagnetic force, and the weak and strong nuclear forces. There is no natural way to incorporate the fourth force, gravity, into the SM; gravity is currently well described by the theory of General Relativity. Much of the drive behind theoretical developments at the high-energy frontier is the hope that all these forces can be incorporated into one Grand Unified Theory (GUT) at some very large energy scale of order 1 TeV or greater. Some of these theories will be discussed further in Section 1.2.

In the SM, all known matter is composed of a few elementary pointlike structureless spin-1/2 (in units of $\hbar$) particles, the *fermions*. The interactions (or forces) between these particles are described by the exchange of *gauge bosons* of integral spin which are the physical manifestations of *gauge fields*. The gauge fields in the SM describe the three interactions: the electromagnetic interaction by *quantum electrodynamics* (QED) which is subsumed in the *electroweak theory* which also describes the weak nuclear force, and the strong nuclear force, described by *quantum chromodynamics* (QCD). The fermions are further subdivided into two groups, the *quarks* and *leptons*, according to their interactions. Quarks interact via all four forces (including gravity), the charged leptons interact via all except the strong interaction and the neutral leptons (neutrinos) only via the electroweak and gravitational force.

The two groups of fermions are further subdivided into three families or *generations*, of different *flavor* and mass, with the generations ranked according to the increasing masses of the constituent particles. Within a generation there are two members in each group: a lepton and its neutrino and an up-type quark with its down-type partner. These pairs of particles will be grouped into doublets and singlets of weak-isospin later in the description of the electroweak theory (see Section 1.1.4).

The fermion generations and flavors are shown in Table 1.1 along with their masses and electric charges. Each fermion has an anti-particle partner with opposite quantum numbers, but the same mass.

Quarks are bound together by the strong force into hadrons. The hadrons are composed of two groups, the mesons ($q\bar{q}$), and the baryons (qqq) (where q stands for a quark and $\bar{q}$ stands for an anti-quark). Due to *quark confinement* (described in

	Generation		
	1st	2nd	3rd
quarks	**up** (u) mass: 2–8 MeV/c^2 charge: $+\frac{2}{3}$	**charm** (c) mass: 1.0–1.6 GeV/c^2 charge: $+\frac{2}{3}$	**top** (t) mass: 174 GeV/c^2 charge: $+\frac{2}{3}$
	down (d) mass: 5–15 MeV/c^2 charge: $-\frac{1}{3}$	**strange** (s) mass: 0.1–0.3 GeV/c^2 charge: $-\frac{1}{3}$	**bottom** (b) mass: 4.1–4.5 GeV/c^2 charge: $-\frac{1}{3}$
leptons	**electron** (e^-) mass: 0.511 MeV/c^2 charge: -1	**muon** (μ^-) mass: 106 MeV/c^2 charge: -1	**tau** (τ^-) mass: 1.78 GeV/c^2 charge: -1
	e^- **neutrino** (ν_e) mass: 0 charge: 0	μ^- **neutrino** (ν_μ) mass: 0 charge: 0	τ^- **neutrino** (ν_τ) † mass: 0 charge: 0

Table 1.1: The fundamental matter particles (fermions) in the Standard Model in their mass eigenstates. Electric charges are in units of $|e|$. Each particle has an antiparticle with the same mass and opposite quantum numbers. † ν_τ is the only particle which has not been directly observed.

Section 1.1.3), free quarks are not to be found in nature; hence, their masses cannot be determined precisely and the measurements are dependent on the energy probes used and the hadronic systems the quarks are in.

The lepton masses have been measured to very high precision: better than 1 part in 10^6 for the electron and muon and to a precision of nearly 1 part in 10^4 for the tau. In the SM, neutrinos have zero mass. Extensions of the SM would allow for non-zero masses of the neutrinos. Many experiments are underway trying to measure the properties of the neutrinos precisely. Currently, the electron and muon neutrino masses have been determined to be $\lesssim 15$ eV and $\lesssim 0.3$ MeV, respectively [8]. The tau neutrino is the only fundamental fermion in the SM that has not yet been observed directly, although its mass from indirect measurements must be less than

31 MeV [8]. There are a number of experiments trying to observe the tau neutrino directly and via neutrino-oscillations (DONUT at Fermilab [9], and NOMAD [10] and CHORUS [11] at CERN). There is also recent evidence from the Super-Kamiokande experiment that neutrinos created in the atmosphere from cosmic-ray interactions might oscillate, which would indicate that they have mass [12].

The top quark was discovered at Fermilab in 1995 by both the CDF [13] and DØ [14] detectors. This was the last quark awaiting discovery in the SM. The top quark and its properties are discussed in further detail in Section 1.3.

The LEP experiments have shown that the e^+e^- annihilation cross section in the Z^0 mass energy region, primarily within the width of the resonance peak, is consistent with the SM assumption of three light neutrino generations [8]. Any further fermionic generations would, therefore, need an extension of the SM.

1.1.1 Gauge Theories

The interactions among the fundamental constituents of matter are described by quantum field theories. In these theories, the forces are mediated by the exchange of particles called *gauge bosons*. There are no direct, "action-at-a-distance" interactions of the matter particles (fermions) with each other. The photon, γ, mediates the electromagnetic interaction, the weak vector bosons, $W^{\pm}$ and Z^0, mediate the weak interaction and the gluons, g_i, mediate the strong interaction.

The SM gauge bosons are listed in Table 1.2 along with the force mediated by each and their relative coupling strengths and ranges.

In a gauge field theory, arbitrary gauge transformations acting on the matter or gauge fields leave the Lagrangian of the theory, and thus all observable quantities, invariant. All gauge field theories obey a global gauge-invariance, characterized by the symmetry of the theory (described by Lie groups), which leads to a conserved quantity, the quantum number of the theory. Requiring local gauge invariance naturally gives rise to the gauge fields which govern the interactions of the theory. The quanta of the gauge fields are the exchange particles mediating the interaction. The gauge

Boson	Quantum Theory	Quantum number	Coupling Strength	Range (m)	Mass (GeV/c^2)
Photon (γ)	QED	Charge	$\alpha = \frac{e^2}{4\pi\hbar c} = \frac{1}{137}$	∞	0
Z^0 $W^\pm$ H^0	Electroweak	Weak Isospin	$G_F m_p^2 \simeq 10^{-5}$	10^{-18}	91.2 80.2 > 90.0
Gluons (g_i) $i = 1, .., 8$	QCD	Color	$\alpha_s \approx 1$	10^{-15}	0
Graviton (G)	(None)	(Mass)	$G m_p^2 \simeq 6 \times 10^{-39}$	∞	0

Table 1.2: The gauge and Higgs bosons of the Standard Model with their properties and the forces they mediate. The coupling strengths to particles of mass m_p are given for low-energy interactions ($q^2 \approx 0$). The graviton and Higgs boson have not been observed. The lower bound on the SM Higgs mass is from LEP [15].

theories are also required to obey causality and to be renormalizable. The following sections describe the quantum electrodynamic (QED), quantum chromodynamic (QCD) and unified electroweak theories in more detail.

The final component of the SM is the addition of the electroweak symmetry-breaking sector via the Higgs mechanism. This spontaneous symmetry breaking results in a neutral scalar Higgs boson, H^0, that gives the weak vector bosons and fermions their mass. This is discussed in detail in Section 1.1.5.

The classical theory of General Relativity provides the best description of the gravitational force. So far, there is no satisfactory way to quantize the gravitational interaction in a field theory, although there is a postulated spin-2 massless gauge boson, the graviton, that would mediate this interaction.

Grand Unified Theories attempt to further unify some or all of these forces. Some of these models are discussed in Section 1.2.

1.1.2 QED

The electromagnetic interaction is well described by the theory of quantum electrodynamics (QED), developed in the late 1940's [16]. The global U(1) gauge symmetry

in QED gives rise to the conservation of electromagnetic charge, Q. Imposing local gauge invariance on the theory necessitates the introduction of a gauge field; this gauge field is the massless gauge boson which describes the interactions among charged particles and corresponds to the photon (γ).

The strength of the interaction between the photon and the fermions is described by the coupling constant α. This is actually a *running* coupling constant, $\alpha(q)$, as its value depends on the momentum transfer, or q^2, of an interaction. At $q^2 = 0$, the coupling constant is the familiar fine structure constant, $\alpha = e^2/4\pi\hbar c = 1/137$, and at the scale of the heaviest vector boson, the Z^0, $\alpha(M_Z) \approx 1/128$.

Photons do not carry charge, due to the Abelian nature of the unitary U(1) symmetry group, and therefore do not interact with each other (*self-couple*) at tree-level, but do so only through higher-order fermionic loops. Therefore, the electromagnetic interaction is long range.

1.1.3 QCD

The gauge theory of the strong force is called quantum chromodynamics (QCD). The symmetry group for QCD is SU(3) which leads to eight conserved quantities, called *color charge* or simply *color*. There are three primary color charges (normally termed red, green and blue) which come in color–anticolor pairs. Quarks form an SU(3) color triplet. Color symmetry is exact, so QCD calculations are independent of the color of the quarks (a red quark scattering off of a green quark is the same as a red quark scattering off of a blue quark). The gauge bosons of the theory, called gluons, result from imposing local gauge invariance. Gluons are neutral massless vector bosons that form an SU(3) color octet, meaning that they carry one color and one anti-color charge, and are thus subject to the color force themselves. The available color configurations for quarks and gluons are given below (where R=red, B=blue, G=green, and $\overline{\text{R}}$=anti-red, etc.)

quarks	R, B, G
antiquarks	$\overline{\text{R}}$, $\overline{\text{B}}$, $\overline{\text{G}}$

$$\text{gluons} \qquad \mathrm{R\overline{B}},\ \mathrm{R\overline{G}},\ \mathrm{B\overline{G}},\ \mathrm{B\overline{R}},\ \mathrm{G\overline{R}},\ \mathrm{G\overline{B}},\ \frac{1}{\sqrt{2}}(\mathrm{R\overline{R}} - \mathrm{B\overline{B}}),\ \frac{1}{\sqrt{6}}(\mathrm{R\overline{R}} + \mathrm{B\overline{B}} - 2\mathrm{G\overline{G}})$$

QCD is a non-Abelian theory, where the gluons carry color, in contrast to the photon in QED which did not carry electric charge. This results in the very different behavior of the strong interaction compared to the electromagnetic interaction. Gluons interact with each other directly and as strongly as they do with quarks. Due to this gluon-gluon interaction, the strong force increases with distance. As two quarks move apart from each other, gluons exchanged between the two quarks interact with each other as well as with the quarks. The increasing force either binds the quarks together, or the "color string" breaks when the energy density of the color field between the quarks is great enough to create a quark-antiquark pair, resulting in two separate hadrons. This results in *quark confinement*; quarks appear only in bound states forming colorless SU(3) singlets, not as free particles. The confinement radius is approximately 1 fm. The lowest energy color singlet configurations of quarks are quark-antiquark pairs ($q\bar{q}$), known as *mesons* or as a quark triplet (qqq) called *baryons*. Collectively these strongly bound states are called *hadrons*. The lowest mass mesons are the pions (e.g. $\pi^+ = u\bar{d}$). The lowest mass baryon is the proton ($p = uud$), which is the only stable free hadron in the SM. All other free hadrons eventually decay through a cascade of particles into the lightest leptons (the electron and neutrinos), photons and protons. The time scale for these decays range from 10^{-24} seconds for resonances (e.g., ρ, η, ϕ) to 10^{-8} seconds for the "almost stable" pions and kaons to about 10^3 seconds for the free neutron. Grand Unified Theories even predict the eventual decay of free protons on the time scale of $> 10^{31}$ years.

Even without directly observing colored objects, the number of colors is measurable. One example is via the ratio of e^+e^- annihilation cross sections into hadrons to those into $\mu^+\mu^-$ [4],

$$R = \frac{\sigma\left(e^+e^- \to \text{hadrons}\right)}{\sigma\left(e^+e^- \to \mu^+\mu^-\right)} = N_c \sum_{\text{flavors}} q_i^2 \tag{1.1}$$

where N_c is the number of colors, q_i is the charge of the quarks u, d, s, ..., and the sum is over the active flavors (see below).

The color-string fragmentation is the way that partons "hadronize" after a high-energy collision. Partons are the constituents of hadrons, namely the quarks and gluons. A parton, knocked out of a proton say, in a high-momentum transfer interaction will hadronize into a "jet" of colorless hadrons travelling roughly collinearly with each other and with the original direction of the outgoing parton. Thus, information about the outgoing partons from the high-q^2 interaction is largely preserved in the resulting jets. The rest of the quarks in the original proton (called *spectators*) also reform into colorless objects.

The amplitude of a strong interaction process at a given momentum scale, q^2, can be parameterized in terms of the running coupling constant $\alpha_s(q)$. A conventional definition of α_s is given by Reference [8]:

$$\begin{aligned} \alpha_s(q) &= \frac{4\pi}{(11-\frac{2}{3}n_f)}\,\frac{1}{\ln(q^2/\Lambda^2)}\left[1-2\,\frac{51-\frac{19}{3}n_f}{(11-\frac{2}{3}n_f)^2}\,\frac{\ln(\ln(q^2/\Lambda^2))}{\ln(q^2/\Lambda^2)}\right] \\ &+ \quad \text{higher order terms.} \end{aligned} \tag{1.2}$$

where n_f = the number of *active* quark flavors and q^2 is the center-of-mass energy of the reaction. An active flavor is a quark flavor whose mass is less than one-half the center-of-mass energy of the reaction. The dimensional parameter, Λ, is the *QCD scale parameter* and it is only adjustable parameter in QCD, apart from the quark masses. The scale parameter is determined by comparing QCD predictions to experimental data and is also dependent on the momentum scale of the interaction. For most processes, the measured value of $\Lambda_{\rm QCD} is consistent with \sim 200$ MeV/c.

From the $1/\ln(q^2/\Lambda^2)$ behavior in the equation above, the coupling becomes vanishingly small at large q^2 or, equivalently, at small distances. This phenomenon is called *asymptotic freedom*. At high energy, where $\alpha_s \to 0$, quarks behave as if they are free particles. Therefore high-q^2 processes can be described very well by perturbative calculations in expansions of the coupling constant α_s. At the scale of the mass of the heaviest vector boson (Z^0), $\alpha_s(M_Z) \approx 0.12$. However, for low-$q^2$ interactions ($\lesssim 300$ MeV$^2/c^2$), the coupling approaches unity. Perturbative calculations tend to break down in this region and we therefore rely mostly on phenomenological models.

In a typical proton-antiproton collision, only one parton from each proton is involved in the hard scatter. Asymptotic freedom makes it possible to calculate this collision process, to first-order, as the interaction between a single parton in each of the colliding hadrons, where the remaining spectator partons only interact with the struck partons during hadronization. The hadronization process occurs at a much lower energy scale, and is therefore non-perturbative, but it occurs well after the high-q^2 interaction. The particles from the remnant hadronization form what is usually referred to as the *underlying event*. The structure of the underlying event is similar to that of the bulk of the soft inelastic $p\overline{p}$ collisions, usually termed *minimum bias events*.

In a typical perturbative calculation, infinities arise that must be *renormalized* or *regularized* in a consistent manner [17]. A particular renormalization scheme must be chosen. We refer to calculations that typically use the common modified-minimal-subtraction method ($\overline{\text{MS}}$) [18, 19]. Also, calculations to finite order in perturbation theory need to introduce a *renormalization scale*, μ. Physical predictions should be independent of this choice of scale, but, as calculations can only be carried out to finite order in practice, this scale should be specified when quoting results of perturbative calculations.

1.1.4 Electroweak Theory

The electromagnetic and weak nuclear forces were combined in a SU(2) $\times$ U(1) Electroweak theory, originally proposed by Weinberg and Salam in 1967 [20, 21]. The unification of the two interactions is accomplished in two steps. First, global gauge invariance under the SU(2) gauge transformation leads to the conservation of the *weak-isospin charge*, T. Requiring the Lagrangian to be invariant under local SU(2) transformations necessitates the introduction of a weak-isospin triplet of gauge fields, $\mathbf{W}^i_\mu$, $i = 1, 2, 3$. The SU(2) group is non-Abelian which leads to the self-interactions of these gauge fields.

The second step involves requiring invariance under the U(1) transformation which leads to the conservation of *weak-hypercharge*, Y. Demanding local gauge

invariance as well necessitates the introduction of a weak-hypercharge singlet vector gauge field, $\mathbf{B}_\mu$.

The gauge fields can be rewritten as follows:

$$\begin{aligned}
\mathbf{W}_\mu^\pm &= \frac{1}{\sqrt{2}}\left(\mathbf{W}_\mu^1 \mp i\mathbf{W}_\mu^2\right) \\
\mathbf{Z}_\mu &= \mathbf{W}_\mu^3 \cos\theta - \mathbf{B}_\mu \sin\theta \\
\mathbf{A}_\mu &= \mathbf{W}_\mu^3 \sin\theta + \mathbf{B}_\mu \cos\theta. \qquad (1.3)
\end{aligned}$$

$\mathbf{A}_\mu$ has the gauge form of the electromagnetic interaction in QED and is identified with the photon. The weak-hypercharge, Y, third component of weak-isospin, T_3, and electric charge, Q, are linearly related by:

$$Q = T_3 + \frac{1}{2}Y \ . \qquad (1.4)$$

Therefore, the global and local conservation of weak-isospin and hypercharge naturally imply charge conservation, as required by QED. Once again, since the U(1) symmetry is not violated, the photon still does not interact with itself, just as in QED. Since U(1) is Abelian, none of the gauge bosons carry weak-hypercharge. As SU(2) is non-Abelian, the weak vector boson fields $\mathbf{W}_\mu^\pm$ and $\mathbf{Z}_\mu$ do carry weak-isospin and, therefore, electric charge. The three weak-isospin fields have weak-isospin projections $T_3 = -1, 0 + 1$ and hence, from $Q = T_3$, there are two charged currents and one neutral current.

The $\mathbf{W}_\mu^\pm$ and $\mathbf{Z}_\mu$ fields are identified as the $W^\pm$ and Z^0 bosons. The observation of these vector bosons at the CERN $p\overline{p}$ Collider in 1983 provided an important test of the SM [22, 23]. The *weak mixing angle*, θ, often referred to as the *Weinberg angle*, θ_W, determines the mixing between the third component of weak-isospin and weak-hypercharge (or equivalently, the mixing of the weak and electromagnetic interactions). The measured value, from many different processes at the M_Z pole, is $\sin^2\theta_W = 0.2312 \pm 0.0003$ [8]. As the $W^\pm$ and Z^0 bosons carry weak-isospin, they can interact directly. Measurements of these gauge couplings, though difficult, are very good tests of the SM.

	Generation 1	2	3	T	T_3	Y	Q
Fermions							
lepton-type (spin 1/2)	$\begin{pmatrix} \nu_e \\ e \end{pmatrix}_L$	$\begin{pmatrix} \nu_\mu \\ \mu \end{pmatrix}_L$	$\begin{pmatrix} \nu_\tau \\ \tau \end{pmatrix}_L$	$1/2$ $1/2$	$+1/2$ $-1/2$	-1 -1	0 -1
	e_R	μ_R	τ_R	0	0	-2	-1
quark-type (spin 1/2)	$\begin{pmatrix} u \\ d \end{pmatrix}_L$	$\begin{pmatrix} c \\ s \end{pmatrix}_L$	$\begin{pmatrix} t \\ b \end{pmatrix}_L$	$1/2$ $1/2$	$+1/2$ $-1/2$	$+1/3$ $+1/3$	$+2/3$ $-1/3$
	u_R d_R	c_R s_R	t_R b_R	0 0	0 0	$+4/3$ $-2/3$	$+2/3$ $-1/3$
Bosons							
(spin 1)							
γ				0	0	0	0
Z^0				1	0	0	0
W^+				1	$+1$	0	$+1$
W^-				1	-1	0	-1
Higgs (spin 0)		$\Phi = \begin{pmatrix} \phi^+ \\ \phi^0 \end{pmatrix}$		$1/2$ $1/2$	$+1/2$ $-1/2$	$+1$ $+1$	$+1$ 0

Table 1.3: The particle properties in the Standard Model for the electroweak interaction. The quantum numbers of *weak-isospin*, T, and its projection, T_3, *weak-hypercharge*, Y, and the *electric charge*, Q, are given ($Q = T_3 + \frac{1}{2}Y$). The right-handed fermions (labelled by the index R) are weak-isospin singlets ($T = 0$), while the left-handed fermions (labelled L) are weak-isospin doublets ($T = 1/2$). Massless neutrinos appear only as left-handed particles and right-handed antiparticles. The Z^0 and photon have the same quantum numbers ($T_3 = Y = Q = 0$) and can therefore mix. The gluons have $T = Q = Y = 0$ and therefore do not interact in the electroweak interaction.

The electroweak force is usually described as $\mathrm{SU}(2)_L \times \mathrm{U}(1)_Y$. The subscript L indicates that only the left–handed components of the fermion fields interact via weak-isospin (and conversely, the right–handed antifermion fields). The weak-hypercharge interaction does not distinguish between the fermion *chirality* (handedness). Consequently, the fermions appear as left–handed doublets and right–handed singlets (scalars) for the electroweak interaction. The fermion and boson states in the electroweak theory are given in Table 1.3 along with their quantum numbers for Q, Y, T, and T_3.

In the SM, where neutrinos are massless, there are no right–handed neutrinos. The leptons do not change flavor (i.e. generation) in the weak interaction. The quarks, however, are observed to change generations in weak interactions. This implies that the strong flavor eigenstates are not the same as the weak eigenstates. Note that the strong eigenstates are also the mass eigenstates. This *mixing* is parameterized in a 3×3 unitary matrix, V_{ij}, which determines the superposition of the strong flavor eigenstates to form the weak-isospin eigenstates, $d'_i = \sum_j V_{ij}\, d_j$. Only the down-type quarks (d, s, b) are mixed in the theory; the up-type quark weak and strong eigenstates are fixed to be identical by a choice of phase. The unitary transformation matrix, V_{ij}, is known as the Cabibbo-Kobayashi-Maskawa (CKM) matrix:

$$\begin{pmatrix} d' \\ s' \\ b' \end{pmatrix} = \begin{pmatrix} V_{ud} & V_{us} & V_{ub} \\ V_{cd} & V_{cs} & V_{cb} \\ V_{td} & V_{ts} & V_{tb} \end{pmatrix} \begin{pmatrix} d \\ s \\ b \end{pmatrix}. \tag{1.5}$$

This matrix can be reduced to three independent real parameters (angles) which describe the mixing, and one complex phase which, if non-zero, generates CP-violation. Applying the unitarity of the CKM matrix to the 1st and 3rd columns implies

$$V_{ud}V_{ub}^* + V_{cd}V_{cb}^* + V_{td}V_{tb}^* = 0. \tag{1.6}$$

The *unitarity triangle*, shown in Figure 1.1, is a geometric representation of the above expression in the complex plane and succinctly summarizes the information in the CKM matrix. The area of the triangle represents the amount of CP violation.

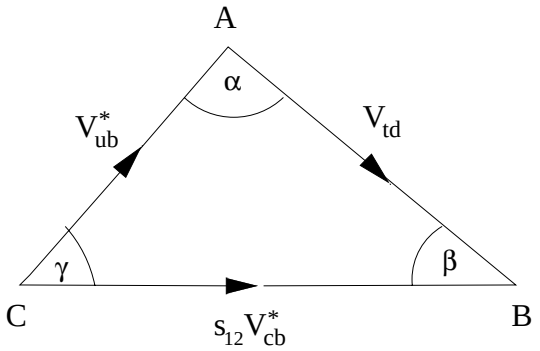

Figure 1.1: Unitarity triangle for the CKM matrix, assuming three generations. $s_{12} = \sin\theta_{12}$ is the mixing between the first and second generations.

The diagonal entries in the CKM matrix are close to unity; the off-diagonal entries are close to zero. The values are approximately [8]: $V_{ud} \approx V_{cs} \approx 0.97$, $V_{tb} \approx 1.0$, $V_{cd} \approx V_{us} \approx 0.2$, $V_{ts} \approx V_{cb} \approx 0.04$, and $V_{td} \approx V_{ub} \approx 10^{-3}$–$10^{-2}$.

Since weak-isospin couples only to left-handed particles, this force violates parity (P) and charge conjugation (C) symmetries maximally. Right-handed fermions (and left-handed antifermions) have zero weak-isospin. Due to the vector – axial vector (V–A) structure of the weak interaction, the combined CP symmetry is *almost* conserved. So far, CP violation has been observed only in the decay of K^0 and $\overline{K}^0$ mesons. The SM predicts additional CP violation only in the decay of B^0 and $\overline{B}^0$ mesons. All CP violation seen so far in the kaon system can be explained due to the phase in the mass matrix. Measuring CP asymmetries in the B system (where the asymmetries are predicted to be large) will allow the unitarity triangle to be over–constrained, determining if CP violation comes only from the mass matrix. This is an active area of research in current collider physics programs.

The electroweak coupling constants are conventionally taken to be g for weak-isospin and $g'/2$ for weak-hypercharge. In the SM, these can be related to the electron electric charge by

$$g \sin\theta_W = g' \cos\theta_W = |e| \ . \tag{1.7}$$

The weak interactions governed by the $W^\pm$ gauge bosons are termed *charged current* interactions and those by the Z^0 gauge boson, *neutral current* interactions.

The neutral currents do not change flavor at the tree level in the SM. These *flavor-changing neutral currents* (FCNC) are predicted however in higher-order loop diagrams in the SM or from other interactions in extensions to the SM. The very small values measured for FCNC rates provide rigorous constraints on possible extensions to the SM (see Section 1.5.5).

The relative strength of the charged to neutral current is measured by the ρ *parameter*

$$\rho = \left(\frac{g_Z^2}{M_Z^2}\right) / \left(\frac{g^2}{M_W^2}\right) = \frac{M_W^2}{M_Z^2 \cos^2\theta_W} \tag{1.8}$$

In the SM, $\rho = \rho_0 \equiv 1$; therefore, $M_W/M_Z = \cos\theta_W$. Non-SM processes can give rise to $\rho \neq 1$. These deviations from the SM prediction are measured via $\Delta\rho$, where $\rho = \rho_0 + \Delta\rho$. Experimental fits to data give $\rho = 1$ within 0.1% [8], severely constraining models that predict large $\Delta\rho$ deviations.

1.1.5 Electroweak Symmetry Breaking in the Standard Model — The Higgs Mechanism

The major success of the electroweak theory is the mechanism for giving the particles their masses. The theory, as explained above so far, only contains massless fermionic and bosonic fields. However, the observed fermions and the $W^{\pm}$ and Z^0 bosons are massive. Explicit mass terms are not gauge invariant and therefore cannot simply be added to the Lagrangian density without violating the renormalizability of the theory.

In the Higgs mechanism, a fundamental weak-isospin $\mathrm{SU}(2)_L$ doublet of complex scalar fields (with weak-hypercharge $Y = 1$),

$$\Phi = \begin{pmatrix} \phi^+ \\ \phi^0 \end{pmatrix} , \tag{1.9}$$

is added to the Lagrangian of the theory. The addition of these scalar fields leaves the Lagrangian gauge invariant. The most general renormalizable and $\mathrm{SU}(2)_L \times \mathrm{U}(1)_Y$ invariant Lagrangian allowed involving only the gauge bosons and scalar fields is

given by [24]

$$\mathcal{L} = -\frac{1}{4}W^i_{\mu\nu}W^{\mu\nu i} - \frac{1}{4}B_{\mu\nu}B^{\mu\nu} + (D_\mu\Phi)^\dagger(D^\mu\Phi) - V(\Phi), \tag{1.10}$$

where W^i_μ are the three massless $\mathrm{SU}(2)_L$ gauge bosons, B_μ the massless $\mathrm{U}(1)_Y$ gauge boson, and

$$\begin{aligned} W^i_{\mu\nu} &= \partial_\mu W^i_\nu - \partial_\nu W^i_\mu - g\epsilon^{ijk}W^j_\mu W^k_\nu \ , \\ B_{\mu\nu} &= \partial_\mu B_\nu - \partial_\nu B_\mu \ , \\ D_\mu &= \partial_\mu + \frac{1}{2}ig\tau^i W^i_\mu + \frac{1}{2}ig'YB_\mu, \end{aligned} \tag{1.11}$$

and

$$V(\Phi) = \mu^2|\Phi^\dagger\Phi| + \lambda|\Phi^\dagger\Phi|^2 \ . \tag{1.12}$$

The theory therefore depends on the $\mathrm{SU}(2)_L$ and $\mathrm{U}(1)_Y$ gauge coupling constants (g and g') and the scalar mass and quartic coupling parameters (μ^2 and λ) which appear in the scalar potential V.

For a choice of $\lambda > 0$ and $\mu^2 < 0$, the state of minimum energy for the potential V is not at zero, but at $|\Phi^\dagger\Phi| = -\mu^2/2\lambda \equiv v^2$. The scalar field therefore develops a nonvanishing vacuum expectation value (VEV), which is degenerate. A single value of the VEV can be chosen, which is essentially a choice of a preferred "direction" in the Higgs-doublet phase space. The usual choice is

$$\langle\Phi\rangle = \frac{1}{\sqrt{2}}\begin{pmatrix} 0 \\ v \end{pmatrix} \ . \tag{1.13}$$

The choice of this new ground state "spontaneously" breaks the $\mathrm{SU}(2)_L \times \mathrm{U}(1)_Y$ symmetries, by a change of variables, to $\mathrm{U}(1)_{EM}$, while maintaining the renormalizability and unitarity of the theory. As the $\mathrm{U}(1)$ gauge symmetry remains unbroken in this transformation, the associated gauge boson, the photon, remains massless. However, three of the degrees of freedom of the scalar doublet (corresponding to Goldstone bosons) are "eaten" or transformed into the longitudinal polarization components of the weak-isospin triplet of bosons, giving the $W^\pm$ and Z bosons their masses.

The remaining degree of freedom corresponds to a massive weak-isospin singlet neutral scalar particle, the Higgs boson, H^0. It is a physical scalar which can be produced and detected experimentally. The Higgs particle is the last remaining undetected piece of the SM. Much of the effort at future high-energy particle experiments will be in trying to observe this so far elusive particle.

The scalar potential, V, of Equation 1.12 initially has two free parameters, μ and λ. We can trade these in for the VEV and the scalar Higgs mass via:

$$v^2 = -\frac{\mu^2}{2\lambda}, \quad M_{H^0}^2 = 2v^2\lambda \ . \tag{1.14}$$

The muon decay rate, , ($\mu \rightarrow \nu_\mu e \overline{\nu}_e$), determines $v^2 = (\sqrt{2}G_F)^{-1} = (246 \text{ GeV})^2$. Thus, *the only remaining unknown parameter is the Higgs mass.* One of the most important properties of the Higgs boson is that the strength of its couplings to fermions and gauge bosons is proportional to the corresponding known particle masses and gauge couplings. As a result, the SM Higgs boson production and decay rates can be computed unambiguously in terms of the Higgs boson mass.

The gauge invariant Yukawa couplings of the Higgs boson to "up-type" (u) and "down-type" (d) fermions gives the quarks and charged leptons their masses and is given by the Lagrangian

$$\mathcal{L}_f = -\lambda_d \overline{Q}_L \Phi d_R - \lambda_u \overline{Q}_L \Phi^c u_R + \text{hermitian conjugate} \tag{1.15}$$

where $\Phi^c \equiv i\tau_2 \Phi^*$ and $\overline{Q}_L \equiv (\overline{u}_L, \overline{d}_L)$. No mass is generated for the neutrinos as there are no right-handed neutrinos in the SM. Replacing Φ by its VEV in the above generates the mass terms for the fermions, with Yukawa coupling strength

$$\lambda_f = \frac{M_f\sqrt{2}}{v} = \frac{gM_f}{2M_W} \ . \tag{1.16}$$

The Higgs coupling to the W (Z) bosons is of strength g ($g/\cos\theta_W$). The couplings of the Higgs boson to the weak vector bosons and the fermions are shown in Figure 1.2.

Therefore, the sole prediction of this model is the existence of a neutral scalar particle, the Higgs boson, of unknown mass, but with fixed couplings to other particles. The most recent 95% confidence level lower bound on the SM Higgs mass

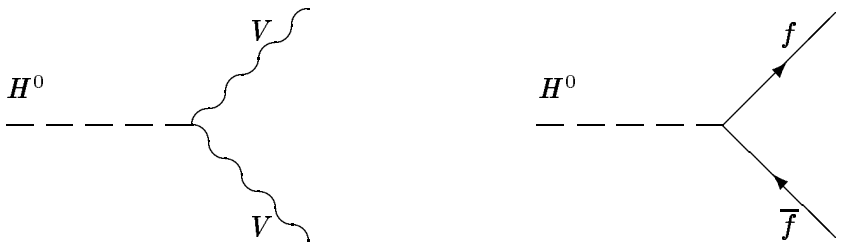

$$ig_V = 2i\frac{M_V^2}{v} = \begin{cases} igM_W & V = W \\ ig\frac{M_Z}{\cos\theta_W} & V = Z \end{cases} \qquad ig_f = -\sqrt{2}i\frac{M_f}{v} = -i\frac{g}{2}\frac{M_f}{M_W}$$

Figure 1.2: Yukawa couplings of the standard Higgs boson to weak vector bosons and fermions. The coupling to weak vector bosons is multiplied by the metric tensor $g^{\mu\nu}$.

of $M_{H^0} > 90.0$ GeV/c^2, comes from the direct searches at the four LEP experiments running at a center-of-mass energy of $\sqrt{s} = 183$ GeV/c^2 with approximately 55 pb^{-1} of integrated luminosity collected for each experiment [15]. Loop effects in electroweak radiative corrections give a limit of $M_{H^0} < 300$ GeV/c^2 at 95% confidence level from precision electroweak measurements. This limit, however, depends sensitively on which pieces of experimental data are included in the fit and assumes the correctness of the minimal SM.

Other spontaneous symmetry breaking mechanisms have been posited, some of which include extensions to the Higgs sector, others which invoke some strongly-coupled weak sector at some high-energy regime $\geq \mathcal{O}(1$ TeV). The SM Higgs mechanism is the simplest scheme known. The existence of the Higgs boson, or other particles associated with symmetry breaking in the electroweak sector, are critical to the renormalizability of the theory, and hence the validity of the Standard Model.

1.2 Extensions to the Standard Model

As discussed in the previous section, The Standard Model (SM) is a gauge theory based on $\mathrm{SU}(3)_C \times \mathrm{SU}(2)_L \times \mathrm{U}(1)_Y$. This model has provided an extremely successful, and so far, very robust description of electroweak and strong interaction phenomena. The SM has been tested to remarkable accuracy and precision measurements

have confirmed its predictions to the level of radiative corrections. No deviations have been found from predicted SM parameter values by more than two standard deviations [25].

With the discovery of the top quark, the SM matter sector is essentially complete, but there is the missing, elusive ingredient, the Higgs boson, which forms a crucial part of the SM. Despite many active searches at particle accelerators, the Higgs boson has not yet been observed and experiments in the energy regime available to date cannot give us much insight into its mass or properties.

The SM however does not qualify as a "theory of everything". There is no method to incorporate gravity which becomes important at energy scales approaching the Planck scale ($M_{\text{planck}} = (8\pi G_N)^{-1/2} \sim 2.4 \times 10^{18}$ GeV/c^2) and so the SM must be considered an *effective theory* at energies below this scale. There are also 19 parameters in the SM, including the masses of all the fermions and Higgs boson, which are not predicted and must be determined from experiment.

There are also problems in the Higgs sector itself. The introduction of a fundamental scalar field is *ad hoc*; the other fields in the theory are spin-1 gauge fields and spin-1/2 fermion fields. Furthermore, the model does not explain why the scalar field acquires a vacuum expectation value, nor why it produces the curious pattern of fermion masses and the CKM matrix. Thus the standard Higgs model accommodates, but does not explain, those features of the electroweak theory for which it is responsible [24].

Little is known about the mechanism which breaks the electroweak symmetry. The fact that the relation $\rho = M_W^2/M_Z^2 \cos^2\theta_W = 1$ is nearly satisfied suggests that the symmetry-breaking sector possesses a global SU(2) symmetry, often called a "custodial" symmetry [26]. Models that introduce large differences to this ratio (measured by $\Delta\rho$, where $\rho = 1 + \Delta\rho$) at low-energy scales can be ruled out (see Section 1.2.2).

Another problem is that self-coupling effects in the scalar Higgs field involving higher-order fermionic loops are quadratically divergent. This self-coupling is shown in Figure 1.3a where the coupling between the Higgs and fermions is given by λ_f.

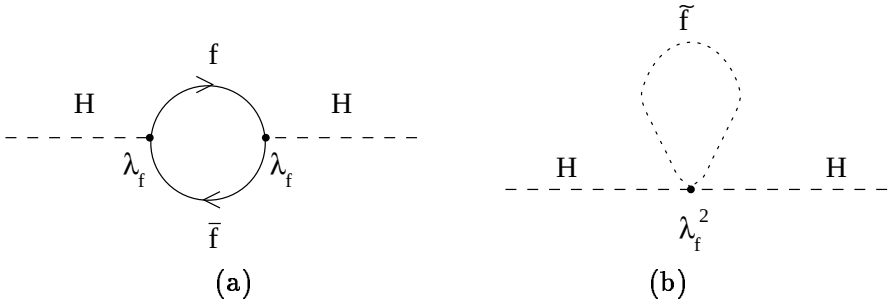

Figure 1.3: Loop corrections to the self-energy of the SM Higgs boson for (a) fermionic loops and (b) sfermions loops from supersymmetric partners.

The corrections to the mass, employing some energy cutoff scale Λ_{cutoff}, gives

$$M^2_{H^0} = M^2_{H^0}(\Lambda_{cutoff}) - \alpha\Lambda^2_{cutoff} \ , \tag{1.17}$$

where $M^2_{H^0}$ is defined in Equation 1.14. These corrections blow up as we go to larger and larger energy scales, Λ_{cutoff}. To explain $M^2_{H^0} \sim \mathcal{O}(M_W)$ we need either $\Lambda_{cutoff} \lesssim 1$ TeV, or extreme fine tuning to all orders of perturbation theory to give unnatural cancellation between terms such as $M^2_{H^0}(\Lambda)$ and $\alpha\Lambda^2$. This is known as the *fine-tuning problem.*

The SM also suffers from what is perceived as a *hierarchy problem*, where there is no natural way to explain why the natural scale for the electroweak symmetry-breaking is of order $v = (\sqrt{2}G_F)^{-1/2} = 246$ GeV, which is many orders below the Planck scale energies.

Therefore, the SM cannot be a fundamental theory; at best it is a low-energy approximation or effective field theory, to a more fundamental theory of particle interactions, that must be applicable at about the electroweak scale ($v = 246$ GeV) or by at least $\Lambda \lesssim 1$ TeV. This was the strong motivation for building the Superconducting Supercollider, now unfortunately defunct, and the Large Hadron Collider being constructed at CERN.

There are already some possible hints of an underlying structure unifying all gauge interactions. At the energy scale of the mass of the Z^0 boson (91 GeV), there is a large discrepancy between the electromagnetic, electroweak and strong coupling constants. Renormalization group equations (RGE) however predict the evolution ("running") of these coupling constants and imply that all these couplings

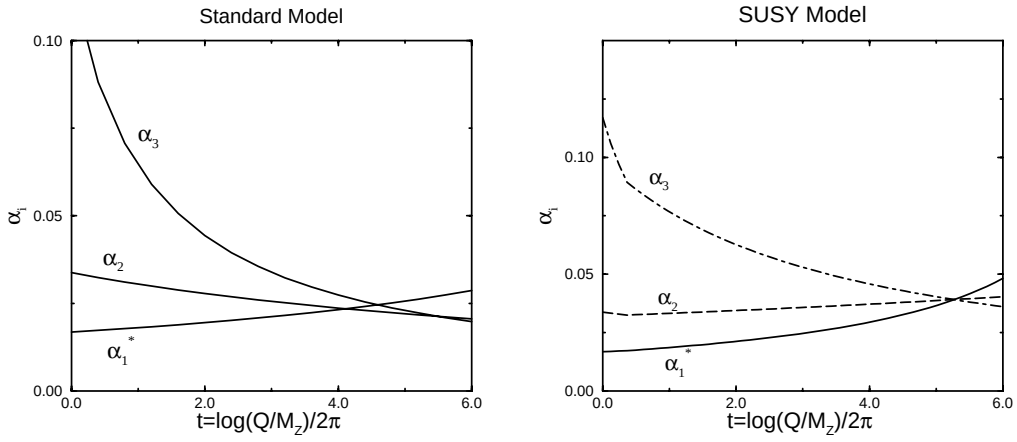

Figure 1.4: Running of the gauge coupling constants (shown as the inverse) up to the GUT scale ($\sim 10^{16}$ GeV) for the (a) SM and (b) MSSM. Figures are taken from Reference [27].

might evolve to the same value at some Grand Unified Theory (GUT) energy scale ($M_{GUT} \sim 10^{16}$ GeV). The running of these couplings in the SM is shown in Figure 1.4a. The couplings do not quite meet at the GUT scale in the SM.

The calculations made for this running are strongly dependent on the accuracy of data at low-energy scales but it already seems that very simple GUT scenarios including SU(5) models can be ruled out [27].

One of the most attractive methods of extending the SM comes from *supersymmetric theories* (SUSY). SUSY is a generalization of the Lorentz space-time symmetries of quantum field theory that posits a superfield which automatically associates a spin-1/2 field (fermion) with every spin-0 field (boson) and vice-versa. SUSY is generally considered to be the leading candidate for extending the SM. It naturally solves some of the problems mentioned above, albeit by introducing many new degrees of freedom. If SUSY is formulated as a local symmetry, then a spin-2 (graviton) field must be introduced, thereby leading automatically to *supergravity* (SUGRA) models in which gravity is unified with the other interactions. In the appropriate limit, SUGRA can be reduced to general relativity. Another motivation is that SUSY is a natural consequence of superstring theories.

The introduction of so many new parameters into the theory via the superfield

makes it extremely difficult to derive general results and constraints for both theory and experiment. A few more simplified scenarios are usually used to compare experimental results and to provide a coherent framework for predictions. There is an enormous amount of development and discussion about SUSY and SUSY-inspired models, for which it would be impossible to do justice here. Rather, I will sketch out a little of the phenomenology of the minimal supersymmetric model (MSSM) below and will discuss general extensions to the SM in the Higgs sector in Section 1.2.2 in somewhat more detail, and relate these extensions to the MSSM. The reader is referred to some excellent review articles and lectures by, among others, H. Haber and S. Dawson [8, 27, 28], J. Gunion [29, 30], M. Dine [31], S. Martin [32] and M. Carena [33].

1.2.1 The Minimal Supersymmetric Standard Model

The minimal supersymmetric extension of the Standard Model (MSSM) consists of adding a supersymmetric partner (*sparticle*) for every particle of the SM, of equal mass and coupling strengths. In addition to the sparticles, the MSSM contains two weak-hypercharge ($Y = \pm 1$) Higgs doublets, $H^0_{1,2}$. This is the minimal Higgs structure needed for an anomaly-free SUSY extension of the SM. As in the SM, the doublets generate mass for both the up-type and down-type quarks and the charged leptons. The Higgs spectrum then comprises two CP-even Higgs bosons (h^0, H^0), a CP-odd Higgs boson (A^0), and a charged Higgs pair ($H^\pm$). This will be discussed in detail in the next section.

The particles and corresponding sparticle mass eigenstates are listed below.

$$\begin{array}{lccccc} \text{particles}: & [u,d,c,s,t,b]_{L,R}\,[e,\mu,\tau]_{L,R}\,[\nu_{e,\mu,\tau}]_L & g & \underbrace{W^\pm, H^\pm} & \underbrace{\gamma, Z^0, H^0, h^0, A^0} \\ \text{sparticles}: & [\tilde{u},\tilde{d},\tilde{c},\tilde{s},\tilde{t},\tilde{b}]_{L,R}\,[\tilde{e},\tilde{\mu},\tilde{\tau}]_{L,R}\,[\tilde{\nu}_{e,\mu,\tau}]_L & \tilde{g} & \widetilde{\chi}^\pm_{1,2} & \widetilde{\chi}^0_{1,2,3,4} \end{array}$$

The fermionic-superpartners normally have an "s" prepended to the SM particle name to indicate the spin-0 scalar nature (i.e. *s*fermions, *s*quarks, *s*neutrinos, etc). The bosonic-superpartners have the suffix "-ino" attached (e.g. phot*ino*, glu*ino*, gaug*ino*, w*ino*, Higgs*ino* etc.). The left- and right-handed fermions have separate

scalar partners, which, in general, can have different masses and can mix with one another (e.g. $\tilde{t}_L$ and $\tilde{t}_R$ could mix). The partners of the charged vector and scalar bosons are the spin-1/2 *charginos* denoted by $\tilde{\chi}_i^{\pm}$, and for the neutral bosons, the *neutralinos*, denoted by $\tilde{\chi}_i^0$.

In the MSSM, another symmetry is added called *R-parity* (or "matter" parity) which eliminates boson (B) and lepton (L) number violating terms. The R-parity of a particle of spin S is given by

$$P_R = (-1)^{3(B-L)+2S} \ . \tag{1.18}$$

All SM particles and Higgs bosons have even R-parity ($P_R = +1$) while all the squarks, sleptons, gauginos and higgsinos have odd R-parity ($P_R = -1$). The consequence of R-parity conservation is that any physical process must always involve an even number of sparticles. Sparticles must be produced in pairs, and in most formulations of SUSY, there is a lightest neutral SUSY particle (termed the LSP), normally the $\tilde{\chi}_1^0$, that is stable[1] and to which all sparticles eventually decay via cascade decays.

The sfermion contributions in the radiative corrections to the SM Higgs mass, shown in Figure 1.3b, would lead to exact cancellations of the SM quadratic divergencies discussed in Equation 1.17, if SUSY was an exact symmetry. However, we know that supersymmetry must be a broken symmetry in nature as no superpartners have ever been observed at the mass scales of the SM particles. Therefore,

$$\Delta M^2 \equiv M_{\tilde{f}}^2 - M_f^2 \neq 0 \tag{1.19}$$

and therefore the radiative corrections to the Higgs mass give

$$M_{H^0}^2 = M_{H^0}^2(\Lambda) + \alpha \Delta M^2 \ln(\Lambda / v) \ . \tag{1.20}$$

For $\Delta M^2 \approx v^2 = (246 \text{ GeV})^2$ we have a natural solution to the hierarchy problem.

Supersymmetry theories also imply accurate gauge coupling unification at M_{GUT}, as shown in Figure 1.4b. This assumes no other particles or interactions occur in the

[1] at least on the time scale of collider physics processes.

mass range between $M_{SUSY} \approx 1$ TeV and $M_{GUT} \approx 10^{16}$ GeV (the *desert hypothesis*) and that the sparticles have masses $\lesssim$ 1–10 TeV. Unification also only occurs if there are exactly two Higgs doublets (and possibly additional singlets).

As mentioned above, we know that SUSY is a broken symmetry in the everyday world as we do not see any sparticles at the current energy regime of collider physics. Supersymmetry breaking in the MSSM is accomplished by introducing the most general renormalizable terms in the effective MSSM Lagrangian which break supersymmetry explicitly. Supersymmetry is called *softly* broken when these extra SUSY-breaking couplings are of positive mass dimension; this maintains the hierarchy between the electroweak and Planck scales. If SUSY is relevant for explaining the scale of electroweak interactions, then the mass parameters introduced by the soft SUSY-breaking terms should be in the TeV range or below. In models of spontaneously broken supergravity, the gravitino, the spin-3/2 partner of the graviton, acquires mass, but is weakly interacting and forms the LSP.

Most SUSY-breaking schemes involve a *hidden sector* where the SUSY breaking occurs at some large energy scale (typically M_{GUT} to M_{planck}) which is decoupled from the low-energy *visible sector* of the particles of the MSSM. The SUSY-breaking is transmitted to the visible sector by some mechanism, usually via the exchange of gravitons in *gravity-mediated* SUSY-breaking (SUGRA) or via gauge forces in *gauge-mediated* SUSY-breaking (GMSB). Much of the focus of current theoretical work is on the exact mechanism for supersymmetry breaking.

The SUSY-breaking terms, in addition to those from the SUSY-conserving sector of the MSSM, introduce many new parameters. In addition to the parameters of the SM, there are 105 new independent parameters in the most general MSSM model. There are strong theoretical and phenomenological constraints on some of this parameter space, however, especially as these models predict large lepton-number violations, CP-violations and FCNC's in general, which are not observed in experiments. There are again a number of schemes available to constrain these parameters, the most developed of which are minimal supergravity (mSUGRA), GMSB and Supersymmetric Grand Unified Theories (SGUT).

Minimal supergravity reduces the parameter space by requiring related parameters to be equal at the unification scale (M_{GUT}). Thus the gaugino masses are equal with value $m_{1/2}$, and the slepton, squark and Higgs masses depend on a common scalar mass parameter, m_0. There are three other parameters in this model, in addition to the 19 from the SM: A_0 which governs the Higgs-sparticle trilinear couplings in the superpotential, $\tan\beta$ the ratio of the VEV's for the two Higgs doublets (see the next section) and μ_0, the supersymmetric Higgsino-mass parameter. Details on these parameters can be found in the references mentioned above. It is much easier relating experimental results in searches for SUSY to this reduced parameter set, but caution is needed in interpretations as evolving these results up to the SUSY-breaking scale is very model dependent.

The minimal gauge-mediated SUSY-breaking approach posits one effective mass scale of $\mathcal{O}(100$ TeV) that determines all the low-energy scalar and gaugino mass parameters through loop effects. There is no complete, simple and compelling model for the minimal GMSB yet.

Supersymmetric grand unified theories (SGUT) use the constraints imposed by gauge-coupling unification and add unification of the Higgs-fermion Yukawa couplings, and gaugino-mass parameters. As these are related at a very high energy scale, detailed knowledge of the SUSY particle spectrum is needed to make progress.

In evolving the MSSM parameters down from the high-energy scale using the renormalization group equations, typically one of the diagonal Higgs-squared-mass parameters is driven negative by the large top-quark Yukawa contribution. Thus, electroweak symmetry breaking is generated radiatively, and the resulting electroweak symmetry-breaking scale is intimately tied to the scale of low-energy supersymmetry breaking. This is very dependent on the high-energy scale assumptions and the communication mechanism to the low-energy scale.

The particle spectrum predictions for the MSSM are fairly robust but the very uncertain state of knowledge of the supersymmetry-breaking mechanism implies that there is a great deal of uncertainty as to the exact mass scale at which we should see the new sparticles and as to the new experimental signatures that will appear

when sparticles are produced. The search for SUSY promises to be an exciting field of experimental and theoretical work for the next century.

1.2.2 The Extended Higgs Sector

The simplest extension to the Standard Model is the addition of extra Higgs doublets and/or singlets. These are the most attractive since these models automatically preserve the custodial SU(2) symmetry tree-level prediction of $\rho \equiv M_W^2/M_Z^2 \cos^2\theta_W = 1$ (see Section 1.1.4). There has been extensive discussion and development of these models, the primary reference being the *Higgs Hunter's Guide* [34]. More recent developments can be found in References [35, 36, 37, 38].

The general non-supersymmetric two-Higgs doublet extension (2HDM) of the SM posits two complex $SU(2)_L$ doublet scalar fields, denoted by Φ_1 and Φ_2 with weak-hypercharge $Y = \pm 1$:

$$\langle \Phi_1 \rangle = \begin{pmatrix} \phi_1^{0*} \\ -\phi_1^- \end{pmatrix}, \qquad \langle \Phi_2 \rangle = \begin{pmatrix} \phi_2^+ \\ \phi_2^0 \end{pmatrix} \tag{1.21}$$

where * denotes complex conjugation. The most general gauge-invariant scalar potential built from these fields which spontaneously breaks $SU(2)_L \times U(1)_Y$ down to $U(1)_{EM}$ (i.e. is consistent with the electroweak sector of the SM) is given by

$$\begin{aligned} V(\Phi_1, \Phi_2) \;=\; & \lambda_1(\Phi_1{}^\dagger\Phi_1 - {v_1}^2)^2 + \lambda_2(\Phi_2{}^\dagger\Phi_2 - {v_2}^2)^2 \\ & + \lambda_3\left[(\Phi_1{}^\dagger\Phi_1 - {v_1}^2) + (\Phi_2{}^\dagger\Phi_2 - {v_2}^2))\right]^2 \\ & + \lambda_4\left[(\Phi_1{}^\dagger\Phi_1)(\Phi_2{}^\dagger\Phi_2) - (\Phi_1{}^\dagger\Phi_2)(\Phi_2{}^\dagger\Phi_1)\right] \\ & + \lambda_5\left[\mathrm{Re}(\Phi_1{}^\dagger\Phi_2) - v_1 v_2\right]^2 + \lambda_6\left[\mathrm{Im}(\Phi_1{}^\dagger\Phi_2)\right]^2 \end{aligned} \tag{1.22}$$

where the λ_i are all real parameters due to hermiticity. This potential is the most general one subject to gauge invariance and a discrete symmetry $\Phi_1 \to -\Phi_1$ which would only be softly violated by dimension-two terms ($\Phi^\dagger\Phi$), which are absent in the above. This discrete symmetry ensures that flavor-changing neutral currents (FCNC) do not appear at the tree-level in Higgs-mediated processes.

The potential, V, is also CP-invariant. A CP-violating Higgs sector is possible with two SU(2) doublets and would be introduced into the theory by allowing a

relative phase difference ($e^{i\xi}$) between the two doublets Φ_1 and Φ_2 [39]. This does not occur in supersymmetric theories however and is beyond the scope of this discussion.

The above potential guarantees the correct pattern of electroweak symmetry breaking over a large range of the parameters, λ_i. For a choice of λ_i that maintains $V(0,0) > 0$ and yields positive-squared masses for the physical Higgs bosons, the potential is minimized by the vacuum expectation values (VEV's) of the Higgs fields

$$\langle \Phi_1 \rangle = \frac{1}{\sqrt{2}} \begin{pmatrix} 0 \\ v_1 \end{pmatrix}, \qquad \langle \Phi_2 \rangle = \frac{1}{\sqrt{2}} \begin{pmatrix} 0 \\ v_2 \end{pmatrix} \tag{1.23}$$

which breaks the $\mathrm{SU}(2)_L \times \mathrm{U}(1)_Y$ down to $\mathrm{U}(1)_{EM}$ as desired. The v_i can be chosen to be real. The VEV's are related to v in the minimal SM Higgs scenario by (cf. Equation 1.14):

$$v^2 \equiv {v_1}^2 + {v_2}^2 = \frac{4M_W^2}{g^2} = (246 \text{ GeV})^2 \ . \tag{1.24}$$

A convenient notation is introduced:

$$\tan\beta = v_2/v_1 \ . \tag{1.25}$$

This parameter, $\tan\beta$, the ratio of the VEV's of the two Higgs doublets, plays a key role in describing models with extra Higgs doublets.

After shifting the neutral scalar fields by their VEV's, we can diagonalize the mass matrices to give five physical Higgs boson states. Originally, there are eight scalar degrees of freedom in the Higgs sector from two doublets with two complex components each. In diagonalizing the masses there are three Goldstone bosons, $G^{\pm}$ and G^0, which get "eaten" or absorbed as the longitudinal components of the $W^{\pm}$ and Z^0 bosons of the SM.

Due to the CP-invariance of the potential, V, the imaginary and real parts of the neutral scalar fields decouple. The real (CP-even) sector contains two physical Higgs scalars which mix through the mass-squared matrix

$$\mathcal{M} = \begin{pmatrix} 4{v_1}^2(\lambda_1 + \lambda_3) + {v_2}^2\lambda_5 & (4\lambda_3 + \lambda_5)v_1 v_2 \\ (4\lambda_3 + \lambda_5)v_1 v_2 & 4{v_2}^2(\lambda_2 + \lambda_3) + {v_1}^2\lambda_5 \end{pmatrix} \tag{1.26}$$

The physical mass eigenstates are given by

$$\begin{pmatrix} H_1^0 \\ H_2^0 \end{pmatrix} = \sqrt{2} \begin{pmatrix} \cos\alpha & \sin\alpha \\ -\sin\alpha & \cos\alpha \end{pmatrix} \begin{pmatrix} \mathrm{Re}\,{\phi_1}^{0*} - v_1 \\ \mathrm{Re}\,{\phi_2}^{0} - v_2 \end{pmatrix} \tag{1.27}$$

Typically, the two neutral CP-even mass eigenstates (H_1^0 and H_2^0) are labelled h^0 and H^0, with the convention chosen such that $M_{H^0} \geq M_{h^0}$. The masses are given by

$$M^2_{H^0,h^0} = \frac{1}{2}\left[\mathcal{M}_{11} + \mathcal{M}_{22} \pm \sqrt{(\mathcal{M}_{11} - \mathcal{M}_{22})^2 + 4\mathcal{M}_{12}^2}\right] \tag{1.28}$$

where the *mixing angle*, α, is obtained from

$$\begin{aligned} \sin 2\alpha &= \frac{2\mathcal{M}_{12}}{\sqrt{(\mathcal{M}_{11} - \mathcal{M}_{22})^2 + 4\mathcal{M}_{12}^2}} \\ \cos 2\alpha &= \frac{\mathcal{M}_{11} - \mathcal{M}_{22}}{\sqrt{(\mathcal{M}_{11} - \mathcal{M}_{22})^2 + 4\mathcal{M}_{12}^2}} \end{aligned} \tag{1.29}$$

The neutral CP-odd mass eigenstate, labelled A^0, is obtained from the imaginary part

$$A^0 = \sqrt{2}(-\mathrm{Im}\,{\phi_1}^{0*}\sin\beta + \mathrm{Im}\,{\phi_2}^{0}\cos\beta) \tag{1.30}$$

with mass $M^2_{A^0} = \lambda_6({v_1}^2 + {v_2}^2)$.

There are also two physical *charged Higgs* states

$$H^{\pm} = -{\phi_1}^{\pm}\sin\beta + {\phi_2}^{\pm}\cos\beta \tag{1.31}$$

with mass $M_{H^\pm} = \lambda_4({v_1}^2 + {v_2}^2)$.

To summarize, this model possesses five physical Higgs bosons: two neutral CP-even scalars (H^0 and h^0 where $M_{H^0} \geq M_{h^0}$), a neutral CP-odd scalar (A^0) and a pair of charged scalars ($H^\pm$). A^0 is sometimes called a *pseudoscalar* due to the way it couples to the fermions in supersymmetric theories. Instead of the one free parameter of the SM Higgs sector (the Higgs mass) we now have six free parameters: four Higgs masses, the ratio of the VEV's ($\tan\beta$), and a Higgs-mixing angle (α). Note that v is fixed by Equation 1.24.

In the most general 2HDM, the masses and angles are independent parameters. In the MSSM, however, further restrictions reduce these to two free parameters,

normally taken to be M_{A^0} and $\tan\beta$. The other Higgs masses can be derived at tree-level from

$$M^2_{H^\pm} = M^2_{A^0} + M^2_W \ , \tag{1.32}$$

$$M^2_{H^0,h^0} = \frac{1}{2}\left[M^2_{A^0} + M^2_Z \pm \sqrt{(M^2_{A^0} + M^2_Z)^2 - 4M^2_Z M^2_{A^0}\cos^2 2\beta}\right] \ , \tag{1.33}$$

and the mixing angle α can be derived from

$$\tan 2\alpha = \tan 2\beta \left(\frac{M^2_{A^0} + M^2_Z}{M^2_{A^0} - M^2_Z}\right) \ . \tag{1.34}$$

The phenomenology of the 2HDM depends in detail on the various couplings of the Higgs bosons to each other, to the vector gauge bosons, and to the fermions. As in the SM, the coupling to the Higgs bosons gives the fermions and vector bosons their masses. A necessary and sufficient condition for the elimination of tree-level FCNC's is that each quark of a given charge must receive its mass from at most one Higgs field. Further constraints on the 2HDM Higgs masses arise from requiring that the Higgs sector higher-order contributions to $\Delta\rho$ be small. This implies a limited mass splitting between any two Higgs bosons that couple significantly to either the Z or W bosons.

There are four distinct models possible in the general 2HDM, depending on the pattern of Yukawa couplings of the Higgs doublets to the fermions. Models of type I have all the fermions couple only to one doublet, usually chosen to be ϕ_2; ϕ_1 then decouples entirely from the fermion sector. Models of type II have the pattern of couplings found in supersymmetry where up-type quarks couple to ϕ_2 and the down-type quarks and charged leptons couple to ϕ_1. Both models of types I and II satisfy the Glashow-Weinberg theorem [40] which states that tree-level FCNC's mediated by Higgs bosons will be absent if all fermions of a given electric charge couple to no more than one Higgs doublet. Models of types III and IV violate this theorem. Models of type III are similar to those of type II but have the charged leptons couple to ϕ_2 instead of ϕ_1. Models of type IV has the quarks couple to ϕ_2 and the charged leptons couple to ϕ_1. Types III and IV couplings lead to tree-level FCNC's. There are severe constraints on such FCNC models from low-energy experiments involving K^0-$\overline{K}^0$ and B^0-$\overline{B}^0$ mixing and $K_L \to \mu^+\mu^-$ (see Section 1.4). There is therefore

little theoretical justification for these types of models, and they are ignored in most discussions, as we shall do here.

The Lagrangian density for the charged Higgs coupling to the fermion sector, assuming massless neutrinos, is:

$$\begin{aligned}\mathcal{L} &= \frac{g}{2\sqrt{2}M_W} H^{\pm}\Big[V_{ij}M_{u_i}A_u\bar{u}_i(1-\gamma_5)d_{jL} + V_{ij}M_{d_j}A_d\bar{u}_i(1+\gamma_5)d_{jR} \\ &\quad + M_\ell A_\ell \bar{\nu}_i(1+\gamma_5)\ell_R\Big] + \text{h. c.} \qquad (1.35)\end{aligned}$$

where V_{ij} are the usual CKM matrix elements, M_x is the mass of particle x, and γ_5 indicates a pseudoscalar coupling. The couplings are given by:

type I: $A_u = \cot\beta$ and $A_d = A_\ell = -\cot\beta$

type II: $A_u = \cot\beta$ and $A_d = A_\ell = \tan\beta$

As the type II couplings are the ones found in the MSSM, we will concentrate mainly on these for the remainder of the discussion. Since the type I couplings only have one Higgs doublet coupling to the fermion sector, most of the results for the fermions derived below with the type II couplings apply to the type I couplings by setting $\tan\beta = 1$. Results for the other couplings can be found in the literature [34].

The Higgs couplings to the vector bosons follow from gauge invariance and are thus independent of the couplings to fermions. The couplings of the neutral Higgs bosons ($\Phi = h^0, H^0, A^0$) to the up (u) and down-type (d) fermion pairs and the vector bosons ($V = W^\pm, Z^0$) are given below relative to the SM couplings $g_f \equiv gM_f/2M_W$ and $g_V \equiv gM_W$ or $gM_Z/\cos\theta_W$ for $V = W$ or Z, respectively

Φ	$g_{\Phi u\bar{u}}/g_f$	$g_{\Phi d\bar{d}}/g_f$	$g_{\Phi VV}/g_V$	$g_{\Phi ZA^0}/g_V$
h^0	$\dfrac{\cos\alpha}{\sin\beta}$	$-\dfrac{\sin\alpha}{\cos\beta}$	$\sin(\beta-\alpha)$	$\frac{1}{2}\cos(\beta-\alpha)$
H^0	$\dfrac{\sin\alpha}{\sin\beta}$	$-\dfrac{\cos\alpha}{\cos\beta}$	$\cos(\beta-\alpha)$	$\frac{1}{2}\sin(\beta-\alpha)$
A^0	$\gamma_5\cot\beta$	$\gamma_5\tan\beta$	0	0

From the above, all the neutral Higgs boson–vector boson couplings cannot vanish simultaneously, hence the Higgs sector cannot be completely decoupled from the electroweak sector.

There are no tree-level couplings of A^0 or $H^\pm$ to vector boson pairs VV, where V = any of W, Z, γ. Therefore the decays of the charged Higgs bosons are dominated by the couplings to the heaviest fermions of the third generation. The charged Higgs boson Yukawa coupling to fermion pairs (with all particles pointing into the vertex) is given by

$$g_{H^-t\bar{b}} = \frac{g}{2\sqrt{2}M_W}\left[M_t \cot\beta\,(1+\gamma_5) + M_b \tan\beta\,(1-\gamma_5)\right] \tag{1.36}$$

As mentioned above, the h^0, H^0 and A^0 couplings to fermions depend on $\tan\beta$ and are either enhanced or suppressed relative to the couplings in the SM. In the MSSM, the Higgs masses and couplings depend on additional parameters of the supersymmetric model that enter via virtual loops. The impact of these corrections can be significant. Including these corrections, and assuming that the sparticle masses are $\lesssim 1$ TeV, the upper bound on the lightest neutral Higgs bosons is $M_{h^0} \lesssim$ 125–130 GeV/c^2. This limit does not in general apply to non-minimal supersymmetric extensions. If additional Higgs singlet and/or triplet fields are introduced, then new Higgs self-coupling parameters appear, which are not significantly constrained by present data. However, under the assumption that all couplings stay perturbative up to the Planck scale, one finds in almost all cases that $M_{h^0} \lesssim 150$ GeV/c^2, independent of the details of the low-energy supersymmetric model [30].

Experiments at LEP are able to exclude ranges of masses for neutral Higgs particle production in these SUSY models. The current experimental lower limits on the lightest MSSM neutral Higgs are about 80 GeV/c^2 at $\tan\beta = 1$ for neutral Higgs bosons that decay to fermion pairs [15, 41].

The radiative corrections to the charged Higgs mass are typically small in the MSSM [30]. A discussion of the current constraints on the charged Higgs mass and the $\tan\beta$ parameter is deferred until Section 1.4.

The SM top quark decay $t \to W^+ b$ is discussed in the next section. If the charged Higgs boson exists with $M_{H^\pm} < M_t - M_b$, then it is possible for the top quark to decay via the channel $t \to H^+ b$. The branching fractions for these competing decay modes depend on the masses of the particles involved and on $\tan\beta$. Similarly,

the subsequent decay of this relatively light charged Higgs boson proceeds mostly through two competing channels: $H^+ \to \tau^+\nu$ or $H^+ \to c\overline{s}$. A third decay channel via a virtual top quark, $H^+ \to t^*\overline{b} \to W^+b\overline{b}$, becomes significant for $\tan\beta < 1$ and $M_{H^\pm}$ close to M_t. The other decay modes to the lighter quarks are insignificant.

The calculation of the partial widths and branching fractions for top quark decays via $W^\pm$ and $M_{H^\pm}$ bosons and the subsequent decay widths of the charged Higgs boson to $\tau\nu_\tau$ or $c\overline{s}$ in the 2HDM with MSSM couplings (type II) is shown in Appendix A. The branching fractions $\mathcal{B}(t \to H^+b)$ (from Equation A.9) and $\mathcal{B}(H^+ \to \tau^+\nu)$ (from Equation A.10) are plotted in Figure 1.5 as functions of $\tan\beta$ for various charged Higgs masses and a top quark mass of 175 GeV/c^2. In the type I 2HDM, the branching ratio of $H^+ \to \tau^+\nu$ is about 30% independent of $\tan\beta$ and corresponding to the value at $\tan\beta = 1$ in the figure. Leading logarithmic QCD corrections are included by using the renormalized masses for the quarks. The full MSSM electroweak and SUSY-QCD corrections, not shown here, would be moderate ($\lesssim 10\%$) in most cases [42].

In the region $\tan\beta \gtrsim 10$, the top quark decays to charged Higgs start to compete with the SM $t \to W^+b$ mode. In this region, the Higgs decays predominantly in the $\tau\nu_\tau$ channel. This is the channel we search for, using the subsequent tau decay to hadronic by-products. The search topology and strategy are discussed in greater detail in Chapter 3. The region of low $\tan\beta$ ($\lesssim 1$) has also been examined at CDF, using the standard top quark decays in the various leptonic decay channels (discussed in Section 1.3.3) and looking for distortions and depletions in the relative decay rates [43, 2].

1.3 The Top Quark

1.3.1 Evidence for the Top Quark

There were many indications of the top quark's existence before its discovery at the Tevatron in 1995, not to mention excitement over a slight excess in events at CERN in 1984 [44] which dissipated with higher statistics and a better understanding of

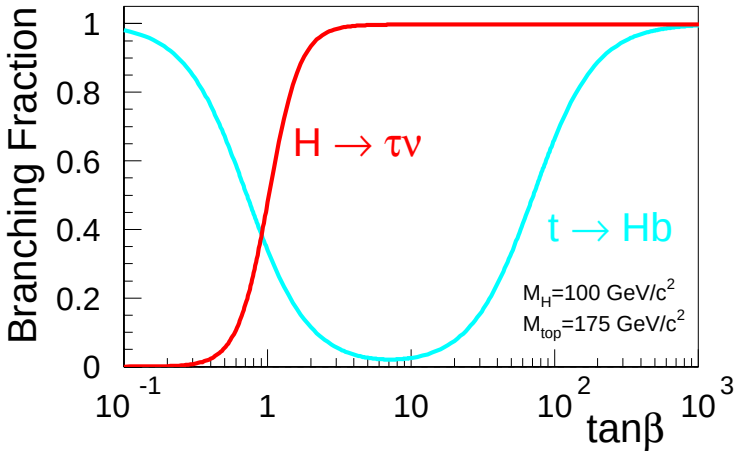

Figure 1.5: Branching fractions for $t \to H^+ b$ and $H^+ \to \tau^+ \nu$ in a type II 2HDM with M_t= 175 GeV/c^2 and $M_{H^\pm}$= 100 GeV/c^2. The analysis in this thesis concentrates on the $\tan\beta > 10$ region.

the background processes!

The discovery of the bottom quark in 1977 (through the production of the Υ $(b\bar{b})$ meson [45]) at Fermilab and the subsequent detailed measurement of its properties at e^+e^- colliders (LEP and SLAC) and at the Υ threshold by the CLEO experiment at CESR indicated that it was a member of a weak-isospin doublet in analogy to the other two quark families. This requires a weak-isospin partner — the top quark.

The establishment that the b-quark is not a weak-isospin singlet but is a member of a doublet came from several different theoretical arguments and experimental observations, a few of which are mentioned below. The reader is referred to Reference [46], a Review of Modern Physics article written by two CDF collaborators, which contains extensive discussion and details of the history leading up to and including the top quark discovery. Another earlier good review article is Reference [47].

- To have a renormalizable gauge theory of the weak interactions, anomalies arising from *triangle* diagrams (in which three external gauge bosons are attached to triangular fermion loops) must cancel for every fermion contribution. This requires $\Sigma_f T_3^f Q_f^2 = 0$, where the sum is over all fermions in a given generation, taking the three color states for each quark into account. This in turn implies $\Sigma_f Q_f = 0$. Given the existence of the b-quark and the τ lepton, a charge $+2/3$,

weak-isospin $T_3 = +1/2$ top quark is required to complete the third generation.

- The branching ratio to lepton pairs, $\mathcal{B}(b \to \ell^+\ell^- X)$, for a left-handed singlet b-quark would be a factor of approximately 10^4 greater than for a doublet, due to FCNC decays [48]. These FCNC decays are suppressed by the GIM[2] mechanism [49] if each family has the same singlet/doublet isospin structure. CLEO has measured this branching fraction to be less than 1.2×10^{-3} at 90% confidence level [50], which is at least 10 times too small to be consistent with a singlet left-handed b quark.

- The forward–backward asymmetry (A_{FB}) in b-quark production at e^+e^- colliders would be zero if the b-quark were a singlet instead of the measured value which is within 10% of the expected SM asymmetry prediction of 0.0997 [51].

- The measured width of the decay of Z^0 bosons to pairs of b-quarks, , ($Z^0 \to b\overline{b}$) (see Section 1.5.3), is consistent only with a weak-isospin $T_3 = -1/2$ quark [52].

- Finally, the observed rate of B^0–$\overline{B}^0$ meson mixing, which arise from second-order weak interactions (so called *box* diagrams — see Section 1.5.4), includes a significant contribution from the exchange of massive virtual top quarks, necessitating the top quark's existence [53].

The mass of the top quark is not determined in the SM but is a free parameter, like the other fermion masses, and must be measured. Precision electroweak measurements give an indirect measure of the top mass from the contributions from leading order one-loop correction diagrams to the boson masses, M_Z and M_W. A fit to the electroweak measurements made at LEP from 1989–93 data favored a top quark of $M_t = 177 \pm 11^{+18}_{-19}$ GeV/c^2 [54]. The second error reflects the uncertainty in the SM Higgs mass; a range of 60–1000 GeV is used in the calculation.

Direct evidence for top quark production from $p\overline{p}$ collisions at $\sqrt{s} = 1.8$ TeV

[2]The GIM mechanism requires that all the right-handed and left-handed quarks in different generations having the same electric charge to also have the same weak-isospin.

was first seen at CDF in 1994 [55] in the Run 1A data (using 19.3 pb^{-1} of integrated luminosity) with the firm discovery published by both CDF and DØ in April 1995 [13, 14]. The discoveries used combined data sets from Run 1A and part of Run 1B: 67 pb^{-1} of integrated luminosity for CDF and 50 pb^{-1} for DØ. The discovery channels were the *dilepton* and *lepton + jets* modes, which are described in Section 1.3.3. Each experiment had roughly a 5σ excess of $t\bar{t}$ candidate events over the background. Both experiments also reconstructed peaks in the mass distribution corresponding to the top quark mass. The current status of the production cross section and mass measurements is discussed in Section 1.3.4.

1.3.2 Top Quark Production

At the Tevatron's Run 1 $p\bar{p}$ center-of-mass energy of $\sqrt{s} = 1.8$ TeV, top quarks are dominantly produced in pairs from pure QCD processes: $q\bar{q} \rightarrow t\bar{t}$ and $gg \rightarrow t\bar{t}$. The quark annihilation process dominates at the Tevatron energies. To produce the heavy top quark pair, the initial partons must carry a large fraction of the total momentum of the proton and antiproton. Since the gluons typically carry only a small fraction of the total momentum, the gluon fusion process is suppressed. The theoretical predictions for the cross sections through these channels is approximately 5 pb at $M_t = 175\ \mathrm{GeV}/c^2$, with a dominant 90% contribution from the $q\bar{q}$ annihilation process.

Single top production mechanisms such as $q\bar{q}' \rightarrow W^* \rightarrow t\bar{b}$ and $qg \rightarrow q't\bar{b}$ (via W–gluon fusion — see Reference [46]) have about a 2.5 pb production cross section [56]. Figure 1.6 shows the lowest order Feynman diagram for Drell-Yan production of a single top quark. Due to the reduced cross sections for these processes and the low experimental acceptance in the final charged Higgs kinematic and topological selection (see Chapter 3), single top production processes are not considered further in this thesis.

The leading order Feynman diagrams for the $p\bar{p} \rightarrow t\bar{t} + X$ processes are shown in Figure 1.7. Other processes, for example gluon-quark scattering, can contribute at higher order. The relative importance of the quark and gluon diagrams depends on

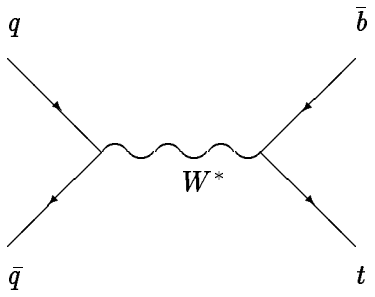

Figure 1.6: Lowest order Feynman diagram for Drell-Yan production of $t\bar{b}$, $p\bar{p} \rightarrow W \rightarrow t\bar{b}$.

the top quark mass, M_t. Understanding and correctly modelling the gluon radiation in $t\bar{t}$ events is crucial for a precise determination of the top mass.

Due to the large top quark mass, large momentum transfer (q) interactions are required at the Tevatron energies to produce top quark pairs, where $q^2 \gg \Lambda^2_{QCD}$. Hence the cross section for top quark pair production can be calculated in perturbative QCD. The total inclusive cross section for heavy quark production can be written as a product of the parton distribution functions (PDF) inside the proton (and antiproton) and the parton-parton point cross section [57] :

$$\sigma(p\bar{p} \rightarrow t\bar{t}) = \sum_{i,j} \int dx_i F_i(x_i, \mu^2) \int dx_j F_j(x_j, \mu^2) \hat{\sigma}_{ij}(\hat{s}, \mu^2, M_t). \qquad (1.37)$$

The sum is over the individual contributions from the parton components (quarks, antiquarks, and gluons) of the proton (i) and antiproton (j), respectively. F_i (F_j) is the PDF evaluated at a momentum scale μ, for a parton with a momentum fraction x_i (x_j) of the incoming proton (antiproton) momentum, P ($-P$), in the center-of-mass frame. The integrations are over the two parton momentum fractions, x_i and x_j.

The function $\hat{\sigma}_{ij}$ is the total short distance cross section for the process $i + j \rightarrow t\bar{t}$. It is calculated from the Feynman diagrams representing the production of the top quark pairs (Figure 1.7 shows the lowest order diagrams). The square of the center-of-mass energy in the i-j parton system $\hat{s}$ is related to the $p\bar{p}$ center-of-mass energy, s, by $\hat{s} = 4x_i x_j P^2 = x_i x_j s$.

The cross section for the $q\bar{q} \rightarrow t\bar{t}$ subprocess, which dominates at high top mass,

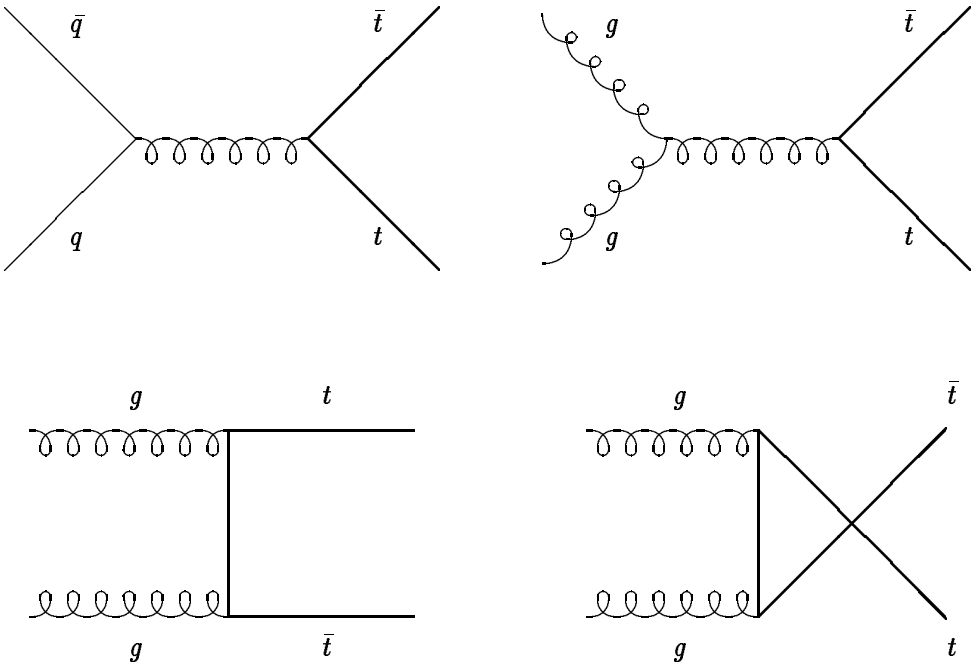

Figure 1.7: Lowest order Feynman diagrams (leading order in α_s^2) for production of $t\bar{t}$ pairs in $p\bar{p}$ collisions. The first diagram represents the $q\overline{q}$ annihilation mechanism and the remaining are gluon–gluon (gg) fusion.

is given at lowest order by (see for example Reference [58]) :

$$\hat{\sigma}_{q\overline{q}} = \frac{8\pi\alpha_s^2}{27\hat{s}}\sqrt{1-\frac{4M_t^2}{\hat{s}}}\left(1+\frac{2M_t^2}{\hat{s}}\right) \tag{1.38}$$

At threshold, where $\hat{s} \sim 4{M_t}^2$, the cross section from gg processes actually dominates the $q\overline{q}$ processes by about a factor of 3. However, the $t\bar{t}$ cross section also depends on the parton luminosities or, equivalently, the parton structure functions, F_i. The quark-quark luminosity dominates the gluon-gluon luminosity for $M_t \gtrsim 100$ GeV/c^2, at the high x needed for top production. After folding in the relative effects of these parton luminosities the relative contribution from $q\overline{q}$ to gg processes to the total $t\bar{t}$ cross section is about 5 to 1 for a top mass in the region of 175 GeV/c^2.

In most calculations, the factorization scale is chosen to be the same as the renormalization scale, μ. This is normally taken to be of order the top mass, M_t. The sensitivity of the perturbative calculations to reasonable variations in μ is used as an estimate of the accuracy of the prediction for the total cross section. F_i and F_j are extracted from parameterizations of fits to experimental results, mostly from

deep inelastic scattering.

In addition to the uncertainty in the renormalization scale, there is the uncertainty due to the limited knowledge of the input parton distribution functions, F_i, and the assumed value of the QCD parameter Λ_{QCD}. The Λ_{QCD}–dependence arises from the fact that the assumed value of Λ_{QCD} affects the μ^2 evolution of both the strong coupling, α_s, and the quark and gluon distributions. It is particularly important in the extraction of the gluon distribution functions from deep inelastic scattering data. The total theoretical uncertainty on the $t\bar{t}$ production cross section at $\sqrt{s} = 1.8$ TeV is estimated to be of order 20% with about equal contributions from the scale and parton distribution uncertainties.

Full next-to-leading order (NLO) (i.e. of $\mathcal{O}(\alpha_s^3)$) cross section calculations of $\hat{\sigma}$ have been made [58, 59] and the total $\sigma(p\overline{p} \rightarrow t\bar{t})$ has then been calculated by convoluting this partonic cross section with parameterizations of the parton distribution functions [60, 61]. Refinements have been made by including corrections due to initial-state gluon bremsstrahlung, which are large near the $t\bar{t}$ threshold [62, 63]. These corrections are resummed to all orders in perturbative QCD. This procedure introduces a new infrared cutoff scale $\mu_0 \gg \Lambda_{QCD}$ where the calculation is terminated to avoid the dominant nonperturbative effects as $\mu_0 \rightarrow 0$. The corrections from gluon bremsstrahlung are positive at all orders of the perturbative calculation. Therefore, the lower limit on the $t\bar{t}$ cross section is estimated by the sum of the full $\mathcal{O}(\alpha_s^3)$ prediction and the $\mathcal{O}(\alpha_s^4)$ soft gluon correction, using the conservative value of $\Lambda_{QCD} = 105$ MeV. The best estimate of the cross section includes the full effects of gluon resummation. The dominant source of uncertainty is in the choice of μ_0.

A more recent calculation, also including the perturbative resummation of gluon radiative corrections, has been performed using the Principal Value Resummation (PVR) techniques [64, 65]. This method is independent of the arbitrary infrared cutoff μ_0. The effects of the gluon resummation have been shown to contribute less than previously thought [66].

Table 1.4 summarizes the results of the various recent calculations of the $p\bar{p} \rightarrow t\bar{t}$ cross section at the Tevatron energies for a top mass of 175 GeV/c^2, which are in

Calculation	$\sigma(p\bar{p} \rightarrow t\bar{t})$ (pb)
Ellis 1991 [61]	$4.20^{+0.28}_{-0.54}$
Laenen *et al.* 1994 [63]	$4.94^{+0.71}_{-0.45}$
Berger and Contopanagos, 1995 [64]	$5.52^{+0.07}_{-0.45}$
Catani *et al.*, 1996 [65]	$4.75^{+0.63}_{-0.68}$

Table 1.4: Summary of the most recent calculations of the $p\bar{p} \rightarrow t\bar{t}$ total cross sections at $\sqrt{s} = 1.8$ TeV for $M_t = 175$ GeV/c^2.

the range 4–6 pb. The calculations are also shown in Figure 1.8 which shows the $t\bar{t}$ production cross section predictions as a function of the top mass, along with the measured values from CDF and DØ (see Section 1.3.4).

Note that the total inelastic cross section for $p\bar{p}$ collisions at $\sqrt{s} = 1.8$ TeV is about 50 mb which is approximately ten orders of magnitude higher than the $t\bar{t}$ production cross section. Obviously detecting top quarks against this background is a formidable challenge and both excellent background rejection and high luminosities are critical.

1.3.3 Standard Model Top Quark Decay

As discussed in the section on QCD (Section 1.1.3), quarks are not observed as free particles but are confined to form hadronic bound states. The top quark however is unique in that its mass is high enough that it can decay before hadronization. In the Standard Model, a top quark decays via the charged weak current into a real W boson and a b quark ($t \rightarrow W^+b$). The W boson is real due to the large top mass. Decay modes such as $t \rightarrow W^+s$ and $t \rightarrow W^+d$ are also allowed in the SM, but their rates are suppressed relative to the $t \rightarrow W^+b$ decay mode by factors of $|V_{ts}|^2/|V_{tb}|^2 \approx 10^{-3}$ and $|V_{td}|^2/|V_{tb}|^2 \approx 5$ x 10^{-4} respectively, where V_{ij} denote the CKM mixing-matrix elements (see Section 1.1.4) [8]. Therefore, the SM top decays to Wb with a branching fraction very close to unity.

The two-body partial decay width for the top quark, , ($t \rightarrow W^+b$), is given in

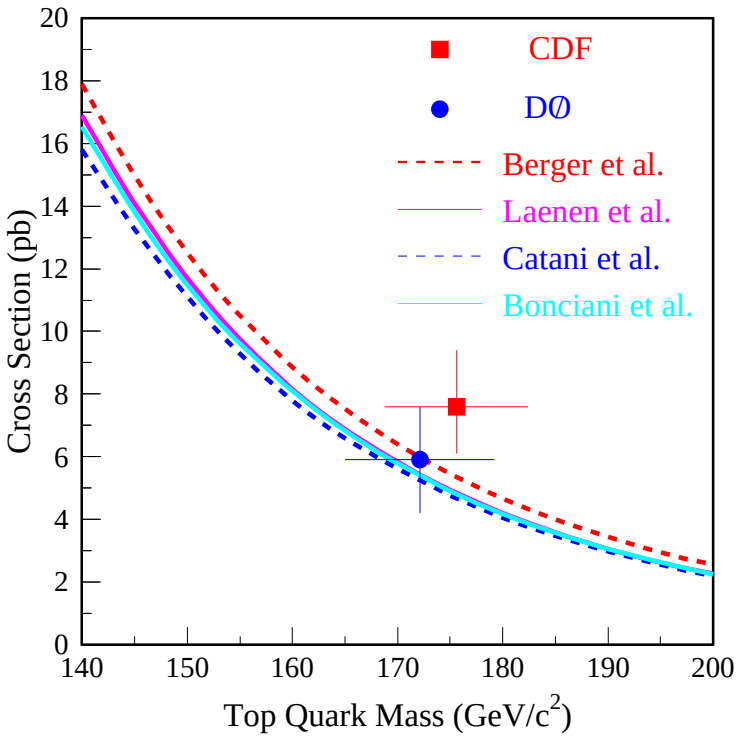

Figure 1.8: Theoretical predictions for the top production cross section versus top mass. The measured masses and cross sections at CDF and DØ are shown. This figure is from Reference [67].

Equation A.1. Taking $|V_{tb}| = 1$, and assuming M_t, $M_W \gg M_b$, the width becomes :

$$, (t \to W^+ b) \approx 175 \text{ MeV } \left(\frac{M_t}{M_W}\right)^3 . \tag{1.39}$$

For a top mass of 175 GeV/c^2, , $(t \to W^+ b) \approx 1.55$ GeV. The corresponding lifetime is $\tau = (1/,) \approx 4 \times 10^{-25}$ sec. This very short decay time means that the top quark is expected to decay before top-flavored hadrons or $t\bar{t}$ quarkonium bound states can form. Hadronization, which is a non-perturbative process, is characterized by the typical hadronic time scale of $\mathcal{O}(1 \text{ fm}/c) \approx \mathcal{O}(\Lambda_{QCD}^{-1}) \approx \mathcal{O}(10^{-23} \text{ sec})$ [68], i.e. about ten times longer than the time scale for the top decay. The exceedingly short top-quark lifetime is due to the very large top mass, especially in the large mass-splitting between M_t and M_b, and to the lack of any CKM suppression in the main decay mode. If QCD radiative corrections are included, the partial width as determined by Equation A.1 is reduced by only about 10% [69].

Because of the short decay time, the top decays essentially as a free quark and

hence will "remember" its original spin-1/2 state; its spin will be manifest in the angular distribution of its decay products [70]. This is in contrast to the expected isotropic angular distribution of the b quark decay products as a result of b quark fragmentation, typically to a spin-0 meson, before decaying. It is also worth mentioning that the SM top decay is dominated by longitudinally polarized W bosons, a measurement of which could be sensitive to new physics. It is expected that for the decay $t \to W^+b$, longitudinal W bosons (helicity $= 0$) are favored over left-handed W bosons (helicity $= -1$) by a factor of $M_t^2/2M_W^2 \approx 2.4$ [71]. The helicity $= +1$ amplitude for W bosons is essentially zero, as right-handed W bosons are forbidden from top decay if one assumes $M_b \approx 0$. For a top mass of 175 GeV/c^2, it is expected that 70% of the W bosons emitted from top decay will be longitudinally polarized. If X_L is the fraction of longitudinally polarized W bosons, then the decay angular distribution of the leptons in the W rest frame is given by:

$$dN/d\cos\theta^* \propto (1 - X_L)(1 - \cos\theta^*) + 2X_L \sin^2\theta^* \ , \tag{1.40}$$

where θ^* is the angle between the lepton momentum vector in the W rest frame and the W momentum vector in the top rest frame. The first term comes from the helicity $= -1$ decay amplitude for $W \to \ell\nu_\ell$, and the second term from the helicity $= 0$ amplitude.

This angular distribution of the top decay products will be discussed further in Chapter 3 in reference to the top quark decays to charged Higgs scalar bosons.

In discussing the experimental measurements of top quarks, the decay mode of the top quark pair is characterized by the decay modes of the W bosons. The top decays to Wb and the subsequent decay of the W's to pairs of fermions is shown in Figure 1.9. At tree level, the W couples with equal strength to leptons and quarks, so each W decay mode occurs with roughly equal probability. There are three leptonic channels ($e\nu$, $\mu\nu$, and $\tau\nu$), and six hadronic channels available ($u\bar{d}$ and $c\bar{s}$, with three possible color assignments), hence each decay mode has a branching ratio of $\sim 1/9$. Explicitly, these are:

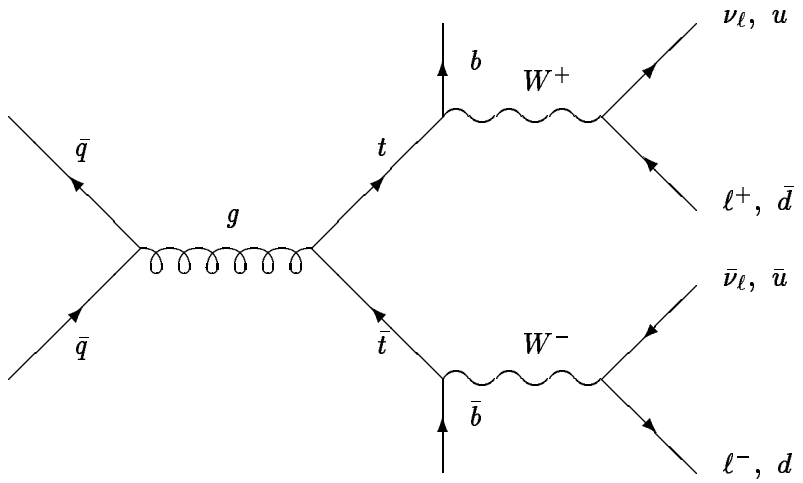

Figure 1.9: Feynman diagram for top pair production and decay in the SM. The decay modes for the W bosons are indicated into lepton-neutrino or an up-type (u) and down-type (d) quark pair.

$$\begin{aligned} W^+ &\longrightarrow (e^+\nu_e)(\mu^+\nu_\mu)(\tau^+\nu_\tau)(u\overline{d})(c\overline{s}) \\ W^- &\longrightarrow (e^-\overline{\nu}_e)(\mu^-\overline{\nu}_\mu)(\tau^-\overline{\nu}_\tau)(\overline{u}d)(\overline{c}s) \end{aligned} \tag{1.41}$$

QCD corrections enhance the branching ratios of the hadronic modes by a factor of $(1 + \alpha_s/\pi) \approx 1.05$.

The top quark decays are listed in Table 1.5 as characterized by their experimental signatures and with their lowest-order SM branching fractions.

The *dilepton* mode, where each W boson decays into a $e\nu$ or $\mu\nu$ pair, is experimentally characterized by two high-momentum charged leptons, substantial missing energy from the two undetected neutrinos and two jets from the fragmentation of the b quarks. This category provides the cleanest signal (with $\sim 2.5 : 1$ ratio for signal over background) and was the discovery channel for the top, but it also has the smallest branching ratio of $\sim 5\%$.

The *lepton + jets* category has one W boson decaying to $e\nu$ or $\mu\nu$ and the other decaying hadronically. This occurs about 30% of the time. The signal for this category is therefore a single high-momentum lepton, missing energy from the undetected

	Decay mode	Branching ratio
All jets	$t\bar{t} \to q\bar{q}\ q\bar{q}\ b\bar{b}$	36/81
Lepton + jets	$t\bar{t} \to q\bar{q}\ \ell\nu\ b\bar{b}$	24/81
Tau + jets	$t\bar{t} \to q\bar{q}\ \tau\nu\ b\bar{b}$	12/81
Dilepton	$t\bar{t} \to \ell\nu\ \ell\nu\ b\bar{b}$	4/81
Tau dilepton	$t\bar{t} \to \ell\nu\ \tau\nu\ b\bar{b}$	4/81
Ditau	$t\bar{t} \to \tau\nu\ \tau\nu\ b\bar{b}$	1/81

Table 1.5: Decay modes for a $t\bar{t}$ pair and their lowest order branching ratios assuming Standard Model decays. They are grouped according to the decay mode of the W bosons. Here $\ell\nu$ refers to $e\nu$ or $\mu\nu$ decay modes only, with the tau decay modes listed separately.

neutrino, and four jets: two from the b quarks, and two from the hadronic W decay. Both CDF and DØ use techniques to identify the b quark jets and kinematic requirements to observe a signal above the background.

In the *all jets* mode, both W bosons decay hadronically. The resulting final state then is nominally made up of six jets, two from the b quark decays, with no leptons and low missing energy. Therefore, although the branching ratio for this category is the largest (44%), it faces formidable QCD backgrounds making the extraction of the $t\bar{t}$ signal difficult. CDF has succeeded in observing a signal in this channel by requiring tight kinematical cuts on the jets, and with at least one jet identified as originating from a b quark [72, 73]. Another separate CDF analysis requiring double b-tagged events and large amounts of energy has also had success in observing a $t\bar{t}$ signal [74].

These three categories of W decay modes represent the standard $t\bar{t}$ analyses. In 21% of the cases, however, the $t\bar{t}$ pair decays into a final state containing at least one τ lepton. These are normally excluded in the standard analyses because of the added difficulty in identifying a τ decay from either its leptonic or hadronic decay products amidst the background sources (see Section 3.1 for a description of tau decay modes). A separate analysis at CDF looking in the tau-dilepton mode has been conducted which measured a top production cross section that is consistent with those measured in other channels [75, 76].

	Method	$t\bar{t}$ Cross Section (pb)	Top Mass (GeV/c^2)	Reference
CDF	Lepton + jet (SLT)	$9.2^{+4.3}_{-3.6}$		[77]
	Lepton + jet (SVX)	$6.2^{+2.1}_{-1.7}$	$175.9 \pm 4.8 \pm 4.9$	[78, 79], [80]
	Dileptons	$8.5^{+4.4}_{-3.4}$	$161 \pm 17 \pm 10$	[81, 82], [81]
	All jets (≥ 1 SVX)	$9.6^{+4.4}_{-3.6}$	$186 \pm 10 \pm 12$	[83, 84]
	All jets (≥ 2 SVX)	$11.5^{+7.7}_{-7.1}$		[73]
	Tau dilepton	10^{+16}_{-10}		[75, 76]
	Combined	$7.6^{+1.8}_{-1.5}$	$176.8 \pm 4.4 \pm 4.8$	[85]
DØ	Lepton + jets	4.1 ± 2.1	$173.3 \pm 5.6 \pm 6.2$	[86],[87]
	Lepton + jets/μ	8.3 ± 3.6		[86]
	Dileptons + $e\nu$	6.4 ± 3.4	$168.4 \pm 12.3 \pm 3.7$	[86],[88]
	All jets†	7.1 ± 3.2		[89]
	Combined	5.9 ± 1.7	$172.1 \pm 5.2 \pm 4.9$	[86],[90]

Table 1.6: Results from CDF and DØ top quark measurements in the Run 1 data. The uncertainties for the mass results are statistical first, then systematic. †Preliminary result.

1.3.4 Top Quark Measurements

Top quark production has been measured in a number of different channels at both CDF and DØ in the Run 1 data. The top quark mass has also been determined in some of these channels. CDF analyses typically use an integrated luminosity of ~ 109 pb^{-1} and DØ uses ~ 125 pb^{-1}. Tables 1.6 lists a summary of these results. Details can be found in the references. The relevant CDF theses are also listed where appropriate. The results for the cross sections are also summarized in Figure 1.10 and compared to the theoretical predictions. The mass measurements are summarized in Figure 1.11.

Both collaborations have reported results in the dilepton, lepton + jets and all jets modes. CDF also has a result in the tau-dilepton channel. Cross sections are reported at a top mass of 175 GeV/c^2 for CDF and at 172 GeV/c^2 for DØ.

CDF uses two techniques in the lepton + jets channel. One uses a *soft-lepton tagging* (SLT) technique to identify muons in semileptonic decays of the b-quark.

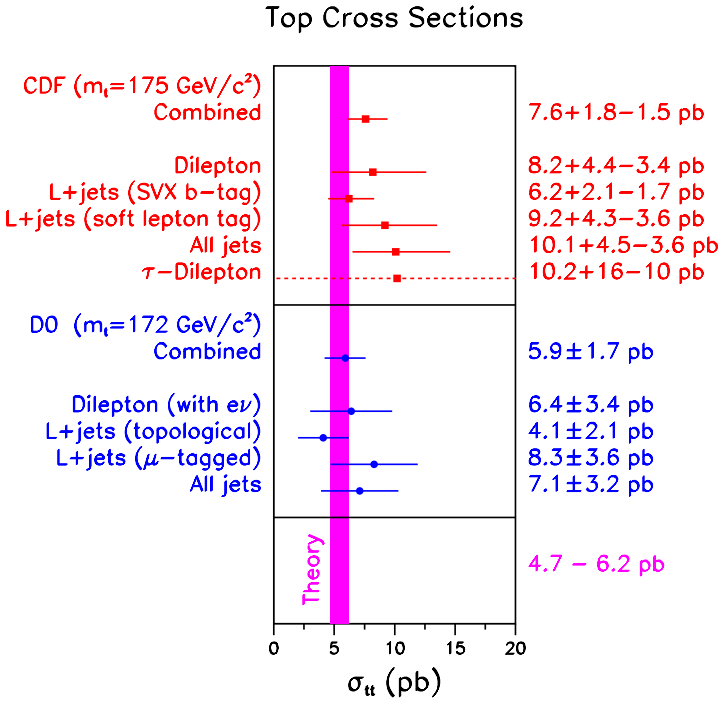

Figure 1.10: Measured values of the $t\bar{t}$ production cross section from CDF and DØ in the various channels. This figure is from Reference [67].

The other uses the high-precision silicon vertex detector (SVX — described in Section 2.5.1) to identify secondary decay vertices resulting from the long-lived b quarks. This is known as *secondary vertex tagging* — see Section 5.8 for a description of this technique.

The dilepton channel at DØ consists of two orthogonal searches: a search for two charged leptons (e or μ) or for $e\nu$ via a high-p_T electron, large missing energy and two or more jets. They also use two methods in the lepton + jets channel: the first uses topological and kinematical cuts, the second uses a similar method to CDF's SLT technique to identify low momentum muons coming from bottom-quark decays.

CDF used two independent analyses in the all jets channel: one uses a single SVX b-tag and strict kinematic requirements, the other uses two or more SVX b-tags.

The combined cross section result for CDF is $7.6^{+1.8}_{-1.5}$ pb [85]. For DØ, the combined result is 5.9 ± 1.7 pb [86].

The top quark mass is also reconstructed from the lepton + jets, dileptons and all

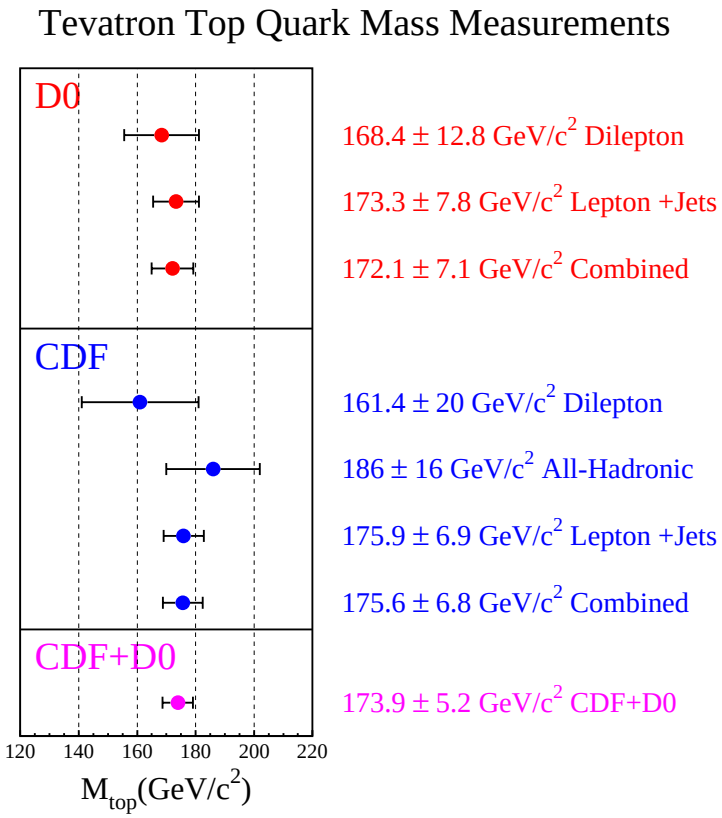

Figure 1.11: Latest measured values of the top mass from CDF and DØ. This figure is from Reference [91].

jets channel under the $t\bar{t}$ hypothesis using constrained fits and likelihood estimations. For CDF, the combined measurement is $M_t = 176.8 \pm 4.4 \pm 4.8$ GeV/c^2, and for DØ $M_t = 173.3 \pm 5.6 \pm 6.2$ GeV/c^2, where the first uncertainty is statistical and the second is systematic. Taking correlations in systematic uncertainties into account, the preliminary combined CDF/DØ top mass measurement is 173.9 ± 5.2 GeV/c^2. A joint CDF/DØ working group is working on finalizing the combined result.

1.4 Limits on Charged Higgs Bosons from Direct Searches

There have been a number of direct searches for a charged Higgs signature at colliders.

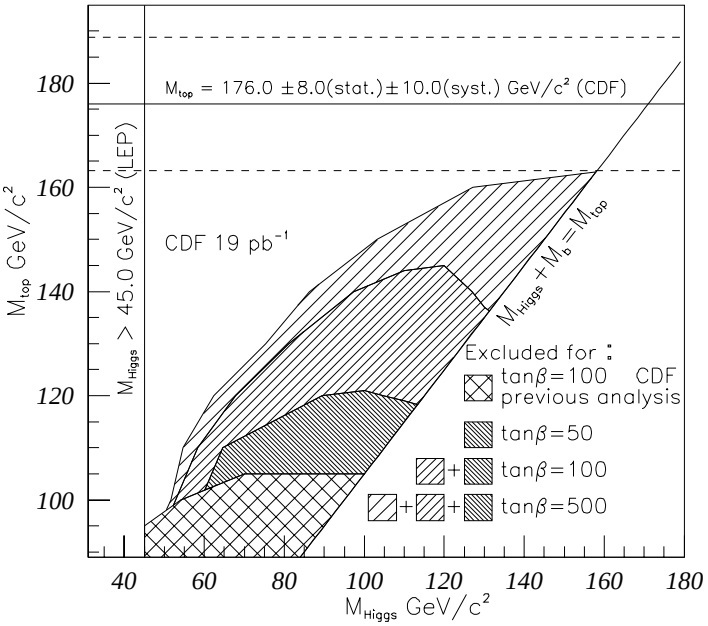

Figure 1.12: Limits on charged Higgs mass plotted in the $M_{H^\pm}$—M_t plane from the CDF Run 1A analyses. The LEP limits at the time of this publication were $M_{H^\pm} > 45$ GeV/c^2.

1.4.1 Previous CDF Limits

All searches at CDF have been for the production of top quark pairs and their subsequent decays via a charged Higgs boson and bottom quark. Initial interest in the late 1980's at CDF in the charged Higgs was because of the possibility that it would provide an alternative decay channel for a light top quark (via $t \to H^+ b$), and therefore searches for SM top decay signatures might have missed detecting the top. As the charged Higgs couplings are dependent on $\tan\beta$, these searches could only set limits in regions of parameter space where large couplings of the charged Higgs to the top quark are expected. A search in the 1988-1989 CDF data for a charged Higgs with mass below the W mass was reported in 1994 in Reference [92]. The latest results prior to the analysis presented in this dissertation were based on the CDF Run 1A data consisting of 19 pb^{-1} of data. A search in these data for taus coming from charged Higgs decays with the tau decaying to leptonic decay products was reported in Reference [93]. A more sensitive search for tau decays of the charged Higgs with the tau decaying hadronically was reported in 1996 in Reference [94] as

well as in C. Couyoumtzelis's thesis [95]. This search was begun before the top quark discovery and therefore set limits in the $M_{H^\pm}$–M_t mass plane. The final results plot from this search is shown in Figure 1.12. The search did not have enough sensitivity to set limits in the region of the current known top mass, but fell just short for large values of $\tan\beta$ and the charged Higgs mass.

1.4.2 Limits from Direct Searches in e^+e^- Collisions

The LEP experiments have taken data with e^+e^- collisions up to $\sqrt{s} = 183$ GeV. In the strict MSSM, where we expect $M^2_{H^\pm} \approx M^2_A + M^2_W$, the LEP energies are insufficient to produce charged Higgs pairs. However, further extensions beyond the MSSM might allow this channel.

In these collisions, charged Higgs pairs are expected to be produced directly via couplings to the Z boson or the photon, $e^+e^- \rightarrow Z/\gamma \rightarrow H^+H^-$. The LEP experiments then look for the subsequent decay signatures of charged Higgs decaying into either $H^+ \rightarrow \tau^+\nu$ or $H^+ \rightarrow c\bar{s}$. The non-observation of such a signal over the background provides the most stringent, model-independent limits on the charged Higgs boson so far. Experimentally, the signature is difficult to extract due to WW contamination which provides the same decay modes into $c\bar{s}$ and $\tau\nu$. The limits reported are, in general, independent of the branching ratios of the charged Higgs decays.

The published charged Higgs boson mass limits from the most recent LEP experiments are shown in Table 1.7. These result from running at center-of-mass collision energies of $\sqrt{s} = 130$–172 GeV, with a total integrated luminosity of ~ 25 pb^{-1} for each LEP experiment.

1.5 Indirect Limits on Charged Higgs Bosons

In addition to direct searches for the production of new particles, the presence of an extended Higgs sector or other new particles might be inferred by examining

Experiment	Lower bound on $M_{H^\pm}$ at 95% C.L.	Reference
DELPHI	54.5 GeV/c^2	[96]
ALEPH	52.0 GeV/c^2	[97]
OPAL	52.0 GeV/c^2	[98]
L3†	41.0 GeV/c^2	[99]

Table 1.7: Limits at 95% confidence level on the mass of the charged Higgs boson ($M_{H^\pm}$) from the LEP II experiments. †The L3 result is from LEP I only, running at the Z^0 resonance ($\sqrt{s} = 91$ GeV).

deviations from SM predictions in precision measurements. It is also possible processes that are rare or forbidden in the SM might be enhanced by the presence of these other particles, leading to complementary, indirect methods for observing new physics at relatively low energies. Both these scenarios have been pursued with the increasing number of precision measurements coming from e^+e^- colliders (e.g. LEP, CLEO, SLAC, etc.).

Theoretical considerations also offer constraints on the allowed parameter space in these models. The parameter $\tan\beta$ is constrained to yield perturbative Yukawa couplings of the Higgs bosons to the fermion sector. In general, $\tan\beta$ values much greater than $\sim 10^2$ or less than $\sim 10^{-1}$ are disfavored as they tend to lead to large non-perturbative contributions, yielding unphysical couplings and widths.

In the 2HDM of type II, the mass hierarchy $M_t \gg M_b$ tends to favor large $\tan\beta$ due to the couplings of Φ_2 to the up-type quark sector (which are proportional to v_2) and Φ_1 to the down-type quarks (proportional to v_1). The large top quark mass, in combination with the enhancement of the top Yukawa coupling for small values of $\tan\beta$ (see Equation 1.36) also tend to give lower bounds on $\tan\beta$. In type I models, where all the fermion couplings are to only one of the Higgs doublets, the couplings are all the same and are proportional to the quark masses; hence, the Yukawa couplings of the bottom quark are negligible compared to those of top quark regardless of the value of $\tan\beta$.

Precision measurements of electroweak current processes (e.g. decays via the $W^{\pm}$ or Z^0 bosons) are sensitive to other bosons that might mediate the same interactions. Those involving the $W^{\pm}$ boson especially might be affected if the charged Higgs boson exists. Measurements involving the heavier fermions, in particular, are also sensitive to the charged Higgs existence due the Higgs coupling to mass. There are model dependent limits from leptonic decays of the tau lepton and the bottom quark, which are discussed in Sections 1.5.1 and 1.5.2. Precision measurements of the Z^0 boson decays, especially of those to $b\overline{b}$ pairs, are also sensitive to other bosons through loop contributions. This is discussed in Section 1.5.3.

Constraints on the elements of the CKM matrix and in particular on the CP-phase angle are usually derived under the assumption of the SM but these could be affected fairly dramatically due to the presence of extra Higgs doublets or other SUSY particles [100]. The observed CP violation behavior can be influenced without necessarily introducing new sources of CP violation. The mixing rates in B^0-$\overline{B}^0$ and K^0-$\overline{K}^0$ meson systems, as discussed in Section 1.5.4, provide good testing grounds for these contributions and give constraints on the charged Higgs boson.

As discussed in Section 1.1.4, flavor-changing neutral currents (FCNC) are suppressed at the tree-level in Standard Model processes. These processes do occur at the loop level however, which makes them particularly sensitive to the gauge structure of the theory. In particular, there can be sizable loop-level contributions in the B-sector compared to other meson systems due to the presence of the massive top quark. The large mass-splitting between the top and bottom quarks means the GIM cancellations are not exact at the level of radiative corrections. The diagonal nature of the CKM matrix, which gives $|V_{tb}| \simeq 1$, means the coupling to top–bottom pairs in electroweak processes is dominant. Therefore, FCNC processes in the B-sector can occur at reasonable rates in the SM. Experimentally, these processes are particularly suited to determining the fundamental parameters of the SM, such as the CKM matrix elements and leptonic decay constants.

Many classes of new models can also give significant and testable contributions to these rare B transitions, particularly those involving the heavier generations.

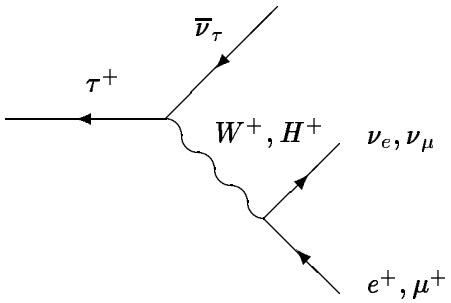

Figure 1.13: Feynman diagram for tau decay to leptons (e or μ). The charged Higgs boson (H^+) is a scalar in contrast to the vector W^+.

The FCNC $b \to s\gamma$, discussed in Section 1.5.5, gives some of the strongest, model-dependent, constraints on the charged Higgs boson. The case of $b \to s\gamma$ has been studied extensively. Radiative B decays have become one of the exciting forefronts in particle physics due to recent progress on both the theoretical and experimental fronts in recent years.

1.5.1 Limits on Charged Higgs from Tau Decay

The tau lepton decays to leptonic decay products, i.e. $\tau^+ \to \overline{\nu}_\tau e^+ \nu_e$ or $\tau^+ \to \overline{\nu}_\tau \mu^+ \nu_\mu$ are mediated by the charged electroweak vector current (W^+) in the SM. A charged Higgs scalar (H^+) would contribute to the tau decay at tree-level and would be chirality blind compared to the contributions from the W vector boson which only couples to left-handed fermions and right-handed antifermions. These decays are shown in Figure 1.13. Note that the Higgs boson is a scalar whereas the W is a vector (this is discussed further in Section 3.1). Based on the Lorentz structure of these charged weak currents in tau decays and the experimentally determined branching ratios in leptonic decays to e and μ, a lower limit of $M_{H^\pm} > 1.5 \tan\beta$ GeV/c^2 at 90% confidence level has been calculated in Reference [101] and $M_{H^\pm} > 1.86 \tan\beta$ GeV/c^2 at 95% confidence level in Reference [102].

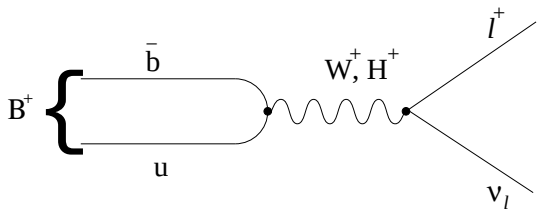

Figure 1.14: Feynman diagram for pure leptonic $B^+ \to \ell^+\nu$ decay.

1.5.2 Leptonic Decays of Bottom Mesons

A Feynman diagram for the pure leptonic decay of a B meson is shown in Figure 1.14. The SM transition rate for the purely leptonic decays $B \to \ell\nu_\ell$ is helicity suppressed and yields tiny branching fractions in the SM [100]. Current experimental 90% confidence level upper bounds on $\mathcal{B}(B^+ \to \tau^+\nu_\tau)$ are 1.8×10^{-3} from CLEO [103] and 5.7×10^{-4} from L3 [104], which are an order of magnitude above the SM prediction of 6.6×10^{-5} [100]. In models with an enlarged Higgs sector, tree-level charged Higgs exchange (H^+ in Figure 1.14) can also mediate this transition. In the type II 2HDM the SM branching fraction is multiplied by a factor $\left(\tan^2\beta\, M_B^2/M_{H^\pm}^2 - 1\right)^2$ [100]. The mass of the charged Higgs cannot be too small or $\tan\beta$ too large without exceeding the experimental limits.

The L3 bound on $B \to \tau\nu_\tau$ then gives an lower bound for the charged Higgs mass of $M_{H^\pm} > 2.63\tan\beta$ GeV at the 90% confidence level. ALEPH has also measured the inclusive branching fraction for the decay $B \to X\tau\nu_\tau$ (shown in Figure 1.15) to be $2.75\pm0.48\%$ [105] which yields a similar constraint of $M_{H^\pm} > 1.9\tan\beta$ GeV [106], which is independent of some of the theoretical uncertainties mentioned above. However, this bound could be weakened in the MSSM due to one-loop QCD corrections mediated by the exchange of SUSY particles [107]. In particular, this limit could be evaded completely for positive values of the Higgsino mixing parameter, μ.

1.5.3 Limits from Z^0 Boson Decays

The decay width of the Z^0 boson to fermions , $(Z^0 \to f\bar{f})$ is sensitive to radiative corrections to the couplings through self-energy and vertex corrections. The Z^0

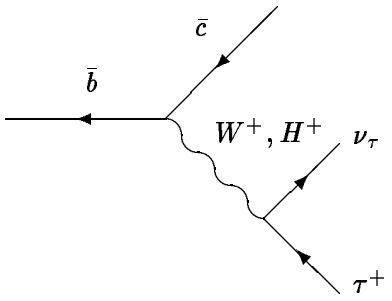

Figure 1.15: Feynman diagram for leptonic decay $\bar{b} \to \bar{c}\tau^+\nu_\tau$.

width into b quarks is of particular interest because of the presence of virtual top quarks in the vertex correction and because of the sensitivity to new physics which couples primarily to the heavy families. This width is normally measured as the ratio

$$R_b \equiv , (Z^0 \to b\bar{b})/, (Z^0 \to \text{all hadrons}). \tag{1.42}$$

Corrections to R_b from extended Higgs models can be used to constrain $\tan\beta$ and the charged Higgs mass, and, to a lesser extent, the mixing angle α and the neutral Higgs masses. In the 2HDM, radiative correction diagrams involving charged Higgs exchanges enter negatively and suppress R_b for small values of $\tan\beta$. This suppression is enhanced with lighter charged Higgs masses. The measured value at LEP of $R_b = 0.2170 \pm 0.0009$ [8] is within 1.3σ of the SM expectations which therefore puts constraints on a light charged Higgs. These contributions also exclude lower values of $\tan\beta$. R_b can be enhanced relative to the SM result when $\tan\beta$ is large and two or more of the neutral scalars are light.

The full Z^0 width, measured at LEP to be , $(Z^0 \to \text{all}) = 2.4948 \pm 0.0025$ GeV [8], also provides constraints on the charged Higgs mass. The Z^0 width is quite sensitive to "oblique" corrections ($\Delta\rho$) to the ρ parameter (defined in Equation 1.8). Positive contributions to $\Delta\rho$ tend to enhance the Z^0 width. Thus measured values for the total width constrain the mass-splittings in the Higgs sector of the type II 2HDM and forces $M_{H^\pm}$ to lie in the range (at the 1σ level) [108]

$$M_{h^0} - 130 \text{ GeV} \leq M_{H^\pm} \leq M_{H^0} + 130 \text{ GeV}. \tag{1.43}$$

Without knowledge of the neutral scalar masses though, this is a somewhat weak constraint.

In contrast, in the type I 2HDM, where both the top and bottom quark Yukawa couplings are proportional to $1/\tan\beta$, the positive vertex corrections from neutral Higgs exchange are far smaller than the negative corrections from charged Higgs exchange, and so one does not expect significant enhancements of , $(Z^0 \to b\bar{b})$ at large values of $\tan\beta$.

The various corrections to the $Z^0 b\bar{b}$ vertex also modify the $b\bar{b}$ forward–backward asymmetry of the Z^0, which is measured by the parameter A_{FB} [108]. Vertex corrections tend to modify the left–handed coupling of the b for small values of $\tan\beta$, and the right–handed coupling of the b for large values of $\tan\beta$.

The forward–backward asymmetry shows much the same behavior as R_b as a function of the Higgs masses and mixing angles: $A_{FB}(b\bar{b})$ is suppressed at small values of $\tan\beta$ as a result of charged Higgs effects. The large $\tan\beta$ scenario is more complicated where the effects on A_{FB} also depend on the neutral Higgs bosons masses and can be suppressed or enhanced slightly [108].

The Z^0 width is obviously also sensitive to other supersymmetric particles which can affect some of the limits on the Higgs bosons. See Reference [109] for a discussion of these influences.

1.5.4 Limits from B^0–$\overline{B}^0$ Mixing

The CP eigenstates in the K^0–$\overline{K}^0$ and B^0–$\overline{B}^0$ systems can mix via box diagrams, an example of which is shown in Figure 1.16. In the kaon system, this admixture is parameterized by $|\epsilon_K| = (2.280 \pm 0.013) \times 10^{-3}$ [8]. In the bottom meson system this is parameterized by $x_b \equiv \Delta M_B/$, where ΔM_B is the mass difference between the heavy and light admixtures of B^0 and $\overline{B}^0$, which is currently measured to be $\Delta M_B = (0.474 \pm 0.031)\ \mathrm{ps}^{-1}$ [8] and , is their average width. The weighted average of the values of x_b from ALEPH and DELPHI from the mass splitting, and from ARGUS and CLEO measuring the time integrated mixing probability, is $x_b = 0.706 \pm 0.068$.

As shown in Figure 1.16, there are additional contributions from WH and HH

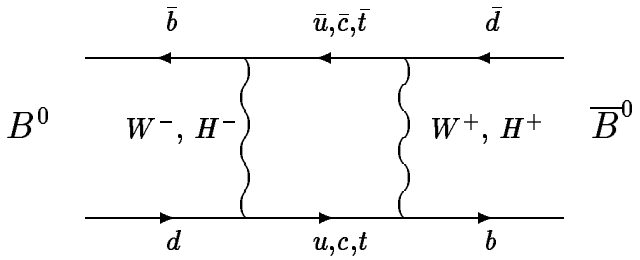

Figure 1.16: Example of a box diagram for B^0-$\overline{B}^0$ oscillations in the SM by the exchange of weak vector bosons ($W^{\pm}$) and in extended Higgs models by $H^{\pm}$ scalar exchange. K^0-$\overline{K}^0$ mixing can be depicted in a similar way by replacing the b's with s's in the diagram.

states in the box diagram if the charged Higgs boson exists. Comparisons of the measured values of the mixing to that predicted in these models place constraints on the charged Higgs mass for low $\tan\beta$ due to the Yukawa contributions (from $H^+t\bar{b}$) which are proportional to $1/\tan\beta$ for left-handed particles in both type I and II 2HDM's (see Equation 1.35). These effects are much more prominent in the bottom meson system than in the kaons due to the Higgs-fermion mass coupling.

The constraints in the charged Higgs mass and $\tan\beta$ planes for the type II 2HDM for the various indirect methods discussed so far are shown in Figure 1.17 from A. Grant [108]. The plot also includes a constraint from $b \to s\gamma$ which will be discussed in more detail in the next section. The $b \to s\gamma$ results give bounds on charged Higgs contributions with large $\tan\beta$ and have received much attention recently. The bounds shown here have been improved with more recent calculations.

The Z^0 width results give a lower bound on the value of $\tan\beta \gtrsim 0.7$. All these results however are calculated under the assumption of no other supersymmetric particle contributions which could affect these results greatly.

1.5.5 Limits from the Electromagnetic Penguin Decay $b \to s\gamma$

As $b \to s\gamma$ provides some of the most stringent, albeit model dependent, limits on the charged Higgs boson with large $\tan\beta$, it warrants further discussion.

In 1993, the CLEO collaboration reported the observation of the exclusive decay $B \to K^*(892)\gamma$ [110]. This was the first evidence for a *penguin decay* (described

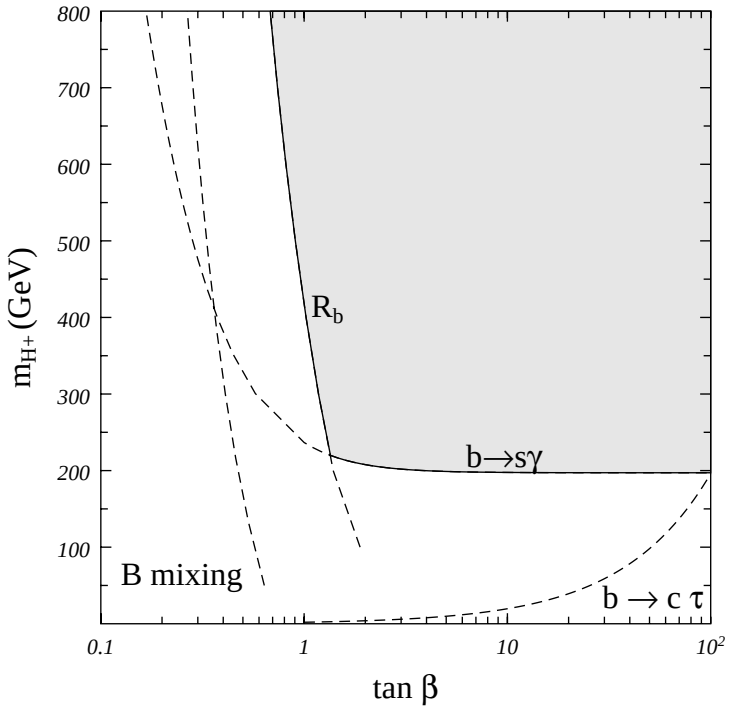

Figure 1.17: Limits in $M_{H^\pm}$–$\tan\beta$ plane via indirect methods for type II 2HDM. Limits are calculated assuming $M_t = 174$ GeV$/c^2$. This figure is from Reference [108].

below). This measurement established the existence of the decay $b \to s\gamma$ but due to the large theoretical uncertainties in the hadronization process for the B meson this only gave a rough measure of the decay width , $(b \to s\gamma)$. The latest updated result from CLEO-II gives [111]

$$\mathcal{B}(B \to K^*\gamma) = (4.2 \pm 0.8 \pm 0.6) \times 10^{-5}, \tag{1.44}$$

averaged over various modes.

CLEO then reported on a measurement of the branching ratio for the inclusive process $b \to s\gamma$ in 1995 [112]. The latest (preliminary) result from CLEO for this process is [113]

$$\mathcal{B}(B \to X_s\gamma) = (2.50 \pm 0.47\ (\text{stat.}) \pm 0.39\ (\text{syst.})) \times 10^{-4}, \tag{1.45}$$

with the 95% confidence level bounds of $1 \times 10^{-4} < \mathcal{B}(B \to X_s\gamma) < 4.2 \times 10^{-4}$. The ratio of exclusive to inclusive rates is 0.17 ± 0.08. ALEPH [114] has also recently reported results for the observation of the inclusive $b \to s\gamma$ decay at a rate compatible

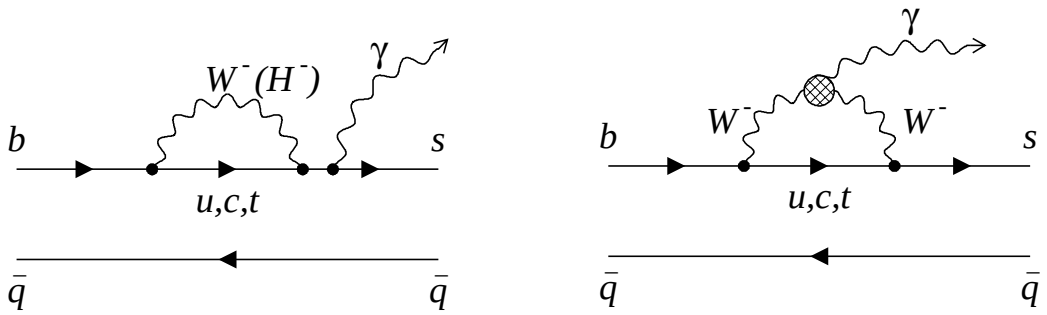

Figure 1.18: Penguin diagrams for FCNC of $b \to s\gamma$. A charged Higgs boson (H^-) in the loop would provide an enhancement to the SM rate in the type II 2HDM.

with that from CLEO:

$$\mathcal{B}(B \to X_s\gamma) = (3.11 \pm 0.80 \pm 0.72) \times 10^{-4}. \tag{1.46}$$

The transition $b \to s\gamma$ is a flavor-changing neutral current (FCNC) process. In the SM, it is described by a *penguin* diagram in which a virtual W is exchanged in a loop with an up-type quark, with a photon or Z^0 emitted in an *electromagnetic* penguin, or a gluon emitted for a *strong* penguin [115]. Figure 1.18 shows Feynman diagrams for electromagnetic penguins leading to the $b \to s\gamma$ decay. The top quark contributions dominate due to the mass and CKM matrix elements. In principle, large QCD corrections are also expected.

The calculation of $\mathcal{B}(b \to s\gamma)$ in the SM and extensions has been discussed extensively in the literature: see References [100, 116, 117] for good overviews. To obtain the branching fraction, the inclusive rate is scaled to that of the combined CLEO semileptonic decay branching fraction $\mathcal{B}(B \to X\ell\nu_\ell) = 0.1087 \pm 0.0034$ [8]. This removes some uncertainties in the calculation due to an overall factor of m_b^5 which appears in both width expressions, and reduces the ambiguities involved with the imprecisely determined CKM factors. The leading order logarithmic QCD corrections are calculated using an operator product expansion and give:

$$\mathcal{B}(b \to s\gamma) = \frac{6\alpha_{EM}}{\pi g(z)} \left| \frac{V_{tb}V_{ts}^*}{V_{cb}} \right|^2 |c_7^{eff}(\mu)|^2 \mathcal{B}(B \to X\ell\nu) \tag{1.47}$$

where $g(z)$ is the phase space corrections for the semileptonic decay $\simeq 0.316$, μ is

the renormalization scale, normally taken to be of order the b-quark mass, and

$$c_7^{eff}(\mu) = \eta^{16/23} c_7(M_W) + \frac{8}{3}(\eta^{14/23} - \eta^{16/23}) c_8(M_W) + C(\eta) \ , \tag{1.48}$$

where $\eta = \alpha_s(M_W)/\alpha_s(\mu)$. The $c_{7,8}(M_W)$ are the Wilson coefficients of the electromagnetic and chromomagnetic dipole operators used in the expansion; explicit expressions for these coefficients can be found in [117, 118]. The Wilson coefficients are evaluated perturbatively at the W scale, where the matching conditions are imposed, and evolved down to the low-energy renormalization scale, $\mu = M_b$, using renormalization group equations (RGE). The $C(\eta)$ term is induced by operator mixing during this evolution. The largest theoretical uncertainty in the calculation arises from the uncertainty in the renormalization scale, which is usually estimated using $m_b/2 < \mu < 2m_b$.

Next-to-leading order (NLO) perturbative calculations in the SM have been completed recently which significantly reduce the uncertainty due to the choice of renormalization scale. The theoretical uncertainties are now under control at the 10% level [119, 120, 121]. Assuming unitarity of the CKM matrix to constrain $|V_{ts}|$, the NLO calculations give

$$\mathcal{B}(B \to X_s\gamma) = (3.48 \pm 0.13 \pm 0.28) \times 10^{-4}, \tag{1.49}$$

where the first error is due to renormalization scale dependence and the second is due to uncertainties on the input parameters. This result is in good agreement with the experimental values.

Extensions to the SM introduce new operators into the effective theory and therefore affect the Wilson coefficients in Equation 1.48. The effects on the branching fraction of $b \to s\gamma$ can therefore lead to severe restrictions on these models under certain circumstances. The effect on the Higgs sector in the 2HDM and in the case of supersymmetry are discussed below. See References [122, 100] for a discussion of restrictions on other new physics (e.g. anomalous $WW\gamma$ couplings) from the $b \to s\gamma$ results.

In both types I and II 2HDM's, which naturally avoid tree-level FCNC's, the $H^{\pm}$ contributes to $b \to s\gamma$ via virtual exchange together with the top-quark, similar to

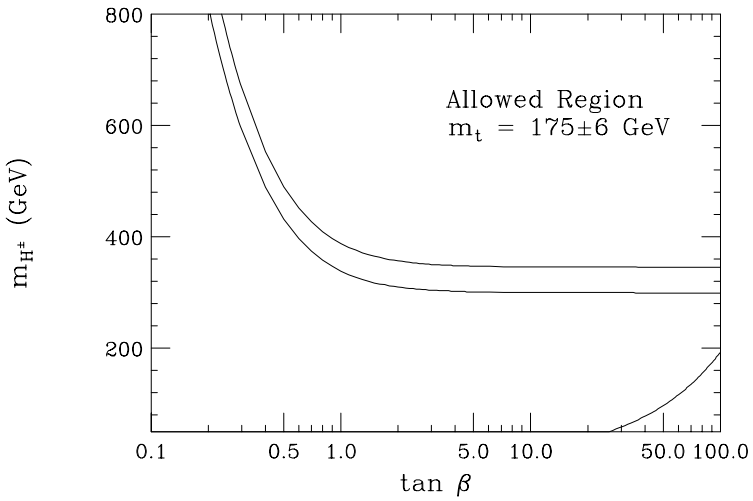

Figure 1.19: Lower limit on the charged Higgs mass in the type II 2HDM as a function of $\tan\beta$, based on the upper limit of the CLEO $\mathcal{B}(b \to s\gamma)$ measurement. The excluded region is that to the left and below the curves. The top curve is for $M_t = 181$ GeV/c^2 and the bottom curve is for $M_t = 169$ GeV/c^2. The restriction from $\mathcal{B}(B \to X\tau\nu_\tau)$ of $M_{H^\pm} > 1.9 \tan\beta$ GeV is also shown as the lower right curve. This figure is from Reference [118].

the W exchange in the loop shown in Figure 1.18. The operators involved in the calculation of the decay rate receive contributions to the SM Wilson coefficients in Equation 1.48 and become

$$c_{7,8}(M_W) = c_{7,8}^{SM}(M_t^2/M_W^2) + \frac{1}{3\tan^2\beta} c_{7,8}(M_t^2/M_{H^\pm}^2) + \lambda F_{7,8}(M_t^2/M_{H^\pm}^2), \quad (1.50)$$

where $\lambda = -1/\tan\beta$ for type I and $\lambda = +1$ for type II couplings. The analytic form for the $F_{7,8}$ functions can be found in Reference [123].

The charged Higgs contributions depend on $\tan\beta$ and $M_{H^\pm}$ and the coupling pattern. For type I, the $H^\pm$ contributions scale as $1/\tan^2\beta$, therefore enhancements to the SM decay rate only occur for small values of $\tan\beta$. The relative minus sign between the two $H^\pm$ contributions interfere destructively for large $\tan\beta$ and decrease the SM branching ratio. Limits on R_b (see Section 1.5.3), however, restrict this decrease to be at most 20% [124]. Limits on the charged Higgs mass from the measured $b \to s\gamma$ rates can therefore only be derived for $\tan\beta < 1$ [122].

In type II couplings, large enhancements appear for small values of $\tan\beta$, but there are also significant enhancements to the SM rate for large $\tan\beta$ as the $F_{7,8}$ terms in Equation 1.50 enter positively and scale as $\tan\beta$. Since the present CLEO

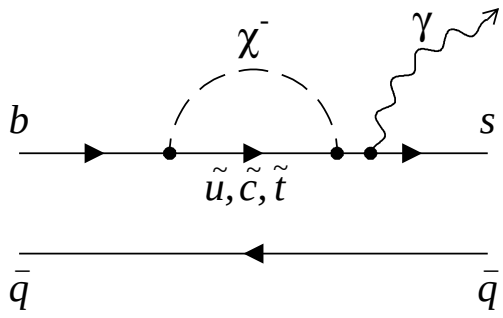

Figure 1.20: A penguin diagram for the FCNC $b \to s\gamma$ mediated by charginos and squarks. This diagram could interfere constructively or destructively with the SM and charged Higgs contributions, depending on the Higgsino mass parameter, μ.

measurement lies below the SM result, $B \to X_s\gamma$ provides quite stringent bounds on the charged Higgs mass in this model.

The original bounds from the CLEO experiment using LO calculations [112] gave $M_{H^\pm} > 244 + 63/(\tan\beta)^{1.3}$ GeV/c^2. Complete NLO calculations for $b \to s\gamma$ have been completed for the 2HDM [124] which again significantly reduce the renormalization scale uncertainty. The NLO result improves the CLEO lower bound on the charged Higgs mass from 244 GeV/c^2 to 340 GeV/c^2. These mass bounds might be less restrictive if the experimental values are closer to the preliminary ALEPH results. The lower bound on the charged Higgs mass versus $\tan\beta$ derived from the CLEO results and the NLO calculations is shown in Figure 1.19.

The limits obtained here for the type II 2HDM can be weakened in supersymmetric theories. Other supersymmetric particles can contribute in the penguin loop (an example is shown in Figure 1.20), either constructively or destructively. There are additional contributions from charginos ($\tilde{\chi}_i^\pm$) and up-type squark loops, gluino ($\tilde{g}$) and down-type squark loops and neutralino ($\tilde{\chi}_i^0$) and down-type squark loops. The contribution from $\tilde{\chi}_i^0$ are known to be small compared to those induced by $W^\pm$ and $H^\pm$ exchange and can therefore be neglected [118]. The $\tilde{\chi}_i^\pm$ and $\tilde{g}$ loop contributions depend on the mass and mixing of the particles inside the loop. The chargino contributions especially can be large, and for some range of the parameter space can cancel the $H^\pm$ contributions to give a value of $B(b \to s\gamma)$ at or even below the SM

prediction [125].

In the supersymmetric limit, there is an exact cancellation of the different SUSY contributions with those from $H^{\pm}$, hence $\mathcal{B}(b \to s\gamma) \to 0$ and would be lower than that predicted by the SM. However, in the realistic case where SUSY is broken, the cancellation is not exact and rates greater or less than that from the SM are possible. The various contributions have been calculated in the minimal supergravity (mSUGRA) and electroweak symmetry breaking scenarios [125, 126, 127].

In the mSUGRA case, unification of the gaugino and squark masses is assumed at a large energy scale ($M_{SUSY} = M_{GUT}$ or beyond). The soft SUSY-breaking parameters are then evolved down to the electroweak scale by solving the renormalization group equations (RGE) of the MSSM. The radiative electroweak symmetry breaking conditions are also applied.

During this evolution, the first and second generation squarks with the same gauge quantum numbers remain highly degenerate in mass but the third generation squarks, especially the top squark (*stop*) can experience a large mass splitting due to the renormalization effects of the top Yukawa coupling constant and the potentially sizeable off-diagonal terms in the stop mass matrix. Therefore a light stop, $\tilde{t}_1$, can be generated from the mixing of $\tilde{t}_L$ and $\tilde{t}_R$. It is possible to simultaneously obtain a relatively light stop and chargino with masses around 100 GeV/c^2, especially for $\tan\beta \sim 2$ [118].

Even in the presence of this mass splitting, the gluino, neutralino, and chargino couplings are not strongly modified in comparison to the case of exact degeneracy.

Figure 1.21 from Goto and Okada [126] shows the results of scanning the complete SUGRA parameter space for a fixed value of the top mass (175 GeV/c^2) and two representative values of $\tan\beta$: (a) $\tan\beta = 2$ and (b) $\tan\beta = 30$. The plots show the branching ratio of $b \to s\gamma$ as a function of the charged Higgs boson mass. Each point represents a different choice of parameters. The predictions for the SM and for the type II 2HDM are shown along with the CLEO experimental bounds.

In the case (a) with $\tan\beta = 2$ there are two branches for $B(b \to s\gamma)$. In one

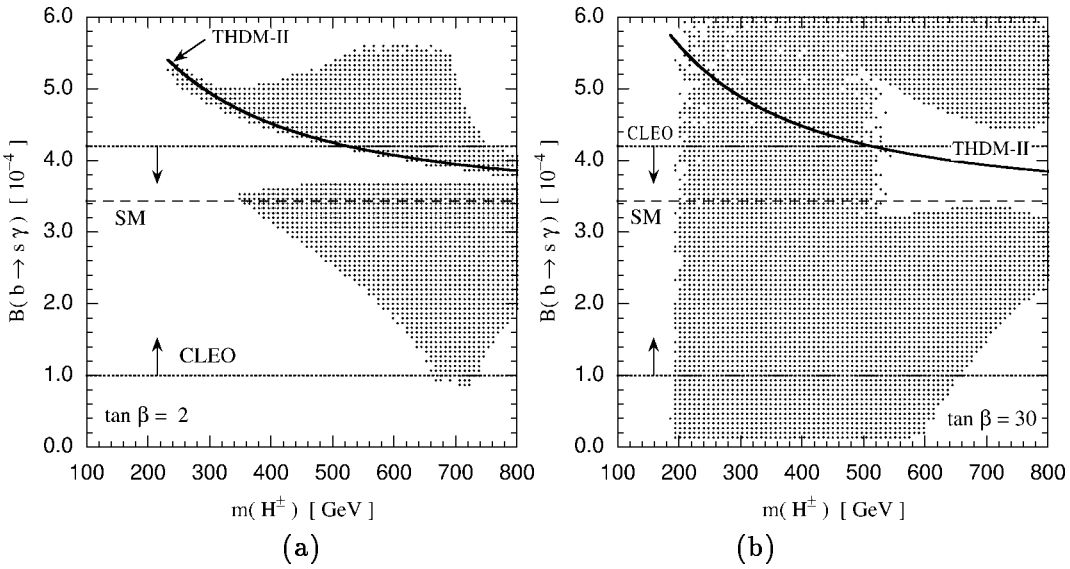

Figure 1.21: $\mathcal{B}(b \to s\gamma)$ as a function of the charged Higgs mass in SUGRA with $M_t = 175$ GeV/c^2 and (a) $\tan\beta = 2$, and (b) $\tan\beta = 30$. The solid curve corresponds to the 2HDM Model II value, while the dashed-dot curve represents the SM. Each dot corresponds to a sample point of the complete SUSY parameter space. These figures are taken from [127].

branch the branching ratio is close to the type II 2HDM prediction, where the contributions from SUSY particles are small. In the other branch it is consistent with the SM value, where the charged Higgs boson contribution is canceled by the SUSY contributions. It can also be clearly seen in the case (b) with $\tan\beta = 30$ that there are regions of parameter space where $B(b \to s\gamma)_{\rm SUSY}$ is at or below the SM value and is consistent with the CLEO bounds.

The sign of the SUSY loop contributions with respect to those of the SM and charged Higgs is strongly correlated with the sign of the Higgsino mass parameter, μ, in the minimal supergravity model. In general, for $\mu < 0$, the branching fraction for $b \to s\gamma$ is enhanced from the predictions in the type II 2HDM and is suppressed in the case $\mu > 0$. In particular, the regions of the most suppression correspond to a light top squark ($\tilde{t}_1$) and chargino sector, large $\tan\beta$ and $\mu > 0$. There can also be substantial contributions, positive or negative, from the gluino and down-type squark loops due to left-right mixing in the sbottom sector.

This dependence on the Higgsino parameter is further demonstrated in another figure from Goto and Okada [126], Figure 1.22, which shows the excluded region in

(a) (b)

Figure 1.22: Excluded regions in the $\tan\beta$–$M_{H^\pm}$ plane based on the CLEO $b \to s\gamma$ result in the type II 2HDM (dot-dashed) and in SUGRA (solid) for (a) negative Higgsino mass parameter ($\mu < 0$) and (b) $\mu > 0$. The dashed line represents the excluded region without the $b \to s\gamma$ constraint. Regions to the left of the curves are excluded. These figures are from Reference [126].

the $\tan\beta$ and $M_{H^\pm}$ planes derived from the SUSY contributions to the $b \to s\gamma$ rate in the two scenarios (a) $\mu < 0$ and (b) $\mu > 0$. The $\tan\beta$ range shown is chosen to yield perturbative Yukawa couplings up to the GUT scale. For values of $\tan\beta$ larger or smaller than this range, the Yukawa coupling constant from the top or bottom/tau contribution blows up below the GUT scale. The lower bounds on the charged Higgs mass in the type II 2HDM case are also shown as well as the limits without taking any cognizance of the $b \to s\gamma$ results.

The excluded region in the minimal supergravity is much larger when $\mu < 0$; the bound reaches a maximum of about $M_{H^\pm} > 600$ GeV/c^2 for $\tan\beta \approx M_t/M_b \sim 35$. However in the $\mu > 0$ case, the large cancellations from the SUSY particle contributions can totally negate those from the charged Higgs and can actually drive the $b \to s\gamma$ rate below the SM predictions. In this case then there are few constraints of the charged Higgs mass.

Note that if all the up-type squarks remain degenerate in the RGE evolution, and therefore there are no light supersymmetric particle loops, the chargino contributions exactly cancel due to a SUSY-GIM mechanism, and the 2HDM mass constraints hold.

Chapter 2

Apparatus

2.1 Introduction

The Tevatron at the Fermi National Accelerator Laboratory accelerates protons and anti-protons to 900 GeV each and collides them. The resulting center-of-mass energy in the collision is therefore 1.8 TeV. The Collider Detector at Fermilab (CDF) is located at one of six nominal interaction regions (B0), and is a three-story, 5000-ton, multi-purpose detector which is used to record the remnants of these high-energy collisions, both to make detailed measurements of known physics processes and to look for evidence of new ones. The accelerator complex at Fermilab is described in more detail in Appendix B. The rest of this chapter describes the proton-antiproton collisions at B0 and the CDF apparatus used to measure the interactions.

2.2 Luminosity

The number of collisions per second (N) at the CDF interaction region is given by the golden formula of experimental particle physics

$$N = \sigma \times \mathcal{L} \tag{2.1}$$

where σ (in units of cm^2) is the cross section of the desired physics process, in this case proton–anti-proton collisions, and $\mathcal{L}$ is the instantaneous luminosity of the colliding beams, which is measured in units of collisions/cm^2/sec. The instantaneous luminosity for a collider is calculated from [128]

$$\mathcal{L} = \frac{f B N_p N_{\bar{p}}}{2\pi(\sigma_p^2 + \sigma_{\bar{p}}^2)} F(\sigma_l, \beta^*) \tag{2.2}$$

where f is the revolution frequency ($\sim$ 50 kHz), B is the number of bunches in each beam (6), N_p ($N_{\bar{p}}$) is the number of protons (anti-protons) in a bunch with typical values of 2 (0.6) $\times 10^{11}$ for Run 1B, σ_p ($\sigma_{\bar{p}}$) is the r.m.s. proton (anti-proton) beam size at the interaction point $\sim$ 40–70 μm, and F is a form factor that depends on the bunch length, σ_l, and the beta function at the interaction point, β^* ($\sim$ 0.6 m for Run 1B).

The peak luminosity in Run 1A was about 1.0×10^{31} cm^{-2}sec^{-1} with typical values of 0.54×10^{31} cm^{-2}sec^{-1}. The Linac (see Appendix B) was upgraded during the summer of 1993 between Runs 1A and 1B and the resulting lower emittances in the proton transfer to the Booster facilitated the more than doubling of the Tevatron's instantaneous luminosity for Run 1B. For Run 1B, the peak luminosity was about 2.8×10^{31} cm^{-2}sec^{-1} with typical values of 1.6×10^{31} cm^{-2}sec^{-1}.

The total cross section for $p\overline{p}$ collisions at the center-of-mass collision energy $\sqrt{s}$ = 1.8 TeV is about 50 mb [8] (where 1 barn = 10^{-24} cm^2) which therefore corresponds to a million collisions a second at a typical instantaneous luminosity of 2.0×10^{31} cm^{-2}sec^{-1}.

The total integrated luminosity ($\int \mathcal{L}dt$) of beam delivered to the CDF interaction region during Run 1A was about 30 pb^{-1} and during Run 1B was about 126 pb^{-1} (where 1 pb^{-1} = 10^{36} cm^{-2}).

2.3 CDF Coordinate System and Units

CDF employs a right-handed coordinate system with the positive z-axis along the beam line in the proton direction (East), the positive y-axis pointing vertically upward and the positive x-axis pointing radially outwards in the horizontal plane of the Tevatron. The center of the detector is taken as the origin and is also the nominal interaction point for $p\overline{p}$ collisions.

To describe the detectors and, consequently, the derived physical quantities of the detected particles, it is more natural to use a spherical coordinate system. The polar angle, θ, is taken from the positive z-axis and the azimuthal angle, ϕ is taken

anti-clockwise from the positive x-axis, with the radial distance r measured from the center of the beamline. Figure 2.2 (inset) shows the coordinate system used for CDF.

For a collider detector, however, a more natural unit to describe the polar angle is the *rapidity*, y, defined as

$$y = \frac{1}{2} \ln \left(\frac{E + p_z c}{E - p_z c} \right). \tag{2.3}$$

This is because under boosts along the z-axis to an inertial frame with velocity β, the rapidity transforms as $y \rightarrow y + \tanh^{-1} \beta$. Therefore the shape of the particle density distribution in rapidity, dN/dy, is invariant under Lorentz transformations. For highly relativistic particles, however, where $p \gg mc$, the rapidity is well approximated by the *pseudorapidity*, η, defined as

$$\eta = -\ln \tan \left(\frac{\theta}{2} \right) \tag{2.4}$$

which is the unit used for the segmentation of the CDF detector and for describing measurements. Two forms of pseudorapidity are actually used: η_{det} measures the pseudorapidity from the nominal interaction point at the center of the detector ($z = 0$), whereas η (also called the *event* η) measures the pseudorapidity of the decay products from the z-position (*z-vertex*) of a $p\overline{p}$ collision which could occur at any z along the beam-axis.

High-momentum transfer interactions occurring in the Tevatron generate particles with significant momentum transverse to the beam line. The CDF detector has been optimized to measure these events, allowing individual processes to be identified. Low-momentum transfer interactions, termed *elastic* or *diffractive interactions* or *minimum bias events*, and by-products from the spectator quarks from high-momentum transfer interactions, have most of their energy directed longitudinally, along the beampipe, and will not be measured by the detector. The number of charged particles per unit of rapidity (dN^{charge}/dy) in the central region of the detector for elastic $p\overline{p}$ collisions at $\sqrt{s} = 1.8$ TeV is about 4. Most of the hadrons in these minimum bias events only have a momentum transverse to the beam line of about 0.5 GeV/c

For this reason, most physics analyses utilize the *transverse energy* (E_T) and *transverse momentum* (p_T), which are defined by

$$E_T = E \times \sin\theta \tag{2.5}$$

$$p_T = p \times \sin\theta \tag{2.6}$$

Energy as measured by the calorimeters at CDF is treated as a "vector" quantity as the energy in each tower (see Section 2.6) is weighted by its azimuthal and polar position. The transverse energy is therefore a two-dimensional vector quantity, similar to the p_T.

At the high energies dealt with in the collider environment, E_T is approximately equal to $p_T c$ for a particle or a jet of particles. In CDF analyses, E_T is usually used to describe the transverse energy deposited by particles in the calorimeters, and p_T describes the transverse momentum measurements of charged particles made in the tracking chambers from the particles' track-curvatures in a magnetic field (see Section 2.5).

In a $p\overline{p}$ collision, the particles that escape transverse to the beampipe will carry significant amounts of transverse momentum. Some of the energy in the collision will be carried away down the beampipe, however, by the spectator quarks and their hadronization products. These particles will be undetected, and will carry significant longitudinal momentum but little transverse momentum. Therefore, we do not expect the total detected energy and momentum in the detector for a collision to balance, but the transverse energy and momentum should balance, assuming we can measure all the particles passing through the detector. Non-interacting particles, such as neutrinos, or minimum ionizing particles, such as muons, however, may leave little or no trace in the calorimeters and the imbalance of measured transverse energy is used as an indicator of these particles — this imbalance is termed *missing transverse energy*. Detector resolution effects and particles passing through uninstrumented regions ("cracks") can also be sources of significant missing transverse energy. Minimum ionizing particles and charged particles travelling down a crack are detected by their tracks in the tracking chambers, and the resulting momentum

measurement can be used to correct the energy misbalance. However, particles that do not interact with the detector at all, such as neutrinos, must be inferred from the missing energy and momentum.

The *missing transverse energy*, $\not\!\!E_T$, is calculated by summing up all the calorimeter towers, treating the E_T as measured in each tower as a vector quantity. We therefore define the $\not\!\!E_T$ as the magnitude of the vector sum over towers of E_T:

$$\not\!\!E_T = \sqrt{\left(\sum_{towers} E_T \cdot \sin\phi_{tower}\right)^2 + \left(\sum_{towers} E_T \cdot \cos\phi_{tower}\right)^2}. \qquad (2.7)$$

Note that the $\not\!\!E_T$ is a sum of energy misbalance in the detector which could arise from real missed particles and/or detector effects. Physics analyses try to identify the sources of detector effects and make corrections for them. An important detector effect is the fluctuation of energy deposits in the calorimeter modules. Since this resolution effect scales as $1/\sqrt{E_T}$, a measure of the *significance* of a $\not\!\!E_T$ measurement is given by the quantity $\not\!\!E_T/\sqrt{\sum_{towers} E_T}$. For values of this $\not\!\!E_T$ significance well above 1.0, there is increased confidence that a real particle, such as a neutrino, was the source of the $\not\!\!E_T$ and not some measurement fluctuation.

In the analysis, we recalculate the $\not\!\!E_T$ after identifying all the particles from the hard-$p\overline{p}$ interaction. This naturally corrects for the energy of the muons. This is discussed further in Section 5.10.2.

2.4 CDF Detector Overview

The CDF detector is shown in a 3-D external view in Figure 2.1 and Figure 2.2 shows a longitudinal planar view of one quadrant of the CDF detector. The detector is cylindrically symmetric in the azimuthal and the backward-forward planes about the nominal interaction point at the geometric center of the detector. It measures approximately 27 m from end-to-end and is about 10 m high and weighs about 5000 tons. The detector sub-elements, discussed below, are segmented roughly uniformally in pseudorapidity and azimuth. A good review of the CDF detector components is given in Reference [129] and the designs for the upgrades for the second half of Run 1

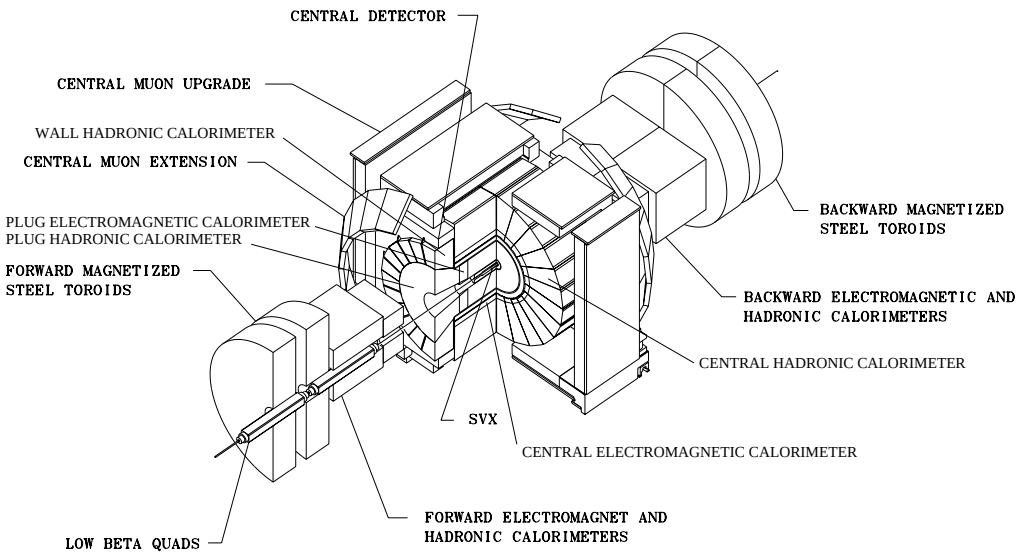

Figure 2.1: Three dimensional view of the CDF detector for Run 1.

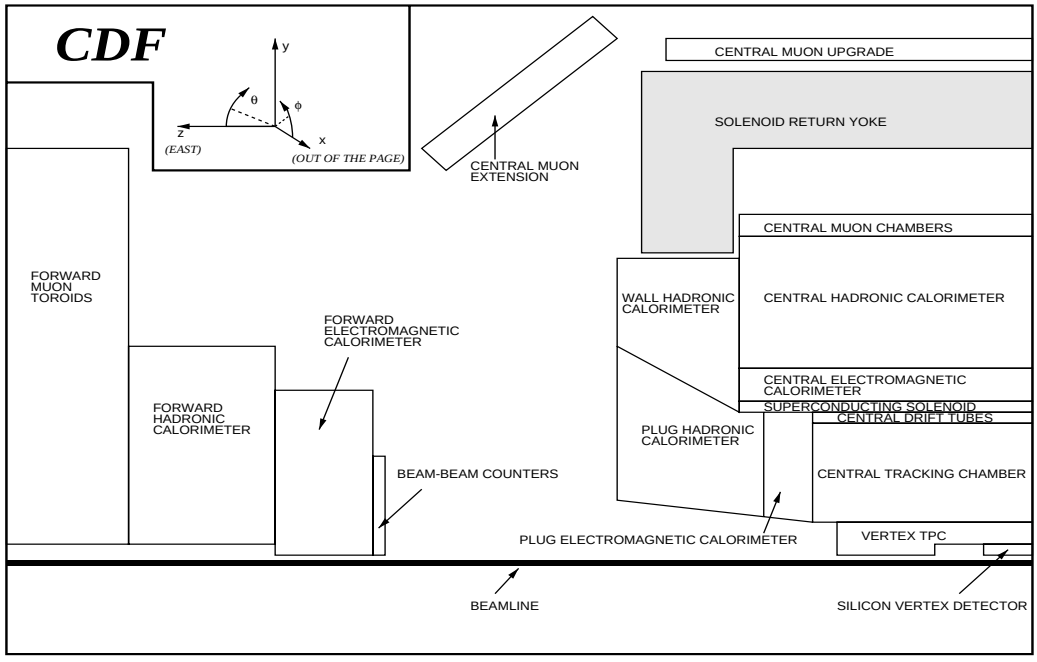

Figure 2.2: Longitudinal view of one quadrant (upper East) of the CDF detector for Run 1. The interaction point is at the lower right corner. The CDF coordinate system is also shown.

are given in Reference [130].

The overall design goal of the detector is to accurately measure the properties of particles emerging from the interaction region at the center of the detector from a $p\overline{p}$ hard scatter. The high precision and good coverage allow particle identification with good efficiency, especially for electrons and muons. This goal must also be accomplished in an environment with very short times (on the order of a few microseconds) between bunch crossings and with possible multiple $p\overline{p}$ interactions per crossing.

The detector has been divided up into a number of subsystems each having a particular task and using different detector techniques to accomplish it. At the center of the detector, close to the interaction region, there are tracking chambers. These are constructed of low-mass materials to minimize secondary interactions and multiple scattering of the incident particles within the detector material itself. The central tracking systems reside inside a magnetic field, produced by a superconducting solenoidal magnet, which facilitates momentum and charge measurements for charged particles. The tracking systems therefore provide non-destructive measurements of momenta, charges, tracks, positions and vertices of charged particles.

The tracking chambers are surrounded by calorimeters. These provide destructive measurements of the energy of the emerging particles (both charged and neutral) as the incident particles dump their energy into the large mass of the calorimeter elements which sample the resultant radiant energy for read out. The calorimetry coverage is accomplished by dividing the calorimetry into several systems, each using a projective tower geometry so as to measure the energy flow in uniform bins of azimuthal angle and pseudorapidity. This facilitates the reconstruction of jets (described later). The CDF calorimeter systems are further divided into electromagnetic and hadronic components. Comparisons between these elements provides crucial information for particle identification.

Calorimetry is an important tool in high-energy colliding beam environments. A calorimeter will measure all the energy of the particles directed at a tower, both charged and neutral (except for the neutrinos and minimum ionizing particles such

as muons) and does not suffer any ambiguities in a high particle multiplicity environment. The energy resolution of a calorimeter improves as the energy deposition increases whereas momentum measurements in tracking chambers degrade with "stiffer" (i.e. higher momentum) tracks. The combination of tracking and calorimeter detectors therefore provide complementary methods for particle detection and measurement. Calorimeters also provide simple signatures for triggering on interesting events. For example, a large electromagnetic deposit in an isolated tower with little or no associated hadronic energy would be indicative of a high-p_T electron or photon which is a signature for many interesting physics processes, including top production.

These various systems complement one another and provide overlapping information that can be used for particle identification and to determine if any particles escaped detection.

Electrons and photons are identified as highly electromagnetic showers in the calorimeters and by the presence (e) or absence (γ) of a track in the inner tracking systems. If momentum information from the tracking system is available for an electron, consistency between the measured momentum of the electron candidate and the energy of the corresponding electromagnetic shower provides a powerful handle for rejection of backgrounds that might mimic an electron (e.g. hadronic shower fluctuations and overlaps between hadron tracks and photons from $\pi^0 \to \gamma\gamma$ decay). Information from the transverse and longitudinal shapes of the shower, from ionization measurements in the tracking chamber, and from the response of transition radiation and preshower detectors, are also used for electron identification.

As discussed in Section 1.1.3, a *jet* is a collection of particles travelling in approximately the same direction (*collimated*), originating from the fragmentation and hadronization of a quark or gluon. A hadronic jet is characterized by high track multiplicities and extended calorimeter *clusters* (deposits over one or more calorimeter towers). The segmentation of the calorimeters in η and ϕ is fine enough that quark and gluon jets will normally spread over more than one tower. In contrast, tau leptons decaying to hadronic end products tend to produce narrower jets that have

relatively fewer charged tracks associated with them. These properties are exploited for statistical separation of tau decays from the large hadronic jet background in the analysis discussed in this dissertation (see Chapters 3 and 5).

Jet clusters are reconstructed by summing up the energy deposited in the calorimeter cells within a fixed cone in η–ϕ space, $\Delta R = \sqrt{(\Delta\eta)^2 + (\Delta\phi)^2}$, where η is the pseudorapidity defined in Equation 2.4 and ϕ is the azimuthal angle. The fixed cone algorithm is used because jets are approximately circular in η–ϕ space; the η–ϕ size of a jet of a given p_T is independent of the rapidity of the jet. For most of the analysis discussed in Chapter 5 we use a fixed cone size of $\Delta R = 0.4$ radians, which contains most of the decay products from a parton fragmentation. This cone size is also the most suitable for distinguishing hadronic tau decay clusters from QCD jet clusters. Other cone sizes used at CDF are 0.7 and 1.0 radians.

Muons, which are highly penetrating particles (also called *minimum ionizing particles*), tend to escape the calorimeters without depositing much energy and are detected by further tracking chambers (now termed *muon chambers*) on the outside of the calorimeters. Again these chambers have been divided into several subsystems to provide adequate coverage. The calorimeters in front of these muon chambers provide shielding from the hadronic debris from the collision so that the few muons are not overwhelmed by the many hadrons from a typical hard $p\overline{p}$ collision. Muons are identified by the presence of a track in the muon chambers matched to a track in the central tracking chamber and possibly matched to a small calorimeter energy deposit (termed a minimum ionizing signal).

Neutrinos, which are essentially non-interacting as far as CDF is concerned, pass through all the detector elements without leaving a trace. Their presence and energies are inferred from the measured transverse energy and momentum misbalance in an event.

A vital part of the CDF detector is the data acquisition system consisting of fast analog triggering systems which do real-time online selection of events which are then read out by sophisticated fast digitizing electronics for subsequent further selection and for storage to long-term data media for offline reprocessing and analysis.

The design, construction and operation of the various CDF detector subsystems are described in the rest of this chapter. The data acquisition system is described in Appendix C.

2.5 Inner Tracking Systems

The tracking systems at CDF are used to measure the momenta of charged particles and to determine their charge. The information from these *tracks* is also used to reconstruct the position where the original interaction occurred, termed the *primary vertex*), and also to distinguish *secondary vertices* for particles that travel macroscopic distances (on the order of a few hundred microns) from the original interaction point before decaying.

The tracking systems consist of: the Silicon Vertex Detector (SVX) positioned very close to the beamline which provides very precise information to resolve tracks close to the interaction point, the Vertex Time Projection Chamber (VTX) surrounding the SVX which provides vertex information in the longitudinal r–z view, and the main tracking chamber, the Central Tracking Chamber (CTC), surrounding the VTX, which provides information for 3-dimensional track reconstruction. The SVX is constructed from very thin silicon microvertex detectors and the VTX and CTC are gas drift chambers using a mixture of 50/50 argon/ethane with small admixtures ($< 1\%$) of isopropanol or ethanol which are quenching agents (i.e. prevent ionization cascades building up in the detectors).

All these inner tracking chambers reside in a 1.41 Tesla axial magnetic field provided by a superconducting solenoid that surrounds the central tracking chambers (see Figure 2.2). Charged particles bend in the magnetic field, allowing determination of their momenta and charges.

Tracks are reconstructed from hits in these chambers, starting with the vertices in the VTX. Full three dimensional tracks are reconstructed from the information in the CTC. These tracks are then extrapolated back to the SVX to improve both position and momentum resolutions. In event reconstruction, these tracks are then

matched with shower centroids measured in the calorimetry. This is particularly useful in removing the pion backgrounds from electron candidates.

The charged particle tracks also provide information for studying the response of the calorimeters as a function of momentum and position inside individual elements of the calorimeter modules.

2.5.1 Silicon Vertex Chamber (SVX)

The first silicon vertex detector installed in a hadron collider environment was the SVX [131] at CDF for the 1992 Run 1A. Due to the degradation over the run from the cumulative radiation exposure, this detector was replaced in 1993 for Run 1B by the radiation hardened SVX′ ("SVX prime") detector [132, 133, 134]. The two detectors are very similar in design and performance and a comparison is shown in Table 2.1 and will be discussed below.

Silicon vertex detectors are placed very close to the interaction region at particle colliders to provide very high-precision tracking information close to the beam interaction. This provides the ability to distinguish *secondary vertices* displaced from the primary vertex (or vertices), which are indicative of heavy-flavor quark decays coming from hadrons containing bottom and charm quarks. This ability to resolve the impact parameters (the distance of closest approach for a track to the primary vertex) for tracks from secondary vertices played a major role in the discovery of the top quark at Fermilab and has opened up a growing field in B-meson physics at hadron colliders. We use the secondary vertex finding algorithms developed for the top analyses to tag jets originating from b-hadron decays in the charged Higgs analysis. This is discussed in Section 5.8.

Silicon microstrip vertex detectors, such as the SVX, consist of thin silicon wafers implanted with very narrow, closely-spaced conducting strips. Electrons, promoted into the conduction band of the semiconductor material when an ionizing particle passes through the detector, are drawn to these strips by high electric fields. The strips undergo a voltage drop proportional to the amount of the original ionization. The strips are then read out by fast electronics. Position resolutions on the order of

Feature	SVX	SVX′
Channels	46080	46080
z coverage	51.1 cm	51.1 cm
Gap at $z = 0$	2.15 cm	2.15 cm
Radius of layer 0	3.0049 cm	2.8612 cm
Radius of layer 1	4.2560 cm	4.2560 cm
Radius of layer 2	5.6872 cm	5.6872 cm
Radius of layer 3	7.8658 cm	7.8658 cm
Overlap of layer 0	-1.26° (gap)	0.17° (0.24 strips)
Overlap of layer 1	0.32° (4 strips)	0.32° (4 strips)
Overlap of layer 2	0.30° (4 strips)	0.30° (4 strips)
Overlap of layer 3	0.04° (0 strips)	0.04° (0 strips)
Power	DC	AC, FOXFET bias
Passivation	none	silox
Atmosphere	argon/ethane + alcohol	dry nitrogen
Readout chip	SVX IC Rev.D	SVX IC Rev.H3
Sampling	quadruple	double
Noise	2200 electrons	1300 electrons
Gain	15 mV/fC	21 mV/fC
Signal/Noise		
begin of run	9	16
end of run	6.5	8
Reset/integrate time	3.5 μs	3.5 μs
Readout time	2.7 μs	2.1 μs
Radiation limit	$>$ 20 krad	$>$ 1 Mrad
Bad channels	1.59%	1.73%
Typical occupancy	7 – 10%	5%
Maximum occupancy	12 – 20%	25%

Table 2.1: Comparison of the SVX detector for Run 1A and the SVX′ detector for Run 1B.

Layer	Crystal Width [cm]	Active Area Width [cm]	Readout Strips	Number of Chips
0	1.6040	1.5360	256	2
1	2.3720	2.3040	384	3
2	3.1400	3.0720	512	4
3	4.2930	4.2240	768	6

Table 2.2: Physical characteristics of the silicon detectors.

a few tens of microns are possible, sufficient to observe b-quark hadron decays which travel distances of $c\tau \sim 300$–400 μm before decaying.

The length of the SVX along the beampipe is governed by the need for good acceptance within the constraints of the budget and by limitations due to increases in capacitance and leakage currents for longer strips. The $p\overline{p}$ luminous region at the CDF interaction region is roughly Gaussian in the longitudinal (z) direction with a r.m.s. width of approximately $\sigma \sim 30$ cm, due to the longitudinal size of the proton and anti-proton bunches. The total active length of the SVX is 51.0 cm which means that only about 60% of the $p\overline{p}$ collision vertices are in the acceptance region (known as the *fiducial* region) of the SVX.

The SVX has 4 layers of DC-power-coupled strip detectors that lie parallel to the beamline (along z) and therefore provides tracking in the r–ϕ plane only. SVX′ uses AC-power-coupled FOXFET[1] biased [135] silicon strip detectors which provide for lower noise readout and are more radiation-hard than those used in the SVX. Other improvements of the SVX′ over the SVX detector include radiation-hardened readout chips and complete ϕ coverage for the inner layer. All the improvements lead to better hit-detection efficiency over the thermally-induced noise in the detector which results in a higher efficiency for track finding.

Both the SVX and SVX′ were made up of two independent cylindrical barrels, each 25.5 cm long, separated by a 2.15 cm gap at $z = 0$. An isometric view of one of the barrels is shown in Figure 2.3. The barrels were placed symmetrically about the average interaction point and aligned coaxially with the beams. The inner layer of the SVX is 3.0 cm from the nominal position of the beam and lies just outside the beryllium beampipe (which has an external radius of 1.9 cm), to give the best possible impact parameter measurements. The inner layer of the SVX′ is closer to the beamline by approximately 1.5 mm. The pseudorapidity coverage is $|\eta| < 1.9$ for both detectors.

Each barrel is further divided into twelve sections (wedges) which subtend 30° in

[1] Field OXide Field-Effect Transistor

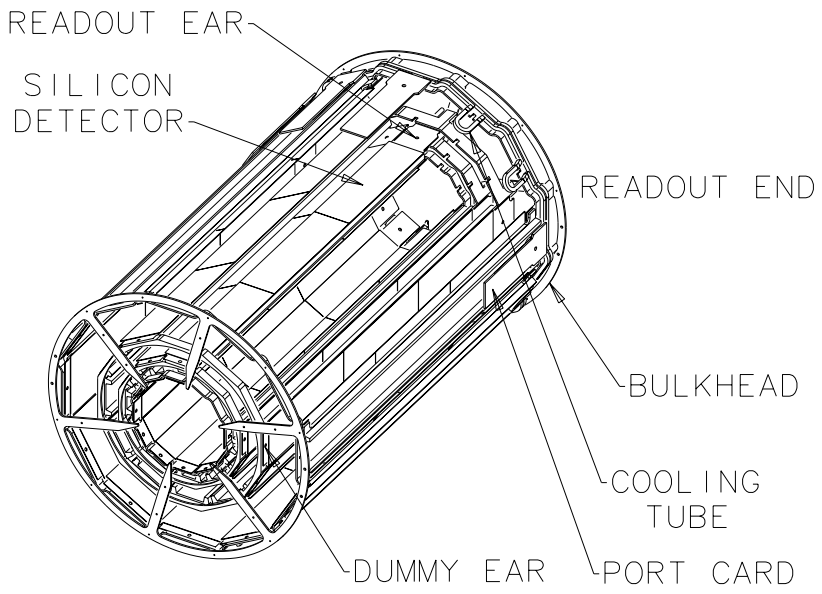

Figure 2.3: An isometric view of one of the SVX barrels.

azimuth (ϕ). Each wedge consists of four layers, numbered from 0 (inner layer) to 3 (outer layer), of single-sided silicon detector modules, known as *ladders*, with silicon microstrips running parallel to the beam axis. Each ladder (shown in Figure 2.4) consists of three 8.5-cm-long, 300-μm-thick microstrip detectors with the strips in adjacent detectors wirebonded together to reduce the number of readout channels. The strip pitch is 60 μm for the inner three layers and 55 μm for the outer layer. The silicon wafer widths increased from the inner to the outer layers and are given in Table 2.2, along with the number of readout strips and chips per layer. Each ladder is rotated by 3° about its major axis to provide some overlap between adjacent wedges (see Table 2.1). The geometry of the inner layer was changed for the SVX′ in order to achieve complete ϕ coverage corresponding to an overlap of 0.17° or 0.24 strips. The inner layer for the SVX had a 1.26° gap.

A single ceramic readout hybrid circuit board (ear card) at one end of a ladder holds all the readout chips. There are a total of 360 readout chips with 128 readout channels per chip, with each channel recording hits on one microstrip, for a total of 46,080 channels. The data is read out from these chips by *front-end* electronics, mounted on the outside of the detector, in a *sparse mode* where only those strips

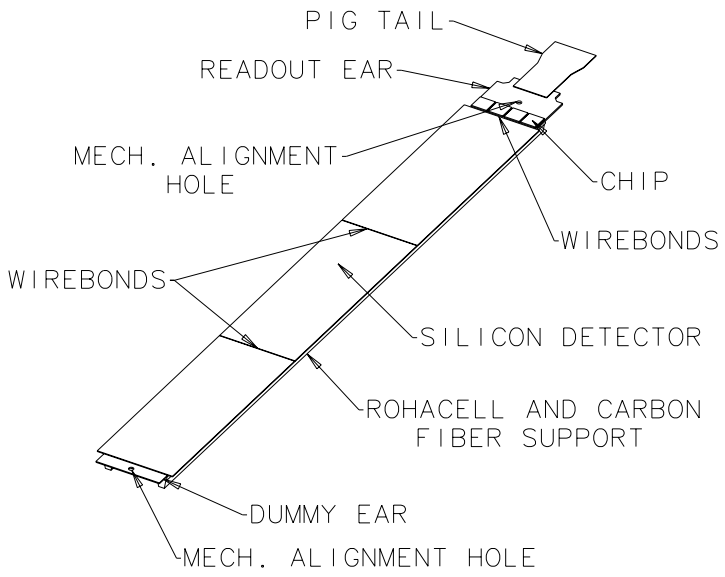

Figure 2.4: One ladder of the SVX.

which have a signal above some hardware threshold are read out. This means the readout time and the data size are set by hit occupancy rather than the total channel count. With typical occupancies $\leq 10\%$, readout times are about 2 μs, one of the longest among the CDF detector subsystems.

The amount and mass of the materials making up the SVX has been minimized to reduce the transverse radiation length of the detector and the multiple scattering of particles created in a $p\overline{p}$ collision. The average particle trajectory through the SVX, including the beryllium support bulkheads, only encounters $\lesssim 5\%$ of a radiation length. Each barrel is surrounded by a conductive cylindrical shield which isolates it from electromagnetic noise, external high voltage breakdown and which adds mechanical rigidity. The shield also protects the rest of the CDF detector components from noise from the SVX electronics. A chilled-water system at a temperature of 20–25° C is used to prevent thermal expansion of the detector and to cool the electronics.

As the SVX is so close to the beampipe, it is vulnerable to radiation damage resulting from the $p\overline{p}$ collision and from beam interacting with gas in the beampipe.

Another significant source of radiation damage is during beam tuning of the Tevatron, when errant protons or antiprotons in the Tevatron orbit are scraped from the beam bunches (see Appendix B). There is also a possibility of a catastrophic failure if a Tevatron magnet fails so that the entire proton or antiproton beam is dumped into the detector.

A radiation loss monitor and Tevatron beam abort were installed at CDF to ensure that the SVX was not destroyed by the Tevatron beam losses. The SVX received about 15 krad of radiation over the course of Run 1A which caused some bulk damage in the silicon itself and to the CMOS electronic readout chips. Despite the damage, the signal-to-noise ratio was sufficient for the SVX to perform adequately through to the end of the run. The SVX′ received about 70 krad in Run 1B. By lowering the bias-voltages and operating temperature and decreasing the integration times later in the run, the signal-to-noise for this device was kept above 8 for all of Run 1B, retaining full efficiency [136, 137].

The SVX sits snugly inside the VTX (described in the next section) and is supported by it. Proper alignment of the SVX components was critical to its performance. After careful mechanical alignment during the construction, the SVX barrel alignments were checked in the detector environment after installation by an extensive program of fitting high-p_T tracks passing through them and the Central Tracking Chamber (see Section 2.5.3). The maximum mechanical misalignments were measured to be less than 10 μm. The average spatial hit resolution from the track fitting is approximately 13 μm (11 μm for SVX′) and the impact parameter resolution, based on the p_T of the track (in GeV/c), is about $(16 + 40/p_T)$ μm.

The primary vertex position for interactions occurring in the SVX fiducial region is measured to roughly ± 40 μm in the x-y plane, with the resolution dominated by the beam spot r.m.s. spread of $\sigma \sim$ 36–38 μm. This varied somewhat with time and the position in z of the beam spot.

Individual layer hit-finding efficiencies varied from layer to layer but were in the range 91–93% (95–97% for SVX′), including corrections for dead regions. These efficiencies fell about 2–8% by the end of the run for the SVX due to the radiation

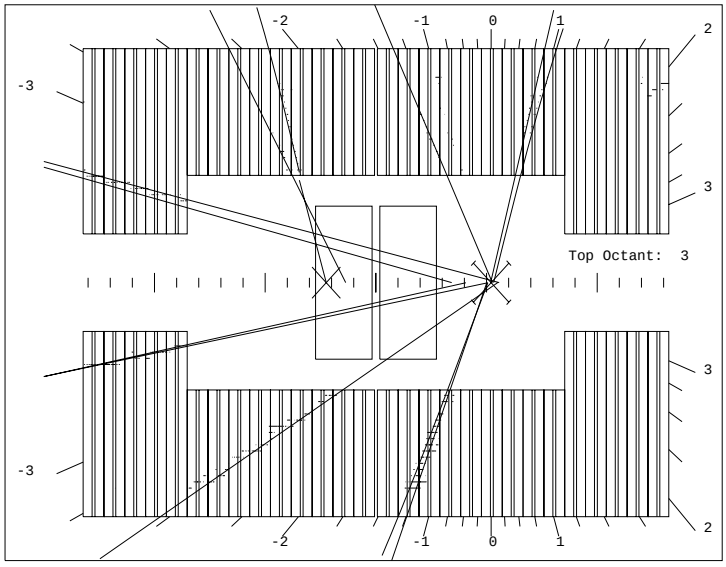

Figure 2.5: Event display showing a longitudinal view of the VTX. The beams travel horizontally through the center with protons travelling to the right. The straight lines are VTX track segments formed by the reconstruction software. Hits are visible along the track segments. The X's along the horizontal centerline indicate vertices found by the VTX algorithm; the X with bars at the tips indicates a high-quality primary vertex. The event pseudorapidity calculated from the primary vertex is indicated at the top and bottom of the picture by the scale -3 to $+3$. The two large boxes at the center of the picture indicate the positions of the two SVX barrels.

damage.

The SVX does not operate as a stand-alone tracker. Instead, tracks found in the main outer tracker (Central Tracking Chamber) are extrapolated back to the SVX, where the SVX hit information is used to further constrain and refine the track parameters. Track finding efficiency in the SVX was about 98% with approximately 70% (23%) of tracks having 4 (3) hits, one hit per layer. This degraded to about 60% (30%) with 4 (3) hits by the end of the run, but the track finding efficiency only dropped by about 1%. The efficiencies were slightly higher in SVX′ but comparable [138].

2.5.2 Vertex Time Projection Chamber (VTX)

The Vertex Time Projection Chamber (VTX) [139] is a gas drift chamber that surrounds and supports the SVX. Its main functions are to provide precise tracking

information for charged particles in the r–z plane, to determine the location along the beamline (in z) of the primary vertex and to distinguish multiple $p\overline{p}$ interactions in the same beam crossing. It is also provides the only forward/backward angle track information ($\theta < 10^\circ$ from the beamline) for particles that are directed towards the forward calorimeters (see Section 2.6.3).

The VTX has been designed to handle on the order of one hundred or more charged particle tracks per beam crossing. Like the SVX, it is also of low-mass construction to minimize the amount of material a particle needs to traverse. This minimizes secondary interactions and multiple scattering effects within the bulk of the detector itself, such as the photon conversion contamination of electrons (i.e. $\gamma \rightarrow e^+e^-$).

The VTX has an outer radius of 22 cm and provides a pseudorapidity coverage of $|\eta| < 3.5$. It consists of 28 drift modules, each divided into two drift regions (about 5 cm long each) by a central high-voltage grid. These modules are stacked end-to-end along the beam direction (z-axis). A longitudinal view of the VTX, showing the layout, can be seen in the event display picture in Figure 2.5. Each module is segmented into 8 wedges, each covering 45% in azimuth to give total ϕ coverage. There are 24 sense wire pairs arranged azimuthally in each plane for the 10 end modules with only 16 pairs in the 18 inner modules, due to the space needed for the SVX. Sense wires are strung in each drift region of a module on either side of the high voltage grid. The sense wires form an octagon, with eight straight sections, one in each wedge of a drift region. Ionized gas particles, created from the passage of an energetic ionizing (charged) particle, drift along z towards the center of a module to the sense wires, with the drift-time providing z information for the track and radial information coming from the position of the wire. Each module is canted 15° in ϕ relative to its neighbors, therefore rudimentary ϕ information can be obtained for a track crossing through more than one module.

The VTX measures the z-vertex of a track with a resolution of about 2 mm. This information is used by the tracking algorithms as a seed for 3-dimensional track reconstruction in the CTC (described next), as the z-vertex resolution in the

VTX is much more accurate than in the CTC.

2.5.3 Central Tracking Chamber (CTC)

The Central Tracking Chamber (CTC) [140] surrounds the SVX and VTX. It is a gas drift chamber that provides 3-D tracking information at the single particle level. The CTC also helps in identifying sources of missing energy for charged particles directed towards uninstrumented regions of the calorimeters.

The CTC is a cylindrical chamber of 0.28 m inner radius, 1.38 m outer radius, and 3.20 m length and covers $|\eta| < 1.0$ in pseudorapidity. It consists of 84 layers of 40 μm diameter gold-plated tungsten sense wires arranged into 9 superlayers. Five of the superlayers have their wires arranged parallel to the beam line (*axial*). These are interleaved with four superlayers that have *stereo* sense wires which are alternately arranged at $\pm 3^\circ$ to the beam line. The axial superlayers contain 12 sense wire layers each whereas the stereo superlayers contain 6 sense wire layers, for a total of 4,392 axial and 1,764 stereo sense wires. The axial layers give tracking information in the r–ϕ plane only while the stereo layers provide information in the r–z plane as well. Together, the axial and stereo layers measure the full helical path of charged particles traversing the chamber and bending in the magnetic field, yielding momentum and charge measurements for the tracks.

The superlayers are further subdivided into *cells* such that the maximum drift distance across a cell is less than 40 mm, corresponding to about 0.8 μs of drift time, which is shorter than the time between bunch crossings in the Tevatron (3.5 μs). Two planes of stainless steel field wires define and shape an electric field of 1350 V/cm in each cell. The sense wires lie midway between these with a potential wire separating each from its neighbor which is also used to control the gas gain on the sense wires.

Figure 2.6 shows a transverse end view of the CTC, showing the cells in each superlayer and their overlap. There is significant (about 20%) overlap in azimuth between the cells. All the cells are tilted by 45° with respect to the radial direction in order to compensate for the Lorentz angle, β, of the drift electrons in the crossed 1.41 T magnetic field and 1350 V/cm electric drift field, which gives the drift electrons

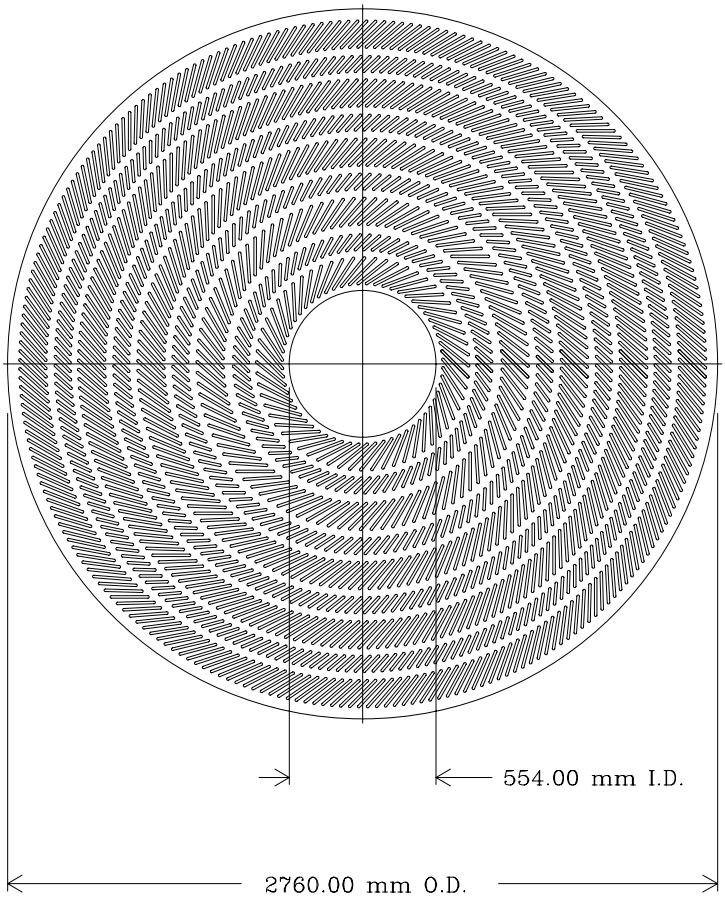

Figure 2.6: End view of the Central Tracking Chamber. This schematic shows the grouping of sense wires into superlayers, as well as the tilt and overlap of the sense wire cells; every second slot contains sense wires. The five superlayers with larger cells contain the axial wires, alternating with the four layers of smaller cells contain the stereo wires.

trajectories perpendicular to the radial direction. A benefit of this tilt is that it clears up the right-left ambiguity—an ionization electron can approach a sense wire from the left or right, and there is no instrumentation to distinguish between these alternatives. However, with the 45° tilt to the drift cells, only one of these two alternatives will point toward the event vertex for a high-p_T track which came from the event vertex. The tilt also guarantees that every radial high-p_T track must pass close to at least one sense wire in every superlayer. This is exploited in the online trigger system (see Section 2.9.5). This "zero crossing" condition on the drift times may be further exploited to help resolve closely spaced tracks.

A charged particle follows a helical trajectory in the CTC and leaves an ionization trail in the gas that is picked up as *hits* on the sense wires. Track reconstruction is done by fitting these hits to an arc of a helix which gives the track transverse momentum. The tracking algorithms begin by using information from the axial wires to fit the particle tracks in the r–ϕ plane. The z-position for the track is determined from the primary vertex in the VTX and this is used as a seed for reconstructing the three-dimensional track from the stereo wire information. These tracks are then projected into the SVX where the additional r–ϕ information is used to gain a transverse momentum resolution of $\delta p_T/p_T \approx 0.001 \times p_T$, with p_T in GeV/c (the resolution is $\approx 0.002 \times p_T$ for the CTC information alone).

Correlations between the multiple neighboring sense wires in a single cell are used to identify ambiguous or corrupted hit information. Internal data consistency checks in the pattern recognition algorithm allows resolution of tracks spaced as closely as about 5 mm. The longitudinal (z) resolution from the stereo wires is about 4 mm, equal to the position resolution of the calorimetry (see Table 2.3).

2.5.4 Central Preradiator (CPR)

The Central Preradiator (CPR) is positioned just outside the solenoid at 1.68 m in the radial direction from the interaction point. It is a multi-wire proportional drift chamber consisting of nearly rectangular cells which are approximately 2 cm wide in the azimuthal and radial directions. Each chamber of the CPR has 32 sense wires ganged in pairs and is filled with argon–carbon-dioxide gas. The CPR records the passage of charged particles in r–ϕ and is used to distinguish multiple electrons from photon conversions ($\gamma \rightarrow e^+e^-$) in the intervening 1.075 radiation lengths of material between the interaction point and the CPR; most of the material encountered is in the solenoid. The CPR is also used for statistical separation of single photons from multiple photons (from $\pi^0 \rightarrow \gamma\gamma$ decay, for example).

Figure 2.7: A lateral view of one quadrant of the CDF detector, showing the calorimeter subsystems and segmentation in pseudorapidity. The position of the Forward calorimeters is not to scale since they are moved in closer to the central region. The sharing of towers in the Central Hadronic and Wall Hadronic systems can be seen.

2.6 Calorimetry

The tracking chambers and solenoid are surrounded by calorimeters which provide 2π coverage in azimuth and up to $|\eta| < 4.2$ in pseudorapidity. The calorimeters are split into electromagnetic (EM) and hadronic (HA or HAD) elements and are separated into three main detector regions defined by their pseudorapidity coverage: the Central region containing the CEM and CHA as well as a Wall Hadron calorimeter (WHA), the Plug region containing the PEM and PHA and the Forward (and backward) region containing the FEM and FHA. The CEM also contains strip chambers (the CES) which measure transverse shower developments and improves the position resolution. This hybrid design combines the good energy resolution of a scintillator system (the CEM) with the fine segmentation of a gas layer (the CES).

These detectors subsystems will be discussed below in further detail. Table 2.3

Calorimeter	$\lvert\eta\rvert$ coverage	Energy Resolution $\sigma(E)/E$	Position Resolution [cm^2]	Thickness
Central EM	0 – 1.1	$13.5\%/\sqrt{E_T} \oplus 1.7\%$	0.2×0.2	18 X_0
Central HAD	0 – 0.9	$75\%/\sqrt{E_T} \oplus 3\%$	10×5	4.5 λ_0
Wall HAD	0.7 – 1.3	$75\%/\sqrt{E_T} \oplus 3\%$	10×5	4.5 λ_0
Plug EM	1.1 – 2.4	$28\%/\sqrt{E_T} \oplus 2\%$	0.2×0.2	18 – 21 X_0
Plug HAD	1.3 – 2.4	$130\%/\sqrt{E_T} \oplus 4\%$	2×2	5.7 λ_0
Forward EM	2.2 – 4.2	$25\%/\sqrt{E_T} \oplus 2\%$	0.2×0.2	25 X_0
Forward HAD	2.3 – 4.2	$130\%/\sqrt{E_T} \oplus 4\%$	3×3	7.7 λ_0

Table 2.3: CDF calorimeter information. Energy resolutions quoted are for incident electron and photons for the EM calorimeters and for isolated pions for the HAD calorimeters. The $\oplus$ indicates addition in quadrature of the energy dependent and constant systematic uncertainties. The position resolutions are averages for the calorimeter subcomponents. X_0 refers to *radiation lengths*, quoted for the EM calorimeters, and λ_0 refers to *interaction lengths* or attenuation, quoted for the HAD calorimeters. These are defined in a similar way. A radiation length is the distance over which the average energy of a high-p_T electron decreases by a factor $1/e$, due to bremsstrahlung in the nuclear Coulomb fields. One interaction length is the depth at which, of N neutral incident particles on a material, all but N/e will have interacted with a nucleus of the absorbing material.

summarizes the pseudorapidity coverage, energy and position resolutions, and thickness of each of the calorimeter subsystems. The relationship and positions of these detector subcomponents can be seen in Figure 2.7 which shows a close-up lateral view of the CDF calorimeters. Each calorimeter subsystem is further segmented in pseudorapidity and azimuth to form a *projective tower geometry* which points back to the geometric center of the detector with a segmentation of 0.1 units in pseudorapidity by 15° (central) or 5° (plug and forward) in azimuth. The segmentation and nominal coverage for the various detector subsystems is shown in Figure 2.8 for one quadrant.

Neutral particles and charged particles with a transverse momentum greater than about 350 MeV/c will have a trajectory that takes them out of the solenoid's magnetic field and into the CDF calorimetry. The particles deposit their energy in the sampling calorimeters which gives a measure of their energy. Each *tower* in a calorimeter has an electromagnetic element, followed by an hadronic element which

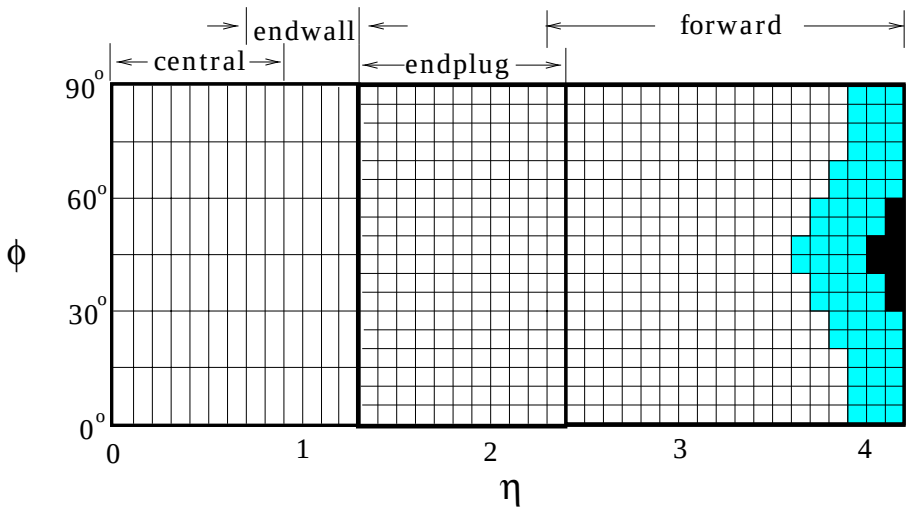

Figure 2.8: Schematic map showing the η–ϕ coverage of the CDF calorimeters for one quadrant. The EM calorimeters have complete coverage out to $\eta = 4.2$. The shaded area shows areas which have only partial coverage for the HAD calorimeters due to the low beta quadrupoles and the black areas have no coverage due to the hole for the beampipe.

allows the comparison of the amount of energy deposited in each to be made for any individual tower. This facilitates the identification of electrons, photons and pions. The absorber in all the electromagnetic calorimeters is lead, due to its high Z-value which promotes electromagnetic showers and iron (steel) is used in all the hadronic calorimeters due to its good structural strength for building large devices.

The detectors are *sampling* calorimeters with the absorber sheets interleaved with layers of either plastic scintillator (in the central) or gas proportional tubes (in the plug and forward) as the active media.

The active medium in the central calorimeters is plastic scintillator: polystyrene in the CEM and acrylic in the HAD elements. The scintillator is doped with wave shifting fluors which convert the scintillator light into green light of 490 nm which is collected via light pipes that direct the emitted light onto photomultiplier tubes (two per module). Gas proportional chambers are used in the plug and forward calorimeters since the light guides needed for a scintillator based system would have introduced substantial dead/hot regions[2]. The proportional chambers use a gas

[2]For Run 2, scheduled for the year 2000, the plug's active medium will be scintillating fiber which avoids the need for light guides

mixture of 50%/50% argon/ethane with a small amount of isopropanol ($< 1\%$) as the quenching agent to prevent wire aging and to control the onset of glow discharges.

The resolution of sampling calorimeters (HAD and EM) is usually dominated by sampling fluctuations, leading to the resolution σ/E scaling inversely as the square root of the incident energy. The energy resolutions quoted in Table 2.3 give the E_T dependent resolution summed in quadrature with a constant resolution uncertainty term determined by the calorimeter characteristics.

The CDF hadronic calorimeters are *non-compensating* as their response to π^0's differ from their response to other hadronic showers components. This is because π^0's decay early and predominantly into two photons which do not lead to a hadronic cascade shower. This, in part, accounts for the worse performance of the hadronic calorimeters as compared to the electromagnetic calorimeters at CDF. The energy measured for a jet depends on how the jet fluctuated and what fraction of the jet fluctuated into π^0's. The CDF hadronic calorimeters have been designed for 95% containment of 50 GeV/c pions. Therefore, higher momentum particles can "punch through" the calorimeter without depositing all their energy, again leading to a degradation in the energy resolution.

2.6.1 Central Calorimeters (CEM/CES/CHA/WHA)

The central calorimeters are divided azimuthally into 24 wedges, each covering 15° in ϕ and extend about 2.5 m along the beam axis on either side of $z = 0$. The modules are stacked into four free-standing "C"-shaped arches which can be rolled into and out of the detector for access to the inner components. One wedge module is notched to allow access to the superconducting solenoid. The sum of the cracks every 15° in ϕ where the wedges meet and the gap at $z = 0$ represents only 4.8% of the complete azimuthal coverage.

Each module of the Central EM calorimeter (CEM) [141] is divided into 10 projective towers, each subtending 0.10 units of pseudorapidity and pointing back to the nominal interaction point. Figure 2.9 shows a schematic of one CEM module. The CEM starts at a radius of 173 cm and is 35 cm thick. It is composed of 31 layers of

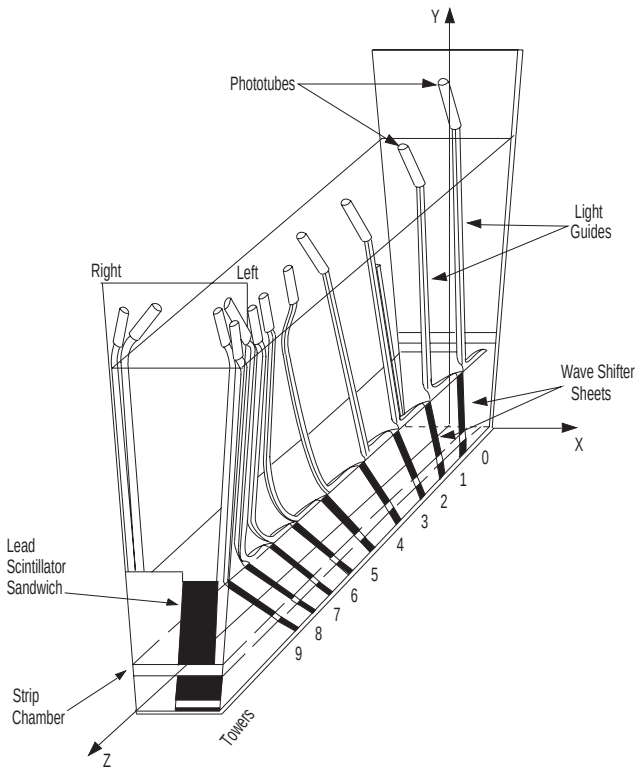

Figure 2.9: One wedge of the central calorimeter showing a CEM module in the lower half of the wedge with its light-guides. The ten projective tower geometry and the placement of the CES strip chambers are also indicated.

3.175 mm thick lead absorber interleaved with 5 mm thick layers of polystyrene scintillator. There are two wavelength shifters per tower, one on each side in azimuth, that direct the green waveshifted light to photomultiplier tubes.

Embedded in each CEM module, between the eighth lead layer and ninth scintillator layer, which corresponds to about 5.9 radiation lengths, is the Central Electron Strip chamber (CES). This is a combined strip-wire gas proportional chamber which is used to measure the positions and transverse shower shapes of electromagnetic clusters in both z and r–ϕ. Figure 2.10 shows a schematic diagram of the CES. The depth of the chamber in the CEM corresponds to the approximate maximum average transverse development of an electromagnetic shower. There are 128 strips that lie perpendicular to the beam direction, that function as cathodes, and 64 anode-wires, ganged in pairs, that lie parallel to the beam direction. These measure the shower profile in the η and ϕ directions respectively, with a position resolution of about

Figure 2.10: Schematic diagram of the Central Strip Chambers.

± 2 mm in both views, independent of the incident particle's energy. Combining information from this chamber with the CPR (see Section 2.5.4) improves the position resolution for electromagnetic showers that develop early.

The CES also provides position information for the identification of photons within particle showers. This is used to identify the neutral components in a hadronic tau decay, which consist mostly of $\pi^0 \rightarrow \gamma\gamma$ (see Sections 3.1 and 5.2.2).

After the CEM come the Central HAD (CHA) and Wall HAD (WHA) calorimeters [142]. Each tower in the CEM is matched by a hadronic tower. The coverage for these two detectors is given in Table 2.3 and a single central calorimeter wedge is shown in the longitudinal and transverse profiles in Figure 2.11. The central region is defined by towers 0 to 8, with towers 6 to 8 sharing the hadronic portion with the endwall calorimeter. Towers 9 to 11 (not shown) are completely in the endwall. Particles coming from the interaction region through this intermediate region will therefore pass through both the CHA and the WHA. The CHA is constructed from 32 layers of 2.5 cm thick steel absorber alternating with 1.0 cm thick plastic scintillator, for the inner seven towers. The WHA is constructed from 15 layers of 5.1 cm thick steel absorber alternating with 1.0 cm thick plastic scintillator.

The extra thickness of the WHA steel layers compared to the CHA is to account for the fact that a particle with a given E_T will have on average $\sqrt{2}$ times more total energy going through the WHA, which is in the more forward direction, than a particle with the same E_T passing through the CHA.

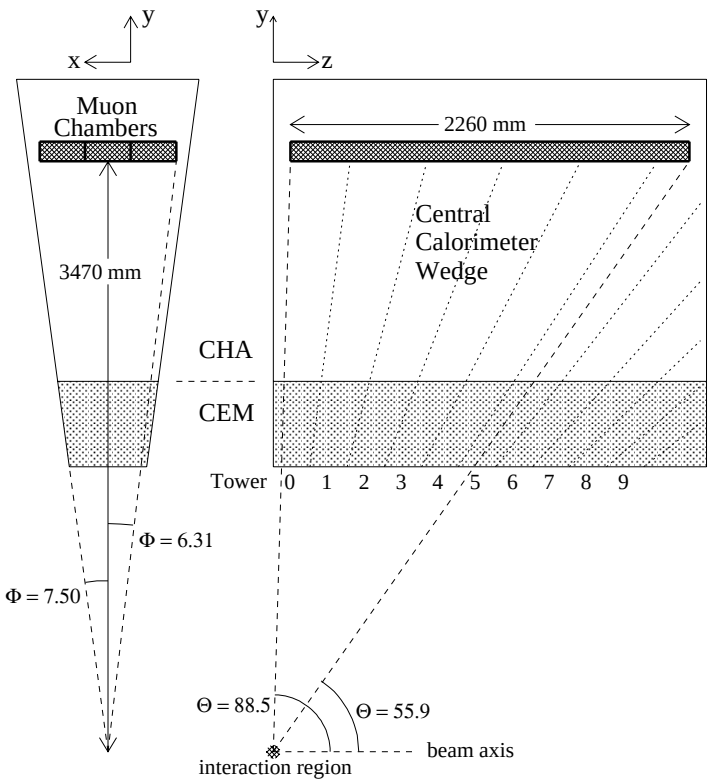

Figure 2.11: One module of the Central Calorimeter showing the ten projective towers for the CEM and the placement of a Central Muon Chamber (CMU) module.

The central and wall calorimeters were calibrated using radioactive sources, cosmic rays, and test beams of 50 GeV/c particles — electrons for the CEM and charged pions for the hadronic elements. Long term monitoring of both the CEM and CHA/WHA detectors is achieved through the use of radioactive sources and light sources to check on the aging of the scintillators and phototubes. Gamma rays from individual ^{137}Cs sources on each module are used to maintain the scintillator gain calibration over long time periods in both electromagnetic and hadronic elements. A ^{60}Co source which is automatically driven on a track is used to set the photomultiplier gains. For the CEM, short term variations are monitored by a xenon-flasher system that tests the response of the waveshifters to light. A light-emitting diode system injects green light into the CEM phototubes via quartz fibers to check on short term variations and a nitrogen laser is used in a similar way for the hadronic phototubes. During Run 1, source runs were done about once a month and the

flasher systems were used for daily calibrations.

2.6.2 Plug Calorimeter (PEM/PHA)

The two endplug calorimeters, consisting of the Plug EM (PEM) [143] and Plug HAD (PHA) [144] calorimeters, fit like end caps into the two 30° holes (as measured from the interaction point) left by the WHA (see Figure 2.2). There is a crack at the interface of the PHA and WHA. Each plug is composed of four azimuthal 90° quadrants that together encircle the beam pipe. The coverage in pseudorapidity is $1.1 < |\eta| < 2.4$ for the PEM and $1.32 < |\eta| < 2.4$ for the PHA. There is a concentric, conical hole of opening angle 10° measured from the interaction point for the inner part of the Plug. Both the PEM and PHA use gas proportional tubes as the active medium, with cathode pad readout. The gas proportional drift tubes are constructed of conductive plastic with a square cross section, and are strung with gold-plated tungsten wire. The tubes are arranged in layers perpendicular to the beam line giving good thickness and hermeticity.

There are 34 layers of proportional tube arrays arranged in the fan-shaped 1.4 m radius quadrants, interleaved with 2.7 mm thick layers of lead in the PEM, for a total depth in z of 50 cm. The strip layers around the shower maximum are four to five times more finely segmented to be able to examine shower cores in greater detail. This helps to identify isolated electrons, π^0's and low-momentum electrons or photons overlapping high-momentum jets. As there is only limited tracking available for the larger η regions (the CTC full coverage is only out to $|\eta| < 1$) there are fewer handles to distinguish electromagnetic showers caused by charged particles (electrons) or neutrals (photons, π^0).

The PHA has 20 layers of proportional tube arrays interleaved with 5.1 cm thick steel. For both the PEM and PHA, the copper plating on the cathode readout panels are etched in a pattern of radial lines and concentric arcs to give the projective tower geometry segmentation of 5° in azimuth (ϕ) and 0.09 in pseudorapidity (η). Figure 2.12 shows an exploded view of one quadrant of the PEM showing the copper cathode pad etching. The energy and position resolution for the Plugs are given in

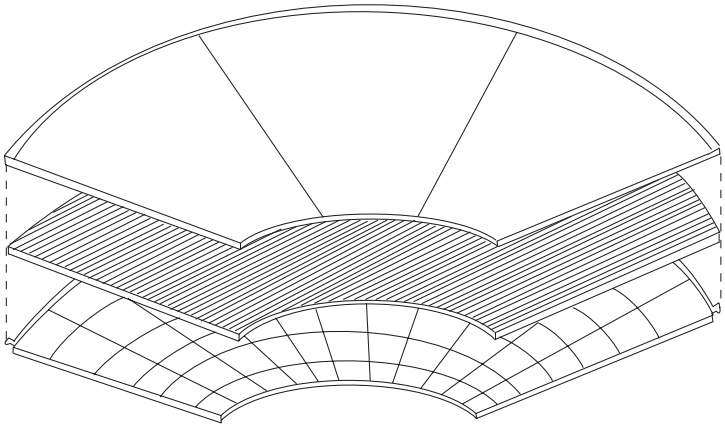

Figure 2.12: One quadrant showing an exploded view of the Plug Electromagnetic Calorimeter. The cathode pad segmentation in η (radial lines) and ϕ (arcs) is shown on the lower layer.

Table 2.3.

2.6.3 Forward/Backward Calorimeters (FEM/FHA)

The forward and backward regions contain the Forward EM (FEM) [145] and Forward HAD (FHA) [146] calorimeters. The FEM is located about 6.5 m from the interaction point and extends about 3 m on a side and 1 m in depth. Both the FEM and FHA cover $2.2 < |\eta| < 4.2$ in the familiar projective geometry and use gas proportional drift tube chambers with cathode pad readout, similar to the plugs. Again, there is a crack between the plug and forward calorimeters in pseudorapidity.

These chambers are not utilized directly in this dissertation as only detected objects out to $|\eta| < 2.0$ are used in the analysis.

2.6.4 Calibration of the Gas Based Calorimeters

The gas gain of the proportional chambers in the gas-sampling calorimeters (the Plug and Forward) is a sensitive function of temperature, pressure, high voltage and gas composition. This affects the energy calibration. The gain is continuously monitored, to better than 1%, via a number of special gas monitor drift tubes identical to the normal drift tubes and distributed among them within the same gas vessel. The

monitoring tubes are irradiated by 5.9 keV gamma rays from ^{55}Fe sources carried on external wires affixed to the tubes.

A test beam was used to calibrate and map the gas calorimeters. The Plug calorimeters were tested with 100 GeV/c incident electrons for the PEM and charged pions for the PHA. The Forward calorimeters were calibrated with particles with a momentum range of 20–200 GeV/c, with electrons used for the FEM and a combination of pions, electrons and muons for the FHA.

2.7 Muon Chambers

Muons are penetrating, hence act as minimum ionizing particles in the CDF calorimeters. Muons of $p_T > 1.5$ GeV/c have sufficient momentum to pass through the calorimeters and enter the muon tracking chambers that surround the calorimetry. The central muon chambers consist of the Central Muon (CMU) and two new chambers added in 1992 before the run: the Central Muon Upgrade (CMP) which improves the muon identification and triggering efficiencies and the Central Muon Extension (CMX) with scintillators (CSX) which extend the muon coverage. An η–ϕ coverage map for the central muon systems is shown in Figure 2.13. The CMU and CMP cover a pseudorapidity of $|\eta| \lesssim 0.6$ and the CMX, $0.62 < |\eta| < 1.0$. There are also the Forward Muons (FMU) systems in the forward and backward regions, covering $2.0 < |\eta| < 3.6$. All these systems are proportional drift chambers which measure charged particle tracks. A 50/50 mix of argon/ethane gas is used in all the chambers, bubbled through either ethanol (CMU and CMP) or isopropanol (CMX) at $-5°$ C as the quenching agent.

The chambers were tested and calibrated with cosmic-ray muons and in a pion test beam. Gamma rays of 5.9 keV from ^{55}Fe sources are used to monitor the gas gain during running.

Muon identification is accomplished through reconstructing tracks, called *muon stubs*, from the hits in the chambers. For the central detectors, these stubs are matched with tracks found in the CTC (see Section 2.5.3). These chambers and

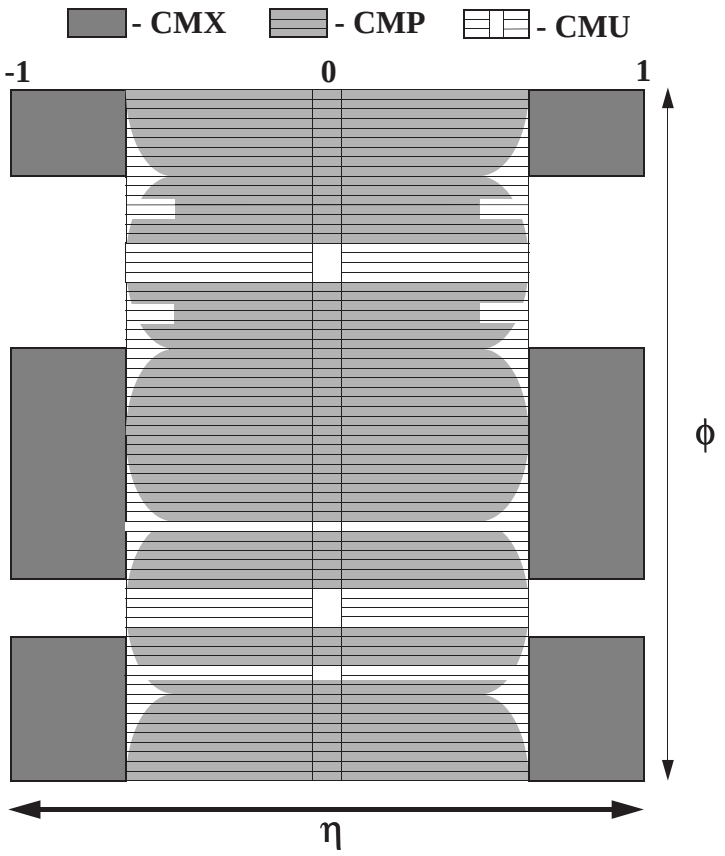

Figure 2.13: Muon coverage for the central CDF muon chambers in pseudorapidity (η) and azimuth (ϕ).

their operation are described in further detail below.

2.7.1 Central Muon Chamber (CMU)

The 48 Central Muon Chamber (CMU) modules [147] consist of four layers of single-wire drift cells attached to the outside of the central calorimeter wedges at a radial distance of 3.47 m from the beam axis. Figure 2.11 shows the placement of the muon chambers in relation to the central calorimeter elements in one wedge. Each muon module covers 12.6° in azimuth (of the 15° wedge), with 2.26 m long drift cells in z, giving coverage in pseudorapidity of $|\eta| < 0.63$. The 2.4° gaps between the CMU modules in adjacent wedges and the gap between the two calorimeter arches at $\eta = 0$ lead to a total coverage of 84% for the CMU for the $|\eta| < 0.63$ region.

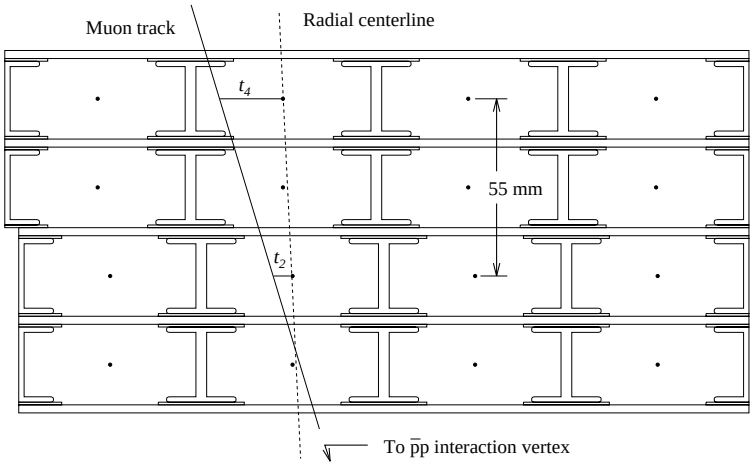

Figure 2.14: One tower of the CMU showing the arrangement of the four planes of drift tubes in a view along the beam direction. Alternating layers' sense wires have a 2 mm offset in their azimuthal position. A particle traversing through one muon tower and the associated drift times are also shown.

Each of the CMU modules is further segmented in ϕ into 3 towers of 4.2° each. One of these towers (consisting of 4 $\times$ 4 rectangular aluminum drift cells) is shown in Figure 2.14. The 50 μm stainless steel sense wire located at the center of a drift cell is held at +3150 V while the drift cell walls are held at −2500 V. This produces a roughly uniform time-to-distance relationship throughout the cell with a maximum drift time of approximately 1.2 μs. A *muon tower* consists of four of these drift cells, one in each layer. One pair of sense wires, from alternating layers, lies on a radial line passing through the interaction point. The other pair of wires are offset by 2 mm in azimuth from the radial pair. This helps resolve the left-right ambiguity as to which side of the sense wires the muon passed by determining the hit sequence on the sense wires.

Tracks are reconstructed in the r–ϕ plane with an intrinsic r.m.s. resolution of 0.25 mm using the drift time information for the hits in the 4 layers. Position information with a r.m.s. resolution of 1.2 mm in the z coordinate is obtained through division of the charges read out at either end of the sense wires. A *muon stub* is formed if a track is measured in at least 3 of the 4 layers in a muon tower. If this stub matches a CTC track then this track is classified as a muon candidate.

A rough transverse momentum (p_T) measurement for the muon track can actually

be made from the track azimuthal angle with respect to the sense wires, obtained from timing differences between alternating layers.

The calorimeters in front of the muon chambers act as absorbers and present an average of 5.4 interaction lengths for pions before they reach the CMU. *Punch-through* on the order of 1 hadron in 220 will occur however when a hadron passes through all the material in front of the CMU without interacting and leaves a track in the muon chambers; these hadrons form a significant source of background for muon identification.

2.7.2 Central Muon Upgrade (CMP)

Outside the CMU, the Central Muon Upgrade (CMP) [148] sits behind further shielding for extra hadron absorption. There are two 60 cm thick walls of steel on the sides of the detector, covering the ϕ regions $-45°$ to $45°$ and $135°$ to $225°$. The steel return yoke of the solenoid provides shielding for the top ($45° < \phi < 135°$) and bottom ($255° < \phi < 315°$) of the detector of roughly the same thickness as the side walls. Behind this extra shielding there are four layers of drift tubes of similar construction to those in the CMU, making up the CMP. There are gaps in the CMP coverage for the ϕ regions 80°–100° and 260°–280°. The pseudorapidity coverage, $|\eta| < 0.60$, is roughly the same as for the CMU with about 76% of the CMU's azimuthal coverage. The η–ϕ map in Figure 2.13 shows this more clearly.

The extra shielding almost doubles the hadron interaction length which reduces the hadronic background in this chamber compared to the CMU but also raises the threshold for detectable muons to a transverse momentum of about 2.2 GeV/c. About 95% of the hadrons making it to the CMU are stopped by this extra shielding.

2.7.3 Central Muon Extension (CMX)

Muon coverage is extended out to $|\eta| < 1.0$ by the Central Muon Extensions (CMX), which are a logical extension of the CMU. These consist of drift chambers (CMX) and two layers of scintillator counters (CSX) [149] which are used for triggering. The CMX modules [150] are mounted on four tall identical "arches" that each hold eight

wedges covering 15° each in azimuth, arranged on the frustum of a cone with its apex at the nominal interaction point. The CMX covers only 240° in azimuth with a 30° gap at the top and a 90° gap at the bottom of the detector. The coverage in pseudorapidity is $0.6 < |\eta| < 1.0$. Figure 2.1 of the CDF detector shows the placement of these arches around the central detector and Figure 2.13 shows the coverage.

A CMX module consists of four logical layers of 12 tubes for each 15° wedge. The drift tubes are of very similar construction to the CMU and CMP modules, only shorter (1.8 m). Successive layers are staggered to eliminate ambiguities.

Particles heading toward the CMX pass through more material than those heading towards the CMU, which leads to a larger pion interaction length on average ($\sim 6.8\lambda_0$) than for the CMU. Consequently, the minimum detectable muon transverse momentum is also slightly higher (> 1.7 GeV/c). The position resolution in azimuth for the CMX is about 0.27 mm.

There are four 2.2 cm thick Central Muon Extension Scintillator Counters attached to either side of each CMX module. Each scintillator is read out by a phototube. Coincidences between these counters and hits in the CMX are used online in the trigger at Level 3 (see Section 2.9.5) and offline to identify muon candidates and to reject background. Tracks from particles scattered from the beamline or off the face of the forward calorimeters are also vetoed using the timing of the CSX as their hits arrive too long after the bunch crossing.

2.7.4 Forward Muon Chambers (FMU)

The Forward (and Backward) Muon Chambers (FMU) [151] consist of pairs of 3.8-m-radius circular magnetized steel toroids with three sets of gas drift chambers and two planes of scintillation trigger counters. The FMU is segmented in r–ϕ and has a coverage in pseudorapidity of $2.0 < |\eta| < 3.6$. Muons are bent in the toroidal magnetic field (1.4 T at $r = 2.0$ m) yielding a momentum measurement with 13% resolution and a position measurement with resolution 0.13 mm. These chambers are not used in this analysis.

2.8 Beam-Beam Counters (BBC)

The Beam-Beam Counters (BBC) [129] are two planes of small scintillation counters mounted on the front of the forward and backward calorimeters, covering $3.24 \leq |\eta| \leq 5.90$ ($0.32^\circ < \theta < 4.47^\circ$) at a distance of 5.8 m from the interaction point. Coincident hits in both counters, in time with the passage of the proton and anti-proton bunches through the detector, serve as both a *minimum bias trigger*, indicating that some sort of beam-beam interaction occurred, and as the primary luminosity monitor. The timing window used is 15.0 ± 0.2 ns around the bunch crossing. The rate (number) of coincidences in these counters, divided by their effective cross sectional areas, is what gives the instantaneous (integrated) luminosity delivered to the B0 interaction region (see Section 4.8).

2.9 Data Acquisition and Trigger Systems

2.9.1 Overview

With the Tevatron operating with six proton bunches colliding with six anti-proton bunches for Run 1, bunch crossings occurred every 3.5 μs in the center of the CDF detector, corresponding to a rate of 285 kHz. At the operational luminosity of $\mathcal{L} \approx 10^{31}$ cm^{-2}s^{-1} for Run 1, and a total $p\overline{p}$ cross section of $\sim$ 50 mb, more than one $p\overline{p}$ interaction is expected per crossing on average ($n = \sigma \times \mathcal{L}/\text{rate} \simeq 1.6$), with each bunch crossing termed an *event* as far as the data and triggering systems are concerned.

The CDF data acquisition system (DAQ) therefore has to contend with a few hundred thousand events per second, a formidable task. Most $p\overline{p}$ interactions are diffractive, giving rise to *minimum bias* events which have no high-p_T end-products and are of lesser interest. Events considered interesting to most CDF analyses tend to produce high-p_T particles and have very small cross sections. For example, the total cross section for the production of a W boson, $\sigma(p\overline{p} \rightarrow W + \text{anything})$, is about 25 nb, which means only one W event is created about every 4 seconds during beam

collisions. As the top pair production cross section is only about 5 pb, only one $t\bar{t}$ event is expected every 5 hours. Note that due to detector acceptances and trigger efficiencies, only a small fraction of these rare events are actually recorded by the experiment.

The other interesting physics processes, such as the production of the heavy charm and bottom quarks, have relatively high cross sections (and therefore rates) but still can be swamped by the much higher rate for the production of the lighter quarks (u, d and s) in $p\bar{p}$ interactions.

To limit the amount of data that needs reprocessing, a sophisticated online trigger system is employed to select interesting events in real time from the data stream for storage. CDF can only record data to permanent storage media (8 mm tape for Run 1A or disk staged to tape for Run 1B) at a maximum rate of a few events per second. We therefore need a rejection factor of about 10^4–10^5, while maintaining high trigger efficiencies for the desired types of events.

Another design concern for the DAQ is to minimize the *deadtime* which is the time during which event information is read out of the detector electronics. During this time, the trigger systems can not react to a beam-crossing. Since every $p\bar{p}$ interaction has equal chance of producing an interesting event, it is important to be able to examine as many of the beam-crossings as possible and as quickly as possible. A three-tier trigger system has therefore been developed at CDF where, progressively, each level examines fewer events in greater detail than the previous level. This allows "uninteresting" events to be rejected quickly at the initial trigger levels and gives more time for the later, more sophisticated, trigger levels to scrutinize potentially interesting events more closely before accepting or rejecting them.

The Level 1 and 2 triggers are implemented on custom-designed trigger boards and the Level 3 trigger is implemented in software running on commercial computing systems. The DAQ controls two parallel data paths, one fed by *fast-out* analog signals from a subset of the CDF detectors into the hardware trigger systems (Levels 1 and 2) while the other uses fully digitized signals coming from *scanners* reading out all the detector electronics and sending these data to the Level 3 trigger system.

Level 1 examines every event and makes a trigger decision within the time between beam crossings (3.5 μs) and is therefore deadtimeless. Level 1 accepts about 1–2% of events, reducing the event rate from a few hundred kHz to a few kHz. If Level 1 accepts the event, the event is passed on to Level 2 which takes about 25–35 μs to process it so that during this time the next 7–10 bunch crossings are ignored by the DAQ. There is no *buffering* (i.e. storage of events in a queue before processing), at this level so the Level 2 trigger decision accounts for a few percent deadtime. The Level 2 accept rate was limited to a peak rate of about 22 Hz for Run 1A and about 40–55 Hz for Run 1B, in order not to swamp the DAQ.

If Level 2 accepts the event, a signal is sent to the *front-end* electronics on the detector to digitize the event and the scanners then read out the full event. The digitization and scanning takes about 3 ms, accounting for another few percent deadtime. The scanners can buffer events, so once the event is read out, the DAQ system is *live* again and can trigger on a new event. The fully digitized event is sent to the Level 3 trigger system which runs event reconstruction software consisting of physics algorithms to determine if the event should be accepted or rejected. The reconstruction algorithms run in Level 3 are a subset of those used offline, with simpler and faster tracking algorithms used due to the time constraints (see Chapter 4 for details of the event reconstruction). Level 3 takes on the order of one CPU second to process an event. The Level 3 output peak rate was about 5–7 Hz for Run 1A and about 10 Hz for Run 1B. Level 3 buffers events and processes them in parallel and usually contributes no deadtime. If an event passes Level 3, it is tagged for data logging. Separate processes (termed *consumers*) log the data to tape and do online monitoring of data quality and of detector subsystem performance.

The details of the design and internal operations of the various trigger levels are discussed separately below in Sections 2.9.3–2.9.5.

The data acquisition system underwent substantial upgrades between Runs 1A and 1B to handle the increased data rates due to the increased luminosity of the Tevatron. The trigger data paths for the Levels 1 and 2 triggers remained essentially the same but the full digitized data path from the electronic scanners onward was

replaced. An outline of the Run 1A DAQ, which has been described in detail elsewhere [152], is given in Appendix C, followed by a somewhat more detailed account of the upgraded system for Run 1B. As the CDF collaborators from Rutgers University (including myself), were responsible for the Level 3 systems for Run 1, I also present a detailed description of the upgraded Level 3 trigger system for Run 1B in this appendix.

2.9.2 Trigger Tables and Prescales

A *trigger* is a collection of physics requirements designed to select specific kinds of events. Event selection criteria for the three trigger levels are determined by a *trigger table* which determines the software modules that are run to make a trigger decision (the trigger *logic path*) and the thresholds for criteria that are used both in the hardware and software in making these decisions (termed *cuts*). The trigger table text file is parsed by the DAQ at the beginning of a run and the thresholds are downloaded to the hardware triggers and scanners. Calibration constants are downloaded to the hardware at the same time. These remain constant during a run which lasts for a Tevatron store or part thereof. Detector calibration data are recorded between Tevatron stores and the calibration constants are updated in between runs. The thresholds and trigger paths used in a run are documented to assist offline reconstruction, trigger efficiency measurements and luminosity calculations. For most of the data collected over Run 1 the trigger table remained essentially the same. Special runs were also occasionally recorded with trigger tables that had special triggers designed for particular physics processes or to establish a baseline dataset for use by many analyses.

Individual trigger paths can be *prescaled* in the Level 2 or Level 3 trigger systems which that means only a certain fraction of the number of times the trigger is passed are accepted. This is done to keep an acceptable livetime for the experiment without raising trigger thresholds too high, and to allow many trigger paths for a diverse

physics program.[3] Some of these prescales are automatically altered during a run to pass a higher fraction of events as the beam's luminosity falls over a store, allowing the maximum use of the available data bandwidth.

As the cross section for any physics process falls rapidly with increasing p_T, most $p\overline{p}$ interactions yield events with low momentum end-products. Most trigger paths therefore required objects with at least 5–10 GeV of energy (or momentum) to gain enough purity for the interesting high-p_T events. The trigger thresholds and efficiencies used for the data selection for this dissertation will be discussed in Chapter 4.

2.9.3 Level 1 Trigger

The Level 1 trigger can only examine very simple event quantities as it needs to make a decision in the relatively short time between bunch crossings (3.5 μs). There is no event buffering at this stage. Level 1 is implemented in custom hardware and uses the analog fast-outs to compare calorimetry and muon detector readouts to trigger thresholds. This is done in parallel paths on separate hardware boards which do the summation and comparison with different thresholds for the different detector subsystems. The separate trigger decisions for each subsystem are sent to FRED (see Appendix C) which makes the final Level 1 trigger decision. A large deposit of energy ($>$ few GeV) in the calorimeters (electromagnetic or hadronic) or a hit in the muon chambers is an indication of a hard $p\overline{p}$ scatter. There is no inner tracking information available at this level.

The Level 1 (and Level 2) trigger uses *trigger towers* for looking at the calorimetry, which span a width of about 15° in azimuth (ϕ) and 0.2 in pseudorapidity (η). This corresponds to two physical towers in η and one physical tower in ϕ for the central calorimeters or three physical towers in ϕ for the plug and forward calorimeters. The general calorimetry trigger (used for all jet physics analyses) required a single trigger tower over some E_T threshold (this will be discussed in Section 4.2.1).

---

[3] There are 128 trigger bits available divided approximately into 10/40/70 for the Level 1/2/3 triggers. Each bit can potentially code for a different physics process.

The event rate (accept rate) out of Level 1 is a few kHz which is determined by the trigger thresholds. These are set so as not to swamp the Level 2 trigger yet to keep reasonable energy thresholds for the interesting physics.

2.9.4 Level 2 Trigger

The Level 2 trigger also consists of custom-built hardware and again uses the fast-outs from the readout electronics. However, it has more programmable hardware, including two DEC Alpha processors added for Run 1B, and can therefore cut on aggregate quantities which are more closely identified with physics objects (such as photons, leptons and jets) than the individual detector components quantities. The maximum Level 2 accept rate for Run 1A was determined by the rate the Event Builders (see Appendix C) could handle, which was about 22 Hz. For Run 1B the Level 2 accept rate was about 40–55 Hz which was governed mainly by the electronics readout times and the processing power available in Level 3. See Appendix C for a more detailed discussion. The trigger thresholds and prescales were tuned to achieve these rates while still maintaining good acceptance for the interesting physics processes.

The Level 2 trigger hardware makes trigger decisions based on various quantities such as jet clusters, the scalar sum of the total transverse energy ($\sum E_T$), the missing energy ($\not\!\!E_T$ — see Equation 2.7), two-dimensional tracks in r–ϕ from a hardware track finder (CFT — see below), and matching of these tracks to calorimetry clusters, to muon stubs and to the output of a neural-net used on electromagnetic clusters to isolate photons (and used on hadronic clusters for taus in Run 1B).

Level 2 *calorimeter clusters* are identified by an algorithm which looks for trigger towers over a seed threshold ($E_T > 3$ GeV) and then adds adjacent trigger towers over a shoulder threshold (> 1 GeV) to the cluster. Electromagnetic clusters are distinguished from hadronic jet clusters by comparing the ratio of the electromagnetic energy to the total energy in the cluster.

The Central Fast Tracker (CFT) [153] is a hardware track finder that uses the axial superlayers in the CTC (see Section 2.5.3) to find two dimensional tracks in

r–ϕ for use by the Level 2 trigger. As the CTC sense wire planes are rotated by 45° relative to the radial direction, the ionized electrons left by a passing charged particle have roughly azimuthal drift trajectories in the applied magnetic field from the superconducting solenoid. A high-p_T track will be roughly radial and will pass close to at least one sense wire plane in each superlayer. The *prompt* hits generated in these sense wires are characterized by their small drift time after the bunch crossing. The CFT uses an 80 ns coincidence gate to collect all these prompt hits. *Delayed* hits are collected from the other sense wires with a coincidence gate of 500–600 ns after the bunch crossing, where the timing is set to allow two delayed hits per superlayer for high-p_T tracks and corresponds to drift distances of about two-thirds the width of a CTC cell.

Tracks are formed from the hit patterns, called *roads*. Starting from a prompt hit in the sense wire of the outermost superlayer (superlayer 8) 32 roads are searched inward through the CTC for hits, split into eight p_T bins and two azimuthal bins for each curvature direction (positive or negative charge track), which gives coverage over the entire momentum range above 2.5 GeV/c. The CFT normally takes about 8 μs to complete its track list. The high-p_T track information is typically available after only about 2.5 μs. From the position of the track and its p_T bin, the track can be matched to calorimeter clusters using a lookup table.

The CFT measures high-p_T tracks with very high efficiency that is independent of track density. The p_T resolution of the CFT is about $\delta p_T/p_T = 0.035 \times p_T$ (in GeV/c). However, as the tracks are based only on one prompt hit out of twelve possible in a superlayer there is still a sacrifice in the accuracy due to the time constraint.

2.9.5 Level 3 Trigger

The Level 3 software trigger was implemented using a "farm" of Silicon Graphics multiprocessor systems running the IRIX operating system — six Power Server 4D/480 series systems with 8 MIPS R3000 CPUs each for Run 1A and four Power Server and four Challenge series systems with R4000/R4400 CPUs for Run 1B. The

number and type of CPUs in Run 1B varied during the run as some Challenge systems were upgraded to 200 MHz processors with 12 CPUs later in the run. The Run 1A CPU power was benchmarked with the CDF analysis software to be about 1100 VUPs (where 1 VUP is the equivalent of one DEC VAX 11/780 processor and corresponds to about 1 million instructions per second) and the Run 1B peak CPU power was over 3200 VUPs.

The Level 3 farm executables ran the same FORTRAN analysis software that was used offline for event reconstruction, with a few modifications for speed. Various software modules are responsible for constructing physics quantities such as tracks or clusters of energy from the fully-digitized, raw information from the detector. Full 3-dimensional track reconstruction is done using the VTX and CTC information but no SVX information is used due to the time constraints. The track reconstruction algorithm was simplified somewhat as only one pass is made through the tracking data compared to the offline reconstruction where an additional, separate algorithm makes another pass through the tracking data and the resulting tracks are merged. The offline package also tries to improve the merged tracks by adding unused hits or removing spurious hits to improve the track resolution. Another difference to the offline is that the calibration constants used in Level 3 are those that are available at the time of the run, which are normally improved later for the offline reconstruction.

After the data reconstruction, various analysis and filtering software modules are run in separate trigger paths specified by the trigger table. The filtering modules select general classes or specific types of events such as those with large missing transverse energies or with a high-p_T isolated lepton. These trigger decisions are compared to the requested events which determine whether an event passes Level 3 and is sent to the consumer processes or is rejected.

As Level 3 buffers and processes events in parallel, it usually incurred no deadtime, as long as there were free buffers available to accept events from the rest of the DAQ. The average time taken to process an event was about 1–2 CPU seconds for the Run 1A system. As the number of interactions per crossing increases for higher luminosities, the typical event in Run 1B was more complex, increasing the

processing time in Level 3, due mainly to the non-linear growth of the time needed for track deconvolution with increasing number of hits in the tracking chambers. Therefore, despite the large increase in processor speed, the average event still took about 0.65–1 CPU seconds in Run 1B.

Chapter 3

Search Strategy

As discussed in Section 1.2.2, in an extended Higgs sector where $M_{H^\pm} < M_t - M_b$, top quark decays via the channel $t \to H^+ b$ are possible. This channel would compete with the standard top quark decay channel, $t \to W^+ b$, discussed in Section 1.3.3. The branching fractions for these channels are dependent on the parameter $\tan\beta$, the ratio of the vacuum expectation values of the two Higgs doublets, and the masses of the top quark and charged Higgs boson, as discussed in Chapter 1 and Appendix A.

Figure 3.1 shows an example of a Feynman diagram for the production of a top quark pair with one of the top quarks decaying via the SM decay $\overline{t} \to W^- \overline{b}$ and the other via a charged Higgs, $t \to H^+ b$. The charged Higgs boson subsequently decays predominantly via $c\overline{s}$ for $\tan\beta \lesssim 1$ or via $\tau^+ \nu_\tau$ for $\tan\beta \gtrsim 1$ (see Figure 1.5 for the relative branching fractions as a function of $\tan\beta$).

The goal of this analysis is to identify top quark pair production and decays via the charged Higgs decay channel, where either one or both of the top quarks decay via a charged Higgs boson and the charged Higgs boson subsequently decays to a tau lepton. We are therefore only sensitive to regions of the parameter space where $\tan\beta \gtrsim 10$, where there is a large branching fraction of top quark decays via the charged Higgs and where the charged Higgs decays predominantly to taus. A separate analysis has been conducted at CDF for the low $\tan\beta$ region ($\tan\beta < 1$) based on the number of top quarks events observed in the dilepton and lepton + jets search channels [43, 2]. These search channels were described in Section 1.3.3.

The analysis conducted here is based on events that are selected online during data acquisition for the large energy misbalance in the events, termed missing transverse energy ($\not\!\!E_T$ — cf. Equation 2.7). This data set is used because we expect a

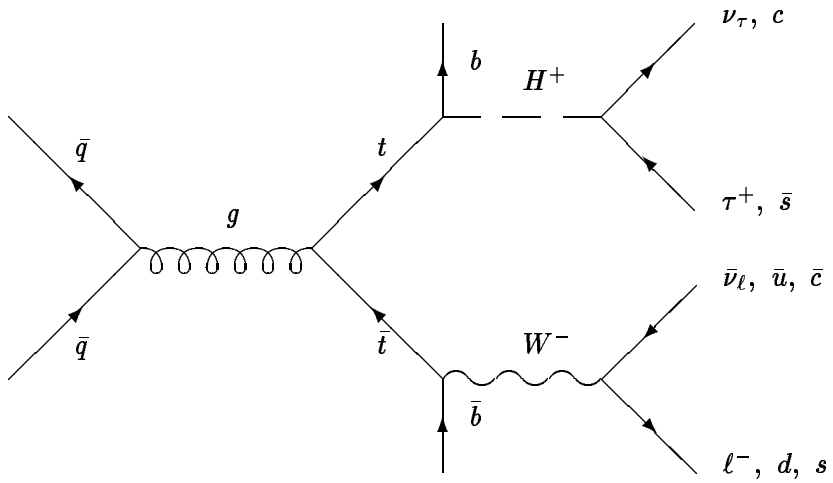

Figure 3.1: Feynman diagram depicting $t\bar{t}$ production with subsequent decays to charged Higgs and W bosons.

large fraction of the momentum from the top decays to be in the form of neutrinos from the charged Higgs and tau decays. These neutrinos escape the detector resulting in an energy misbalance for the events of interest. The data selection and reprocessing are discussed in detail in Chapter 4.

After data selection and the reconstruction of the event quantities, we uniquely assign "objects" in an event to one of five categories — photon, electron, muon, hadronic tau decay or a jet. The jet classification is a catch-all for all objects not identified as some other object. The detailed identification selection criteria (termed *cuts*) used in this analysis are described in Chapter 5. These criteria, apart from the tau identification, are very similar to those used in other CDF top analyses. We then look for a decay topology that resembles the top quark decay via a charged Higgs boson.

The decays and defining characteristics of the tau lepton are discussed below, in particular for the decays to hadronic final states. After that, the motivation for the topologies used in the charged Higgs search are discussed with the detailed event selection discussion deferred to Chapters 5 and 6. The backgrounds to the search and the extraction techniques used for the signal are discussed in Chapters 7 and 8, respectively.

Property	Value
Mass	1777.0 ± 0.3 MeV
Mean lifetime (τ)	$(290.7 \pm 1.3) \times 10^{-15}$ s
Decay length ($c\tau$)	87.2 ± 0.5 μm

Table 3.1: Properties of the tau lepton. $c\tau$ is a measure of the distance a relativistic tau travels before decaying.

3.1 Decays of the Tau Lepton

The tau lepton properties are listed in Table 3.1. The tau lepton is unique in that it is the only lepton that is heavy enough to decay into hadrons. Significant improvements in the experimental measurements of the tau decay branching fractions have been made in the last few years. Most of the branching fractions have an absolute uncertainty in the range of 0.1 to 0.2%. About 100 decay modes have been identified and measured. See Reference [8] for the latest details. Table 3.2 lists the most recent world-average measurements for the major decay modes.

In summary, taus decay to leptonic decay products (e or μ) 35% of the time and to hadronic decay products, consisting mainly of pions and kaons, 65% of the time. Of the hadronic decays, 77% are to final states with one charged decay product, termed *one-prong decays*, and 23% are to final states with three charged decay products, termed *three-prong decays*. Only about 0.2% of the hadronic decays are to final states with five or more charged decay products and these are ignored in this analysis. Due to the difficulties in distinguishing the tau decay modes to leptons from other non-tau related sources of electrons and muons, we only use the hadronic tau decay modes in this analysis. A significant proportion of the original tau momentum would also be undetected in the leptonic decay modes due to the presence of two neutrinos in the decay chain, increasing the tau identification difficulty.

Tau leptons are much harder to identify at hadron colliders than the other two leptons, the electron and muon. They are short-lived, so only their decay products can be detected, and all the decays involve at least one tau neutrino, hence some of the original momentum of the tau cannot be measured, and in general must be

$\tau^- \to X^- \nu_\tau$	Branching Ratio (%)
leptonic	35.18 ± 0.13
$e^- \overline{\nu}_e$	17.83 ± 0.08
$\mu^- \overline{\nu}_\mu$	17.35 ± 0.10
hadronic 1-prong	49.78 ± 0.17
$\rho^- \to \pi^- \pi^0$	25.24 ± 0.16
π^-	11.31 ± 0.15
$a_1^- \to \rho^- \pi^0 \to \pi^- 2\pi^0$	9.50 ± 0.14
$\pi^- \geq 3\pi^0$	1.28 ± 0.10
K^-	0.71 ± 0.05
$K^{*-} \to \overline{K}^0 \pi^- \geq 0$ neutrals	1.54 ± 0.10
$K^{*-} \to K^- \geq 1$ neutrals	0.94 ± 0.10
hadronic 3-prong	14.91 ± 0.14
$2h^- h^+$	9.80 ± 0.10
$(a_1^- \to \rho^0 \pi^- \to 2\pi^- \pi^+)$	(9.44 ± 0.10)
$2h^- h^+ \geq 1$ neutrals	5.08 ± 0.11
$(2\pi^- \pi^+ \geq 1\pi^0)$	(2.76 ± 0.11)
hadronic ≥ 5-prong	0.13 ± 0.02

Table 3.2: A summary of the main decay modes and branching fractions for the tau lepton decay $\tau^- \to X^- \nu_\tau$, where X^- are the modes described in the table. Values are from the latest PDG fit basis modes [8]. The τ^+ modes are charge conjugates of those listed above. The modes have been separated into the leptonic decay modes and hadronic decay modes which are further separated by the number of charged particles in the final state. *Neutrals* refer to π^0's and K_L^0's, and $h^\pm$ refers to $\pi^\pm$ (mostly) and $K^\pm$. Decay modes in parentheses are subsets of the mode above. Due to rounding, and some minor modes not included in the above, the branching fractions do not add to exactly 100%. The two resonances a_1 and ρ contribute a significant fraction of the hadronic decay modes.

inferred from energy and momentum "balancing" in the detector. A typical hadronic tau decay consists of a narrow jet of particles with one or three charged tracks. The invariant mass of all the tau decay products (including neutrinos and π^0's) should sum to the tau mass, 1.78 GeV/c^2. We use this feature as one of the identification cuts, discussed in Chapter 5. Since neutrinos are undetected, however, the invariant mass of all *detected* tau decay daughters is less than this. We also need to account for the significant fraction of the tau's original momentum that could be in the form of π^0 mesons which mostly decay electromagnetically to photons.

The jet of particles from a hadronic tau decay is, in general, narrower than jets

from pure QCD processes and has fewer charged tracks. This confinement of the tau energy along with the lower track multiplicity provides a method for separating hadronically decaying taus from other jets. The decay of the tau in its own rest frame provides only a certain amount of energy to the decay products and is independent of the tau momentum. Hence, as a tau becomes more energetic in the lab frame, its decay daughters subtend an increasingly smaller solid angle due to the Lorentz boost given the particles by the tau momentum. In contrast, the width and charged particle multiplicity for a jet from the hadronization of a prompt high-momentum parton tends to scale with the initial parton momentum due to fragmentation of the color strings between the quarks. These jets also tend to be less isolated due to strong interactions between the other partons during hadronization. We use the narrowness of the tau jets, the low track multiplicity and the isolation to aid in identifying tau leptons, discussed in Section 5.2.2.

For a typical tau momentum of 40 GeV/c from the decay of a W boson, the boosted decay length is of the order $\gamma c\tau = 2.0$ mm. This decay length is a little too short to be reliably tagged as a secondary vertex in the silicon vertex detector. In contrast, b quark decays of similar momenta give a secondary decay vertex of about 4 mm, but with more charged particles in general from the quark decay and, hence, yield better tagging efficiencies.

There have been suggestions that the tau polarization could be used to further extend the sensitivity of the search for the charged Higgs from the decays of top quarks at hadron colliders [154]. Due to the V–A nature of the electroweak force, the weak vector W^- boson couples only to left-handed τ^- states (denoted τ_L^-) and the W^+ couples only to right-handed states, τ_R^+. However, the charged Higgs boson, which is a scalar, couples in the opposite manner where the H^- couples to τ_R^- and the H^+ couples to τ_L^+. This is a consequence of the helicity flip nature of the Yukawa couplings of the Higgs fields and holds for all models containing only left-handed neutrinos (and right-handed antineutrinos). The polarizations of the decay products from the decay of the W^- and H^- bosons is shown schematically in Figure 3.2.

Figure 3.2: Polarization of the tau and tau-neutrino from the decay of W^- and H^- bosons, in the rest frame of the bosons. The W is a vector boson (spin-1) whereas the H is a scalar (spin-0).

The hadronic decays of the tau lepton are dominated by decays to the vector mesons ρ and a_1 or to the scalar pions. Due to parity violation and the left-handedness of the electroweak force, the tau-neutrino from the τ^- decay must be left-handed (ν_{τ_L}) and the τ^+ decay gives a right-handed $\overline{\nu}_{\tau_R}$. This constrains the angular momentum distribution for the hadronic decay products, depending on the handedness of the parent tau. The decay distributions of a τ_R^- are significantly different from those of a left-handed tau, τ_L^-. The most energetic particles from τ_L^- decays are *transversely* polarized ρ^- and a_1^- mesons, whereas the energetic particles arising from τ_R^- decays are π^- and *longitudinally* polarized ρ^- and a_1^- mesons. The transversely polarized ρ^- favor equal splitting of the ρ energy between the two decay pions, whereas longitudinally polarized ρ^-'s lead to large differences between the energy sharing between the π^- and π^0.

For the a_1^- decay to either $\pi^-\pi^-\pi^+$ or $\pi^-\pi^0\pi^0$, two of the pions in the final state are identical. Again the transversely polarized state ($a_{1_T}^-$) tends to share the energy equally among the three pions whereas the longitudinal state ($a_{1_L}^-$) favors configurations where one or two of the pions are soft, enhancing the energy for the third pion.

For τ_L^- decays to $\pi^-\nu$, the pion is a scalar, hence the neutrino, which is also left-handed, carries all the spin. The neutrino is therefore emitted preferentially in the direction of the tau parent and the pion is emitted in the opposite direction (with $1 \pm \cos\theta$ distributions where θ is measured with respect to the tau direction and the "+" case is for the neutrino), reducing the pion energy in the laboratory frame. The opposite occurs for the τ_R^- decay, enhancing the observed pion's energy.

It seems possible therefore that, given enough events and reasonable tau identification, one could distinguish the heavy boson involved in the top quark decays. However, the W boson from SM top decay is predicted to be about 70% longitudinally polarized[1] from the Lorentz boost [155]. The polarization differences are therefore reduced as the taus from the W boson decay will not be 100% polarized in the laboratory frame. Monte Carlo studies showed that the Run 1 data did not provide sufficient luminosity to observe these differences. However, the fact that tau leptons from charged Higgs receive an extra "boost" to the final decay products does enhance the possibility of observing an excess of events in the search channels. These differences could play a more crucial role in future searches with higher statistics. All the polarization effects have been incorporated in the Monte Carlo simulations for the signal data, as discussed in Chapter 6.

3.2 Charged Higgs Decay Search Topologies

After the Run 1A charged Higgs analysis [94] and with the knowledge that the top quark was reasonably heavy, this analysis was geared towards looking for more massive objects than had been done in previous CDF searches. To extend the sensitivity to charged Higgs production into the region of the measured top quark mass, strict kinematic and event structure cuts are required to enhance the top decay to charged Higgs topology. Previous analyses only required $\not\!\!E_T$, a tau and a jet with fairly loose event structure topologies.

Collisions which produce top quark pairs with at least one of the tops decaying via a charged Higgs boson, result in events with at least one tau, a bottom quark from each top decay, and large missing transverse momentum from the neutrinos. If the other top decays via charged Higgs, there will be another tau in the event, otherwise there will be the decay products of a W boson. Due to the large masses of the top quarks and bosons, the decay products from a top event should exhibit

[1] The helicity here refers to the projection of the spin of the W along its direction of motion in the rest frame of the top quark. The zero helicity or longitudinally polarized state has no spin projection along its direction of motion.

reasonable balance and hermeticity in the transverse plane, taking the neutrinos into account as well. Also, as the bosons are not strongly interacting particles they are not involved in the strong interactions which form the underlying event. Therefore particles from the primary decays i.e. the taus and b-quarks tend to be well separated or isolated and can therefore readily be identified.

One of the key features of the top decays to charged Higgs bosons is the presence of the energetic neutrinos: from the charged Higgs decays, $H^+ \to \tau^+\nu$ and from the decay of the tau leptons. We therefore require there to be a substantial misbalance of transverse energy in the detector ($\not\!\!E_T$) which is used both to select events online as described in Chapter 4 and after the full event reconstruction and object identification as described in Chapter 5. The neutrinos from the charged Higgs decays are expected to be well isolated as well, due to the large Higgs mass. There is little correlation between the neutrinos and therefore the resultant $\not\!\!E_T$ vector is still expected to be large and isolated in general; therefore we apply a $\not\!\!E_T$ isolation cut, which helps reject events due to mismeasures of the total energy. As the missing energy increases however, the chances that it occurs from the mismeasure of jets in the event decreases and we can relax the isolation requirement, which improves the signal acceptance without introducing much background.

The tau leptons from the decay of the heavy bosons ($W^\pm$ or $H^\pm$) are expected to have high transverse momentum and should be isolated, i.e. well separated from the other decay products of the two top quarks in a $t\bar{t}$ event. However, as discussed in Section 3.1 above, only about two-thirds of tau leptons decay to hadronic final states and the detection efficiencies for these taus in top events is only of the order 40–50% (see Section 5.2.3). We therefore only require one identified tau object in our initial search topology. Requiring only one of the top quarks to yield an identified tau means we retain acceptance for all the other decay channels of the other top decay in the event.

The first step in this process therefore it to uniquely identify the "objects" in an event, especially the hadronically decaying tau leptons. The identification cuts used are discussed in Chapter 5. As discussed above, hadronic tau decays consist mainly

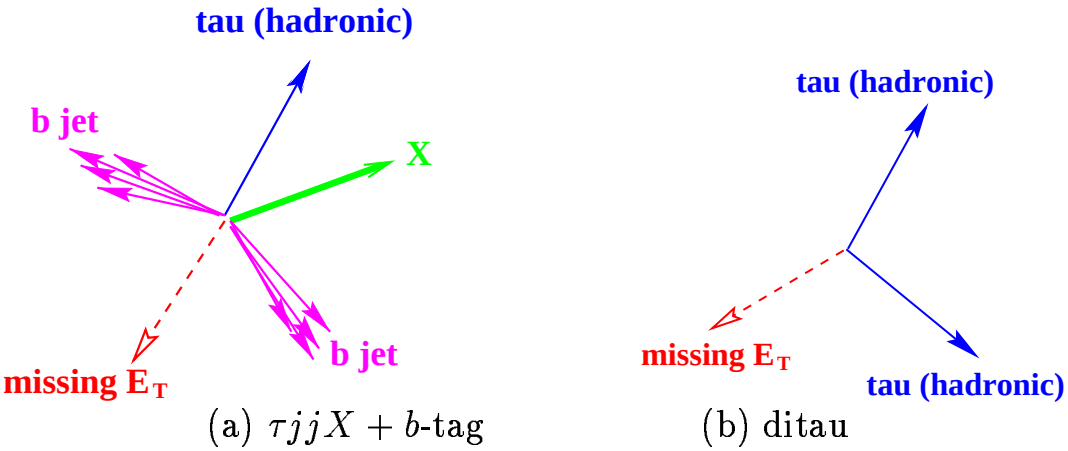

Figure 3.3: Schematic diagram depicting the two search topologies in the transverse (r–ϕ) view.

of decays to final states consisting of either one or three charged decay products. Hadronic tau decays are therefore characterized by a narrow shower or jet of particles with very few charged tracks (low track multiplicity). These characteristics are used in extracting a tau signal from the extensive background of jets created by the QCD interactions of the partons in the proton-antiproton collisions with their subsequent fragmentation and hadronization. It will be shown later in Chapter 7 that the major background to this analysis is the misidentification of a QCD jet as a hadronic tau decay — referred to as a *tau fake*.

The primary search topology, shown schematically in the transverse view in Figure 3.3a, requires a hadronically decaying tau lepton of $E_T > 20$ GeV, two jets of $E_T > 10$ GeV each and some other object in the event, also with $E_T > 10$ GeV. The tau is presumed to come from one of the top quarks decaying via a charged Higgs, and the two jets from the b jets from the top decays. The other top quark would decay via either another charged Higgs or a W, resulting in either another tau (decaying leptonically or hadronically) from the charged Higgs decay or in a lepton ($\ell\nu$) or two jets ($q\overline{q}'$) from the W decay. To gain acceptance for all these channels, we require one other object in the event (labelled X in the figure) which can be either another lepton (electron, muon, or tau) or an additional jet.

To suppress the background even further and enhance the signal, we use the fact that CDF has managed to identify b quark decays by reconstructing the location

of the b quark's decay vertex (called a *displaced* or *secondary vertex*) in the silicon vertex detector. This technique is called b-tagging.

The charged particle trajectories reconstructed in the CTC are extrapolated into the SVX detector to identify the track's hits in the silicon strips. The SECVTX algorithm (discussed in detail in Section 5.8), which was originally developed by the Top Group and used in the top quark discovery and measurement, then reconstructs the secondary decay vertices from these tracks. The algorithm works by iteratively trying to fit the tracks to displaced vertices taking into account the track impact parameters relative to the primary vertex and uncertainties in these measurements.

For the charged Higgs search, we require at least one of the jets in the event to be b-tagged by this algorithm. We call this search channel the $\tau jjX + b$-tag channel. We allow any of the jets in an event to be tagged; this jet does not necessarily have to be one of the jets making up the topology requirement. However, we do not accept any tags for objects identified as leptons. In the top quark analyses using the SECVTX b-tagging, the efficiency to tag at least one of the b-jets in a top event with an identified W boson and three or more jets was about $42 \pm 5\%$ [55]. We expect roughly similar efficiencies in our analysis, due to the similar topologies.

We use Monte Carlo event generators (discussed in Chapter 6) to estimate the signal efficiencies (or *acceptance*). Figure 3.4 shows the transverse energies for the identified objects in a sample of generated $t\bar{t} \rightarrow H^+bH^-\bar{b} \rightarrow \tau^+\nu_\tau b\tau^-\overline{\nu}_\tau\bar{b}$ events with $M_t = 175$ GeV/c^2 and $M_{H^\pm} = 100$ and 160 GeV/c^2, compared to the equivalent objects from the CDF data sample that are used in the analysis (the data selection is discussed in detail in Chapter 4). The data consist mainly of background due to tau fakes.

As the charged Higgs mass approaches the top quark mass, the available energy for the b quark in the $t \rightarrow H^+b$ decay decreases. This can be seen in Figure 3.4, for the $t\bar{t}$ Monte Carlo sample with $M_{H^\pm} = 160$ GeV/c^2 where the jets, especially the b-jets, are "softer" than for the lower $M_{H^\pm}$ case. The b-tagging efficiency drops with decreasing energy (see Section 5.8) and the likelihood of a jet falling below the transverse energy requirement increases. Concurrently, the tau decay products

become "stiffer" due to the larger $M_{H^\pm}$. Therefore, to increase acceptance for these more massive charged Higgs events, we add an additional independent and non-overlapping search topology.

This additional channel accepts energetic *ditau* events with two hadronic tau objects with $E_T > 30$ GeV, which are not back-to-back in the transverse (azimuthal) direction. The not back-to-back requirement mainly rejects dijet events (and some $Z^0 \to \tau^+\tau^-$ events). Requiring $E_T > 30$ GeV for both taus reduces the QCD background dramatically, while retaining reasonable efficiency for the signal, as can be seen in Figure 3.5 which shows the two highest E_T taus in the $M_{H^\pm} = 160$ GeV/c^2 sample. The $\not\!\!E_T$ requirements are also applied as we still expect substantial momentum losses from the neutrinos. This topology is demonstrated schematically in Figure 3.3b. These events are rejected if they are in the standard τjjX channel to avoid double counting.

3.3 Expected Backgrounds

In the spirit of "Today's discovery becomes tomorrow's calibration becomes the following day's background.", we use decays of the W and Z bosons to calibrate our search data, to tune up our tau identification criteria and to check our background calculations. We also assume some of the information from the top discovery, in particular the mass measurements, and assume we can estimate the SM contributions to our signal from the measured SM cross sections. Although the acceptance is small due to the strict kinematic and topological cuts, SM top decays can contribute to the two search topologies as long as at least one of the W bosons decays via a tau lepton. These contributions therefore form an irreducible background to our search which we subsume as signal and do not subtract out. All signal estimates take into account all the possible configurations of the top decays via either $W^\pm$ or $H^\pm$ bosons.

There are a number of potentially large backgrounds to this search, i.e. processes that mimic the search signal. The dominant background is from prompt hadronic jet (QCD) events where one or more of the regular QCD jets fluctuates to form a

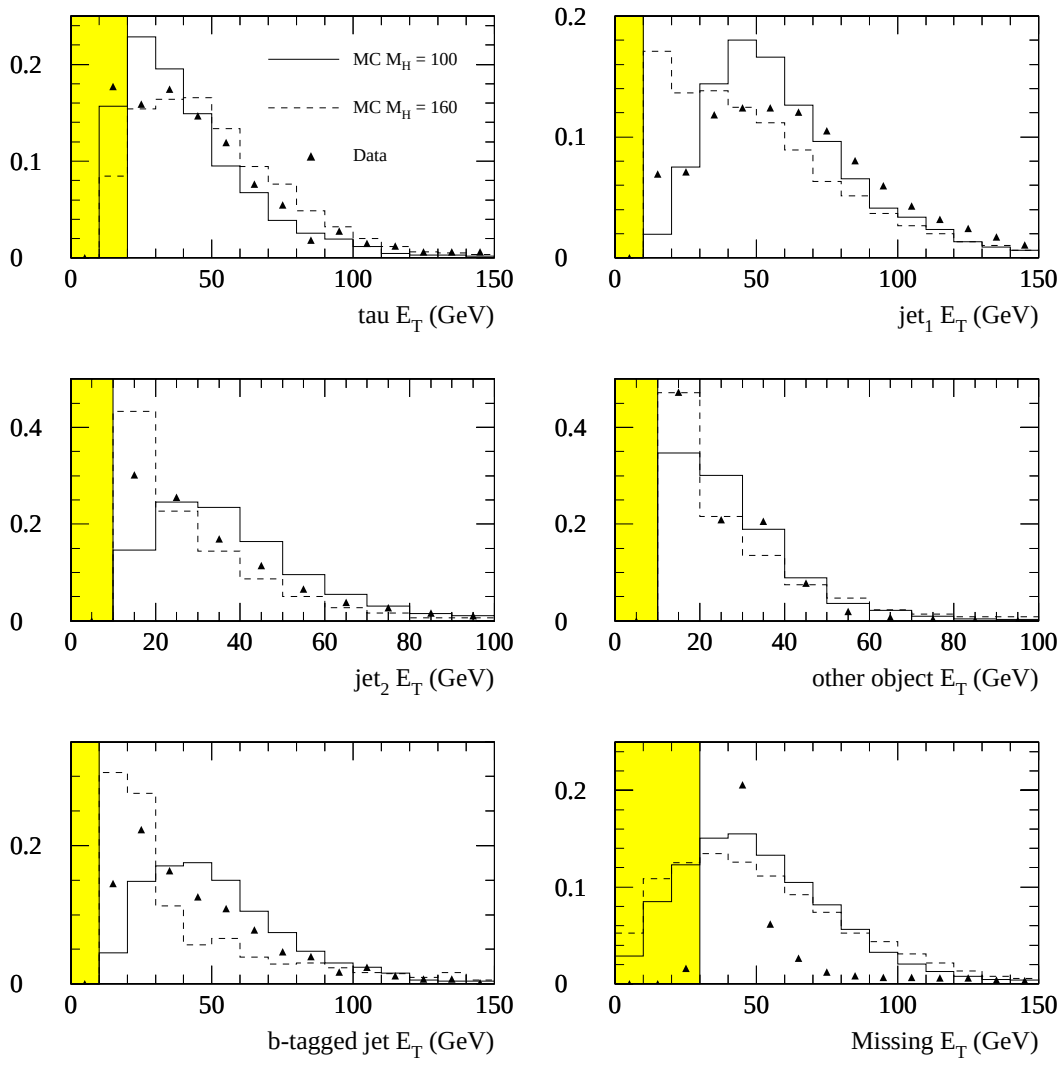

Figure 3.4: Plots of the transverse energies for the leading tau, the two leading jets and the next highest E_T object in an event. The E_T of the jets that are b-tagged in each sample is shown, as well as the missing E_T. Two $t\bar{t} \rightarrow H^+ b\, H^- \bar{b}$ Monte Carlo data samples with $M_{H^\pm} = 100$ and 160 GeV/c^2 and data from the $\not\!\!E_T$ data set are shown. Each histogram has been normalized to unit area so only the relative shapes should be compared. The shaded regions indicate the regions excluded by the kinematic cuts.

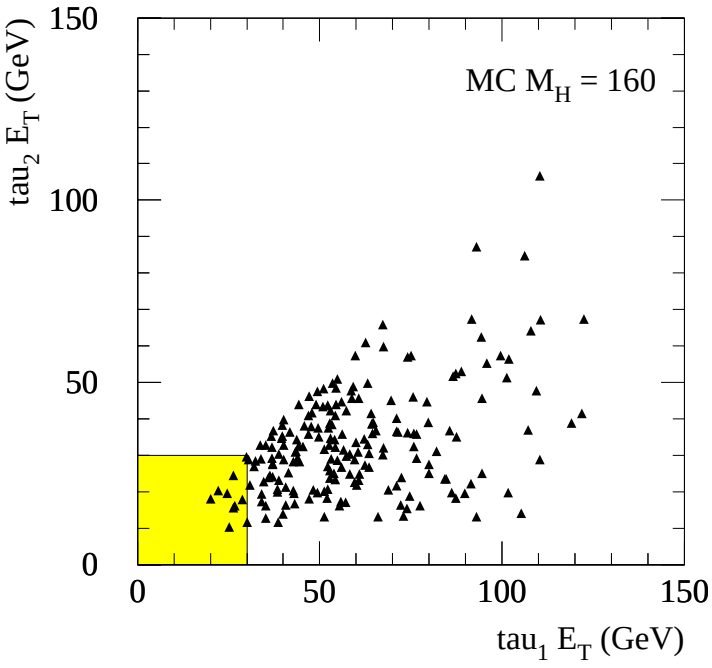

Figure 3.5: The transverse energies of the two leading taus in events from a $t\bar{t} \rightarrow H^{+}b\,H^{-}\bar{b}$ MC data sample with $M_{H^{\pm}} = 160$ GeV/c^2. The shaded region is excluded by the kinematic cuts.

low track-multiplicity narrow cone which gets identified as a hadronic tau decay and where some of the transverse energy in the event is missed or mismeasured due to detector effects or particles going through uninstrumented regions of the detector. The other major source of backgrounds is from processes that produce real energetic and isolated tau leptons. The most significant of these are from the production and decays of the heavy vector bosons ($W^{\pm}$ and Z^{0}) in association with other jets where the bosons decay to hadronically decaying tau leptons. Figure 3.6 shows some example Feynman diagrams for these processes.

The processes $W \rightarrow \tau\nu$ + jets and $Z \rightarrow \tau\tau$ + jets — both next-to-leading order processes — can enter the sample if the neutrinos in the decay are energetic or some of the energy in the event is missed. For the τjjX sample one of the jets would also need to be b-tagged which could either be a fake tag or could be from a real b-quark decay produced from a radiative gluon splitting into b-quark pairs. The back-to-back rejection for tau pairs in the ditau sample should reduce the contribution of $Z \rightarrow \tau\tau$

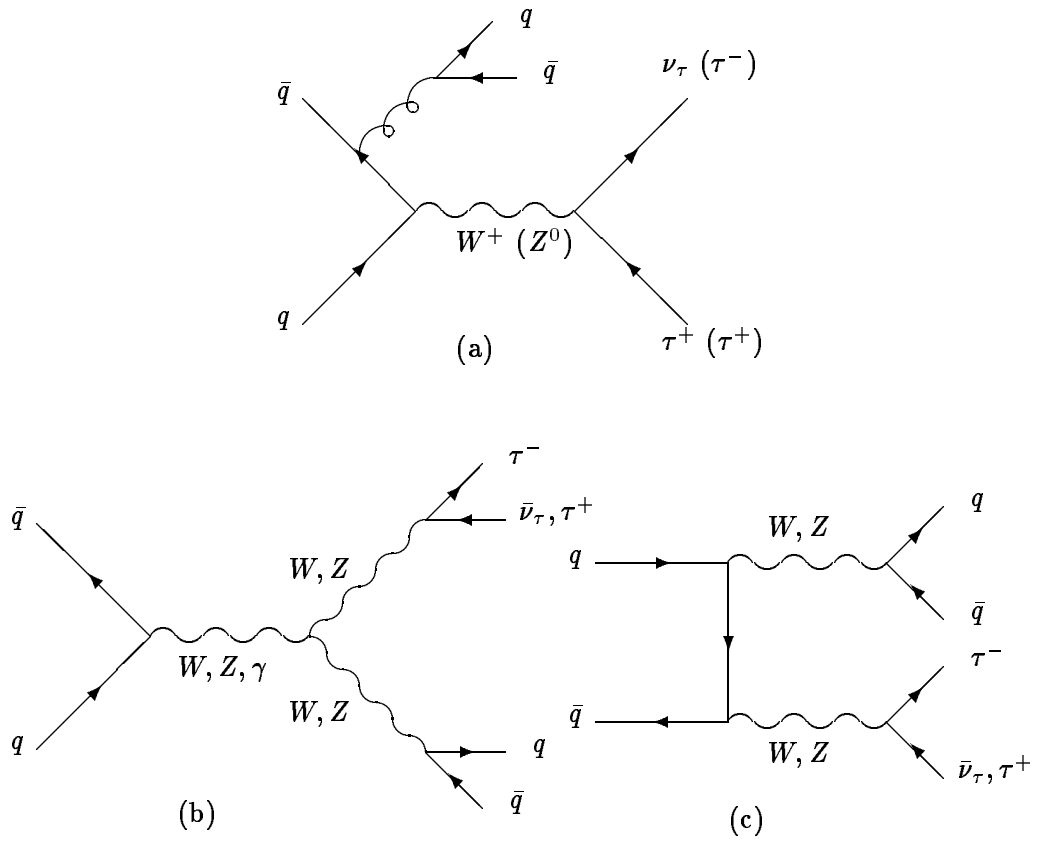

Figure 3.6: Examples of Feynman diagrams for background processes to the charged Higgs search yielding real tau leptons. The first diagram (a) indicates the process of heavy vector boson production and decays to taus with the additional production of jets from radiative processes. Processes (b) and (c) indicate diboson production. There can be radiative contributions to these processes as well.

to the background.

Diboson production (WW, WZ, ZZ) can contribute as well, despite their small cross sections ($\lesssim$ 10 pb) as these processes can be sources of real taus, of $\not\!\!E_T$ and of isolated, energetic jets from the boson decays.

To account for sources of backgrounds from these heavy vector boson processes, we estimate the number expected in our data sample using Monte Carlo calculations and a full simulation of the detector, discussed in Section 7.1. This is similar to the method used to determine the acceptance for the signal, discussed in Chapter 6.

As mentioned above, the dominant background comes from QCD processes with

jets faking taus. Although only a small percentage ($\lesssim 1\%$ — see Appendix E) of energetic, prompt hadronic jets (i.e., jets whose parent particle is a quark or gluon from the $p\overline{p}$ interaction) hadronize in a way that resembles a hadronic tau decay, the much higher cross section for purely QCD processes compared to the production cross section for top quark pairs means the fakes provide a substantial contribution to the background. It is difficult to model these non-perturbative QCD processes well and current Monte Carlo simulations model these processes phenomenologically, with varying degrees of success. Instead of relying on these models, we estimate the backgrounds from these QCD processes directly from our data set. The estimates of the tau fake rates are discussed in Appendix E and the estimates of the backgrounds is performed in Chapter 7.

3.4 Extraction of Limits

Once we have a good understanding of the efficiency for our selection criteria to accept charged Higgs events and of the backgrounds, we can determine whether we see an event count that is inconsistent with the background, or, in lieu of an excess in signal events, set limits on the production of charged Higgs bosons. We set limits assuming the type II Two Higgs Doublet Model couplings (described in Section 1.2.2) and the extraction of limits and results are discussed in Chapter 8.

Chapter 4

Preliminary Event Selection and Data Validation

In this chapter, I present the method used for the initial event selection from the CDF Run 1 data set and will describe the reprocessing and validation steps that were made on these data. These data sets formed the basis for the analyses done by the Tau Working Group at CDF from 1993 to the present.

4.1 Tevatron Run 1

CDF recorded data from the Tevatron running in $p\overline{p}$ colliding beam mode from late 1992 to early 1996. The run was split into two main parts, known as Run 1A (1992–93) and Run 1B (1994–95), coinciding with the Tevatron collider runs Run 1A and 1B nomenclature.[1] A much shorter run (Run 1C) also took place at the end of 1995 to early 1996 but these data are not used in this analysis. For all of Runs 1A and 1B, the Tevatron operated at a center-of-mass energy of 1.8 TeV. During Run 1A about 21 pb^{-1} of data were written to tape with about 30 pb^{-1} delivered by the Tevatron, resulting in a data-logging efficiency of about 70%. During Run 1B about 97 pb^{-1} were written to tape with about 126 pb^{-1} delivered, resulting in a data-logging efficiency of about 77%. Figure 4.1 shows the cumulative integrated luminosity delivered by the Tevatron to CDF and the amount logged to tape. The systematic uncertainties on the luminosity measurements (as discussed later in Section 4.8) are about 3.6% in Run 1A and 8% in Run 1B.

About 16 million events were written to tape in Run 1A and about 64 million in Run 1B. Of these, about 2 million went into the Run 1A Exotics XOX1_3P data

[1] The previous Tevatron collider run at CDF from 1988-89 was relabelled "Run 0".

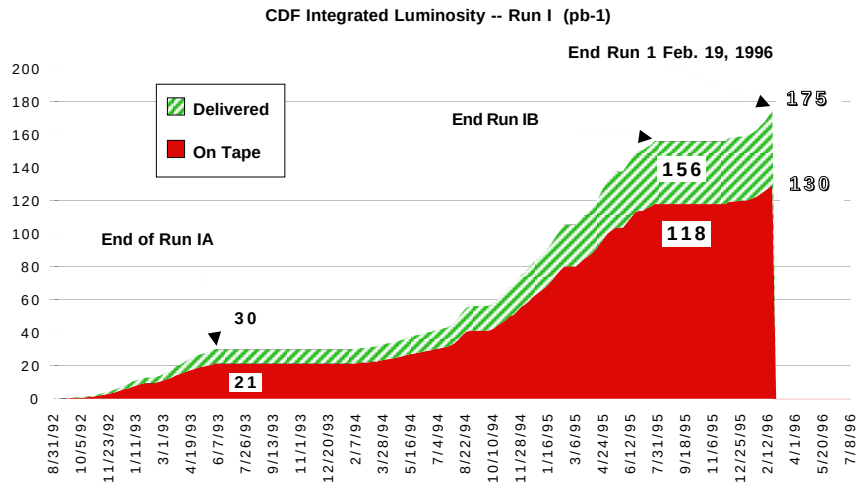

Figure 4.1: Plot of integrated luminosity (in pb^{-1}) delivered to CDF and on tape for the Tevatron Collider Run 1, 1992–96

stream and about 2.5 million into the Run 1B XOXB_5P data stream, the primary data sets used for the charged Higgs search (see Section 4.4).

The main differences in running conditions between Runs 1A and 1B were the upgrade of the SVX (see Section 2.5.1), improvements and some changes in the software and triggers used for selecting events online, and the higher luminosity delivered by the upgraded accelerator complex. All the data from Run 1A and 1B have been reprocessed to form the current data sets, using the same version of the reconstruction algorithms, as will be described below, with all the accumulated software improvements and resolution of known detector and calibration problems.

4.2 Selection of the Initial $\not\!\!E_T$ Data Set

The online trigger system was described in Section 2.9. As described in that section, the various trigger levels make more and more sophisticated decisions about whether to accept or reject an event. The data from the online, after being reprocessed (described in Section 4.5), are split into separate *streams* of common triggers.

For both Runs 1A and 1B there were specific triggers looking for hadronic tau decays (known as *tau triggers*) but these are not used for the final charged Higgs analysis. The tau triggers for Run 1A have been used for a tau charge asymmetry

measurement by Edward Kuns, another Rutgers University doctoral student, and these tau triggers are discussed extensively in his thesis [156]. To date, the Run 1B tau triggers have not been used for a physics analysis. These triggers were based on a hardware analog neural network that was part of the Level 2 trigger [157] and most of Run 1B was spent tuning this network which never achieved the desired efficiency due to hardware problems, instabilities in the analog neural net weighting functions and inherent biases in the Level 2 data processing. The hope was to use these triggers for the charged Higgs analysis but their efficiencies for the relatively "busy" top-like events were never considered adequate.

As discussed in Chapter 3, if top quarks decay via a charged Higgs boson with the charged Higgs decaying subsequently to a tau lepton and a tau neutrino, we expect a substantial fraction of the energy of the event will be in the form of neutrinos, both from the Higgs decay and from the tau decay. Hence the $\not\!\!E_T$ (missing E_T) data stream (XOX) which consists of the $\not\!\!E_T$ triggers used by many analyses in the "Exotics[2]" group seems a likely place to start a search for this signature, given that there were no reliable tau triggers for Run 1B.

The $\not\!\!E_T$ triggers that make up the Exotics XOX data streams are described in detail below. A significant amount of calorimeter energy is required at Level 1, ensuring that a hard $p\overline{p}$ interaction occurred. A sum of the calorimeter energies is performed at Level 2 and $\not\!\!E_T > 35$ GeV is required. Level 3 recalculates the $\not\!\!E_T$ after removing identified sources of spurious energy deposits. The Level 3 trigger requires $\not\!\!E_T > 30$ GeV and a jet in the event with $E_T > 5$ GeV. A cosmic ray filter also rejects events consistent with originating from cosmic rays.

An event passing all these triggers gets written to the XOX data stream after reprocessing.

---

[2]The *Exotics* group at CDF is the working group for most analyses that involve searches for signatures of processes not described by the Standard Model. The Missing E_T triggers are the starting point for many of these searches as many of these non-SM processes involve, as yet, undiscovered particles that may not leave large (or any) signature in the detectors. Their presence in an event is therefore inferred from large amounts of missing E_T.

```
TRIGGER L1_CALORIMETER_V4
    SELECT/VETO  LEVEL1_CALORIMETRY_PRESCALE
        PARAMETER   L1_PRESCALE           = 1
    SELECT  LEVEL1_CALORIMETRY_SINGLE_TOWER
        PARAMETER   WFEM_TOWER_THRESHOLD  >  51. (GeV)
        PARAMETER   WPEM_TOWER_THRESHOLD  >  11. (GeV)
        PARAMETER   CEM_TOWER_THRESHOLD   >   8. (GeV)
        PARAMETER   EPEM_TOWER_THRESHOLD  >  11. (GeV)
        PARAMETER   EFEM_TOWER_THRESHOLD  >  51. (GeV)
        PARAMETER   WFHAD_TOWER_THRESHOLD >  51. (GeV)
        PARAMETER   WPHAD_TOWER_THRESHOLD >  51. (GeV)
        PARAMETER   CHAD_TOWER_THRESHOLD  >  12. (GeV)
        PARAMETER   EPHAD_TOWER_THRESHOLD >  51. (GeV)
        PARAMETER   EFHAD_TOWER_THRESHOLD >  51. (GeV)
```

Figure 4.2: Level 1 Calorimeter Trigger for Run 1B. For Run 1A the corresponding trigger thresholds for most of the run were 6 GeV for the CEM and 8 GeV for all other EM components and 8 GeV for the CHA and 12 GeV for all other hadronic components.

4.2.1 Level 1

There were no explicit requirements at the Level 1 trigger system for $\not\!\!E_T$ as this is a global quantity and could only be calculated at Level 2. However most of the $\not\!\!E_T$ triggers did require the standard Level 1 "calorimeter" trigger to be true. This trigger is true whenever any calorimeter trigger tower read above a certain threshold.

Figure 4.2 shows the Level 1 calorimeter trigger from the trigger table used in Run 1B, which sets the individual thresholds for each calorimeter component. As we are relying on $\not\!\!E_T$, the central calorimeter plays the major role for our analysis, so we are most reliant on the trigger thresholds of 8 GeV for the electromagnetic calorimetry (CEM) and 12 GeV for the hadronic calorimetry (CHA). For Run 1A, the corresponding trigger thresholds for most of the run were 6 GeV for the CEM and 8 GeV for all the other EM components and 8 GeV for the CHA and 12 GeV for all the other hadronic components. All the trigger results are OR'ed together for the Level 1 trigger decision; therefore if any calorimeter is over threshold, the event is accepted at this trigger level.

The trigger thresholds for the plug and forward calorimeters were tuned during the beginning of Run 1A but the majority of data was taken with the thresholds shown for the central calorimeters. The earlier thresholds were lower, making them more efficient, but the data rate was too high so the thresholds were raised. At the beginning of Run 1A, beam-beam coincidence (BBC) was also required (see Section 2.8), indicating that a $p\overline{p}$ interaction had occurred during a bunch crossing. Since the average number of interactions per crossing rose to greater than one with the increase in the average luminosity during the run, this requirement was later removed.

As the charged Higgs signal depends on extremely massive objects and large momenta, the Level 1 trigger efficiency is essentially 100% for this analysis.

4.2.2 Level 2

As we are looking for events where we expect high $\not\!\!E_T$, the general $\not\!\!E_T$ triggers used by the Exotics group at CDF were used for the charged Higgs analysis [158].

The $\not\!\!E_T$ trigger used in the trigger table for Run 1A (titled the MET_35_TEX_2_NOT_FWD trigger) is shown in Figure 4.3. There were actually two similar triggers in Run 1A (the other being the MET_35_NOT_GAS trigger) which operated in a similar fashion and had a fair amount of overlap. The small loss in efficiency from Run 1A by ignoring the second trigger is negligible due to this overlap and the other requirements placed on events in the final analysis. This simplifies the study of the trigger threshold systematic uncertainties (discussed in Appendix D). In Run 1B, these two separate triggers were consolidated as the MET_35_TEX_2_NOT_GAS trigger, which is shown in Figure 4.4.

The Level 2 triggers used in Run 1A and Run 1B were very similar. They both required $\not\!\!E_T > 35$ GeV (which is calculated as $\not\!\!E_T{}^2 > 1225$ GeV^2 to save time in the Level 2 software) and at least one Level 2 calorimeter cluster. They also required the leading calorimeter cluster to have ≥ 2 GeV of electromagnetic E_T which is used to avoid events where a scattering neutron appears to create a large energy deposit in the gas calorimeters, known as a "Texas Tower". The Run 1A trigger also did

```
TRIGGER MET_35_TEX_2_NOT_FWD
    SELECT  MISSING_ET
        CUT         MISSING_ET_SQUARED >= 1225. (GeV**2)
    SELECT  CALOR_CLUSTER
        CUT         NUMBER_OF_CALOR_CLUSTERS >= 1
    SELECT  TEXAS_FILTER                  ! Cut out "Texas Towers"
        CUT         HIGH_ET_JET_MIN_EM_ET >= 2.0 (GeV)
    SELECT  SINGLE_CLUSTER_CUT            ! Lead. cluster not fwd
        PARAMETER   CLUSTER_TYPE = 1      ! highest Et
        PARAMETER   CLUSTER_QUANTITY = 17 ! Yseed
        PARAMETER   COMPARE_TYPE = 5      ! >
        CUT         THRESHOLD = 9         ! (0-9 are fwd West)
    SELECT  SINGLE_CLUSTER_CUT
        PARAMETER   CLUSTER_TYPE = 1      ! highest Et
        PARAMETER   CLUSTER_QUANTITY = 17 ! Yseed
        PARAMETER   COMPARE_TYPE = 6      ! <
        CUT         THRESHOLD = 32        ! (32-41 are fwd East)
```

Figure 4.3: Level 2 $\not\!\!E_T$ Triggers for Run 1A.

```
TRIGGER MET_35_TEX_2_NOT_GAS
    SELECT  MISSING_ET
        CUT         MISSING_ET_SQUARED >= 1225. (GeV**2)
    SELECT  CALOR_CLUSTER
        CUT         NUMBER_OF_CALOR_CLUSTERS >= 1
    SELECT  TEXAS_FILTER                  ! Cut out "Texas Towers"
        CUT         HIGH_ET_JET_MIN_EM_ET >= 2.0 (GeV)
    SELECT  SINGLE_CLUSTER_CUT            ! Lead. cluster not gas
        PARAMETER   CLUSTER_TYPE = 1      ! highest Et
        PARAMETER   CLUSTER_QUANTITY = 17 ! Yseed
        PARAMETER   COMPARE_TYPE = 5      ! >
        CUT         THRESHOLD = 15        ! (0-15: plug and fwd W.)
    SELECT  SINGLE_CLUSTER_CUT
        PARAMETER   CLUSTER_TYPE = 1      ! highest Et
        PARAMETER   CLUSTER_QUANTITY = 17 ! Yseed
        PARAMETER   COMPARE_TYPE = 6      ! <
        CUT         THRESHOLD = 26        ! (26-41: plug and fwd E.)
```

Figure 4.4: Level 2 $\not\!\!E_T$ Trigger for Run 1B.

not allow the lead cluster to be in the forward calorimeters (calculated from the seed tower η of the leading cluster from the Cluster Finder – see Section 2.9.4) and this was tightened in the Run 1B trigger where the lead cluster could not be in the forward or plug regions and therefore had to be in the central calorimeter.

The cross sections for these triggers were about 300 to 120 nb and scaled inversely somewhat with the instantaneous luminosity.

4.2.3 Level 3

The main Level 3 trigger used for the charged Higgs data selection was the EXOB_MET_30_COSFLT trigger, shown in Figure 4.5.[3] The cross section for this trigger was about 20–50 nb.

The operation of the Level 3 online trigger system is described in detail in Appendix C.3. All the digitized detector information is available and a pared down version of the offline event reconstruction algorithm is run on the event. A "cleanup" module is run after calorimeter clusters are identified, which removes spurious calorimeter responses from single photo-tube spikes, Texas towers, main ring splashes, etcetera. A jet clustering module then identifies jet clusters and a tracking module creates the tracking banks. Note that, due to the time and cpu constraints, SVX information is not used in constructing tracks or making trigger decisions at Level 3.

A module METSER [159] (not shown) calculates the missing transverse energy ($\not\!\!E_T$) quantities. At Level 3 all these quantities are calculated assuming the event vertex is at $z = 0$. This avoids any biases at the trigger level that might be introduced if there were any problems in the calibrations or in the vertex finding algorithms. A module METFLT is run (as shown in Figure 4.5) which filters events based on the Level 3 $\not\!\!E_T$ calculation. The trigger logic for this path first requires an event to have $\not\!\!E_T > 30$ GeV; if so, then the leading calorimeter cluster is required to have at least an E_T of 5 GeV. The TRCONTROL lines in the trigger table entry shown in

[3]This trigger was called the EXO1_MET_30_COSFLT trigger in Run 1A but was identical.

```
TRIGGER EX0B_MET_30_COSFLT
    SELECT METFLT
        PARAMETER SETNAME MET30
    EXECUTE TRCONTROL
        PARAMETER TALK_TO SETNAME REGTRK1
            MODE FILTER
            CURVATURE 0.00225       ! Pt> 1 GeV  .
            NEW CTC OFF
            NEW VTC OFF
            NEW SVX OFF
            ENABLE VTC OFF
            ENABLE VTP OFF
            ENABLE SVX OFF
            ENABLE CDT OFF
            SHOW
            RETURN
        END_TALK
    SELECT COSFLT
        PARAMETER TALK_TO SETNAME METCOS
            MIN_EM_FRAC 0.05
            MAX_EM_FRAC 0.95
            REGIONAL_TRACKING ON
            CALC_QFRAC
            EXIT
        END_TALK
```

Figure 4.5: Level 3 $\not\!\!E_T$ Trigger for Runs 1A and 1B.

Figure 4.5 describe the tracks (of $p_T > 1$ GeV/c) that the trigger module needs for its calculations.

Cosmic rays passing through the detector could give large energy deposits that are unbalanced and could therefore be a significant source of events with large $\not\!\!E_T$. However, in general, these energy deposits will occur out-of-time with a $p\overline{p}$ bunch collision. Any tracks left by these cosmic rays will also not point to the event vertex. Similar properties hold for beam interacting with gas in the beampipe. Therefore, a final cosmic-ray filter (COSFLT) is executed in the $\not\!\!E_T$ trigger path, which rejects such events. This filter is designed to be efficient for all real $p\overline{p}$ events, so it is not perfect at rejecting cosmic-ray events. The filter only rejects cosmic rays identified

in the central detectors.

COSFLT first tries to reject cosmic rays that do not coincide with a bunch crossing by examining the out-of-time energy in the central hadronic calorimeters (CHA/WHA). There are time-to-digital converters (TDC) attached to the hadronic calorimeter components which give timing information for the energy deposits read out by the analog-to-digital converters (ADC). If these energy deposits are out-of-time with the Tevatron bunch crossings this is a good indication that the deposit could be from a cosmic ray or from interactions of the beam with gas in the beam pipe. TDC hits in towers with more than 1 GeV of hadronic energy[4] are checked for whether they are in-time with a bunch crossing using a timing window of -20 ns $< t <$ 30 ns for the central wedges and -25 ns $< t <$ 55 ns for the endwall calorimeters. If there is a total of 6 GeV of out-of-time energy anywhere in the CHA or WHA the event is rejected.

The other method COSFLT uses to identify cosmic rays that could be in-time is to apply two criteria to the leading calorimeter cluster in the event. The first is a charge fraction (p_T/E) cut. The charge fraction is the ratio of the sum of the p_T's for all tracks passing certain quality selection criteria in the Central Tracking Chamber (e.g. sufficient hits in each superlayer) which point at a tower in the cluster, to the energy of the cluster. Tracking is done for a cone size of $\Delta R = 0.7$ around the leading cluster with a minimum track p_T of 400 MeV. The command REGIONAL_TRACKING ON ensures that the tracking module is executed. In general, cosmic rays will not have high-p_T tracks pointing at them, so a minimum charge fraction of 0.1 will reject them.

Cosmic rays do not usually leave the right amount of energy in the CES strip chambers either (see Section 2.6.1). Therefore the CES/CEM energy ratio for the central electromagnetic calorimeter tower for the leading cluster is also checked. Before applying this cut, a minimum fraction of electromagnetic energy to the total energy of 0.05 is required. Also, only towers where either the tower energy or the

[4]The calorimeter timing degrades significantly for hits in towers with lower energy.

strip energy are above a threshold of 1 GeV are included in the ratio. If the ratio is extremely small or large (< 0.2 or > 30) and if the cluster failed the charge fraction cut, the event is rejected.

Since timing and strip information are only available for the central calorimeters, the COSFLT cuts only apply to cosmic rays in the central region. Non-central leading clusters will automatically be accepted.

A vertex cut was available at the trigger level for cosmic rays which could be useful as cosmic rays by themselves do not produce good vertices. Unfortunately, occasionally no good vertex is found for a real event, especially if it has low track multiplicity, so this cut will reject non-cosmic-ray events and is not used in the trigger. This is also an argument against using a track requirement in the cosmic-ray filter.

There was another Level 3 trigger that was available in the $\not\!\!E_T$ data stream, the EXOB_MET_30_TRK_3 trigger, which required at least one track in the event with $p_T > 3$ GeV/c, in addition to $\not\!\!E_T > 30$ GeV. However, after removing all the events with large out-of-time energy deposits and requiring the Level 2 $\not\!\!E_T$ trigger, this trigger had almost complete overlap with the EXOB_MET_30_COSFLT trigger which had a higher efficiency. To avoid having to study further trigger overlaps and systematic effects and due to the negligible gain in statistics, the TRK_3 trigger is ignored in the final analysis selection.

4.3 Other Data Sets

Other standard CDF data sets, notably the *inclusive lepton samples* [160, 161] and the *inclusive jet trigger* data sets are also used in this analysis for the tuning of selection cuts, for estimates of background processes, for studies of trigger efficiencies and for checks of tau fake rates. The inclusive lepton samples, which consist essentially of all events that have a high-p_T electron or muon, have been discussed in great detail elsewhere [162, 161]. The inclusive electrons had a cross section of about 5.5 nb resulting in a sample of $\sim$ 500,000 events and the inclusive muons had

a cross section of about 5.8 nb with $\sim$ 650,000 events in the final sample.

The inclusive jet trigger samples consist of four data sets: Jet 20, Jet 50, Jet 70 and Jet 100. Only the first three are used in this analysis. The Jet 20 sample has events that have at least one jet with $E_T \geq 20$ GeV. To avoid too many events caused by discharges in the calorimeter photo-tubes (known as "photo-tube spikes"), a minimum requirement of 0.5 GeV of electromagnetic energy for the highest E_T jet in the event is also required. The Level 2 trigger for these events was *prescaled* by a factor of 25 (i.e. the event is accepted only 1 in 25 times that the trigger condition is met for an event) and the Level 1 single calorimeter tower trigger (which required at least 8 GeV of energy in a central electromagnetic or hadronic cluster or 51 GeV in a plug or forward cluster – as discussed in Section 4.2.1 above) was also a prerequisite for the Level 2 trigger. The Level 1 trigger was prescaled by a factor of 40. The combined prescales on the Level 1 and Level 2 triggers brought the effective rate for the Jet 20 data down by a factor of 1000 which translated into a cross section of approximately 6 nb. There are about 530,000 events in the final sample.

The Jet 50 sample consists of events that come from a Level 2 trigger that also had a prerequisite on the prescaled Level 1 single tower trigger. At least one jet with $E_T \geq 50$ GeV is required. There were no further prescales on this trigger. The cross section for this trigger was about 4 nb which resulted in an event sample of approximately 340,000 events.

The Jet 70 sample consists of events that come from a Level 2 trigger with no Level 1 requirement. At least one jet with $E_T \geq 70$ GeV is required. There was a prescale of a factor of 8 applied to this Level 2 trigger and the effective cross section was about 4 nb. There are approximately 380,000 events in this sample.

4.4 Offline Reconstruction and Filtering

After passing through the online data acquisition system, events that pass all the trigger levels are stored on tape. The raw (RAW) data tapes contain about 130 kB of detector information per event. These tapes are then processed through offline

reconstruction and filtering, known as *production.* In the offline reconstruction, final calibration constants and up-to-date data base constants are applied and all event quantities are recalculated; full tracking is done on the event including the information in the SVX. Any known problems with the data are also corrected at this stage.

During the reconstruction, events are filtered into different *streams* of related triggers. The $\not\!\!E_T$ triggers are all fed to the Exotics data stream, labelled XOX1_3P for Run 1A and XOXB_5P for Run 1B. There were a total of approximately 64 million events written to tape in Run 1B, with about 2.5 million in the Exotics stream, 1.2 million in the inclusive leptons and 1.3 million in the inclusive jet data [163]. For Run 1A there were a total of about 16 million events with about 2 million in the XOX1_3P stream.

The production pass produces two output formats for each data stream: Data Storage Tapes (DST) which include all the original raw detector information plus the reconstructed event data, weighing in at about 200 kB per event and a reduced data set, the Physics Analysis Dataset (PAD), which contains only the reconstructed data and compressed information about the detector which allows a partial re-reconstruction of the event, notably a reconstruction of calorimeter based quantities and refitting of SVX tracks using different alignments. Using the PAD data results in some loss of precision and information as very low momentum tracks (with p_T well below 1 GeV/c) and calorimeter towers with low energy (below 1 GeV) are discarded. However, as the charged Higgs analysis is geared towards looking for massive and high momenta objects, this small loss in precision is negligible. The PAD data are the only data set that could be reprocessed within a reasonable time frame with the available computing resources and is the starting point for almost all CDF physics analyses.

The XOXB DST data consist of about 400 GB which is reduced to about 90 GB in the PAD format. The jet data were about 50 GB of PAD data and the inclusive electron and muon data sets were about 20 GB each.

4.5 Data Reprocessing

The entire Run 1 Exotics data stream (XOX1_3P for Run 1A and XOXB_5P for Run 1B) was reprocessed with a combined retracking, reclustering and preselection analysis control[5] job. The reprocessing was necessary to take advantage of improvements and fixes to bugs which removed biases in the track finding algorithms, used better alignment data for the SVX and improvements in the tau finding algorithms. There were also algorithmic biases in the original SVX track reconstruction which caused increasing inefficiencies in track finding due to the radiation damage to the inner layer of the SVX during Run 1B. These improved algorithms were also incorporated [165].

At the same time as the reprocessing was done, an event selection was made, described below in Section 4.7, and summary binary data files ("PLJ"[6] format) were made of the full data stream which were subsequently used for data validation.

The original PADs (in CDF YBOS data format [167]) produced from the offline contain about 35 kB per event, which still require a few days of processing for a complete run through all the data in our preselected data set. The preselected data set was therefore also processed into the summary PLJ data format, which consists of only about 5 kB per event and contains all the quantities needed for the charged Higgs analysis. The PLJ data format allowed the storage of more events on disk before applying analysis cuts which made subsequent analyses much faster. The complete PLJ sample could be processed within a matter of hours. This format was also used for the storage of on the order of one million simulated events (see Chapter 6).

The reprocessing details of the Exotics data streams for Run 1 are summarized in Table 4.1. The reprocessing took place on a cluster of DEC ALPHA 3000/300 nodes running VMS. The final output resulted in two 8mm tapes which contained

[5] *Analysis Control* [164] is the CDF analysis framework that allows various software modules to be linked together and run in any order under user control. Some of these modules are used for event reconstruction while others are used for event filtering, data analysis, plotting histograms, etcetera. Analysis Control jobs are used in the online Level 3 trigger system, for offline reprocessing and by people doing their independent analyses.

[6] *PLJ* stands for Photon-Lepton-Jets — a software package originally written by Prof. John Conway to store summarized event data in a compact form. [166]

the preselected data for Run 1A, with a total of 187,744 events, and six tapes for Run 1B, with a total of 566,480 events. There were also three tapes each for Run 1A (2,066,995 events) and Run 1B (2,519,475 events) of the summary PLJ files for the complete Exotics data streams.

4.6 Data Validation

The PLJ summary files provide data on which to base rejection of runs with clear detector problems which could arise from malfunctioning detector subsystems or problems with the data acquisition systems.

The tau triggers and tau finding algorithm were declared to be operational in Run 1A after run 41036 (taken on October 7, 1992). Although the $\not\!\!E_T$ triggers are not reliant on the tau triggers, very little luminosity is lost (0.7 pb^{-1}) by excluding the early runs.[7] The $\not\!\!E_T$ and tau triggers were operational from the beginning of Run 1B which starts with run 55408 (January 22, 1994).

The first step in the data validation was to remove "bad" runs as defined by the official CDF "good run" list [168]. This list contains the run numbers of those runs that are good for general analyses and those that that are good for analyses relying on the muon detectors. For Run 1B, the good run list also contains information on whether a run has reliable SVX information or not. As the charged Higgs analysis uses both SVX and muon information, we reject any run that does not have good data for all these components. For Run 1A, approximately 10% of all runs do not have reliable muon information and the corresponding percentage for Run 1B is 3%. Approximately 1.4% of all runs in Run 1B do not have reliable SVX information. This results in a removal of about 0.8 + 2.0 pb^{-1} from Run 1A and 3.1 + 2.5 pb^{-1} from Run 1B of integrated luminosity. See Table 4.2 for details of the final integrated luminosity calculation.

[7] This is a historical decision: originally the plan was to use the tau triggers for the charged Higgs analysis and data selection and tuning of selection cuts proceeded for a while under this assumption.

The PLJ summary files allow determination of data quality based on the distributions of eight quantities from each run which are related to tau analyses in general. These are calculated for each event and averaged over a run:

- total transverse energy ($\sum E_T$),
- missing transverse energy ($\not\!\!E_T$),
- azimuthal angle of $\not\!\!E_T$ ($\phi_{\rm MET}$),
- number of jets ($\rm N_{jet}$),
- number of taus ($\rm N_\tau$),
- pseudorapidity of leading tau (η_τ)
- azimuthal angle of leading tau (ϕ_τ), and
- E_T of leading tau ($\rm E_{tau}$).

If the calculated mean of the distribution for any quantity in a run differs from the mean of all runs by more than four standard deviations then the run is declared unusable. The calculation of the number of standard deviations takes into account the error on the estimate of the mean of the distribution for the quantity (σ_i), and the r.m.s. spread in those estimates for all runs ($\overline{\sigma_i}$). The same four standard deviation requirement applies to the width (r.m.s.) of each distribution relative to the r.m.s. spread in widths for all runs.

The eight tau-related quantities and their r.m.s. spreads discussed above are plotted in Figures 4.6 and 4.7 for Run 1B. Note that events with no taus will have zeroes for the leading tau quantities, shifting the means of the plots of $\rm N_\tau$, ϕ_τ and E_T of the leading tau towards zero. These are still suitable validation quantities.

"Bad" runs for each quantity are indicated by a circular data point in that plot. If a run was found to be bad in a previous plot only then it is indicated with a diamond. The distributions show sizeable variation both from run to run and through the course of the run. In particular the three quantities $\sum E_T$, $\not\!\!E_T$ and $\rm N_{jet}$

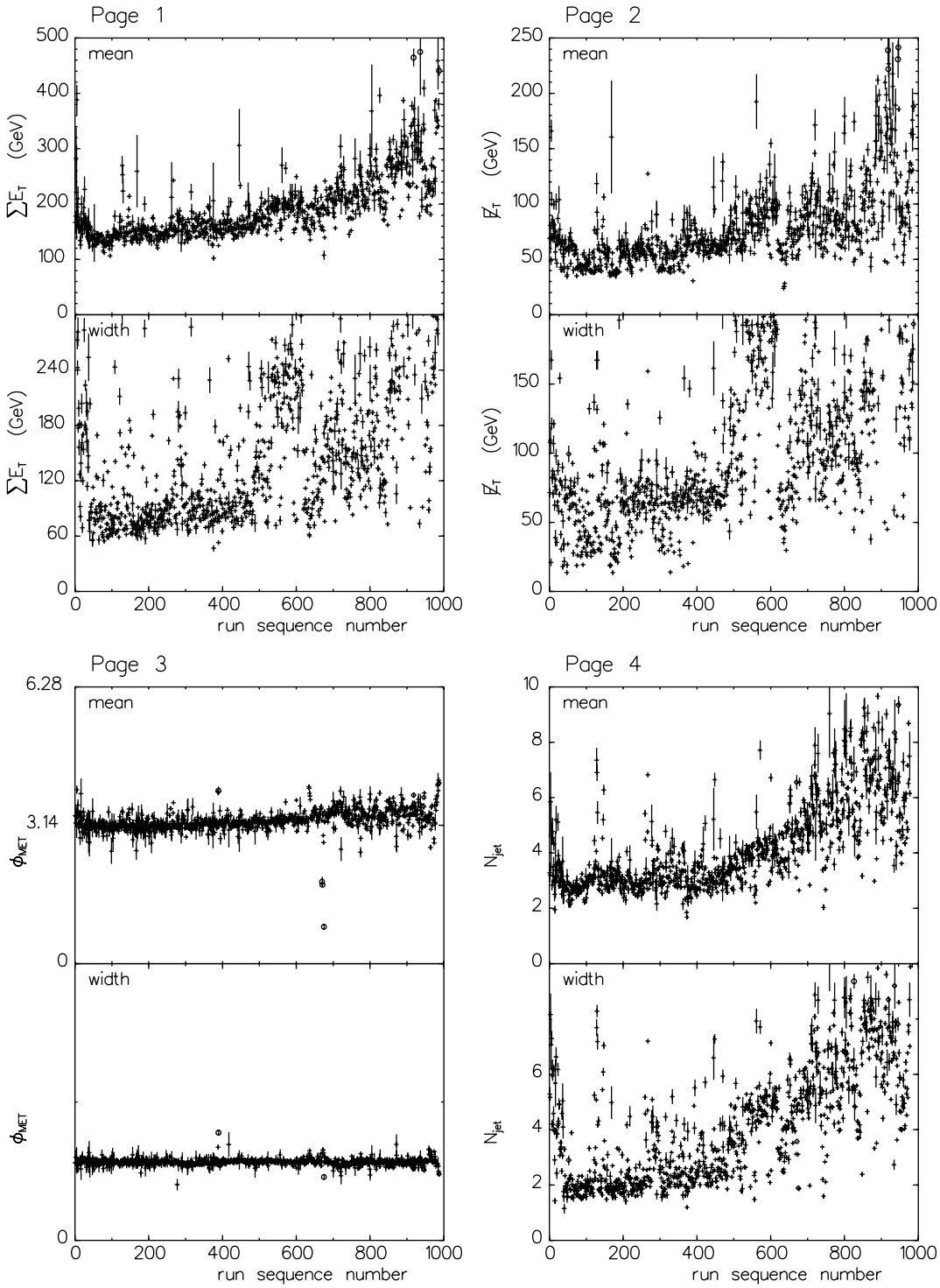

Figure 4.6: Mean and width of $\sum E_T$, $\not\!\!E_T$, $\phi_{\not\!\!E_T}$ and $\mathrm{N_{jet}}$ distributions as a function of run sequence number. Points with circles denote runs excluded on the basis of these quantities in this plot. Points with diamonds denote runs excluded by previous plots.

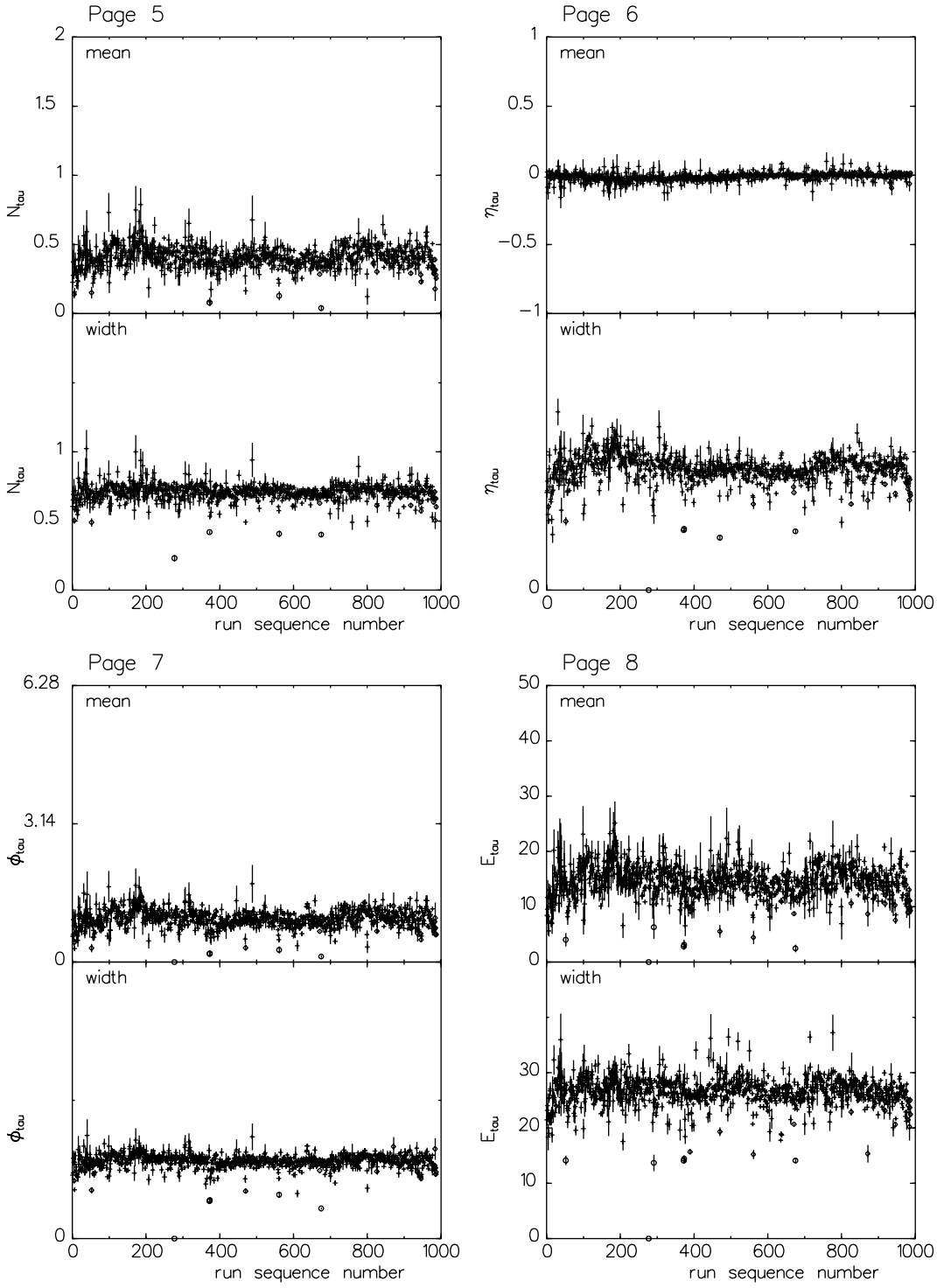

Figure 4.7: Mean and width of N_τ, η_τ, ϕ_τ and E_τ distributions as a function of run sequence number. Points with circles denote runs excluded on the basis of these quantities in this plot. Points with diamonds denote runs excluded by previous plots.

show a steady increase over the run and highly variable widths. This is a result of the increasing multiple interactions due to the increasing luminosity over the course of Run 1B. Runs that were marked bad due to this increase, in these three plots only, were returned to the good run list.

The distributions in these quantities from Run 1A (not shown) look very similar in the spread but without the strong increase over the run as the multiple interaction effect was much less in Run 1A.

A few runs have been removed by hand after the validation step, due to problems found during the data reprocessing stage (the details are discussed in References [169, 170]). There are also some duplicated events due to problems with the "book-keeping" of files that are reprocessed in the offline production and these duplicates are removed from the final data set after the validation.

Overall, 0.6 pb^{-1} of Run 1A data and 0.3 pb^{-1} of Run 1B data was removed by the validation procedure. These numbers are taken into account when calculating the final luminosity for our data sample (see Section 4.8). The details of the reprocessing are shown in the next section on the data selection, in Table 4.1.

4.7 Preliminary Data Selection

During the data reprocessing, to reduce the dataset size for subsequent analysis, a selection of the interesting events for the charged Higgs analysis was made.

Only those events satisfying one of two classes of selection criteria were retained in PAD format for later analysis. These two classes are called the *monojet* and *tau plus missing* E_T ($\tau + \not\!\!E_T$). The monojets were used in an analysis of $W \to \tau\nu$ which was used to tune up the tau identification cuts [171]. As these data were used to tune the tau cuts, the selection criteria for monojets did not use the TAUO banks produced by FINDTAU.[8] Instead, to be selected as a monojet the event must have

[8] A TAUO data bank is the information stored for a jet cluster that passes preliminary selection criteria for a hadronic tau decay — see Chapter 5.

Reprocessing	Run 1A		Run 1B	
Original data tapes	41		60	
PAD data size (GB)	70		90	
Processing time (hrs)	295		506	
Number of runs	612		1 208	
Number of events	2 066 995		2 519 475	
Number of preselected events	260 834		566 480	
Validation	all	good runs	all	good runs
Integrated luminosity (pb^{-1})	19.9	17.1	91.9	86.3
Runs	612	390	1 208	945
Events	2 066 995	1 608 887	2 519 303	2 348 118
Monojet preselection	66 180	51 799	129 364	122 559
$\tau + \not\!\!E_T$ preselection	202 202	162 115	491 855	466 126
inclusive	187 744	237 742	571 702	541 427

Table 4.1: Overall selection statistics prior to tau validation for the XOX1_3P (Run 1A) and XOXB_5P (Run 1B) Missing E_T data streams.

- a jet with $E_T > 15$ GeV, $|\eta| < 1$, and one or more associated tracks,
- no other jet with $E_T > 10$ GeV,
- no other jet with $E_T > 5$ GeV and a 3D angle to the monojet of greater than 160° ("dijet veto"), and
- $\not\!\!E_T > 20$ GeV and $\not\!\!E_T$ significance > 2.4.

To be selected as a $\tau + \not\!\!E_T$ candidate the event must have

- a tau (TAUO) with $E_T > 10$ GeV,
- $\not\!\!E_T > 30$ GeV.

The $\tau + \not\!\!E_T$ selection was deliberately kept simple to be as inclusive as possible for general searches. On average these selections retained about 9% of the events in the Run 1A XOX1_3P stream and about 22% of the Run 1B XOXB_5P stream.

Table 4.1 lists the overall statistics for the reprocessed $\not\!\!E_T$ data from Run 1 and the initial selection steps before tau validation.

4.8 Determination of Integrated Luminosity

The primary method of determining the instantaneous luminosity at the CDF interaction region is from the Beam-Beam Counters (see Section 2.8). There are sixteen counters on either side of the interaction region. Only a single counter on a side is required to fire in coincidence with a counter on the opposite side to register an interaction. These counters are therefore very efficient for $p\overline{p}$ interactions. The coincidence rate is directly proportional to the instantaneous luminosity and therefore provides a means of determining the true instantaneous luminosity. However, the BBC rate tends to saturate at about 5×10^{30} cm^{-2}s^{-1} and therefore the integrated luminosity calculation ($\int \mathcal{L}dt$) becomes less reliable at high rates [172]. Four luminosity telescopes were installed at CDF for Run 1B to check the BBC measurements at the higher rates. These monitors have a much smaller geometric acceptance than the BBC and therefore are less efficient, but they do not saturate in the higher luminosity environment.

Corrections need to be made in the total integrated luminosity calculation for *accidental rates*, which are measurable contributions to the raw rates in the counters due to accidental coincidences which can be large and are luminosity dependent, and for multiple interactions, which are also luminosity dependent [173, 174]. All the systematic uncertainties in these corrections and some disagreement between the telescopes and the BBC rates leads to an uncertainty on the integrated luminosity for Run 1B of 8%. The uncertainty on the Run 1A integrated luminosity is less (3.6%) as the BBC rates were more reliable and the multiple interaction effects were less in the lower instantaneous luminosity regime.

The BBC interaction rates are stored for each data file and have been processed to give the integrated luminosity on a file-by-file and run-by-run basis. Calculation of integrated luminosity for any data set based on particular triggers needs to take into account any prescaling that might have been done on the triggers and needs to account for changes in triggers that evolved during the course of Run 1. We use the list of runs and files that went into our data set and the LUMCONTROL [175]

	Run 1A (pb^{-1})	Run 1B (pb^{-1})
All of CDF Stream B Exotics data	19.9	91.9
Requiring good data runs	19.1	88.8
Requiring good muon and SVX data	17.1	86.3
After tau validation	15.8	86.0
After accounting for lost data files	15.1	84.7
TOTAL	15.1 ± 0.5	84.7 ± 6.8

Table 4.2: Calculation of final luminosities for the validated Tau Working Group data set for Run 1. The final total is 99.8 ± 7.3 pb^{-1}.

program to determine the integrated luminosity for our data. About 4% of the files in Run 1A are "lost" during production (i.e. are unreadable or cannot be processed for some reason), accounting for a loss of 0.7 pb^{-1}. Only 1.5% of the files in Run 1B are lost, accounting for a loss of 1.3 pb^{-1}. Table 4.2 summarizes the calculation for a final total of 99.8 ± 7.3 pb^{-1} for the integrated luminosity in our Run 1 $\not\!\!E_T$ data set. After accounting for bad and lost data files, the integrated luminosity calculated here is consistent with that used in the SM top searches which do not account for these corrupted files [176, 177].

Chapter 5

Particle Identification and Analysis

I will discuss the reconstruction and identification of objects in the detector and the subsequent analysis which looks for the Higgs-like decay topologies. As the method used to identify hadronic tau decays is new for Run 1 and was developed by the Tau Working Group of which I was a part, I will discuss this in some detail. The electron, muon, photon, jet and b-tagging identification algorithms are very similar, if not identical, to those used in many CDF analyses. In particular, as this analysis is looking for decays of the top quark, we use electron, muon and b-tagging identification criteria that are virtually identical to those used in the analyses that searched for and discovered the Standard Model top quark decays in the dilepton and lepton + jets channels [13, 55, 178]. The identification of these other objects is discussed briefly and references are given to sources of more information.

The first step in analyzing an event is to find the event vertex (or the primary vertex in the case of multiple interactions), z_0, in the z-direction, parallel to the beamline. This vertex forms a common point for relating objects identified by our algorithm. Objects are then uniquely identified in the event. We classify objects in the order: photons, electrons, muons, taus and jets. If there is a second object identified within a three-dimensional 10° cone of an already identified one then the second contending object is ignored. Once all the objects in an event have been uniquely classified, we apply some event cleanup selection criteria and the topological requirements to enhance a potential charged Higgs signal. This is described in Section 5.10.

To understand the object identification efficiencies, to tune up the selection criteria, and to model the expected contributions to the search region, requires a detailed

modelling of both the signal and expected background processes that mimic the signal. Top quark decays (into both charged Higgs modes and SM modes) as well as $W \to \tau\nu$ decays and single tau decays are modelled as part of the overall strategy in determining the selection criteria and the number of events expected from an actual signal. This modelling, using Monte Carlo particle generator programs, is discussed in detail in Chapter 6. The contributions expected from background processes are described in Chapter 7. Chapter 8 details the combination of all this information in setting limits on the charged Higgs decay of the top quark.

5.1 Vertex Finding

As the luminous region at CDF is fairly extended and because of the high instantaneous luminosities under normal running conditions, we expect a typical bunch crossing to have multiple $p\overline{p}$ interactions spread along the z-direction. Determining the vertices for these interactions is crucial to reconstructing an event and is the job of the primary vertex finding algorithm [179]. This algorithm identifies and classifies vertices based on a set of quality criteria. These criteria are related to the number of segments and the number of hits within a segment of the VTX for track "stubs" and the density of vertices identified by the algorithm. The vertices are also required to be within the fiducial[1] volume of the vertex detector (i.e. $|z_0| < 150$ cm). In the analysis, we further restrict the vertices to lie within $|z_0| < 60$ cm to get good tracking information.

Primary vertices identified by this algorithm are those considered to be the site of $p\overline{p}$ interactions; these are stored in a VTVZ data bank. If there is more than one primary vertex, the highest quality vertex becomes the *event vertex*. All identified objects from the Tau Working Group algorithm are either associated with the closest primary vertex if they have a track or are assumed to have originated from the event vertex if they do not (e.g. photons or jet clusters with no tracks). The $\not\!\!E_T$ is calculated assuming this event vertex as well.

[1] *Fiducial* refers to the geometric acceptance for the active components of a detector element.

As we now have a single event vertex that we consider throughout the rest of the discussion, the term *event* is used interchangeably to refer to a bunch crossing where at least one $p\overline{p}$ interaction occurred. This concurs with the definition used during data taking and storage where an "event" refers to a single bunch crossing.

A common requirement for all the objects identified in an event to be considered in the charged Higgs analysis is that they all appear to come from the event vertex. We require all objects that have tracks (i.e. electrons, muons, taus and jets with tracks) to point to within 5 cm of this event vertex in z. Objects without tracks (photons and jets with no tracks) are assumed to come from the event vertex. This requirement is useful in cutting away objects that might have come from another interaction vertex in the same bunch crossing. It also eliminates cosmic ray muons.

5.2 Tau Identification

A significant portion of the effort within the Tau Working Group at CDF during Run 1A and early Run 1B was in firming up the tau identification selection criteria [180] and in testing their reliability in identifying hadronic tau decays both in "simple" events such as $W \rightarrow \tau\nu$ and in the more complex environment of heavy quark decays (e.g. for top quark searches).

A similar approach to tau identification [181] was undertaken by a group of CDF collaborators, based mostly at the University of Chicago, and these parallel efforts provided some cross-checks and cross-fertilization of ideas. These efforts resulted in a publication on a measurement of SM top decays into a hadronic tau and another lepton (e or μ) [75, 76].

The set of identification cuts finally arrived at for this analysis within the Tau Working Group are discussed in some detail below. The list is actually fairly short and the cuts are somewhat tuned to identify fairly energetic taus from decays of massive objects i.e. of order the W mass or higher, due to the large E_T and p_T requirements.

In the following discussion, reference is made to generated samples of physics

processes leading to tau particles. As there is no way to extract a pure, independent sample of hadronically decaying tau leptons to motivate the selection criteria discussed below, we need to make extensive use of generated events that simulate the physics processes we are interested in. Chapter 6 contains an extensive discussion of the event generators used and the subsequent detector simulation techniques used in the analysis.

5.2.1 Tau Reconstruction

The first step in reconstructing and identifying tau leptons that decay hadronically is the analysis control module FINDTAU [182, 183]. This software module is run in both the online Level 3 trigger and during the offline event reconstruction and is responsible for creating tau-like objects which are stored as TAUO data banks. FINDTAU is actually a filter module which provides the ability to filter based on tau-like objects in conjunction with other event criteria such as $\not\!\!E_T$ and other objects in the event. This filtering can be done online in the Level 3 trigger, as was used in for the $W \rightarrow \tau\nu$ asymmetry measurement made by E. Kuns [156]. For the charged Higgs analysis, as we are using the $\not\!\!E_T$ data set, we do not rely on taus for triggering on events and therefore do not use the filtering functions of FINDTAU but only rely on the module to construct the TAUO objects. All the data used in this analysis has been reprocessed with the improvements in the offline tracking and tau-finding code, as described in Section 4.5. We therefore are not subject to any triggering problems as far as the tau objects are concerned.

As discussed in Section 3.1, a hadronic tau decay tends to result in a narrow hadronic shower with a small number of tracks associated with the shower. Jets that have a narrow hadronic shower with at least one *stiff* (i.e. high-p_T) track are therefore termed "tau-like jets". FINDTAU uses calorimeter energy clusters and tracking information to identify these objects and creates a TAUO bank for all tau-like jet objects that pass cuts based on this information.

FINDTAU starts the search for tau-like jets from the list of jet clusters produced by the generic jet clustering analysis control module JETCLU, run with a cone size

of $\Delta R = 0.4$ radians in η–ϕ space, where $\Delta R = \sqrt{\Delta\eta^2 + \Delta\phi^2}$. As a reminder, the central calorimeter towers span 0.1 in η and $15^\circ = 0.26$ radians in ϕ (see Section 2.6.1). Calorimeter reclustering is performed for the TAUO cluster based on the jet clusters. This reclustering avoids the problem of merged jet clusters which can occur if there are many jets in the region and also gives an improved measurement of the E_T for the tau cluster.

A loop is made through the list of towers in the calorimeter cluster list (the CALL bank) for the jet cluster to find the highest E_T tower. If the highest E_T tower passes a threshold cut of 3 GeV, this forms the *seed* tower for the tau cluster. Repeated loops through neighboring contiguous towers are then made using the TOWE bank, which is a complete list of all calorimeter tower energies, and these tower energies are added to the tau cluster if they exceed a *shoulder* threshold cut of 0.1 GeV. Diagonal neighbors are considered contiguous. No towers more than 0.4 from the seed tower in η–ϕ space are added. Note that the tau cluster can include towers that were not originally chosen by the original jet clustering algorithm to be included as part of the jet cluster.

As hadronic decays of the tau lepton are expected to be very narrow, if there are more than six towers included in the TAUO reclustering, including both electromagnetic and hadronic towers combined, the cluster is rejected as a tau-like jet. Figure 5.1 shows the numbers of towers in TAUO objects from $W \rightarrow \tau\nu$ Monte Carlo events and from TAUOs from the Jet 50 inclusive jet trigger sample which has very few real taus. Unfortunately, it is impossible to extract an independent comparison sample of hadronically decaying taus from data without making some selection cuts. As indicated in the figure, TAUO objects from real taus are expected to have fewer towers than those from QCD jets. If the cluster passes this *narrowness* cut then it is declared a tau candidate and various quantities are derived from the calorimeter information and stored in the TAUO bank, along with the list of towers associated with the tau cluster. The TAUO object at this point is tentative and is discarded in the next step if no matching tracks are found.

A search is made through the track banks for tracks pointing inside the 0.4 cone

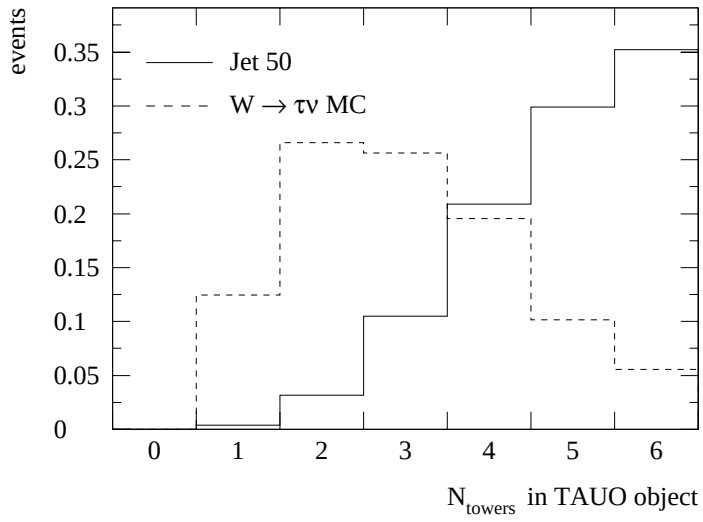

Figure 5.1: Number of calorimeter towers in TAUO objects from $W \rightarrow \tau\nu$ Monte Carlo events and from the Jet 50 data sample. Both histograms are normalized to unit area.

about the tau cluster and having $p_T \geq 4.5$ GeV/c. If no such track is found then the tau cluster is discarded as a tau candidate. The highest p_T track found in the 0.4 cone becomes the *seed* track. The nearest z-vertex for this track is found (within 5 cm) from the event VTVZ bank, and the tau calorimeter quantities are recalculated assuming this z-vertex. Note that there may be many vertices along the z-direction found for an event and the highest quality one is chosen as the event vertex and the event quantities such as E_T of clusters and $\not\!\!E_T$ for the event are calculated using this vertex. As each tau-like jet in an event could, in principle, be associated with a different vertex, the calorimeter quantities, in particular the $\not\!\!E_T$, are recalculated for each tau cluster and are stored in the TAUO bank. In the final analysis, all taus are required to have originated close to the event vertex.

The tau cluster is required to pass an $E_T > 10$ GeV threshold cut from the recalculated energies. If it does, then a count of tracks inside the 0.4 cone about the tau cluster is made for tracks with $p_T > 1.0$ GeV/c (the track *shoulder* threshold) and having the same z-vertex (within 10 cm) as the seed track. Counts of these tracks in a 10° cone (N_{10}) and a 10–30° *isolation annulus* (N_{30}) are also made and stored in the TAUO bank. No cuts are placed on this track count at this stage, but

$E_T > 10$ GeV	Minimum transverse momentum.
$\|\eta_{det}\| < 1.0$	Fiducial region.
$p_T^{seed} > 10$ GeV/c	Minimum seed track p_T.
$\xi > 0.15$	Electron rejection.
$N_{10} = 1$ or 3	Correct number of associated charged particles.
$N_{30} = 0$	Track isolation.
$\|Q\| = 1$	Correct charge.
$M_\tau < 1.8$ GeV/c^2	Total mass consistent with tau lepton.

Table 5.1: Summary of tau object identification cuts.

will be used later.

5.2.2 Tau Identification Cuts

The TAUO banks form the starting point for the hadronic tau decay identification. The selection criteria for creating TAUO banks was deliberately designed to be very inclusive so that we would have a high efficiency for hadronic tau decays, both in the online Level 3 trigger and from the offline production data. This does mean however that fully half of all jet clusters in a normal event do create a tau cluster, the vast majority of these being due to either narrow QCD jets or electrons. We therefore place more stringent cuts on these TAUO objects during the analysis stage in an attempt to enhance the purity of hadronic taus and to reject TAUO candidates from non-tau decay sources.

The identification criteria for hadronic tau decays are summarized in Table 5.1 with the details discussed below.

The minimum transverse energy for any object in our particle identification is 10 GeV. This quantity is obtained from the TAUO object for tau particles. As we later require the tau to be isolated, there is no *out-of-cone correction* to be made for the tau. This issue is discussed further in the context of jet identification in Section 5.7.

We also require the momentum of the seed track to be larger than 10 GeV/c. This requirement significantly reduces the number of QCD jets misidentified as taus

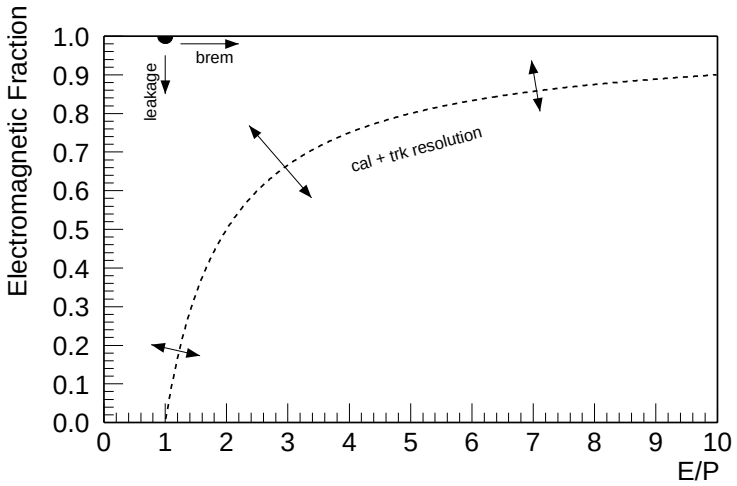

Figure 5.2: The electromagnetic fraction vs. E/p for an ideal detector. Electrons are represented by the dot at $E_{EM}/E = E/p = 1$. Hadronic tau decays would fall around the dashed line which represents $\xi = 1$. The arrows indicate the effects of detector resolutions and electron bremsstrahlung.

in the range $10 < p_T < 30$ GeV/c. This will be discussed further in the tau fake rate discussion.

We define a quantity, ξ:

$$\xi \equiv \frac{E}{\sum p}(1 - \frac{E_{EM}}{E}) \approx \frac{E_{HAD}}{\sum p} \tag{5.1}$$

where the sum is over the momenta of the tracks within a 10° cone of the tau axis and the energies are obtained from the calorimeter quantities stored in the TAUO bank. This quantity has been used in previous tau analyses at CDF [92, 94] to reject electrons that form tau candidates.

For an electron with a well measured track and energy, we expect most of the energy will be deposited in the electromagnetic calorimeters and the momentum and energy measurements should be roughly equal. Figure 5.2 shows the electromagnetic fraction (E_{EM}/E, where $E = E_{EM}+E_{HAD}$) plotted versus E/p for an ideal detector. Electrons would form a cluster at $E_{EM}/E = 1$ and $E/p = 1$, which corresponds to $\xi = 0$. Bremsstrahlung would lead to $E/p > 1$ and leakage out of the back of the electromagnetic calorimeters for high energy electrons will lead to $E_{EM}/E < 1$, leading to some smearing around the ideal case, indicated by the arrows in the figure.

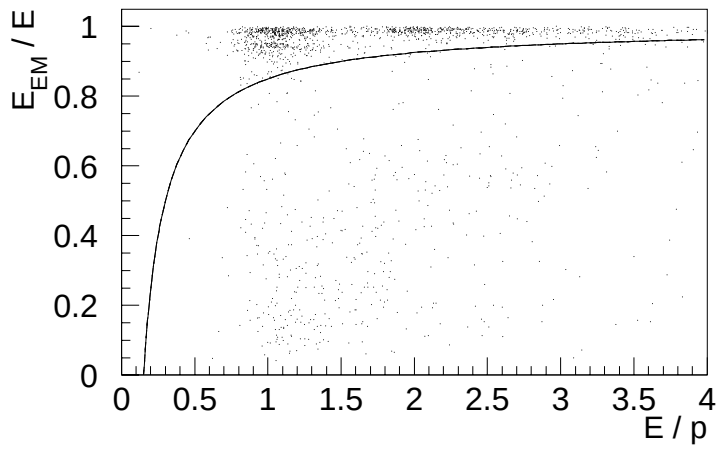

Figure 5.3: The electromagnetic fraction vs. E/p for TAUO clusters in the Run 1B monoTAUO sample. Electrons are clearly visible in the upper left-hand corner. All cuts have been applied except for the electron rejection cut. The curve corresponds to $\xi = 0.15$.

Hadronic tau decays, however, will tend to cluster along the dashed line corresponding to $\xi = 1$. Hadronic tau decays consist mainly of decays to charged pions and kaons possibly accompanied by neutral pions or kaons (see Section 3.1). Most of the charged energy will be deposited in the hadronic calorimeters and the neutral components tend to decay to photons (e.g $\pi^0 \rightarrow \gamma\gamma$) which will give electromagnetic showers. Hence E/p tends to be larger than one and E_{EM}/E tends to be less than one. For example, a hadronic tau decay that shares the tau energy equally between the charged and neutral tau decay products will have $E/p \approx 2$, $E_{EM}/E \approx 0.5$ and $\xi \approx 1.0$. Calorimeter and tracking resolutions will smear this ξ value.

Figure 5.3 shows the electromagnetic fraction plotted versus E/p for TAUO clusters in the Run 1B monoTAUO sample[2] where all the tau identification cuts described in Table 5.1 have been applied except for the electron rejection cut. Electrons forming a TAUO object are clearly evident in the figure as a cluster of points along $E_{EM}/E \approx 1$ and with relatively low E/p. We therefore use a cut of $\xi > 0.15$ on candidate tau clusters (shown on the plot) which rejects most of the electrons. We do not have an explicit cut that removes photon conversions, i.e. energetic photons that

[2]This sample was selected from the monojet sample, discussed in Section 4.7

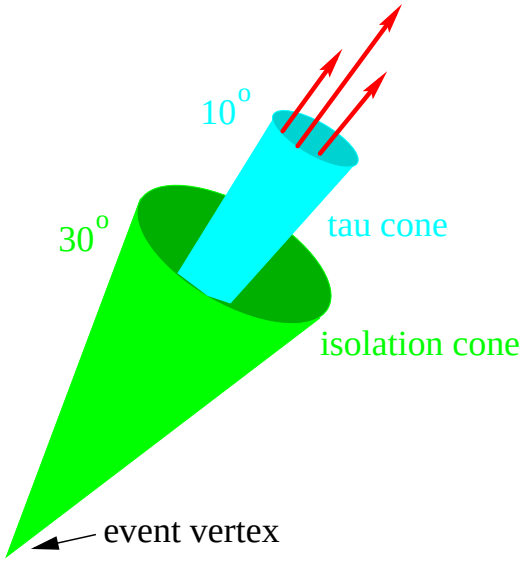

Figure 5.4: Schematic diagram depicting the tau cone and isolation annulus for hadronic tau identification.

pair produce ($\gamma \rightarrow e^+e^-$) soon after creation or within the bulk of the detector. The cut on ξ should remove most of these as well as they have a large electromagnetic fraction.

For the rest of the tracking quantities we re-evaluate the association of the tracks for the tau candidate. FINDTAU, of necessity, uses the closest primary z-vertex to the seed track (the highest p_T track) to calculate the tracking quantities for the tau cluster. We redefine the z-intercept of the tau candidate to be the z-intercept of this seed track. All tracks with $p > 1$ GeV/c within a 30° cone around the tau direction and with a z-intercept within 5 cm of the tau's, are associated with the tau candidate. We define the 10° cone around the highest p_T track as the *tau cone* and the 10–30° annulus around this cone as the *isolation cone* (depicted schematically in Figure 5.4). The number of charged tracks (with $p_T \geq 1$ GeV/c) within the 10° tau cone gives the tau track-multiplicity (N_{10}) and the sum of charges for these tracks gives the tau charge (Q_τ). The total number of charged tracks within the 10–30° isolation annulus give N_{30}. For a tau candidate to be identified it must have $N_{10} = 1$ or 3 (corresponding to a one or three-prong tau decay) with charge $Q_\tau = \pm 1$ and $N_{30} = 0$, i.e. the tau must be isolated. Figure 5.5 shows the effect of the isolation

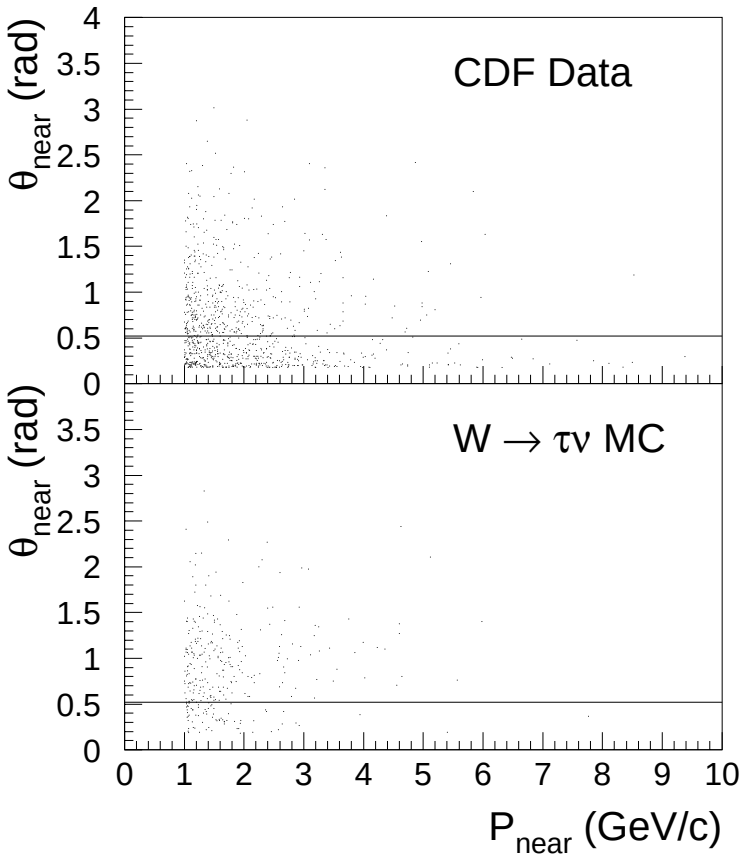

Figure 5.5: The angle of the nearest track to the tau cone plotted versus the track momentum for the Run 1B monojet data and $W \rightarrow \tau\nu$ Monte Carlo. The horizontal line indicates the tau isolation cut ($N_{30} = 0$). All tau cuts, except the isolation cut, have been applied.

requirement. All cuts except the isolation cut have been applied. The effect of this isolation requirement will be discussed in further detail below.

The final identification cut is requiring that the invariant mass of the tau candidate be consistent with the tau mass of 1.777 GeV/c^2. For the invariant mass calculation we include both the charged particles (mostly from $\pi^{\pm}$) and neutrals (mostly from $\pi^0 \rightarrow \gamma\gamma$ decays) associated with the tau candidate (cf. with Table 3.2 for the main tau decay modes). The identification of photons in the tau cluster is discussed below. Only those photons identified within the 10° tau cone are included in the mass calculation. As some of the momentum of a tau decay is always lost in

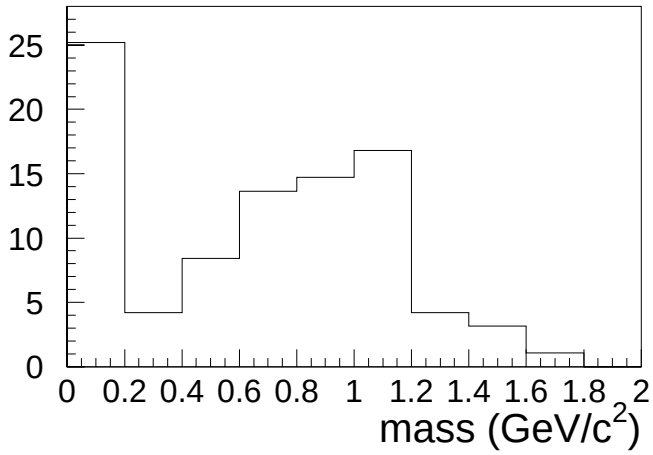

Figure 5.6: Mass distribution for reconstructed tau leptons from $W \rightarrow \tau\nu$ Monte Carlo.

the form of neutrinos, we use a conservative cut of $M_\tau < 1.8$ GeV/c^2 which is very efficient in accepting real hadronic tau decays but rejects QCD jets. Few real taus have a reconstructed mass above 1.8 GeV/c^2. This is shown in Figure 5.6 which shows the reconstructed mass for tau leptons from $W \rightarrow \tau\nu$ Monte Carlo events. The zero mass peak consists mostly of tau decays into single pions.

The photons in tau decays come predominantly from the decay of π^0's ($\pi^0 \rightarrow \gamma\gamma$) which have a short decay length ($c\tau = 25.1$ nm [8]). These neutral components are important in identifying hadronic tau decays and can contain a substantial fraction of the tau momentum. To identify photons, we match the clusters of hits in the strip and wire chambers of the central strip chambers (CES – see Section 2.6.1) to each other. The matching algorithm was developed by C. Loomis [180] based on some original work by CDF collaborators at the University of Chicago [181].

The matching algorithm works as follows. First, a list is made of all strip clusters and wire clusters in a given wedge and quadrant (the wires lie parallel to the beam direction, along z, and the strips lie in the orthogonal direction — see Figure 2.10). The algorithm then attempts to match the strip clusters to the wire clusters based on the energies of each cluster. The quantity

$$\delta = \frac{|E_{\rm wire} - E_{\rm strip}|}{\sqrt{\sigma^2_{E,\rm wire} + \sigma^2_{E,\rm strip}}} \tag{5.2}$$

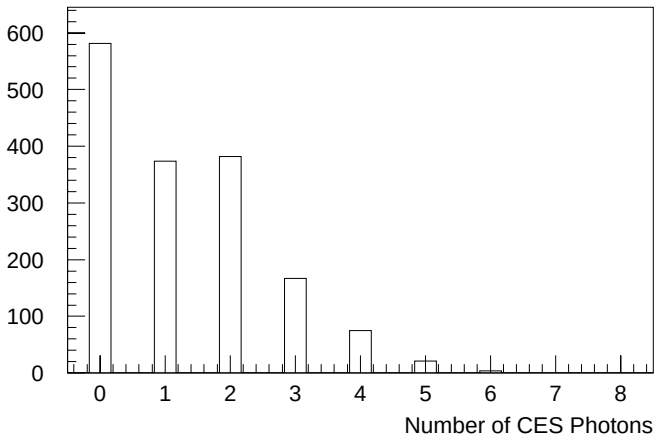

Figure 5.7: The number of associated CES clusters with tau candidates in $W \rightarrow \tau\nu$ Monte Carlo events.

is used as a measure of the quality of the matching. All matches must have $\delta < 2$. The energy dependent resolution is

$$\sigma_E = 0.35 - 0.09 \log_{10}(E) \text{ with } E \text{ in GeV}, \tag{5.3}$$

based on data from an analysis of the CES response [184]. If more than one strip cluster matches a wire cluster, the match with the lowest δ is chosen.

A second pass is made through the strip clusters to try to add an additional strip cluster to an existing one-to-one match. This is only done if adding the cluster improves the match. Finally, from those unused strip and wire clusters, pairs of strip clusters are matched to a wire cluster. The best pair is chosen for each wire cluster, provided that the match has $\delta < 2$.

Each strip cluster in a tower associated with the tau produces a single photon entry. The position is given by the centroids of the combined strip and wire clusters if it is matched or by the strip centroid and the center of the tower if it is not matched. The energy of the photon is the electromagnetic energy of the calorimeter tower distributed among the strip clusters in that tower weighted by the strip cluster energies. The number of CES clusters associated with each tau candidate in the $W \rightarrow \tau\nu$ Monte Carlo is shown in Figure 5.7.

5.2.3 Tau Identification Efficiency

We are concerned with how effective the identification cuts are at identifying real hadronic tau decays and, at the same time, at rejecting fake taus from QCD or leptonic jets. To check the identification efficiencies for real taus we examine the efficiencies of the various tau cuts in a number of different Monte Carlo data samples which simulate real tau decays and also use a tau-enriched sample of real data where we place cuts that should enhance $W \to \tau\nu$ decays. These data samples are also useful in checking the identification efficiencies for the other objects in an event. Complete details of the Monte Carlo studies can be found in Reference [185].

The fake rates for taus have been measured in the inclusive jet data and checked with the inclusive lepton samples and a parameterized function is derived for the fake rates. A summary of this study is given in Appendix E and is discussed in the next section.

We examine the tau identification efficiency in three types of generated data samples, all of which use full detector simulation (see Chapter 6 for a full description of the event generation and subsequent detector modelling). The first sample uses single isolated taus, with no other objects in the detector simulation. Samples of purely left and right-hand polarized single taus were generated and passed through the detector simulation. The different polarization states were generated to check the difference in the kinematics, which was predicted to possibly have some effect, as discussed in Section 3.1. Since these taus are obviously isolated, they allow us to check the isolation cut efficiency independent of anything else in the "event". The taus are generated with a p_T of 10–200 GeV/c over a pseudorapidity range $-2 \leq \eta \leq 2$.

We also look at two simulated physics processes: one being $W \to \tau\nu$ and the other $t\bar{t}$ decays to Hb and Wb where the charged Higgs bosons are forced to decay to $\tau\nu$. The $W \to \tau\nu$ sample is generated using the HERWIG [186] Monte Carlo and gives a good example of a physics process with relatively clean tau events. Tau decays to both hadronic and leptonic final states were simulated.

The Monte Carlo $t\bar{t}$ samples are those used to estimate the acceptance for the signal in the charged Higgs search, discussed fully in Chapter 6. These samples are generated using the ISAJET [187] and PYTHIA [188] Monte Carlo event generators. Two different Monte Carlo generators are used here to get a measure of the systematic uncertainty introduced by the different techniques used to model high-energy $p\bar{p}$ collisions.

To define an efficiency for object identification, we compare the number of detector objects that have been uniquely identified in an event by the algorithm to the number of particles in the appropriate kinematic and geometric (*fiducial*) region that are potential sources of such objects. As we only identify hadronic tau decays in the central region ($|\eta| < 1.0$) with $E_T > 10$ GeV and with a seed track of $p_T > 10$ GeV/c, our denominator in the following is defined as all the generated tau particles that have

- decayed hadronically,
- *visible* tau $E_T > 10$ GeV (i.e. excluding the energy of the neutrinos),
- a seed track of $p_T > 10$ GeV/c, and
- $|\eta_{det}| < 1.0$ of the seed track.

The individual and cumulative effects of the tau identification cuts listed in Table 5.1 on tau candidates (i.e. TAUO bank objects) from the single isolated tau sample, the $W \to \tau\nu$ sample and for a ISAJET $t\bar{t} \to H^+ b\, H^- \bar{b}$ sample (with $M_{H^\pm} = 100$ GeV/c^2) are shown in Table 5.2. The top two rows give the number of *generated* tau particles in the Monte Carlo and the number passing the particle selection criteria described above (*fiducial*). The second two rows show the number of observed tau objects (TAUOs) associated with the generated tau particles in the fiducial region and the number of these that pass all the tau object identification cuts (ID).

The columns in the lower section give the efficiencies (as a percentage) for the number of observed tau objects that pass the various tau object identification cuts

	Single isolated taus			HERWIG $W \to \tau\nu$			ISAJET $t\bar{t} \to H^+ b\, H^- \bar{b}$		
Number generated	24513			61558			12307		
Number fiducial	9548			43957			11206		
Number of TAUOs	8755			22671			7918		
Number ID taus	7138			12496			6031		
Tau particle selection Tau object cuts	Pass cuts %	Marg. loss (%)	Cum. cuts %	Pass cuts %	Marg. loss (%)	Cum. cuts %	Pass cuts %	Marg. loss (%)	Cum. cuts %
Create a TAUO	91.7	—	91.7	91.8	—	91.8	87.7	—	87.7
$\lvert\eta_{det}\rvert < 1.0$	91.6	(0.06)	91.6	91.7	(0.04)	91.7	87.7	—	87.7
$p_T^{seed} > 10$ GeV/c	91.2	(0.23)	91.1	90.4	(0.76)	90.3	87.1	(0.13)	87.1
$\xi > 0.15$	87.6	(2.86)	87.2	87.2	(3.15)	85.9	84.2	(1.41)	83.8
$N_{10} = 1, 3$	88.3	(0.34)	84.2	84.3	(0.22)	79.2	78.1	(0.15)	75.0
$N_{30} = 0$	91.6	(0.02)	84.2	75.3	(13.03)	65.9	49.9	(28.97)	44.3
$\lvert Q\rvert = 1$	89.0	—	84.2	84.7	(0.02)	65.9	78.5	(0.05)	44.2
$M_\tau < 1.8$ GeV/c^2	80.7	(9.22)	74.9	89.9	(0.94)	65.0	81.0	(2.16)	42.0

Table 5.2: Tau identification cut efficiencies for the three Monte Carlo samples.

compared to the number of generated tau particles in the fiducial region. The column labelled *Pass cuts* gives the relative percentage of tau particles passing a particular selection cut. The marginal effect of this selection cut, which is the number of particles that fail this particular cut after all the other cuts are applied, is given in the column labelled *Marg. loss*. The cumulative efficiency for all cuts is given in the column labelled *Cum. cuts*. The last number in the cumulative column is the final efficiency.

The effects of the tau object identification cuts can also be seen graphically in Figure 5.8. The cumulative efficiency for each cut is plotted versus the associated tau particle visible E_T and detector η of the highest p_T track; these quantities are derived from the underlying Monte Carlo tau information. The hadronic tau decays have been separated into the one and three-prong decay modes.

Table 5.3 and Figure 5.9 show the effect of the tau identification cuts on a sample of TAUO objects from the inclusive Jet 50 data for comparison. The number of real taus in this sample is expected to be very small. This will be discussed further in the next section on tau fake rates.

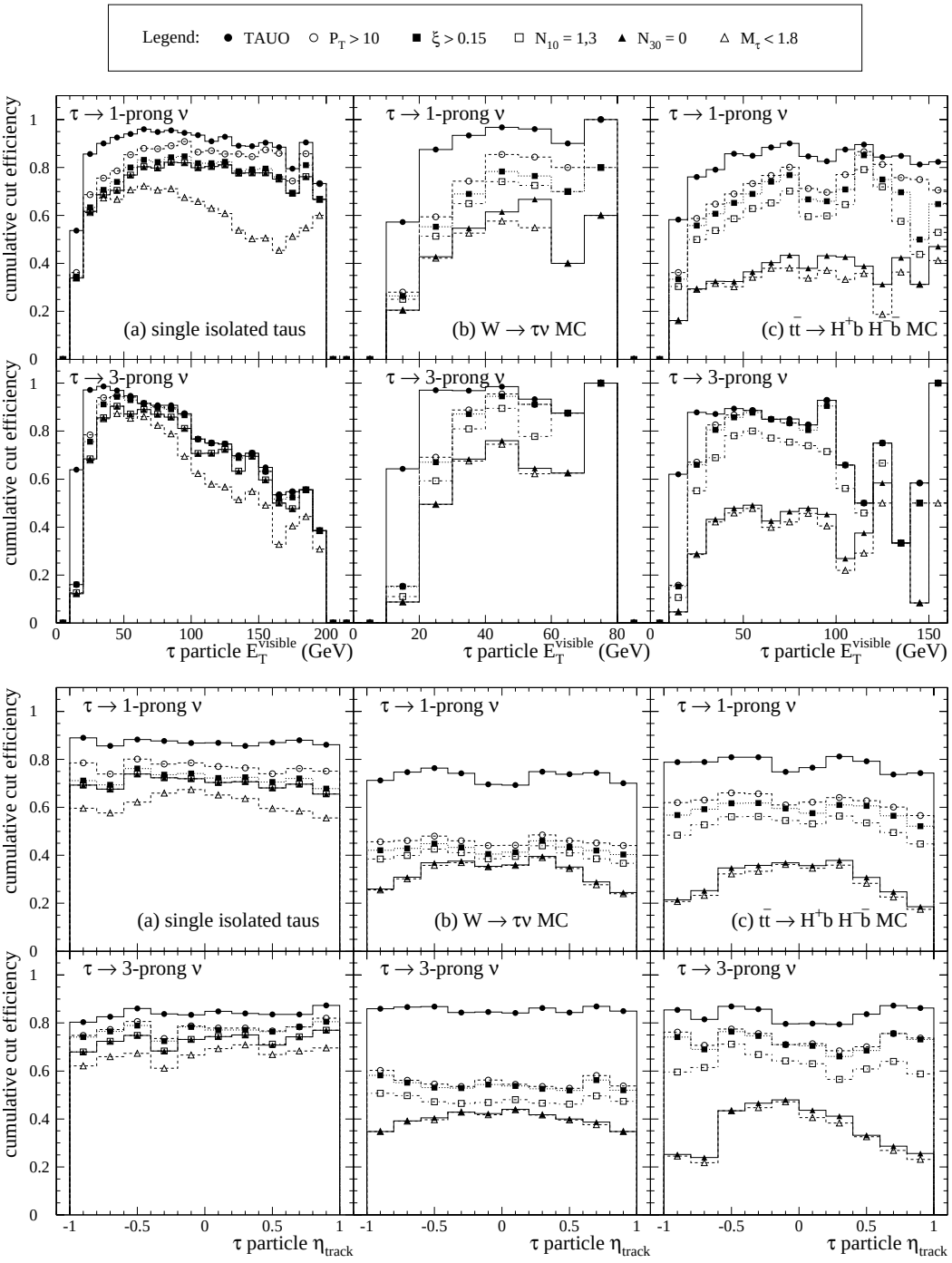

Figure 5.8: The cumulative effects of the tau identification cuts on simulated taus plotted versus the visible E_T (top) and η (bottom) of the underlying tau particle, separated into one- and three-prong decays. The samples are from (a) simulated single isolated tau decays, (b) HERWIG $W \to \tau\nu$ Monte Carlo data, and (c) ISAJET $t\bar{t} \to H^+ b\, H^- \bar{b}$ Monte Carlo data, with $M_t = 175$ GeV/c^2 and $M_{H^\pm} = 100$ GeV/c^2. The $|\eta| < 1.0$ cut and charge cut ($|Q| = 1$) have no significant effect for simulated taus and are not shown.

TAUO objects from Jet 50 Data			
Number of TAUOs	88804		
Number ID taus	1478		
Tau object cuts	Pass cuts %	Marg. loss (%)	Cum. cuts %
Create a TAUO	100.0	—	100.0
$\|\eta_{det}\| < 1.0$	85.0	(1.15)	85.0
$p_T^{seed} > 10$ GeV/c	56.3	(1.67)	48.9
$\xi > 0.15$	96.3	(0.05)	47.7
$N_{10} = 1, 3$	35.7	(0.09)	14.4
$N_{30} = 0$	24.4	(4.07)	4.16
$\|Q\| = 1$	48.9	(0.02)	4.06
$M_\tau < 1.8$ GeV/c^2	41.5	(2.40)	1.67

Table 5.3: The efficiencies for the tau identification cuts when applied to the TAUO objects in the inclusive Jet 50 data.

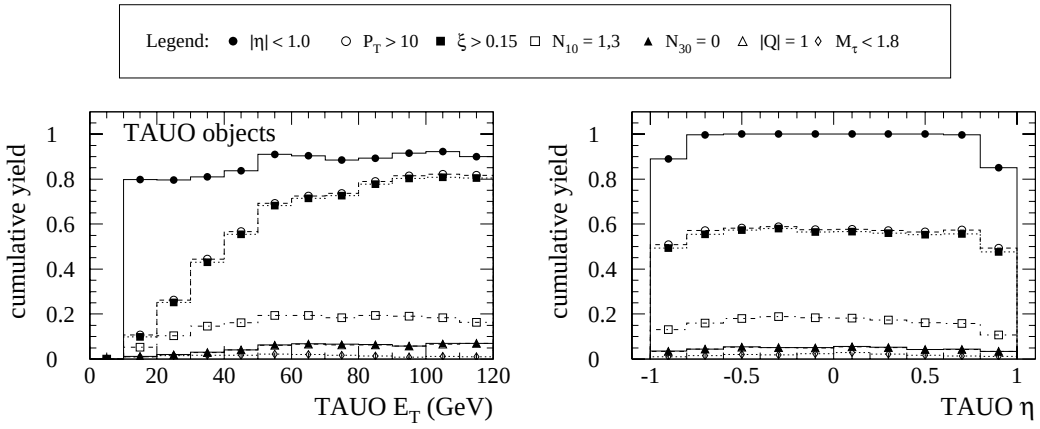

Figure 5.9: The cumulative effects of the tau identification cuts on TAUO objects in the inclusive Jet 50 data, plotted versus (a) the TAUO object E_T and (b) the TAUO object η from the track.

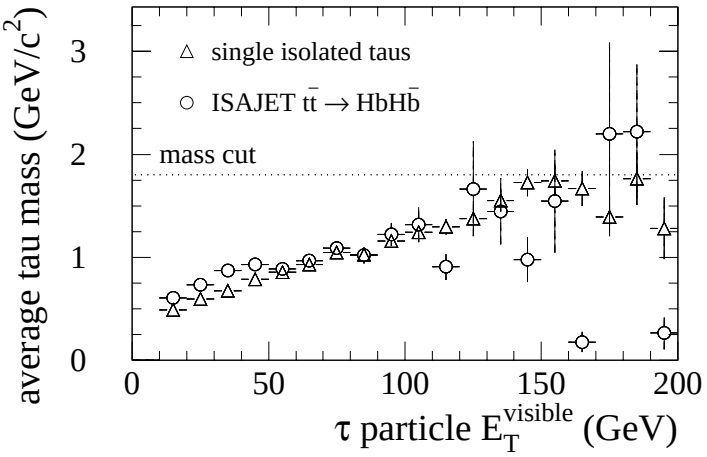

Figure 5.10: Profile of the average mass of the tau object versus the underlying tau particle visible E_T for hadronic tau decays in the single isolated tau sample and from the ISAJET $t\bar{t} \rightarrow H^+b\,H^-\bar{b}$ sample. The mass cut is at 1.8 GeV/c^2.

From Table 5.2 and Figure 5.8 it appears that the mass cut on the tau cluster ($M_\tau < 1.8$ GeV/c^2) has a large marginal effect for the isolated tau sample at large tau E_T. This is especially true for the 1-prong tau decays as any mismeasurements of the p_T of a single stiff track will lead to large errors in the mass calculation, and tends to get worse the stiffer the track. This is less likely for the 3-prong tau decays where the individual tracks tend to be softer. This mass cut inefficiency is not as noticeable in the $W \rightarrow \tau\nu$ or $t\bar{t}$ samples, essentially due to the fact that most of the taus have E_T's that are much lower than 200 GeV. Figure 5.10 shows the average mass of the hadronically decaying taus versus the tau particle's visible E_T for the single isolated tau sample and for the ISAJET $t\bar{t} \rightarrow H^+b\,H^-\bar{b}$ sample. There is a steady rise in the calculated tau mass based on the sum of the tracks and neutrals (with most of the contribution coming from the charged tracks). The statistics peter out for the $t\bar{t}$ sample above about 100 GeV but it is clear that the trend and masses from the two samples are comparable. As, at best, there is an average of about 80 GeV of energy for the tau particle from the top decay, this cut does not introduce any significant inefficiency in the charged Higgs search but helps in the QCD jet rejection (see the fake rates discussion in the next section).

The most significant cut for taus from real physics processes such as $W \rightarrow \tau\nu$ and

$t\bar{t}$ decays is the isolation cut, $N_{30} = 0$. The 10° cone defining the tau is expected to be more than wide enough to contain the complete tau fragmentation, as demonstrated from the negligible effect of the isolation cut in the single isolated tau sample for even very energetic taus (see Table 5.2 first column and Figure 5.8). In real physics processes, the underlying event (formed from the spectator particles in the $p\bar{p}$ collision) can produce low-energy particles that are thrown in the tau direction, effectively "muddying" the tau cone. There can also be radiation (gluon bremsstrahlung) off of the particles involved in the hard scatter; the resultant hadrons can be collimated with the tau particles, especially those from the final states that eventually produce a tau, and give additional tracks in or near the tau cone. Therefore, the cut based on the 10–30° annulus that forms the tau isolation region, designed to reject QCD jets, will introduce some inefficiency in hadronic tau identification.

The major difference between the various Monte Carlo generators used in this analysis is in their modelling and calculation of this fragmentation and radiation and leads to systematic differences between the estimates using the different Monte Carlo data sets. This is clearly evident in Figure 5.11 where the number of tracks in the isolation region for hadronically decaying taus is plotted for the HERWIG $W \rightarrow \tau\nu$ and ISAJET and PYTHIA $t\bar{t} \rightarrow H^+ b\, H^- \bar{b}$ samples. There is a significant difference in the zero tracks bin, where the isolation cut is placed. This leads to an approximately 15–20% percent enhancement in the efficiency for tau identification in PYTHIA versus ISAJET $t\bar{t}$ Monte Carlo. This difference in generators will be discussed further in Chapter 6.

The identification efficiencies for tau particles as a function of the visible E_T of the tau and η_{det} of the highest p_T track are shown in Figure 5.12 for the single isolated tau sample, the $W \rightarrow \tau\nu$ sample and a $t\bar{t} \rightarrow H^+ b\, H^- \bar{b}$ sample. The efficiencies are calculated in a similar fashion to that described above; the denominator is formed from counting the number of generated tau particles decaying within the fiducial and kinematic region in bins of E_T or η. A bin-by-bin comparison is then made of the total number of identified objects that pass versus the number of generated taus in that bin. The error bars on each bin are calculated using binomial error estimates.

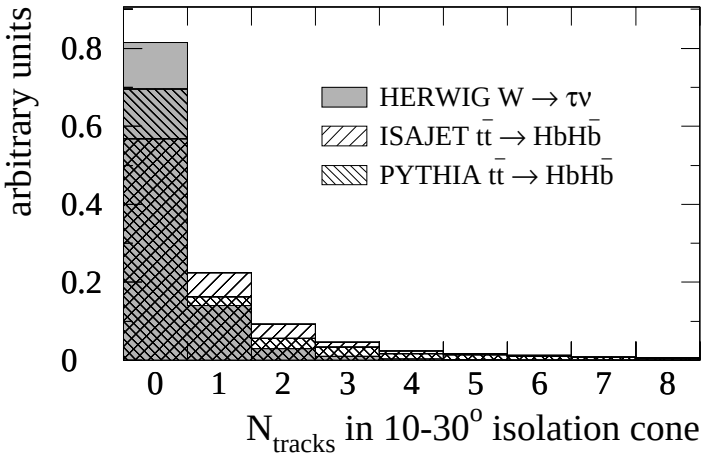

Figure 5.11: Number of tracks in the isolation region for TAUO objects reconstructed from hadronically decaying tau particles in the $W \rightarrow \tau\nu$ and $t\bar{t} \rightarrow H^{+}b\,H^{-}\bar{b}$ Monte Carlo samples (with $M_t = 175$ GeV/c^2 and $M_{H^{\pm}} = 100$ GeV/c^2). Each histogram is normalized to unit area.

The object created by a hadronic tau decay could, in principle, be any of the objects that we identify in the analysis i.e. a photon, electron, muon, tau or jet. However in 99% of the cases, hadronic taus decays in the fiducial region are reconstructed as a tau, a jet, or not reconstructed at all.

The tau decays have been separated in the plots into the different decay modes, with the hadronic tau decays separated into one and three-prong decays. Only the relevant reconstructed objects of interest are shown. Tau decays in the fiducial and kinematic region, not correctly reconstructed as a decay of a particular type, tend to be classified as jets. The leptonic tau decays are shown for comparison and will be discussed separately in the following sections on electron and muon identification.

Table 5.4 summarizes the average identification efficiencies for hadronic tau decays for the various Monte Carlo data samples, split up by the number of tracks identified in the 10° tau cone. The efficiencies for taus from the $t\bar{t}$ samples vary slightly depending on the decay mode of the top, essentially as the E_T of the produced tau will vary. The differences between the efficiencies measured from ISAJET and PYTHIA Monte Carlo are clearly evident.

There is a small probability ($\sim$ 1–4%) for one-prong taus to be reconstructed as

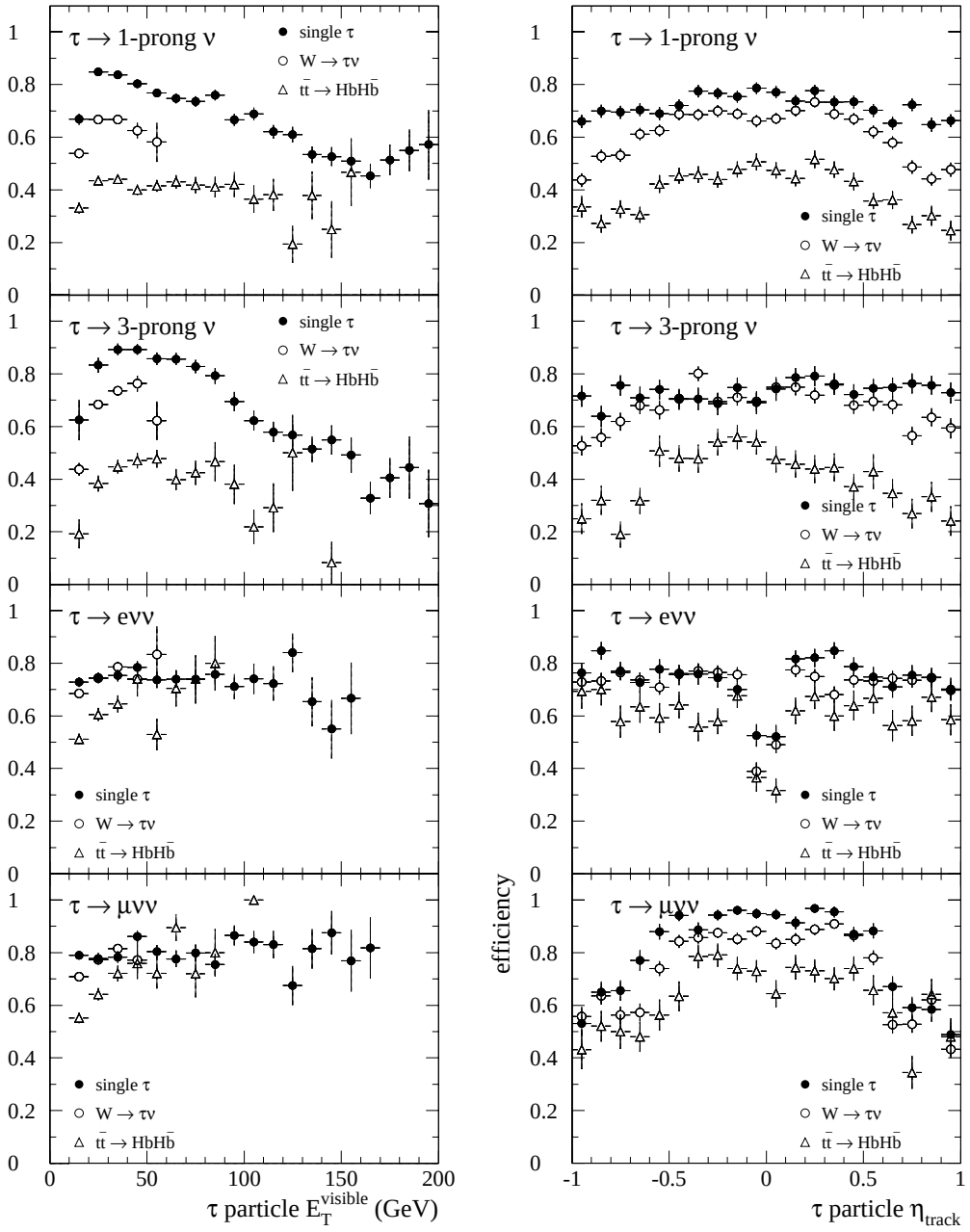

Figure 5.12: Tau identification efficiencies for objects reconstructed from the single isolated tau decays, HERWIG $W \to \tau\nu$ and ISAJET $t\bar{t} \to H^+b\,H^-\bar{b}$ ($H^+ \to \tau^+\nu$ with $M_t = 175$ GeV/c^2 and $M_{H^\pm} = 100$ GeV/c^2) Monte Carlo samples, plotted as a function of the visible tau energy and as a function of the seed track pseudorapidity. The efficiencies (plotted as a fraction of 1), are for an object identified as the appropriate type i.e. as a one or three prong hadronic tau decay or as a leptonic tau decay to an electron or muon.

τ decay mode	isolated tau	HERWIG $W \to \tau\nu$	ISAJET $t\bar{t}$ decay	PYTHIA $t\bar{t}$ decay
1-prong ($N_{10} = 1$)	71.9 $\pm$ 0.5	61.6 $\pm$ 0.5	37–41	42–51
1-prong ($N_{10} = 3$)	3.4 $\pm$ 0.2	2.1 $\pm$ 0.2	1.3	1.7–2.0
3-prong ($N_{10} = 3$)	73.2 $\pm$ 0.9	67.6 $\pm$ 0.8	37–43	45–54
all hadronic	74.8 $\pm$ 0.4	65.0 $\pm$ 0.4	38–42	44–53

Table 5.4: Summary of tau object classification efficiencies (as percentages) for hadronic tau decay modes for all the generated data samples.

a tau with three tracks; this is due to further decays in the detector simulation e.g. further fragmentation of the pions via Dalitz decays or pair production from the γ's from the π^0 decays giving rise to charged tracks. This efficiency is roughly constant over the E_T and pseudorapidity range of the tau particle.

Although right-hand polarized taus (such as those from charged Higgs decays – see the discussion in Section 3.1 on tau polarization) tend to decay with their visible decay products in the forward direction compared to left-hand polarized taus (such as those from W-boson decays), no difference is discernible within the statistics in the hadronic tau identification efficiencies between the right-handed and left-handed single isolated tau samples.

Minimum-bias events have been mixed into the single isolated left-handed tau sample as well to simulate the multiple interaction environment with no discernible difference in the tau identification efficiencies. A similar check was made on the ISAJET $t\bar{t} \to H^+ b\, H^- \bar{b}$ sample, comparing a sample with and without minimum-bias events added in and again no effect within the statistical uncertainties was seen (see Section 6.1.4).

For single isolated tau decays, very few taus decaying in the kinematic and geometric acceptance region are not reconstructed as an object. There is about a 2% inefficiency for hadronic tau decays where no object is reconstructed. This rises to about 7% in the $W \to \tau\nu$ sample but is only about 2–3% in the $t\bar{t}$ samples. Overall there is about a 6–8% inefficiency in reconstructing an object from a tau decay to all modes. Most of this inefficiency (55–65%) is from tau decays to muons.

For the $t\bar{t}$ samples, the 1-prong efficiency is fairly constant as a function of tau particle E_T. There does appear to be some fall-off for the 3-prongs with tau E_T but the statistics in this region are limited.

The overall efficiency for hadronic tau identification (from Table 5.4) is about 75% for single isolated taus, 65% for taus from a HERWIG $W \to \tau\nu$ Monte Carlo and 38–42% for the ISAJET $t\bar{t}$ samples and 44–53% for the PYTHIA $t\bar{t}$ samples. The difference in the $t\bar{t}$ samples will be explored further in the next chapter. The major difference between all these samples is the isolation cone cut. As the event gets "busier" with more objects in the event, there is a greater chance for other tracks to overlap the tau candidate.

5.2.4 Tau Fakes

Non-tau particles can be sources of TAUO objects as well. In fact, as mentioned previously, about half of all jets form a TAUO object. These could be from narrow QCD jets or electrons which form narrow calorimeter clusters and have associated tracks or from muons if they deposit enough energy in the calorimeters. The efficiency of the tau object identification cuts in rejecting these is shown in Figure 5.13. Here, the cumulative effect of the tau identification cuts on all TAUOs in the ISAJET $t\bar{t} \to H^+ b\, H^- \bar{b}$ Monte Carlo sample that are *not* associated with an underlying tau particle (i.e. there is no tau particle pointing towards the TAUO object within a three-dimensional cone of 0.4 radians) are shown.

The tau identification cuts are extremely good at rejecting TAUO candidates that do not come from an underlying hadronic tau decay source. If a muon does deposit enough energy in the calorimeters to form a TAUO (which occurs only at the 1-2% level) then there is a $\sim 10\%$ chance for this muon to pass the tau object identification cuts, giving an overall reconstruction efficiency of $\lesssim 0.2\%$ for muons as a hadronic tau object. Electrons have less than 0.1% chance of being reconstructed as a hadronic tau.

The vast majority of fake taus arise from low track-multiplicity, narrow QCD jets being identified as a hadronic tau. Although the fake rate from QCD jets is small

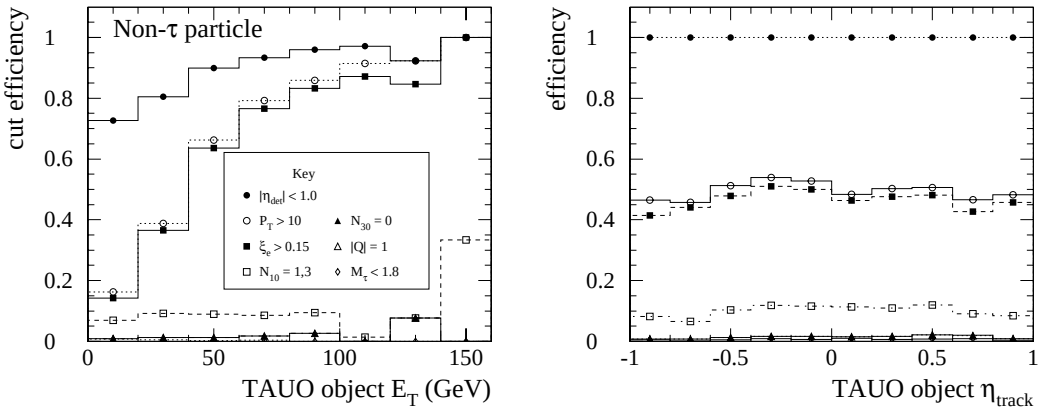

Figure 5.13: The cumulative effects of the tau identification cuts for TAUO objects associated with non-tau particles for the ISAJET $t\bar{t} \rightarrow H^+b\,H^-\bar{b}$ sample, $M_{H^\pm} = 100$ GeV/c^2.

($\sim 1\%$), there are a large number of jets in a typical event from a hard $p\overline{p}$ collision, so these form the major background for the charged Higgs analysis (see Section 7.3). Thus, events from any real physics process containing hadronic tau decays can only be identified on a statistical basis since the number of events with real identified taus and fake identified taus are comparable.

We have measured the fake identification rates for the tau candidates (TAUOs) from a sample of jets from the inclusive jet triggers and have checked these with data from the inclusive lepton triggers. A parameterized function versus the E_T of the tau candidate is obtained that we can apply to our search data set to estimate the number of fake taus (see Chapter 7). This fake study study is described in detail in Appendix E.

5.3 Photon Identification

We do not expect any primary, energetic photons to be produced in a charged Higgs event, hence photon objects are not used in the topology in the final analysis (but they are used in the $\not\!\!E_T$ calculation). We do not want photons to be identified as jet objects (discussed in Section 5.7) as they would then contribute to the search topology, so we keep the photon identification cuts very simple and inclusive. These

$E_{TEM} > 10$ GeV	Minimum transverse energy.
$N_{trk} = 0$	No charged tracks.
$I_{cal} < 0.1$	Calorimeter isolation.

Table 5.5: Photon object identification cuts.

cuts are summarized in Table 5.5.

Photon objects are required to have electromagnetic $E_T > 10$ GeV. Photons are identified from isolated electromagnetic clusters using a cone size of $\Delta R = 0.4$ where there is no track with a transverse momentum $p_T > 1$ GeV/c coming from the event vertex and pointing at the cluster. A calorimeter isolation cut of $I_{cal} < 0.1$ is applied where I_{cal} is the ratio of the calorimeter energies in the 0.4 cone surrounding the photon cluster tower (excluding the photon cluster itself) to the photon calorimeter cluster.

5.4 Electron Identification

For electron and muon identification we use selection criteria common to many analyses at CDF and in particular are very similar to the "tight" electron and muon cuts used in the top discovery analyses. Details of these selection criteria and their efficiencies can be found in References [55, 189].

Electron candidates are formed from a track extrapolating from the central tracking chamber (CTC) to a central or plug electromagnetic cluster which is constructed from a seed tower with $E_T > 3$ GeV and the two neighboring towers in pseudorapidity (η). The cluster is therefore $\Delta\eta \times \Delta\phi = 0.3 \times 15^\circ$ wide. Various identification cuts are then placed on the track and calorimeter quantities to select good electrons.

Electron identification in the central and the plug regions are slightly different as the CTC coverage does not extend fully into the plug region and therefore full three-dimensional tracks cannot be reconstructed. Electromagnetic clusters in this region therefore tend to be reconstructed as photon or jet objects.

The common selection criteria for central and plug electrons are: $E_T > 10$ GeV,

Central and Plug Identification Cuts			
	$E_T > 10$ GeV	Minimum transverse energy.	
	$E_{\rm HAD}/E_{\rm EM} < 0.05$	Low hadronic energy.	
	$I_{cal} < 0.1$	Calorimeter isolation.	
Central Identification Cuts		Plug Identification Cuts	
$E/p < 1.8$	Energy consistent with electron p_T.		
$L_{shr} < 0.2$	Good transverse calorimeter shower shape.	$\chi^2_{trans} < 3$	Good transverse profile.
$\Delta x < 1.5$ cm	Good track match with CES strips.	$\chi^2_{depth} < 15$	Good depth profile.
$\Delta z < 3.0$ cm		$f_{VTX} > 0.5$	Good number of hits.
$\chi^2_{strip} < 10$	Good electron profile.		

Table 5.6: Summary of the electron object identification cuts.

a $E_{HAD}/E_{EM} < 0.05$ cut which ensures that we have a good electromagnetic cluster and selects against electromagnetic clusters from hadronic sources such as pions, and a calorimeter isolation cut, $I_{cal} < 0.1$, similar to that defined above for photons, which ensures the electron is well isolated. I_{cal} measures the transverse energy in the towers within a cone of radius $R = \sqrt{(\Delta\phi)^2 + (\Delta\eta)^2} = 0.4$ centered on the electron but *excluding* the electron cluster's transverse energy as a fraction of the electron E_T.

Figure 5.3 for the electron rejection cut for taus showed that the calorimeter energy to track momentum ratio (E/p) is a good discriminator between electrons and hadronic showers. A cut of $E/p < 1.8$ is applied to the central electron candidates.

For electromagnetic clusters in the central calorimeter, information from the CES chambers is also available to identify electrons. The electron position at shower maximum is determined from a fit to the shower shapes in the CES as compared to a nominal electron profile that was determined from a calibration test beam [190, 191]. The position of the extrapolated track is matched in the longitudinal ($\Delta z < 3.0$ cm) and azimuthal views ($\Delta x = r\Delta\phi < 1.5$ cm) using the fitted shower profile and ensures a good match of the track with the electromagnetic calorimeter cluster. The goodness-of-fit of the shower shape to the nominal electron profile, measured by

χ^2_{strip}, is another useful discriminator. Requiring $\chi^2_{strip} < 10$ ensures a good match.

Another useful measure is the *lateral shower profile* in the calorimeter itself. This variable, L_{shr}, measures the profile of the energy sharing in the seed tower and in the calorimeter towers adjacent to the seed tower in azimuth. This lateral shower profile is compared to test beam data. As hadronic showers have very different lateral development, this variable forms a good discriminator between electrons and jets. A cut of $L_{shr} < 0.2$ is used in the electron identification.

As there is not a full measured track for the plug region, the E/p cut cannot be used. Similarly there are no strip chambers in the plug. However, the profile of an electron candidate in the segmented transverse and depth views in the plug calorimeter can be compared to the profile for a nominal electron. Quality cuts of $\chi^2_{trans} < 3$ and $\chi^2_{depth} < 15$ are applied to the resulting fits. Even though there is no ϕ information for a track pointing towards the plug, a good electron candidate is expected to leave a track in the VTX that would point in z to the plug cluster. At least half the expected number of hits in the VTX road (f_{VTX}) pointing at the PEM cluster are required.

One cut that we do *not* apply which has been used in the top analyses for electron identification is a fiducial cut on the position of the electron candidate inside the tower in the electromagnetic calorimeter. This cut uses the position of the electron candidate in the CES chamber to ensure that the electron candidate is well away from the tower boundaries in azimuth and that the energy is well measured. The CES covers about 84% of the fiducial volume within $|\eta| < 1.0$. As with the photons, discussed in the previous section, we are not as concerned with finding good electron candidates as we are in ensuring that objects that are most likely to have come from an electron are not identified as a jet. Therefore, we do not cut away electrons that might not have a good match in the calorimeters. Some of the cluster energy might be missed as some of the lateral shower could go between the uninstrumented cracks between the calorimeter towers but the extrapolated track should still give a good measure of the electron transverse momentum.

Electrons can only enter into the final selection as the fourth object (X) in the

$E_T > 10$ GeV	Minimum transverse momentum.
$E_{\rm EM} + E_{\rm HAD} > 0.1$ GeV	Minimum calorimeter energy.
$E_{\rm EM} < 2$ GeV	Maximum EM energy.
$E_{\rm HAD} < 6$ GeV	Maximum hadronic energy.
$\Delta x < 2$ cm (CMU) OR	Track matches stub in muon chambers.
$\Delta x < 5$ cm (CMP) OR	
$\Delta x < 5$ cm (CMX)	
$d_0 < 3$ mm	Good impact parameter.
$I_{cal} < 0.1$	Calorimeter isolation.

Table 5.7: Summary of muon object identification cuts.

τjjX channel, and are not eligible to be b-tagged (see Section 5.8 below).

5.5 Muon Identification

Muons are minimum ionizing particles which means they should deposit very little energy in the electromagnetic and hadronic calorimeters. There should however be a good track in the central tracking chamber (CTC) and a track segment (*stub*) in the muon chambers (CMU, CMP or CMX) which matches with the extrapolated track. These properties are exploited to identify muons in the pseudorapidity range $|\eta| \leq 1.0$.

The muon identification cuts are relatively simple and are summarized in Table 5.7. We demand that all muon objects have $E_T > 10$ GeV. This is actually derived from the p_T of the track matching the stubs in the muon chambers. The calorimeter energies for the towers that the muon would have traversed are required to be low; $E_{EM} < 2$ GeV and $E_{HAD} < 6$ GeV. The measured pulse height distribution for minimum ionizing particles in the central tracking chambers peaks near 1.7 GeV for the hadron calorimeters and around 0.3 GeV for the electromagnetic calorimeters so these cuts are very efficient for real muons while cutting away hadrons that "punch through" to the muon chambers.

The impact parameter (d_0) for the muon track (i.e. the closest approach to the beam line) is required to be less than 3 mm, which rejects cosmic-ray muons. We also demand that the extrapolated track matches the track segment in the muon

chambers in azimuth ($\Delta x = r\Delta\phi$) within < 2 mm for the CMU or < 5 mm for the CMP and CMX.

A calorimeter isolation cut ($I_{cal} < 0.1$), similar to that used for photons and electrons, is also required. This cut rejects jets that might have punched through the calorimeters and left track stubs in the muon chambers.

Fiducial cuts similar to those used for electrons are applied to the muons in the top analyses to avoid the ϕ boundaries. Again, we do not apply the fiducial cuts for the charged Higgs analysis.

Some analyses at CDF, in particular the top search in the dilepton channel, try to gain extra efficiency for muons by identifying tracks that do not point at muon tracking chambers and that have very little calorimeter energy, as minimum ionizing particles. This can extend the muon coverage out to $|\eta| \leq 1.2$ and helps fill in some of the gaps in the muon coverage but does not gain very much in efficiency and adds extra systematic uncertainties. We do not include these minimum ionizing particles in this analysis but we do include the minimum calorimeter energy cut of at least 0.1 GeV in the calorimeter towers traversed by a muon track to maintain consistency with the selection criteria used in the top analyses. This cut was designed to exclude misformed tracks due to track reconstruction problems that pointed at empty calorimeter towers.

5.6 Lepton Identification Efficiencies

The efficiency for lepton identification in top-like events has been addressed by the top analyses [55]. We are concerned here with whether leptons (e or μ) can be identified with reasonable efficiency in charged Higgs events, using the object identification scheme described above. Leptons identified as a lepton object (electron, muon or tau) or as a jet object can contribute to the search topology for the charged Higgs analysis, as described in Section 3.2.

The object identification efficiency for electrons and muons from $t\bar{t} \rightarrow H^+ b\, H^- \bar{b}$ Monte Carlo data can be used as a measure of this efficiency. As only objects with

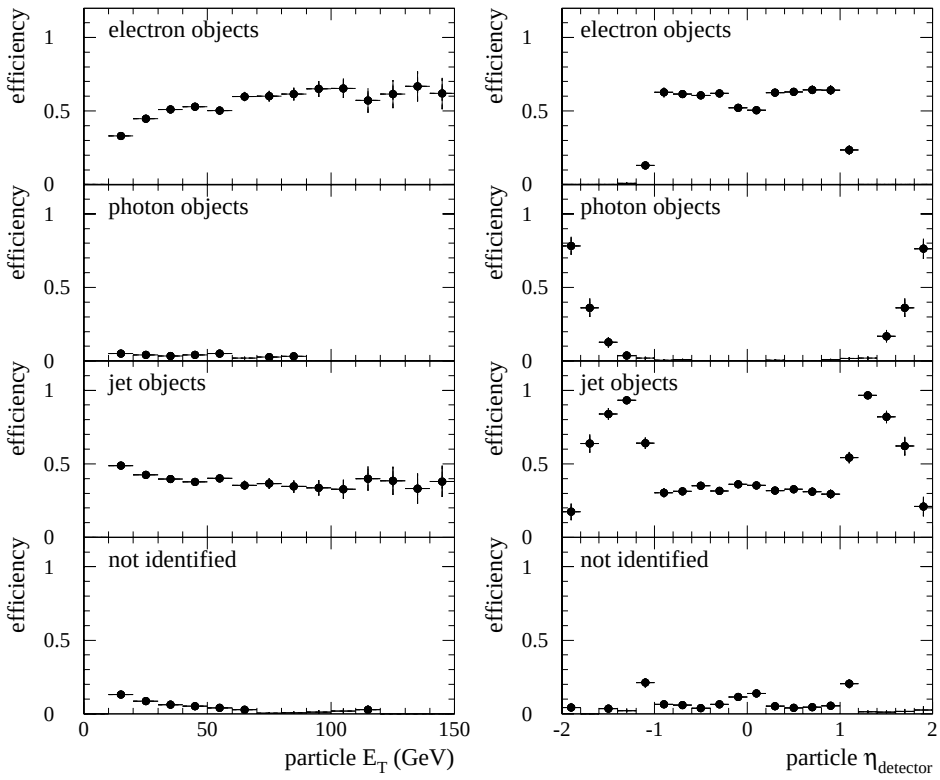

Figure 5.14: Object identification efficiencies for electrons from a $t\bar{t} \rightarrow W^+ b\, H^- \bar{b}$ Monte Carlo sample.

$|\eta| < 2$ and with $E_T > 10$ GeV are identified, we only use the leptons from the Monte Carlo samples at the particle level that have these properties in the efficiency calculation.

Figure 5.14 shows the object identification efficiencies for electrons (including electrons from $\tau \rightarrow e\nu\nu$) and Figure 5.15 for muons (including muons from $\tau \rightarrow \mu\nu\nu$). The efficiency is calculated in a similar method used for the tau particles in Figure 5.12. Each plot shows the fraction of particles in a particular E_T or η bin that give rise to a uniquely identified object of the specified type (photon, electron, muon, jet or not identified). Very few electrons or muons produce a tau object (see Section 5.2.4), and these are not shown.

Identification of an electron particle as an electron object improves with increasing electron particle E_T, to a maximum of about 65%. As expected, there is a substantial drop off to almost zero efficiency for $|\eta| > 1.3$ where most electrons are

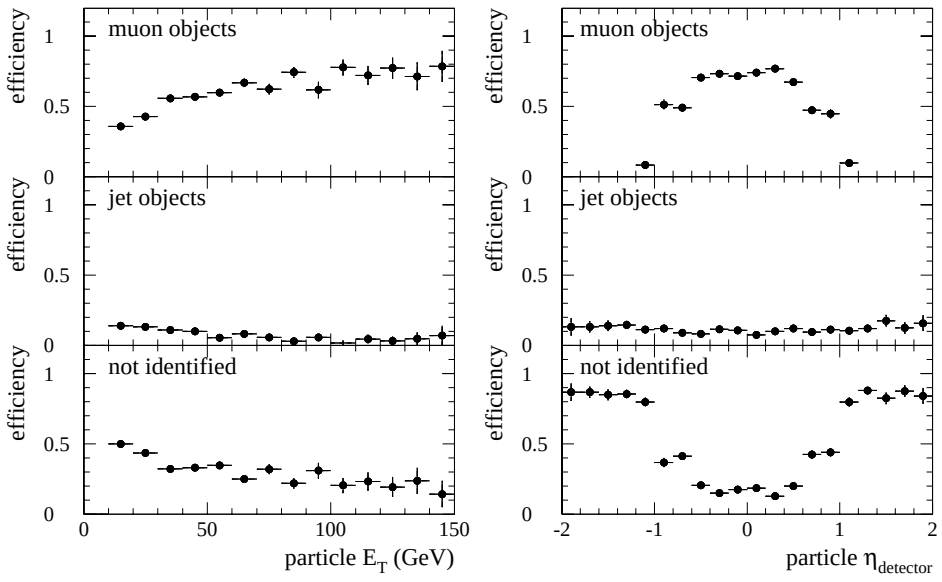

Figure 5.15: Object identification efficiencies for muons from a $t\bar{t} \rightarrow W^+ b\, H^- \bar{b}$ Monte Carlo sample.

identified as either a photon (for lower E_T) or a jet, due to the lack of tracking chambers in these high pseudorapidity regions. Electrons in the kinematic and geometric acceptance region are reconstructed as some object about 92% of the time.

There is also a noticeable dip at $\eta = 0$ in the electron efficiencies, due to the 90° hole in the calorimeter. There is a small concurrent rise in the electron particles identified as jets, but the approximately 10% lower efficiency for electron objects in this region is not fully compensated for.

Muon identification efficiencies also improve from about 50% at low E_T to about 75% at higher E_T for muons in the central region. Since there are no muon chambers between the central and forward regions and because most muons deposit very little energy in the calorimeters, less than 20% of muons in the region $|\eta| > 1.2$ are identified as jet objects and most are not reconstructed at all. This could lead to a miscalculation of the corrected $\not\!\!E_T$ in the charged Higgs analysis, which is performed using only identified objects. This inefficiency does fall off for the more energetic muons so the potential for $\not\!\!E_T$ miscalculation is reduced.

The overall efficiency for correctly identifying an electron or muon, in the central region, is approximately 10–20% percent higher for electron and muons from non-tau

sources than from leptonic tau decays. Most of these electrons and muons are from leptonic W-boson decays ($W \to \ell\nu$). These leptons tend to be more energetic than the leptons from leptonic tau decays as there is an extra tau-neutrino in the tau decay chain.

5.7 Jet Identification

The jet identification criteria are kept deliberately simple. Any object not classified as anything else, and having $E_T > 10$ GeV and $|\eta| < 2.0$, is classified as a jet. This category then is a "catch-all" for all significant energy deposits in the calorimeter that fail the criteria for the other objects. In the final analysis selection, jets with tracks are required to point in z to within 5 cm of the event vertex, z_0. Jets with no tracks are assumed to come from the event vertex.

Identification of strongly interacting particles (i.e. gluons, quarks, mesons and baryons) as jets is very efficient, as shown in Figure 5.16. Here, the efficiency for strongly interacting particles with $E_T > 10$ GeV and $|\eta| < 2.0$ to be reconstructed and identified as a jet object, is shown. Overall the identification efficiency is between 80–90% with the efficiency close to 100% for particles with $E_T > 50$ GeV.

Jet objects are the only objects which are considered for b-tagging in the final data selection. This is discussed in the next section.

Some analyses at CDF, especially those involving mass measurements, try to correct the jet energies for various effects [192, 193, 194]. These effects include out-of-cone energy where not all of the energy associated with a jet falls within a cone of radius 0.4 around the jet centroid. Another effect is that the underlying event can contribute significant energy from the spectator quarks in the interaction or from other minimum bias interactions in the same event. As we are dealing with fairly energetic objects in this analysis, we are not very sensitive to the contributions from the underlying event. Also, most jet corrections work under the assumption that the underlying process can be modelled and that all the energy in an event can be accounted for simply. As we are dealing with events with significant $\not\!\!E_T$

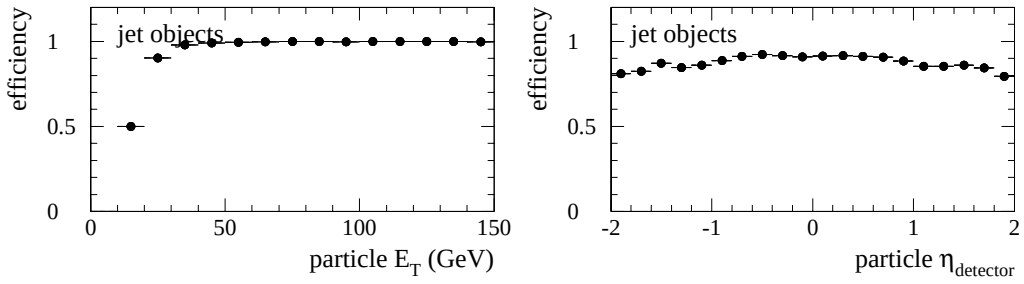

Figure 5.16: Jet object identification efficiencies for strongly interacting particles from a $t\bar{t} \rightarrow W^+ b\, H^- \bar{b}$ Monte Carlo sample.

from a number of neutrinos and as we use a jet definition that can include leptons, these jet corrections are difficult to make and would be inappropriate under certain conditions. We therefore do not apply any further corrections to the jet energies. As we treat the simulated data the same way in the search and since this is a counting experiment, we are somewhat insensitive to the jet energy scale.

5.8 Secondary Vertex Tagging

The high resolution silicon vertex detector (see Section 2.5.1) enables the identification of relatively long-lived particles that decay macroscopic distances (on the order of tens to hundreds of microns) away from the primary production vertex. These decay vertices are referred to as *secondary displaced vertices.* As discussed earlier in Chapter 3, bottom quark hadrons have long lifetimes and therefore travel significant distances (on the order of a few hundred microns, which can be Lorentz boosted to millimeters for high-p_T hadrons) before decaying. This decay results in multiple particles, all coming from a vertex which is displaced from the primary vertex. Charged particles from these decays will leave tracks that point back to the secondary. These tracks can have large *impact parameters* i.e. distance of closest approach of the track projected back to the primary vertex (see Figure 5.17 where the impact parameter is labelled d). A technique called *secondary vertex tagging* (SECVTX) exploits these properties to identify these secondary vertices. Jets that are identified as coming

from a secondary vertex are termed *b-tagged* or *b-jets*. In the charged Higgs analysis we only allow objects identified as a jet to be b-tagged. Note that as taus also have a reasonably long lifetime ($\sim$ 300 fs) they travel on the order of 100 μm before decaying. We do not exploit this feature of tau decays in this analysis as the SVX resolution is not quite good enough to observe these decays reliably; there are too few tracks in general and the decay distance is a little too short.

Another source of secondary vertices is hadrons containing charm quarks which are also relatively long lived and can travel 150–300 μm before decaying, also into multi-particle states. The efficiency for identifying the secondary vertices from these decays is about one-third [78] of that for bottom quark hadrons. This does mean that there are contributions to the b-tagged jets coming from non-b quark decays. There are also fake tags that result from detector resolution and tracking inefficiencies where *prompt* tracks (i.e. those that come from the primary vertex) are mistagged. These form a background for identifying b-jets.

The SECVTX algorithm was originally developed and optimized for tagging b-jets in the top lepton + jets[3] search channel [178, 55, 13]. This channel has a very similar topology to the charged Higgs search and its b-tag method is therefore very suitable for our use with no modifications. The algorithm is described in Appendix F. The measurement of this algorithm's efficiency for tagging bottom hadrons has been described in detail in References [195], [78] and [73]. I summarize some of the results below that are relevant to the charged Higgs analysis.

5.9 Efficiency for b-tagging

Figure 5.17 shows a schematic diagram depicting a view of the primary and secondary vertices in the transverse plane. The decay length of the secondary vertex (L_{xy} – see Appendix F) can be converted into an estimate of the effective proper decay length,

[3]The lepton + jets search looks for $t\bar{t}$ decay signatures with a high-p_T lepton (e or μ), $\not\!\!E_T$, ≥ 2 energetic jets and ≥ 1 b-tagged jet.

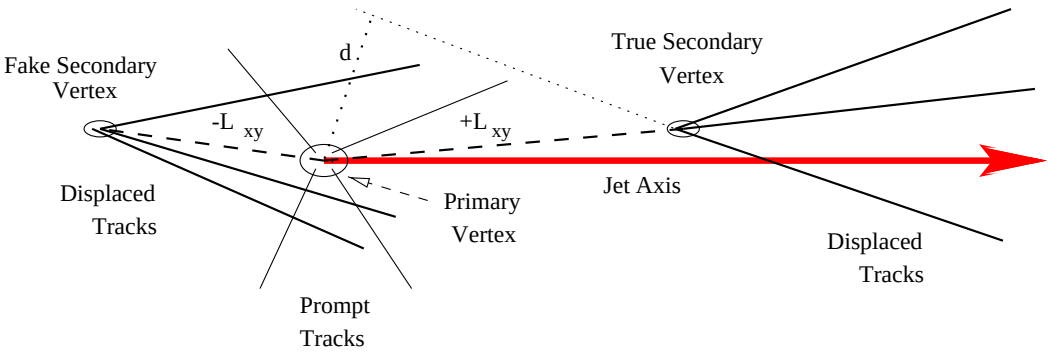

Figure 5.17: A schematic view in the transverse (r–ϕ) plane showing a real and a fake secondary vertex (mistag) displaced from the primary vertex. The bold arrow denotes the direction of the jet axis. The solid lines represent the charged particle tracks. The impact parameter, d, is shown for a representative track. The two-dimensional decay distance L_{xy} is shown for the real (+ve) and fake (−ve) displaced vertices.

$c\tau$, using the expression [196],

$$c\tau = L_{xy}\frac{M}{p_T F(p_T)} \tag{5.4}$$

where M is the invariant mass of the tracks associated with the secondary vertex, p_T is their total vector transverse momentum, and $F(p_T)$ is a scale factor determined from a Monte Carlo of b-decays, which accounts for b-hadron decay products that are not attached to the secondary vertex (see Reference [196] for details on this scale factor).

The two-dimensional $|c\tau|$ of a secondary vertex must be less than 1 cm for a jet to be b-tagged. Figure 5.18a shows the raw, positive $c\tau$ distribution for b-tagged jets (without background subtraction) in the Run 1 $\not\!\!E_T$ data sample which forms the charged Higgs search data set. The slope is consistent with the decay of b-hadrons.

It is interesting to note that although the tau lepton has a significantly shorter lifetime than b-hadrons, it does have a significant lifetime, and hence decay length, that is amenable to tagging by the secondary vertexing algorithm. A check can be made on the jets associated with an identified hadronically decaying tau lepton to see if they are tagged. The raw $c\tau$ distribution for these tagged jets is shown in Figure 5.18b for taus identified in the $\not\!\!E_T$ data sample. Even though no background subtraction has been done, the raw lifetime is considerably shorter than that for the

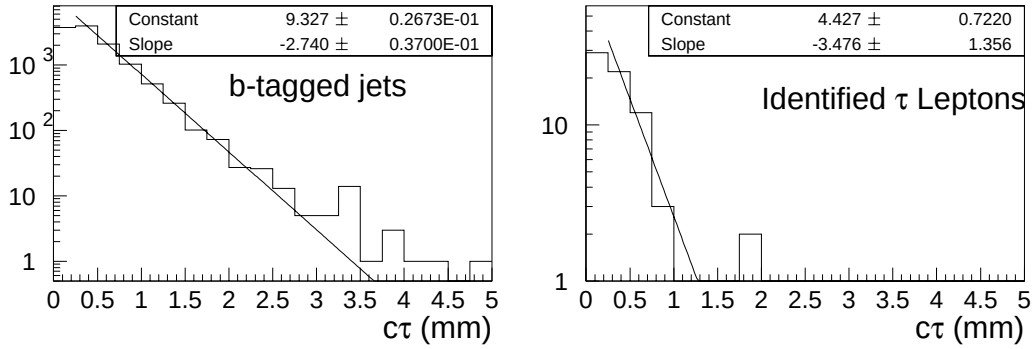

(a) (b)

Figure 5.18: The raw $c\tau$ distributions for (a) b-tagged jets and (b) identified hadronically decaying tau leptons in the Run 1 $\not\!\!E_T$ data. No background subtraction has been made.

b-tagged jets, as expected.

The b-tagging efficiency at CDF has been estimated using the large inclusive electron data set. Events with a central electron ($|\eta| < 1$) with $p_T > 10$ GeV/c are selected as these are relatively rich in $b\bar{b}$ events (from the semileptonic decay $b \to ce\nu$, with a branching fraction of $11.2 \pm 0.4\%$ [8]). The electron tends to be associated with the jet formed from the subsequent decay and fragmentation of the charm quark.[4] The tagging rate for the jet containing the electron and that of the recoil jet have been estimated. An excess of jets with a positively tagged secondary vertex is interpreted as an indication of b-hadron decays. One can also estimate the b-tag efficiency using double-tagged events of this type without having to know the b-quark fraction exactly [198].

The $c\tau$ distribution for tagged jets in the inclusive electron sample is compared to a B-meson Monte Carlo in Figure 5.19.

Another method of estimating the b-tag rate uses information from the CTC and SVX tracking and applies *track degradation* [78, 199] which is explained briefly below. This method has been applied to the Run 1B data and is an improvement over the measurement made using only the inclusive electron sample. This method is not subject to the limitations of the low statistics for higher E_T jets in the inclusive

[4] A second b-tagging method (not used in this analysis) at CDF tries to tag these *soft leptons* (including the muons from the semileptonic $b \to c\mu\nu$ decay) [197]

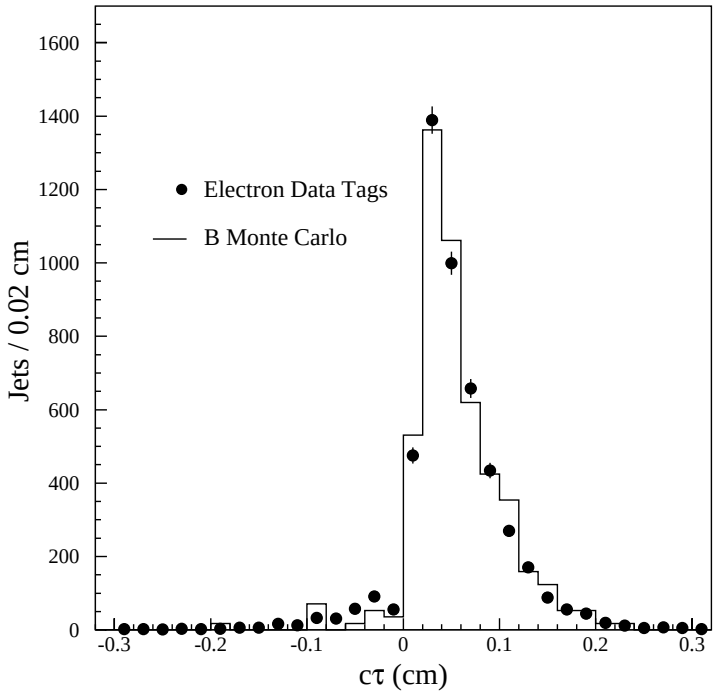

Figure 5.19: The $c\tau$ distribution for jets with a secondary vertex in the inclusive electron data (points with error bars) compared to Monte Carlo simulation (histogram) with the world average B lifetime.

electron measurement. This also give results that are more comparable to the regime of the energetic inclusive b-hadrons decays from top-quark decays, where all b-quark decay modes are possible and not just the semileptonic ones. Another limitation of the inclusive electron measurement is the need to extrapolate into the higher energy regime for the b-quarks from top decays which tend to be more energetic than those in the inclusive electron sample. This extrapolation leads to a large systematic uncertainty.

A $t\bar{t}$ Monte Carlo along with a CDF detector simulation is used to estimate the b-tagging efficiency. As the efficiency for b-tagging is highly sensitive to the simulation of the CTC and SVX tracking efficiencies, these have been studied in detail [200]. The CDF tracking simulations are too optimistic as the reconstruction efficiency of tracks is higher in the Monte Carlo simulations than that observed in the data. The tracking simulations do not fully take into account the decrease in the reconstruction efficiency due to the ambiguities caused when there are a large number

of hits in the tracking chambers. This loss of track reconstruction efficiency has been parameterized as a function of the number of hits around the track. The track finding efficiency is degraded in the Monte Carlo simulations using this parameterization. The track degradation method has been tuned to reproduce Run 1B data with the SVX′ detector. This procedure has been checked using the inclusive electron sample and there is very good agreement. The level of disagreement is used as an estimate of systematic uncertainties introduced by this track degradation procedure [201].

The track degradation affects b-tagging efficiencies in two ways. First, as the quality of tracks is affected, the number of jets deemed taggable by the secondary vertexing algorithm drops as there are fewer jets that have *good* SVX tracks. Second, for a taggable jet, there tend to be fewer associated tracks and therefore less chance of passing the b-tag requirements, so the tagging rate per taggable jet is also reduced. For Run 1B, the b-tagging efficiency for taggable jets (the *jet scale factor*) in the Monte Carlo is lower by a factor of 0.85 ± 0.01 (statistical uncertainty only). An *event scale factor* (F_b) has also been determined which measures the fractional loss in the efficiency to observe at least one b-tagged jet in a $t\bar{t}$ event, after applying the track degradation. For Run 1B data, the event scale factor is measured to be $F_b^{1B} = 0.87 \pm 0.06$, where the uncertainty includes the contribution from all the systematic and statistical sources [200, 201].

A similar event scale factor $F_b^{1A} = 0.72 \pm 0.21$ was determined for correcting the b-tagging efficiencies in the Run 1A Monte Carlo data [55]. However this only used a comparison between the inclusive electron data and $t\bar{t}$ Monte Carlo data, hence the larger uncertainty. In correcting the Monte Carlo efficiencies in the signal estimates in the next chapter, we combine the Run 1A and 1B results. The combined event scale factor for Run 1 is given by

$$F_b = \frac{15.1 \text{ pb}^{-1} \times F_b^{1A} + 84.7 \text{ pb}^{-1} \times F_b^{1B}}{99.8 \text{ pb}^{-1}} = 0.85 \pm 0.06 \qquad (5.5)$$

where the scale factors are weighted by the total integrated luminosity for each run (see Section 4.8).

There could be a concern that b-tagging rates may be different at different instantaneous luminosities as with increased multiple interactions it could be expected that b-tagging could be affected by i) the increase in the number of jets that potentially could be tagged in an average event and ii) tracks from multiple jets could be mis-associated and tracks could be assigned to different primary vertices. These tracks could therefore have artificially large impact parameters and could result in fake displaced secondary vertices. In an analysis looking for SM top decays in the all hadronic mode [73], which has a very similar topology to the charged Higgs analysis, this dependence on luminosity for both positive and negative b-tags was checked and found to have negligible effect.

The b-tagging efficiency from $t\bar{t}$ Monte Carlo events where there are more than three jets in the event has been measured to be about $35 \pm 18\%$ in Run 1A and $43 \pm 12\%$ in Run 1B [73]. The tagging efficiency in $t\bar{t}$ events with an identified leptonic W decay and three or more jets is about $41 \pm 4\%$ [199].

The raw efficiency in the charged Higgs analysis for tagging a b-jet (no scale factor applied) is shown in Figure 5.20 from a $t\bar{t} \rightarrow H^+b\,H^-\bar{b}$ Monte Carlo with $M_{H^\pm}$= 100 GeV/c^2 as a function of both E_T and η. Here the denominator in the efficiency calculation is formed by all b-particles at the particle generator level that have $E_T > 10$ GeV and $|\eta| < 2.0$. The number of these that form an identified jet object that has a positive b-tag forms the numerator. In the central region, the efficiency is about 33% for tagging such a jet. Applying the overall event scale factor of $F_b = 0.85$ for Run 1, this is reduced to 28%. The b-tag rate is dependent on the E_T of the underlying b-particle so b-jets from $t \rightarrow W^+b$ tend to have a slightly higher tag rate than those from $t \rightarrow H^+b$ decays where $M_{H^\pm} > M_W$. Due to the differences in the fragmentation models employed in the different Monte Carlo generators used in this analysis, there is another $\sim 3\%$ systematic uncertainty in the b-tag rate [185]. Overall, we take a systematic uncertainty of 10% in the final signal estimates due to the uncertainties in the scale factor and in the modelling of the b-quark fragmentation.

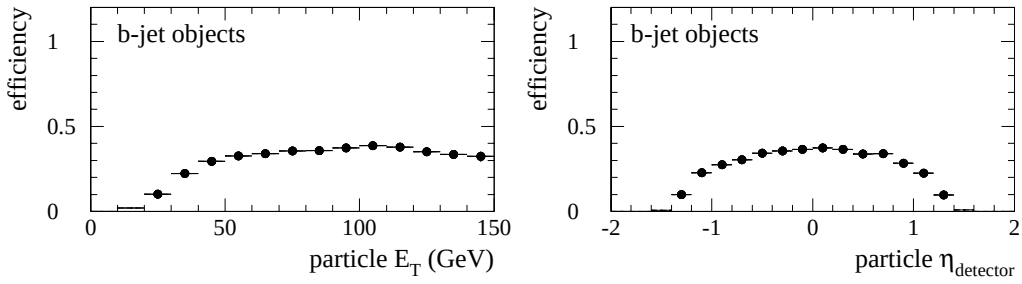

Figure 5.20: The raw b-tag efficiency for identified jet objects in a ISAJET $t\bar{t} \rightarrow W^+ b\, H^- \bar{b}$ Monte Carlo sample, with $M_{H^\pm} = 100$ GeV/c^2. No scale factor has been applied.

5.10 Analysis

The full Run 1A and Run 1B $\not\!\!E_T$ data streams, as described in Chapter 4, provide the primary data sample for this analysis. The sample, with all "bad" events removed, contains 145,732 events from Run 1A and 528,168 events from Run 1B for a total of 673,900 events. This represents an integrated luminosity of 99.8 ± 7.3 pb^{-1}.

To reduce the full sample to a reasonable size, a *preselected* sub-dataset was made which was used in the subsequent analyses. This preselection is described below.

5.10.1 Preselection Cuts

We place a few *preselection* cuts on the overall event quantities to reduce the data sample to a reasonable size for tuning the final selection. We require the event vertex, z_0, to be within 60 cm of the nominal interaction point at the center of the detector. This ensures that a reasonable fraction of the particles created in the collision will pass through the tracking chambers, especially the SVX, and will also have good calorimetry measurements. We also require at least one tau candidate (TAUO data bank) in the event. Since we are working from the $\not\!\!E_T$ data samples, we require $\not\!\!E_T > 30$ GeV as calculated in the offline processing. The offline processing has the full calibration and information on problems in the detector so can ensure a good $\not\!\!E_T$ measurement, which is highly vulnerable to detector problems. We also require both the Level 2 and Level 3 $\not\!\!E_T$ triggers to have fired (as described in Chapter 4).

Table 5.8 shows the number of events failing the specified cuts in the Run 1A

and 1B $\not\!\!E_T$ data samples and also in a $t\bar{t} \rightarrow H^+ b\, H^- \bar{b}$ Monte Carlo data sample with $M_t = 175$ GeV/$c^2$and $M_{H^\pm} = 100$ GeV/c^2. The $\not\!\!E_T$ trigger requirement in the Monte Carlo is simulated using the parameterized $\not\!\!E_T$ trigger efficiency as described in Chapter 6. After preselection, 273,447 events remain from the Run 1 $\not\!\!E_T$ data.

5.10.2 Analysis Cuts

For all events passing the preselection criteria, all objects in an event are *uniquely* identified as described at the beginning of this chapter. The objects are identified in the order photon, electron, muon, tau and jet. If there is a second object identified within a cone of 10° of an already identified object then the second contending object is ignored. This is to avoid any ambiguities in describing an event as many calorimeter clusters with associated tracks will form electron, tau and jet candidates from the same detector quantities. The order of identification ensures clean tau identification. The *jet* category becomes a catch-all for any object that is not identified as something else but that has significant transverse energy and a pseudorapidity $|\eta| < 2$. All identified objects are also required to have a z-intercept within 5 cm of the event vertex. Photons and jets without a matching seed track are assumed to come from the event vertex.

Events are required to pass a set of tighter global event quantities before we apply the topology cuts described in Section 3.2. The missing transverse energy is recalculated using only the uniquely identified objects in the event. This quantity is labelled $\not\!\!E_T^{obj}$; it naturally corrects the $\not\!\!E_T$ for the presence of muons which are not included in the standard $\not\!\!E_T$ calculation where only calorimeter quantities are used. Also, since we are dealing with objects that have a transverse energy > 10 GeV, we are considering only the objects associated with the hard interaction and therefore $\not\!\!E_T^{obj}$ is less sensitive to multiple interactions. As shown in Appendix D, the event $\not\!\!E_T$ in the $t\bar{t}$ Monte Carlo samples does not represent the data very well. The $\not\!\!E_T^{obj}$ quantity models the data better and is less sensitive to the uncertainties in the underlying event simulation. We require $\not\!\!E_T^{obj} > 30$ GeV in addition to the original $\not\!\!E_T > 30$ GeV cut used in making the preselection sample.

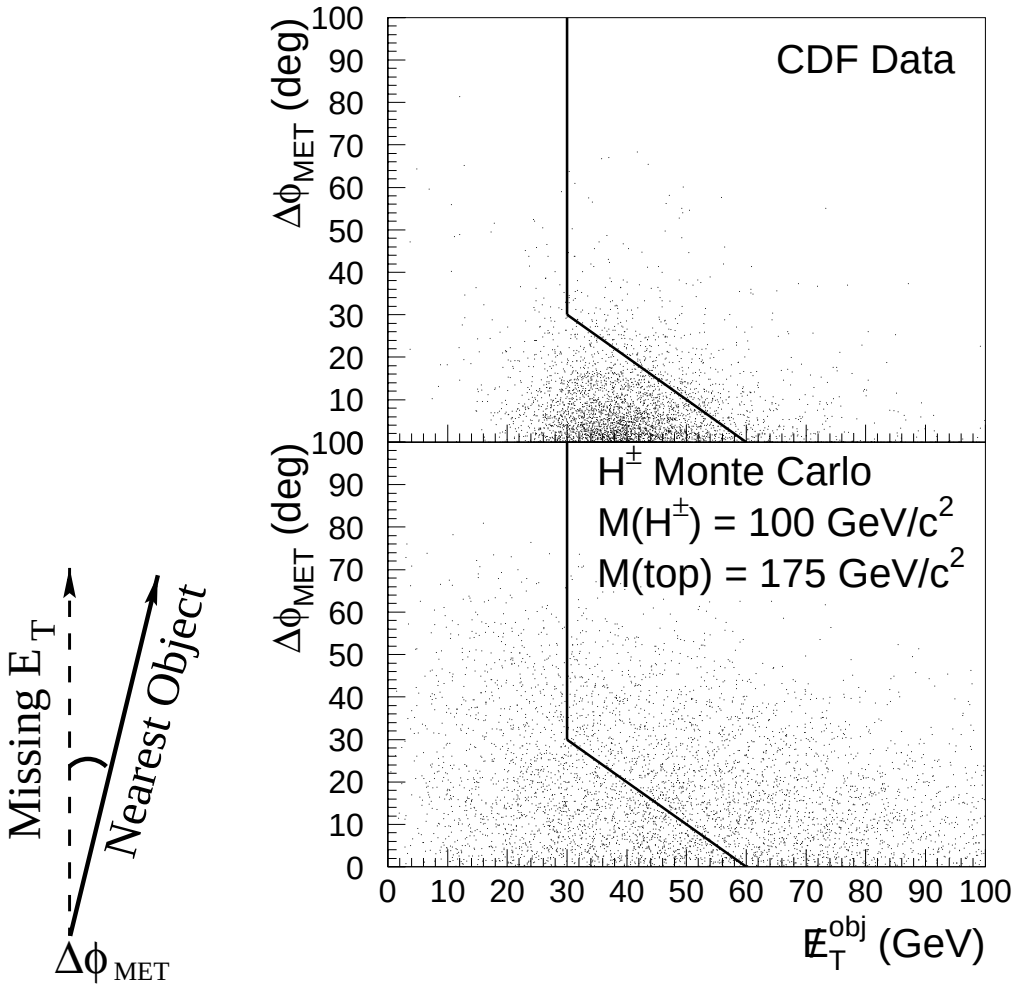

Figure 5.21: The minimum angle $\Delta\phi_{MET}$ between the $\not\!\!E_T^{obj}$ and an identified object in an event versus $\not\!\!E_T^{obj}$. The vertical line corresponds to the $\not\!\!E_T^{obj} > 30$ GeV cut and the diagonal line corresponds to $\Delta\phi_{MET} + \not\!\!E_T^{obj} = 60$.

To get the best separation of signal and background, we also impose a $\not\!\!E_T^{obj}$ isolation requirement which varies with the magnitude of $\not\!\!E_T^{obj}$. A selected event must satisfy

$$\Delta\phi_{MET} \left(\frac{\text{GeV}}{deg}\right) + \not\!\!E_T^{obj} > 60 \text{ GeV} \tag{5.6}$$

where $\Delta\phi_{MET}$ is the minimum angle in azimuth between the nearest uniquely identified object in the event and the direction of the $\not\!\!E_T^{obj}$ vector. Figure 5.21 shows the effect of this cut on the Run 1 $\not\!\!E_T$ data and a $t\bar{t} \to H^+ b\, H^- \bar{b}$ Monte Carlo. This diagonal cut in the $\Delta\phi_{MET}$–$\not\!\!E_T^{obj}$ plane maintains a fairly large acceptance for the charged Higgs sample while cutting significantly into the QCD background. This

isolation quantity is useful as it ensures a good $\not\!\!E_T$ measurement for lower values while regaining efficiency for larger values of $\not\!\!E_T^{obj}$.

We also apply a Z^0-boson mass cut ($75 < M_{ee,\mu\mu} < 105$ GeV/c^2) which removes any event that contains a pair of opposite-sign identified electrons (e^+e^-) or muons ($\mu^+\mu^-$) whose invariant mass is consistent with the Z^0 mass ($M_{Z^0} = 91.187 \pm 0.007$ GeV [8]). Figure 5.22 shows the invariant mass for a sample of opposite-sign electron and muon pairs from the CDF inclusive lepton data [202]. The peaks in both the ee and $\mu\mu$ invariant mass spectra are Z^0-boson decays to pairs of leptons. Note that the vertical scale is logarithmic so that very few events lie outside of the Z^0 mass window. We do not expect many events from leptonic Z^0-bosons decays but they could contribute background to the search channels, especially if produced in conjunction with another heavy vector boson (see Chapter 7). This cut actually has little marginal effect and is very efficient for the signal.

We now apply the topology cuts as described in Chapter 3 to the uniquely identified objects in the event. The τjjX + b-tag topology requires a leading tau of $E_T > 20$ GeV, two other identified jets of $E_T > 10$ GeV and at least one other object (which could be another tau or jet, or an electron or muon) also with $E_T > 10$ GeV. To reduce the QCD background further, we require at least one of the jets in the event to be b-tagged by the SECVTX algorithm as described in Appendix F.

For charged Higgs masses close to the top mass, there is less available kinetic energy for the b-quark decays; therefore the b-jets become soft and start failing both the E_T requirement and the b-tag requirements. To regain acceptance for these events, we also accept events with a *ditau* topology where we only require two energetic hadronically decaying taus of $E_T > 30$ GeV each that are not opposite each other in azimuth ($\Delta\phi_{\tau\tau} < 160°$). No other objects are required but the $\not\!\!E_T$ and $\not\!\!E_T^{obj}$ requirements still apply. Events passing the standard topology are excluded from this additional sample to ensure that this sample is entirely orthogonal to the sample satisfying the standard topology.

Figure 5.23 shows the distribution of ditau events in the $\not\!\!E_T$ data without the back-to-back or $\not\!\!E_T$ cuts applied. The one event in the signal region in this plot,

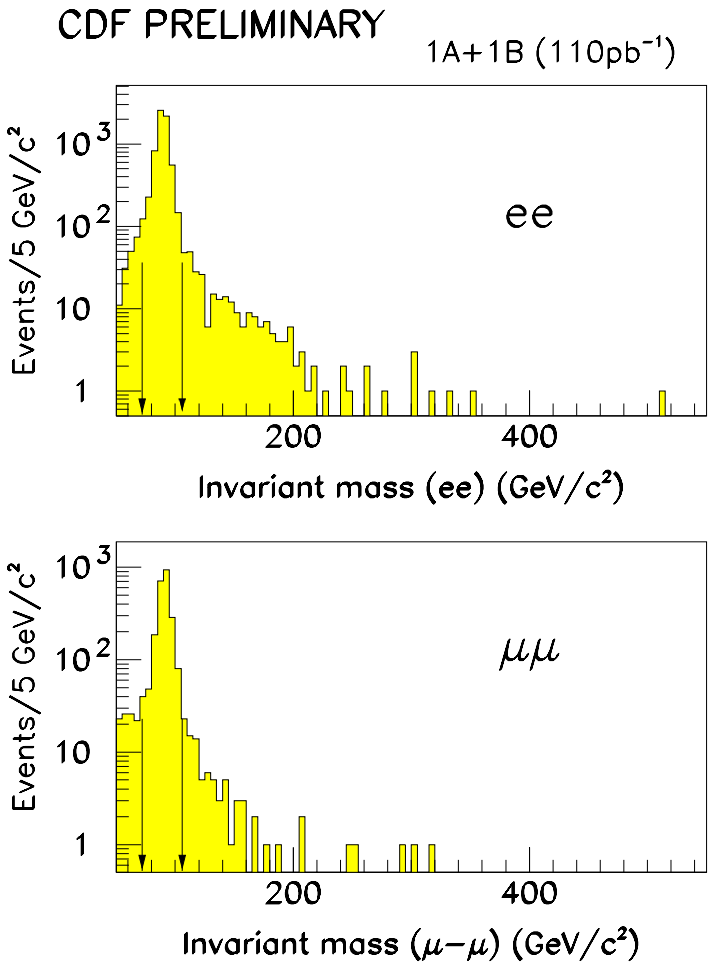

Figure 5.22: Invariant mass of opposite sign electron and muon pairs in the Run 1 inclusive lepton data. The Z^0-mass removal window of $75 < M_{ee,\mu\mu} < 105$ GeV/c^2 is the region between the two arrows.

which fails the back-to-back cut, is most likely a ditau Drell-Yan event. Also shown for comparison is the same distribution from a charged Higgs $t\bar{t} \rightarrow H^+b\,H^-\bar{b}$ Monte Carlo with $M_{H^\pm} = 160$ GeV/c^2. If the E_T requirement on both taus is relaxed to 10 GeV, then the expected number of background events is 4.9 ± 1.5 which agrees well with the observed 5 events.

Table 5.8 shows the numbers of events failing the preselection and final analysis cuts for the Run 1 $\not\!\!E_T$ data sets and a comparison $t\bar{t} \rightarrow H^+b\,H^-\bar{b}$ ISAJET Monte Carlo data set with $M_{H^\pm} = 100$ GeV/c^2 and $M_t = 175$ GeV/c^2. The numbers in parenthesis represent the marginal effect of the cut; that is, the number of events

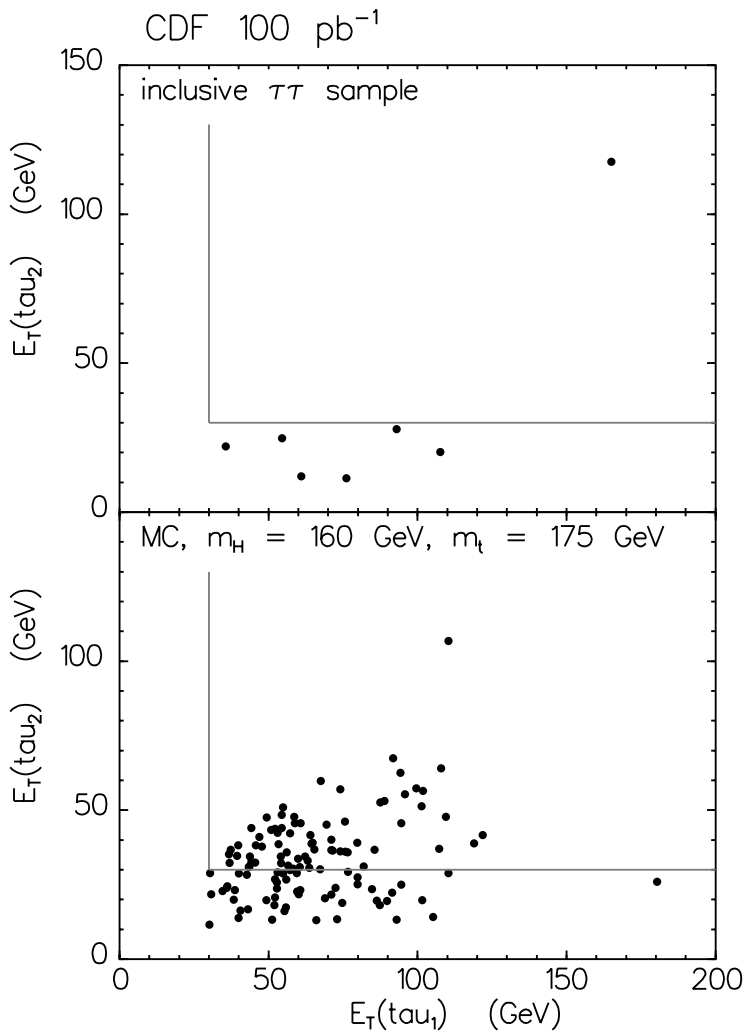

Figure 5.23: Distribution of ditau events with respect to the E_T cuts. The back-to-back and $\not\!\!E_T$ cuts have not been applied. The distribution from a charged Higgs Monte Carlo is also shown for comparison.

which fail *only* that cut. The cut requiring at least one tau does not have a marginal effect listed because it was considered part of the topology cut when applied.

From the Run 1 $\not\!\!E_T$ data samples, one event survives from Run 1A and six events from Run 1B. These all pass the τjjX topology with none passing the ditau topology. Except for one event with an electron as the fourth object (τjje), these are all $\tau + \geq 3$ jets events. The events and some of their kinematic properties are listed in Table 5.9. The kinematic and geometric information is also depicted in the transverse view in Figures 5.24 for the Run 1A event and in Figure 5.25 for the six Run 1B events.

	$\not\!\!E_T$ Sample					
	Run 1A		Run 1B		$t\bar{t} \to H^+ b\, H^- \bar{b}$ MC	
Initial sample	145732		528168		10000	
$\lvert z_0 \rvert < 60$ cm	9454	(3453)	40552	(17847)	349	(196)
$\not\!\!E_T > 30$ GeV	18913	(396)	8149	(892)	2355	(29)
$N_{\mathrm{TAUO}} \geq 1$	27260	(3679)	64343	(19282)	743	(439)
L2 Trigger	78417	(33728)	257071	(202364)	3377	(1186)
L3 Trigger	37542	(2745)	32321	(1729)	2365	(52)
After Preselection	53141		220306		5547	
$\not\!\!E_T^{obj} > 30$ GeV	3756	(0)	19392	(0)	209	(1)
$\not\!\!E_T^{obj}$ Isolation	41859	(0)	175623	(4)	1159	(56)
Z^0 Removal	6	(0)	32	(0)	4	(0)
$N_\tau \geq 1$	52599		217480		4288	
Topology	53098	(0)	220053	(3)	4704	(116)
b-tagging	51698	(19)	213828	(93)	3191	(373)
After All Cuts	1		6		291	

Table 5.8: Events failing the preselection and final analysis cuts for the Run 1A and Run 1B $\not\!\!E_T$ data and a comparison from an ISAJET $t\bar{t} \to H^+ b\, H^- \bar{b}$ Monte Carlo with $M_{H^\pm} = 100$ GeV/c^2 and $M_t = 175$ GeV/c^2. The numbers in parentheses are the number of events failing only this particular cut. The marginal effect is calculated separately for the preselection and analysis cuts.

Figure 5.26 also contains a CDF event display for the "Whopper". This is the event (`run 65769, event 446746`) with the largest E_T tau (173.8 GeV) in the final sample. Approximately 0.3 events are expected in the final sample from fakes with a tau lepton with $E_T > 150$ GeV (see Chapter 7) whereas only 0.02 events are expected from standard top production in this region (see Chapter 6). Therefore, although this event contains a good looking 1-prong tau decay, it is probably a hadronic fake.

		$\not\!\!E_T$	ΣE_T		E_T(GeV)					b-tag
Run	Event	(GeV)	(GeV)	N^{τ}_{trk}	τ	j_1	j_2	j_3/ℓ	N_{jets}	(N_{trk})
43097	31891	35.5	275.3	1	33.5	66.0	61.5	38.7	5	j_1 (2)
61024	476691	79.6	201.2	1	26.1	107.4	29.6	13.5	3	j_2 (4)
61592	636990	39.2	192.6	3	27.2	37.1	37.0	18.0	3	j_1 (4)
64934	416715	52.9	197.0	1	20.0	42.6	15.7	60.1e	2	j_1 (3)
65769	446746	83.8	312.9	1	173.8	67.0	13.0	11.6	3	j_1 (3)
67476	49890	39.7	149.7	3	41.4	57.0	38.9	16.4	4	j_2 (2)
67537	110744	42.4	194.2	3	26.4	82.4	24.4	19.0	4	j_4 (2)

Table 5.9: Properties of events passing all the analysis cuts.

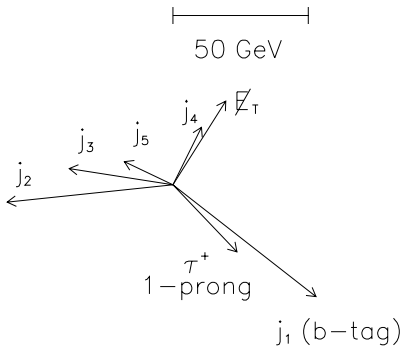

run 43097 event 31891

Figure 5.24: Depiction of the final selected event from Run 1A in the transverse view (r–ϕ). Lengths of the vectors are proportional to E_T of the objects.

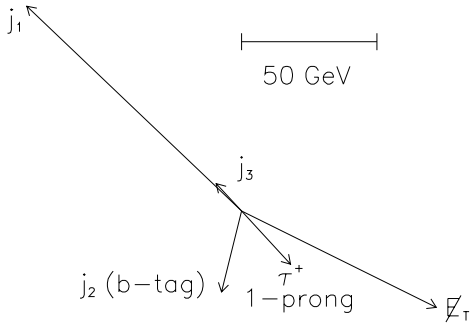

run 61024 event 476691

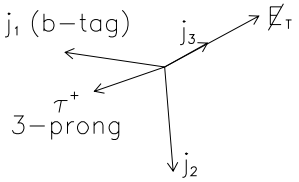

run 61592 event 636990

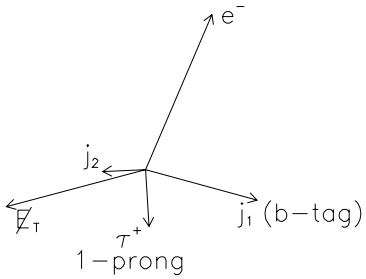

run 64934 event 416715

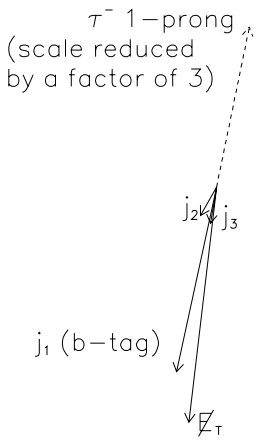

run 65769 event 446746

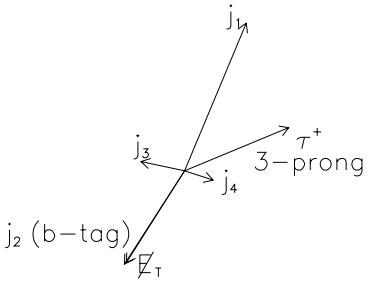

run 67476 event 49890

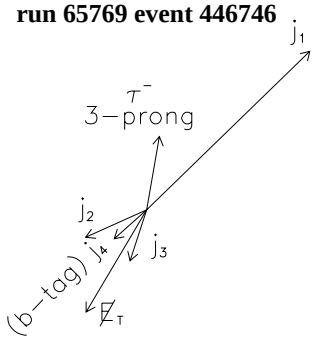

run 67537 event 110744

Figure 5.25: Depiction of the final selected events from Run 1B in the transverse view (r–ϕ). Lengths of the vectors are proportional to E_T of the objects.

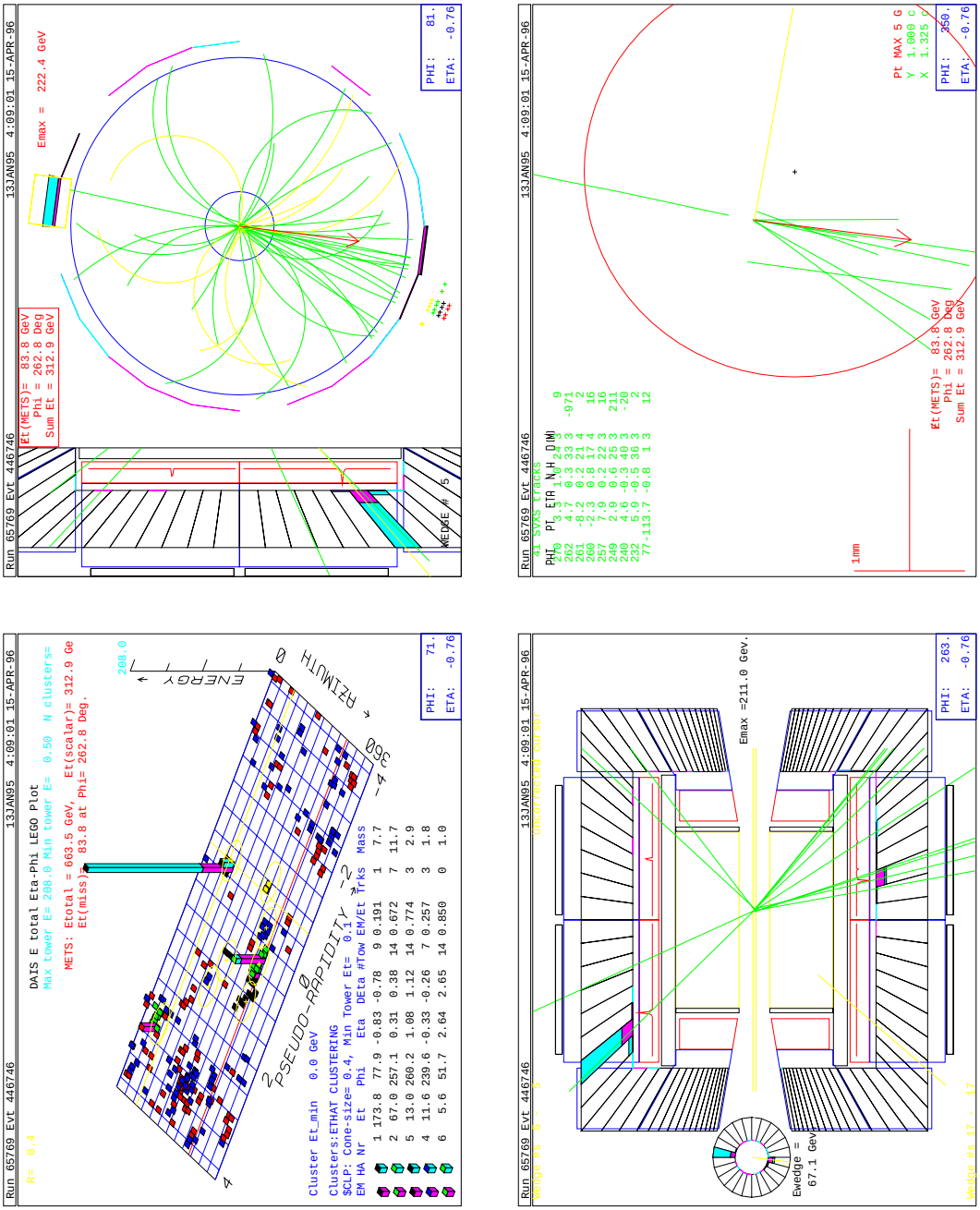

Figure 5.26: The event with the largest E_T tau in the final sample. The displays show, clockwise from the top left are: individual tower cluster energies in the calorimeters, a transverse end view of the central tracking chamber, a transverse end view of tracks in the SVX and a lateral view of tracks and energy deposits in the calorimeters.

Chapter 6

Signal Estimates

This chapter discusses the generation of simulated data used to make signal estimates, i.e. to understand what our acceptance is for top decays via a charged Higgs boson. Simulated data are also crucial for modelling of various background processes. This chapter discusses detection efficiencies for our signal. The generation of the data for background processes is discussed here also, with the actual calculation of the background contributions to the search signal deferred until the next chapter. The use of the simulated data for the investigation of particle identification efficiencies was discussed in Chapter 5.

A number of different Monte Carlo event generators are used to simulate the various physics processes of interest, namely: $W \to \ell\nu$ and $Z \to \ell\ell$ (where $\ell = e$, μ or τ), $t\bar{t}$ production with decays via $t \to W^+b$ and $t \to H^+b$, vector boson (W and Z) + jets production and diboson (WW, WZ, ZZ) production. In all the samples the tau leptons and b-quark hadrons are decayed in a consistent manner. The generated events are then processed by a detector simulation and by the same reconstruction algorithms as were used for the data. Minimum bias events are added to some of the top samples to simulate the multiple interaction environment.

6.1 Monte Carlo Simulations

A variety of Monte Carlo event generators have been implemented by many physicists around the world to simulate high-energy collisions between particles, using both the vast theoretical understanding and predictions of the Standard Model and the copious detailed experimental results available. These simulations have different strengths and weaknesses and do better or worse jobs of modelling particular physical

processes. Models of physics beyond the Standard Model have been incorporated into many of these simulations as well in order to make predictions about future experimental results. Feedback between theoretical and experimental input is used to fine-tune these simulations and they continue to improve over time.

To make predictions of high-energy hard-scattering processes using perturbative QCD calculations, two basic ingredients are needed: (i) the scattering cross sections involving the fundamental partons, leptons and gauge bosons which comes from the theory and are implemented in the Monte Carlo programs and (ii) the parton distributions inside the incoming hadrons. The knowledge of these universal *parton distribution functions* (PDF's) or *structure functions* is based on extensive experimental data from a variety of hard-scattering processes. These data have been incorporated into global analyses along with next-to-leading-order calculations of the subprocesses by the CTEQ[1] collaboration to produce universal fits to the PDF's [203, 204]. They provide a number of fits based on various theoretical assumptions and calculation techniques and these are incorporated in some of the Monte Carlo generator programs.

A number of these Monte Carlo event generators have been incorporated into the CDF software environment and we use these in the charged Higgs analysis in the diverse ways already specified.

At CDF, the primary event generators (discussed below) simulate a desired process and store the information in *generator level banks* (called GENP data banks) in the CDF YBOS data structure [167]. The information stored includes the complete decay chain with the 4-momentum, position, and parent and daughter information for each particle in the decay process. This information forms the basis for subsequent detector simulations. The generator level information also allows comparison with the simulated detector response to determine efficiencies, fake rates, etcetera.

The primary event generator used in the charged Higgs analysis for the $p\bar{p} \rightarrow t\bar{t}$ generation and subsequent decay is ISAJET version 7.06 [187]. ISAJET, written

[1] CTEQ stands for Coordinated Theoretical/Experimental Project on QCD Phenomenology and Tests of the Standard Model.

at Brookhaven National Laboratory, is based on perturbative-QCD calculations of leading-order matrix elements for the hard-scattering subprocess. Radiative corrections to the initial and final states are added in the leading-log approximation, giving incoherent gluon emissions. The outgoing parton and beam jets are fragmented independently using a phenomenological model. Partons, including the top quark[2], are fragmented into hadrons. ISAJET 7.06 correctly models the spin-correlations and subsequent decays via tau leptons of the vector (W,Z) and scalar ($H^{\pm}$) intermediate bosons.

We also also use ISAJET to simulate the production of dibosons — WW, WZ and ZZ — from $p\overline{p}$ collisions, where at least one of the vector bosons is forced to decay to a tau. This sample is used in the physics background estimates discussed in Chapter 7. Samples of $Z \rightarrow \ell\ell$ were also produced.

To provide some cross-checks of the event simulations, we use a second Monte Carlo generator, PYTHIA [188], written originally for CERN but updated to incorporate collisions of a variety of particle beams, including $p\overline{p}$. PYTHIA uses similar perturbative-QCD calculations for the hard-scattering subprocess as ISAJET and patron shower evolution to model the initial and final state radiation corrections. Parton fragmentation is carried out using the Lund string fragmentation model for the light quarks [205] and the Peterson fragmentation for the heavier quarks (c and b) [206]. We use version 5.7 which includes the correct polarization of W bosons from the top decay, and the default leading-order CTEQ2L structure functions [204]. PYTHIA incorporates top decays before any hadronization.

We use PYTHIA to generate $t\overline{t}$ and $Z \rightarrow \ell\ell$ processes, similar to those in ISAJET. The comparisons between the data generated by these two different generators is discussed in Section 6.2.

A third Monte Carlo generator employed at CDF for the simulation of a hard

[2]This means that even though the top quark is known to decay as a free spin-$\frac{1}{2}$ quark, ISAJET will decay it mostly as a spin-0 meson.

collision is HERWIG[3] [186]. Again the high-energy hard-scattering process is modelled via leading-order QCD matrix elements. One of HERWIG's strengths is its detailed simulation of the QCD parton shower evolution which include color coherence effects between initial and final states. This coherent color fragmentation model of HERWIG is also available (as the CDF routine HERPRT [207]) to fragment the partons into jets from purely matrix-element based Monte Carlo generators (such as VECBOS, discussed below). We use version 5.6 to simulate $W \to \ell\nu$ decays and in particular for $W \to \tau\nu$. These simulations were heavily used for the tau lepton asymmetry measurement [156].

VECBOS [208] is a parton-level-only Monte Carlo program based on tree-level matrix element calculations. It is used extensively at CDF for the generation of heavy intermediate vector boson (W and Z) processes along with higher order QCD processes that lead to jets and produces good agreement with the characteristics seen in the data [194, 209, 210, 211]. As VECBOS only performs the tree-level calculations, it provides only the four momenta of the partons involved in the scattering process along with the weight or probability for each event. The subsequent parton fragmentation and evolution and the rest of the underlying event (from the spectator partons) are added in via the HERPRT routines of HERWIG.

We use VECBOS to generate the W and Z + jets processes as part of the background estimate which is discussed further in Chapter 7.

6.1.1 Redecaying the Tau Leptons

Correct simulation of hadronic tau decays is critical to understanding their behavior in the detector. Taus are complicated particles; they are the only lepton that decays predominantly into hadronic decay products. Also, as there is at least one neutrino in the decay chain, it is impossible to capture all the tau decay products and hence some extrapolation and modelling is necessary to reconstruct the full tau decay.

All the event generators used in this analysis simulate the tau decays in slightly

[3]HERWIG stands for Hadron Emission Reactions With Interfering Gluons

τ Decay Mode	%
$\tau \to e\overline{\nu}\nu$	18.32
$\tau \to \mu\overline{\nu}\nu$	17.95
$\tau \to \rho(\to \pi\pi^0)\nu$	25.63
$\tau \to \pi\nu$	11.90
$\tau \to K\nu$	0.68
$\tau \to K^*\nu$	1.47
$\tau \to a_1(\to 3\pi)\nu$	18.33
$\tau \to \pi\pi\pi(\geq 1\pi^0)\nu$	5.72
Total	100.00

Table 6.1: Tau decay modes and branching fractions used in redecaying the taus in TAUOLA.

different ways. They tend to use different branching ratios and model the $\tau \to a_1\nu$ decays differently. There are also inconsistencies in how they handle the τ polarization.

To overcome these discrepancies, we redecay all the generated taus in the simulations using TAUOLA [212, 213, 214, 215]. TAUOLA is a software package designed to take the output of any event generator, before any detector simulation, and remove any tau decay products and redecay the tau taking into account the tau polarization (based on the parent particle) with up-to-date branching fractions. This package was adapted for use as a module in the standard CDF software by C. Loomis [216].

The tau decay branching fractions used in the redecay are shown in Table 6.1. These are based on those listed in the 1994 Review of Particle Properties [217]. The branching fraction to hadronic modes is 63.7% with 49.6% to one-prong hadronic decays and 14.1% to three-prong hadronic decays.

Using TAUOLA for all the simulated data samples allows us to consistently model the tau decays. One of the down sides however is that any spin correlation between τ's in the same event is lost. Also, the TAUOLA module has been implemented assuming that transverse polarizations can be ignored. Due to the relatively high-momentum taus that we deal with in this analysis, these limitations are not of major concern. The polarization of the resulting tau particle is set according to the parent particle; left-handed chirality for taus from W-boson decays and right-handed

chirality for taus from charged Higgs decays. For the isolated taus with no parents, used in detector studies, the chirality can be set by the user. We generated samples of single, isolated left- and right-chiral taus as part of the tau identification efficiency checks (see Section 5.2.3).

6.1.2 Redecaying the b-hadrons

A similar problem occurs for simulation of b-hadron decays. The modelling of b-quarks and their hadronization is still somewhat primitive in most generators and is implemented inconsistently. Instead, CDF has adopted a phenomenologically-based Monte Carlo generator from the CLEO collaboration, called QQ [218]. This package has been adapted for use at CDF (via the CLEOMC analysis control interface module [219]) to decay bottom and charm particles in Monte Carlo events. After an event is generated, CLEOMC removes all daughter particles from the event history that descend from the particle that is to be redecayed by QQ. Typically, this will be a B-meson; however, it is also possible to redecay primary charm particles, B-baryons or $b\bar{b}$-quarkonia (*bottomonia*). For the charged Higgs analysis we simulate all the possible b-decays: B-mesons ($B^{\pm}$, B^0, B_s^0 and $B_c^{\pm}$), bottomonia and B-baryons. We do not use the prompt charm decays.

6.1.3 Detector Simulation and Event Reconstruction

Once the simulated event in the generator format (GENP) is complete, the event is processed by a CDF detector simulation. The detector simulation uses the generator information as input and creates simulated CDF data banks for each event. There are two detector simulations in general use at CDF; QFL and CDFSIM [220, 221]. CDFSIM performs the detector simulation from first principles by tracking the flight of each long-lived particles and applying probabilistic scattering, interaction and decay processes in each detector element. This package has fallen out of favor due to the enormous time taken for this detailed simulation. Instead, QFL is used for all the simulated data in this analysis. We use version 3.59 of QFL, modified to include a simulation of the SVX′ detector (see Section 2.5.1).

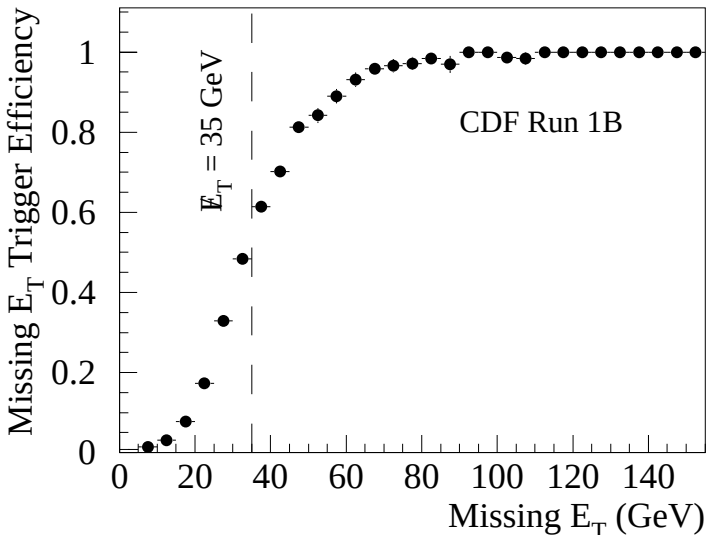

Figure 6.1: Parameterization of the Level 2 $\not\!\!E_T$ trigger efficiency.

QFL performs a fast simulation by using parameterizations of the detector response based on data. There are some known inefficiencies with this simulation. In particular, the modelling of the response and shower shapes of isolated pions in the calorimeters does not agree exactly with the data [222, 223]. There could be a concern that this might influence the simulation of one-prong hadronic tau decays. However, this effect is most pronounced for low-momentum (< 3 GeV/c) pions; we use very energetic taus ($E_T > 10$ GeV) so this should not be a problem.

The results of the detector simulation are then processed by the same reconstruction algorithm as used for data to reconstruct the event for analysis. This enables a direct comparison of the Monte Carlo event samples with the data using the same analysis software and cuts.

As mentioned before in Chapter 4, the online trigger efficiencies for the $\not\!\!E_T$ data set are not reproduced well in the Monte Carlo simulations. Hence we use the parameterized Level 2 $\not\!\!E_T$ trigger turn-on efficiency (shown in Figure 6.1) as derived in Appendix D. This is applied to the $t\bar{t}$ Monte Carlo data to effectively simulate the trigger response for the signal acceptance calculation.

For the top Monte Carlo samples where we require b-tagging, the event scale factor, $F_b = 0.85 \pm 0.06$, derived in Equation 5.5, is applied to the final number

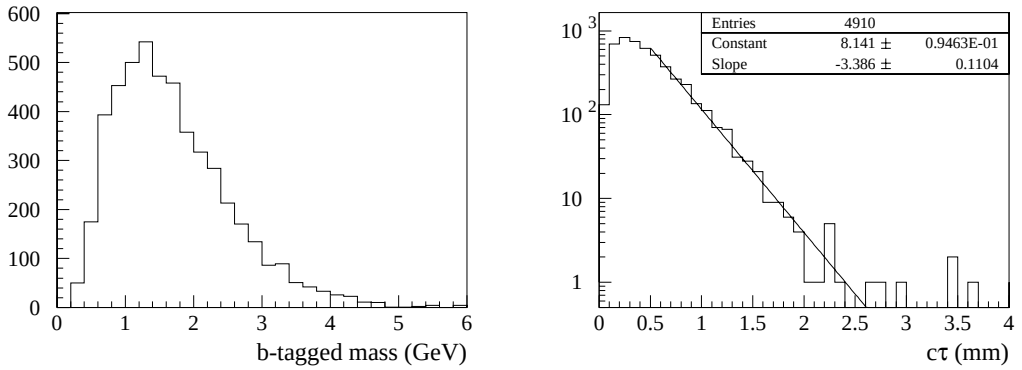

Figure 6.2: Mass and decay length ($c\tau$) of b-tagged jets in the $t\bar{t} \to H^+ b\, H^- \bar{b}$ sample with $M_{H^\pm} = 100$ GeV/c^2 and $M_t = 175$ GeV/c^2.

of events passing the b-tag requirements. This compensates for the known over-efficiency of simulated data as discussed in Section 5.9. Figure 6.2 shows the mass and decay length ($c\tau$) for a sample of b-tagged jets from a ISAJET $t\bar{t} \to H^+ b\, H^- \bar{b}$ sample with $M_{H^\pm} = 100$ GeV/c^2 and $M_t = 175$ GeV/c^2. The distributions look very similar to those found in the data (see Figure 5.18a) and give us confidence in the b-quark simulation.

For the Monte Carlo samples, only those events in which the reconstructed tau lepton matched a generated one within $\Delta R = 0.4$ were used. The contamination from events with jets faking a tau lepton are determined from data, as described in Chapter 7.

All of the final Monte Carlo samples were scaled to the integrated luminosity of the final data sample (99.8 ± 7.3 pb^{-1} — see Section 4.8).

6.1.4 Modelling the High Luminosity Environment

As the instantaneous luminosity at CDF was high enough to expect more than one $p\bar{p}$ interaction per bunch crossing, we would like this to be reflected in the simulated data as well, to see if there is any effect from the "pile-up" of interactions.

There is a software module MIXEVT [224] which takes a primary event (either from real or simulated data) and merges it with one or more secondary events. The event quantities such as calorimeter tower energies and hits in the various tracking

chambers (including the central muon chambers) are all merged correctly, enabling the recalculation of calorimeter clusters and reconstruction of tracks from the pattern recognition modules.

This technique is extremely useful in merging minimum bias events, i.e. events with soft inelastic $p\overline{p}$ collisions, into the Monte Carlo simulated data, which then models the multiple $p\overline{p}$ interaction environment. Secondary minimum bias events are added to give an average of 1.6 interactions per beam crossing, which corresponds to the average number of interactions per crossing over Run 1. We use minimum bias events recorded with a special prescaled trigger designed for this purpose. This allows a better modelling of the multiple interactions than using simulated data.

As we are working from the reduced PAD data sets however (see Section 4.5), there is no individual hit information stored for the tracking chambers, only the reconstructed tracks. Instead of retracking therefore, we merge the reconstructed tracks from the minimum bias data with those from the Monte Carlo event. The original primary vertices are maintained. This merging results in a slight over-efficiency in the track finding as the effect of the hit ambiguities cannot be included. This is not believed to be a problem, however, as over-efficient track finding tends to degrade the classification of jet clusters as hadronic taus since these objects will fail both the number-of-tracks cut in the tau cone and the requirement of no tracks in the isolation cone (see Section 5.2.2). At worst, this will lead to conservative estimates of the efficiency for the signal.

The b-tagging efficiency is not affected dramatically either, as we apply the correction scale factor (see Section 5.9) to the Monte Carlo data to correct for the over-efficiency of track finding.

The calorimeter tower information is stored in the PAD data (as TOWE banks) and MIXEVT allows us to share the calorimeter energies correctly and to recalculate the clusters.

Since the analysis is geared towards energetic objects from a hard scattering process, we do not expect that the additional interactions in the event, which tend to be much softer, will make any significant systematic contributions to the signal

process. Comparisons of the acceptance for ISAJET $t\bar{t}$ samples produced with and without minimum bias events added show no difference within the statistical uncertainties. There was also no difference seen in the tau identification efficiency studies, as discussed in Section 5.2.3.

6.2 Check of the Tau Simulation

The measurement of the tau identification efficiency in the various Monte Carlo samples was discussed in detail in Section 5.2.3. The question addressed here is the difference in the efficiencies in the ISAJET and PYTHIA top samples and how this might affect the overall signal estimates.

The difference between the reconstruction efficiencies for a hadronically decaying tau particle in the central region and with visible $E_T > 10$ GeV from the ISAJET and PYTHIA $t\bar{t}$ samples is shown in Figure 6.3. The one- and three-prong taus have been separated, and are shown as functions of E_T and pseudorapidity. The hadronic tau reconstruction efficiency in PYTHIA is about 20–25% more efficient than in the ISAJET sample, with not much variation over the kinematic or geometric range. The total hadronic tau reconstruction efficiency for these representative samples was $42.0 \pm 0.6\%$ for ISAJET and $52.8 \pm 0.5\%$ for PYTHIA [185].

From a comparison of the individual tau identification cuts in these two samples, the difference can be accounted for almost solely by the difference in the isolation cut efficiencies.

To understand how well the underlying event is modelled in the Monte Carlo data with regard to the tau isolation requirements, a comparison study in $Z \rightarrow ee$ data was performed by C. Loomis [225]. Here a $Z \rightarrow ee$ sample extracted from the Run 1B data is compared to simulated $Z \rightarrow ee$ samples generated by ISAJET and PYTHIA. We use electrons because of their high identification efficiency and because the Monte Carlo generators should, in principle, reproduce the electron clusters well.

To make up the $Z \rightarrow ee$ sample, an event with a central ($|\eta| < 1$) electron is selected from the Run 1B inclusive electron sample using the identification cuts as

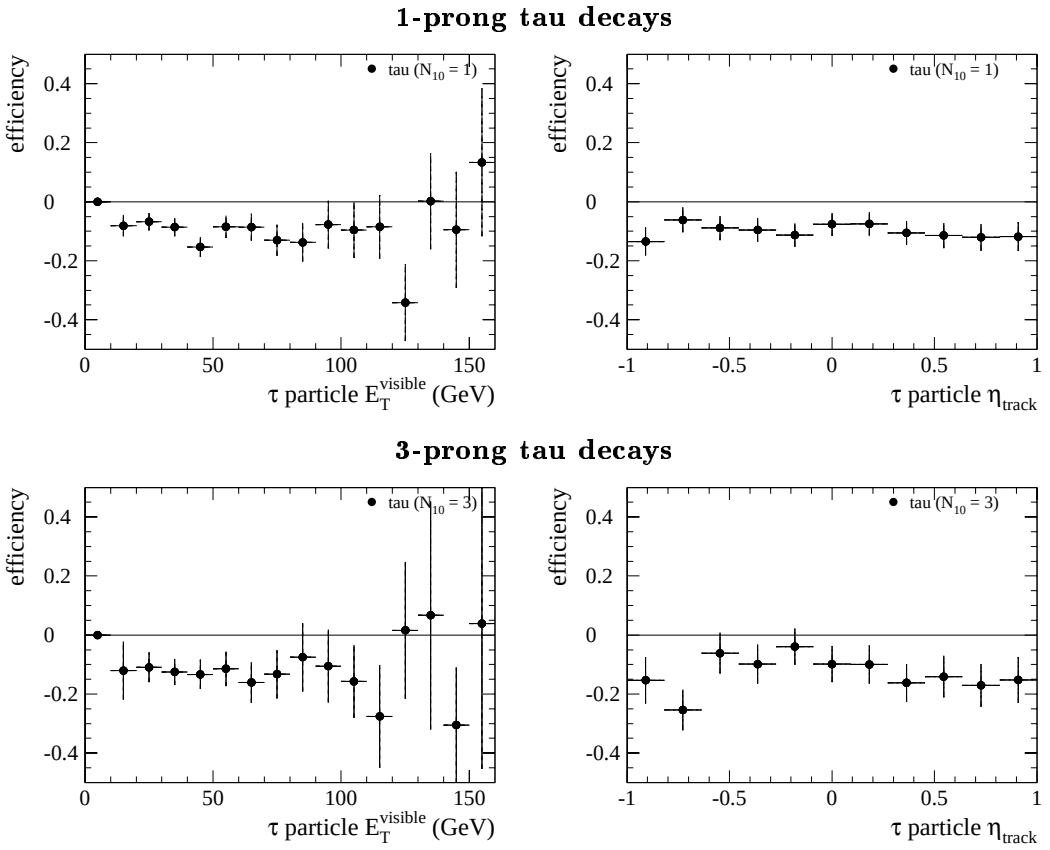

Figure 6.3: Difference in the fraction of hadronically decaying tau particles reconstructed as a tau object with one-prong (top plot) or three-prongs (bottom plot) between ISAJET and PYTHIA $t\bar{t} \rightarrow H^+b\,H^-\bar{b}$ Monte Carlo samples. These samples were generated with $M_{H^\pm} = 100$ GeV/c^2 and $M_t = 175$ GeV/c^2.

described in Section 5.4. The Top Group's fiducial cut is also applied to select good electron candidates — this corresponds to their "tight" electron cuts. All central tracks that have $p_T > 15$ GeV/c, a z-intercept that is within 5 cm of that of the electron and that form an invariant mass with the central electron of $40 < M < 140$ GeV/c^2, are saved. For each of these tracks, two isolation variable are saved: α, the angle to the next nearest track with $p > 1$ GeV/c and $I_{trk} = \sum p_T$ of all the tracks within a 0.4 cone around the track under consideration.[4] In the tau identification, the isolation requirement corresponds to $\alpha > 30^\circ$ (see Section 5.2.2).

The first check is how well the Monte Carlo samples do in reproducing the ratio

[4]The I_{trk} variable is a similar isolation quantity to I_{cal} which measured isolation in the calorimeter. The tau dilepton top analysis (looking for $\tau + e$ or μ) used an absolute track isolation cut of $I_{trk} < 1$ GeV/c [75].

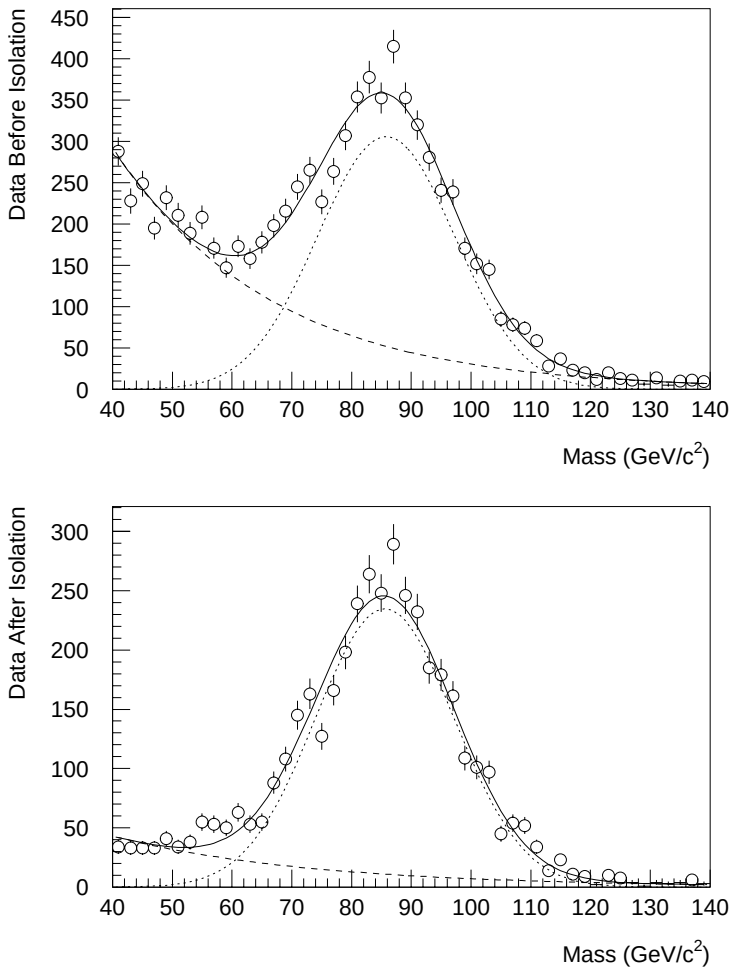

Figure 6.4: Invariant mass distributions in the Run 1B $Z \rightarrow ee$ data before and after the angle isolation requirement. The solid line is the fit of the sum of a Gaussian (dotted) and an exponential (dashed).

of the number of $Z \rightarrow ee$ events before and after the isolation cuts in comparison to the data. To determine the number of $Z \rightarrow ee$ events in the data, the invariant mass distribution is fitted to the sum of a Gaussian and an exponential. Figure 6.4 shows the fit for the data before and after the angle isolation cut. The number of events in the fit Gaussian is taken as the number of Z's for the data. No background subtraction needs to be made for the Monte Carlo samples as only tracks associated with the generated electrons are used.

The efficiencies for the isolation requirements in the data and the Monte Carlo samples are determined by the number of $Z \rightarrow ee$ events that pass either the $\alpha >$

	Number of $Z \rightarrow ee$			Efficiency(%)		Difference (%)	
sample	No cuts	Angle	Sum p_T	Angle	Sum p_T	Angle	Sum p_T
DATA	4396	3415	3616	78±3	82±3		
ISAJET	6135	5019	5177	82±1	84±1	5±4	2±4
PYTHIA	5513	4801	5035	87±1	91±1	12±4	11±4

Table 6.2: Number of $Z \rightarrow ee$ events before and after isolation cuts, efficiency of the isolation requirements and difference in efficiencies between data and Monte Carlo generated samples.

30° isolation cut or the $I_{trk} < 1$ GeV/c cut. The number of Z events from each sample, before and after the isolation cuts, and the calculated efficiencies are shown in Table 6.2. The error on the number of Z's in the data is approximately 5% which includes both the uncertainties of the fit and the statistics. The difference between the efficiencies in the Monte Carlo samples and the data are also shown.

While the significance of the differences in the last column are marginal, both Monte Carlo samples seem to be systematically more efficient than the data. Of the two generated samples, ISAJET more accurately reflects the isolation efficiency of the data.

The percentage difference between the data and the Monte Carlo samples is a reasonable estimate of the systematic uncertainty of the tau identification efficiency for the two Monte Carlo programs. This is $\sim$ 5% for ISAJET and $\sim$ 10% for PYTHIA.

The distributions of the isolation variables can also be compared, although this is of secondary importance compared to the absolute efficiency. Again, to recover the $Z \rightarrow ee$ signal from the background in the data sample a fit to a Gaussian and exponential for the invariant mass is used where the peak ($80 < M < 100$ GeV/c^2) and sideband ($M < 80$ and $M > 100$ GeV/c^2) regions are fitted (see Reference [225] for details). Figure 6.5 compares the isolation variables for the data and Monte Carlo samples. The distributions have been normalized to unit area so that the shapes can be compared.

For the isolation angle plot, the lowest bin (which is negative) shows evidence of

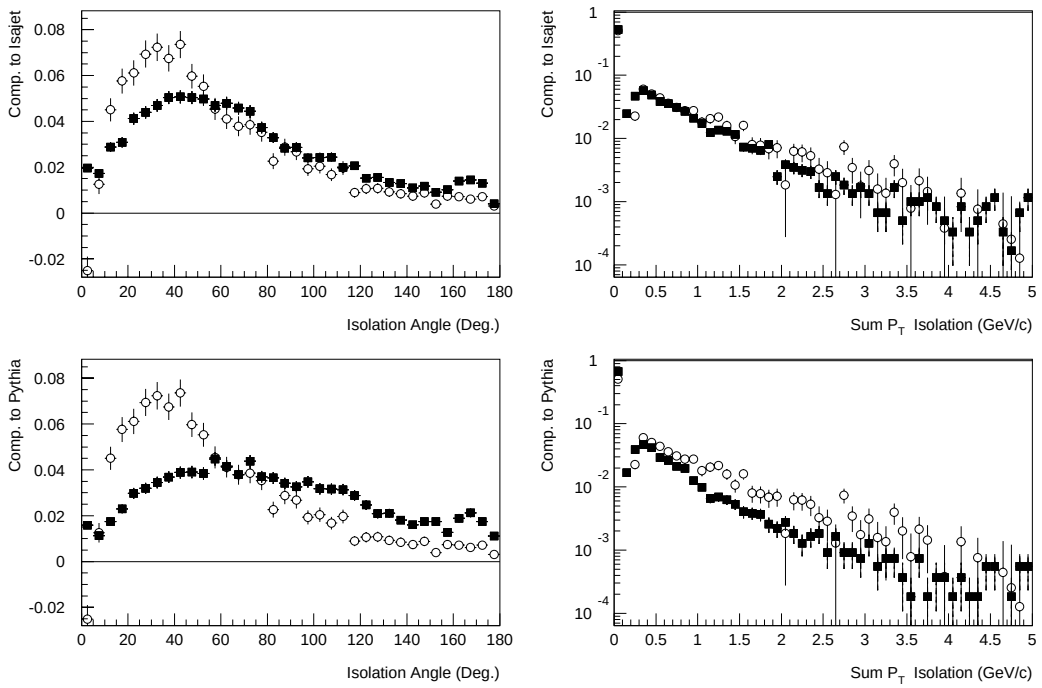

Figure 6.5: The distribution of (left) the isolation angle, α, and (right) the sum p_T isolation, I_{trk}, for the $Z \rightarrow ee$ data (open circles) and Monte Carlo samples (solid squares). ISAJET is compared in the upper plot and PYTHIA in the lower one. All distributions have been normalized to unit area.

overcorrection of the signal distribution. Neither Monte Carlo sample reproduces the shape of the data well. The general shape of the ISAJET distribution is in slightly better agreement with the data.

The agreement between the data and Monte Carlo samples is again not optimal in the sum p_T isolation distribution plot, especially at the high end. Here ISAJET also seems to be model the data a little better.

We use ISAJET to make the final signal estimates and assume a systematic uncertainty of 10% on the tau lepton identification, based on the above studies. In the next chapter, a comparison is made of the absolute number of taus expected in the Run 1 $\not\!\!E_T$ data compared to the number predicted from the Monte Carlo simulation of the background processes, for cuts tightened to enhance a $W+ \geq 3$ jets signal. This concurs with a 10% systematic uncertainty for the tau identification in simulations (see Figure 7.14).

6.3 Acceptance for the Charged Higgs Signal

As described in Chapter 3, this analysis is sensitive to charged Higgs boson production and decay in the region of $\tan\beta > 1$. The branching fraction for top quarks decaying via charged Higgs only becomes substantial for $\tan\beta \gtrsim 5$. In this region, the branching fraction for $H^+ \to \tau^+\nu$ is essentially 100%. Therefore we only need simulate top decays via the Standard Model mode ($t \to W^+b$) or via charged Higgs bosons with the Higgs decaying subsequently to a tau and neutrino ($t \to H^+b$, $H^+ \to \tau^+\nu$).

To estimate the acceptance for the analysis cuts for these various top decays, a linear combination of three ISAJET Monte Carlo samples is used. They all simulate $p\overline{p} \to t\bar{t}$. The first sample has both top quarks decaying to charged Higgs bosons ($t\bar{t} \to H^+b\,H^-\bar{b}$) and the second sample has one top quark decaying to a charged Higgs boson and the other to a W boson ($t\bar{t} \to W^+b\,H^-\bar{b}$ or $t\bar{t} \to H^+b\,W^-\bar{b}$). The charged Higgs is forced to decay into a tau lepton ($H^+ \to \tau^+\nu$); the W decays are unconstrained. The third sample contains events with both top quarks decaying into W bosons (i.e. standard top decay $t\bar{t} \to W^+b\,W^-\bar{b}$), again with the W decays unconstrained.

A range of charged Higgs masses was generated for the samples containing a charged Higgs decay: $M_{H^\pm}$ = 40, 60, 80, 100, 120, 140, 160, 165 and 168 GeV/c^2. This analysis was started before the firm discovery of the top quark. Therefore a range of different top masses was generated as well: M_t = 135, 155, 175, 185 and 195 GeV/c^2. Since the discovery of the top quark and the relatively precise measurement of its mass by both CDF[5] and DØ, we only use the M_t = 175 GeV/c^2 data to set limits. Signal acceptances and limits for the other generated top masses can be found in Reference [226].

For each (M_t, $M_{H^\pm}$) mass-pair combination, 10,000 events were generated in each of the three possible combinations ($t\bar{t} \to H^+b\,H^-\bar{b}$, $t\bar{t} \to W^+b\,H^-\bar{b}$, $t\bar{t} \to H^+b\,W^-\bar{b}$). The W^+H^- and W^-H^+ cases are combined and are referred to as $t\bar{t} \to W^+b\,H^-\bar{b}$. For the SM $t\bar{t} \to W^+b\,W^-\bar{b}$ case, where there is no $M_{H^\pm}$ dependence, 50,000 events

[5] the best result from CDF is in the lepton + jets channel: $M_t = 175.9 \pm 4.8 \pm 4.9$ GeV/c^2 [80].

$M_{H^\pm}$	$t\bar{t} \to H^+ b\, H^- \bar{b}$		$t\bar{t} \to W^+ b\, H^- \bar{b}$	
(GeV/c^2)	Standard	Ditau	Standard	Ditau
40	2.13 ± 0.13	0.10 ± 0.03	1.12 ± 0.07	0.02 ± 0.01
60	2.07 ± 0.13	0.05 ± 0.02	1.19 ± 0.07	0.02 ± 0.01
80	1.98 ± 0.13	0.13 ± 0.04	1.28 ± 0.07	0.00 ± 0.00
100	2.52 ± 0.14	0.12 ± 0.03	1.44 ± 0.08	0.01 ± 0.01
120	2.21 ± 0.14	0.20 ± 0.04	1.48 ± 0.08	0.00 ± 0.00
140	1.72 ± 0.12	0.48 ± 0.07	1.59 ± 0.08	0.05 ± 0.02
160	0.42 ± 0.06	0.64 ± 0.08	1.21 ± 0.07	0.04 ± 0.01
165	0.09 ± 0.03	0.68 ± 0.08	1.02 ± 0.07	0.03 ± 0.01
168	0.07 ± 0.02	0.66 ± 0.08	1.02 ± 0.07	0.05 ± 0.02

$t\bar{t} \to W^+ b\, W^- \bar{b}$	
Standard	Ditau
0.22 ± 0.02	0. ± 0.

Table 6.3: Acceptance for the ISAJET $t\bar{t}$ Monte Carlo samples with M_t = 175 GeV/c^2, in the τjjX (standard) and ditau channels, given as a percentage of the number of generated events.

were generated.

The generated data were run through the analysis discussed in Chapter 5. The effect of the analysis cuts on a $t\bar{t} \to H^+ b\, H^- \bar{b}$ sample was shown in Table 5.8 as an example. Table 6.3 shows the acceptance of the τjjX and ditau topologies for each generated sample. These are calculated from the number of events that pass the analysis cuts divided by the number generated in the sample. In calculating the acceptance, we only use tau objects that match an underlying generated hadronically decaying tau particle.

As expected (see Section 3.2) the acceptance in the τjjX channel drops as the Higgs mass approaches the top quark mass. The ditau analysis is efficient only in this region.

Figure 6.6 graphically presents the acceptances for both channels as a function of the generated Higgs mass. It is obvious here that the fall-off in the τjjX channel at high $M_{H^\pm}$ is somewhat compensated for by the ditau channel. These acceptances are used later in Chapter 8 to set limits.

Running a few samples of the PYTHIA $t\bar{t}$ Monte Carlo events generated with the

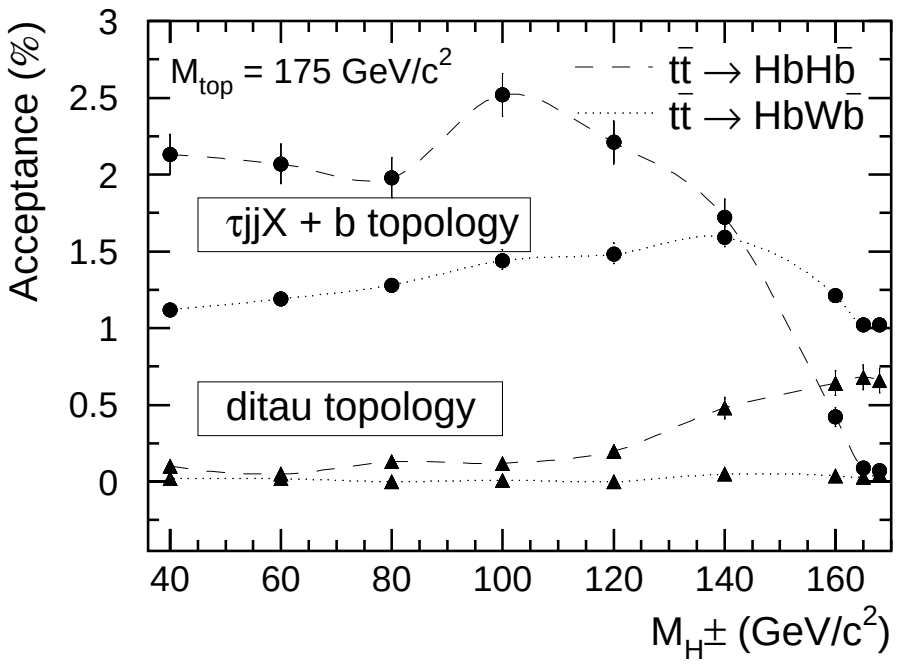

Figure 6.6: Acceptance for the two search topologies in $t\bar{t} \to H^+b\,H^-\bar{b}$ and $t\bar{t} \to W^+b\,H^-\bar{b}$ ISAJET Monte Carlo data. $M_t = 175$ GeV$/c^2$ for the simulations. Error bars indicate statistical uncertainties only. The acceptance for $t\bar{t} \to W^+b\,W^-\bar{b}$ (not shown) is $0.22 \pm 0.02\%$ in the τjjX topology, independent of $M_{H^\pm}$.

same masses as those in the ISAJET case tends to give higher overall acceptances on the order of 10%, with a somewhat better acceptance in the ditau case. This is consistent with the observed better efficiency for hadronic tau decays seen in the PYTHIA $t\bar{t}$ samples compared to those from ISAJET.

6.4 Systematic Uncertainties in the Signal Estimates

As we are performing a counting experiment, the detailed differences in the uncertainties at each generated mass point are less important than the overall trend. Also, the interplay between the two search topologies tends to nullify the systematic effects at different generated masses, as is shown below. We therefore calculate a global systematic uncertainty on the acceptance for all the generated mass points.

One of the major uncertainties in the Monte Carlo simulations is in the modelling of the higher order radiative effects of gluons off the initial and final state partons. To

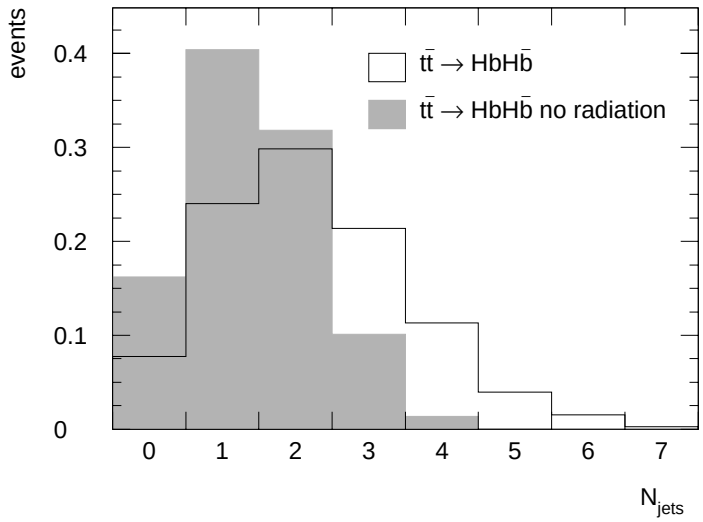

Figure 6.7: Number of jets in an event from a ISAJET Monte Carlo $t\bar{t} \rightarrow H^{+}b\,H^{-}\bar{b}$ sample with $M_t = 175$ GeV/c^2 and $M_{H^{\pm}} = 160$ GeV/c^2 with (open) and without (shaded) gluon radiation. Both histograms have been normalized to unit area.

estimate this uncertainty, samples of ISAJET $t\bar{t}$ were generated with the threshold for radiative decays set to the beam energy (900 GeV). This effectively cuts off any radiation.

Figure 6.7 shows the relative number of jets in an event in for a $t\bar{t} \rightarrow H^{+}b\,H^{-}\bar{b}$ sample (with $M_{H^{\pm}} = 160$ GeV/c^2) with and without gluon radiation. On average, there are far fewer jets in an event without gluon radiation.

Figure 6.8 compares the transverse energies for the identified objects in these two samples. The average tau E_T is higher and the average number of events with one or more identified taus is 25% higher in the case with no radiation. The tau identification is enhanced as there is less "contamination" from gluon jets which could leave tracks in the tau isolation cone. Fewer jets in an event also decreases the chance of a jet accidentally overlapping and obscuring a tau. This higher efficiency for identifying taus enhances the acceptance of the ditau topology; about 30% (50%) more taus pass the primary (secondary) ditau requirements.

The $\sum E_T$ and $\not\!\!E_T$ (not shown) are peaked a little lower in the no radiation case which will tend to decrease the τjjX topology acceptance. The average jet energy in an event also peaks at lower values, especially for the second and subsequent jets

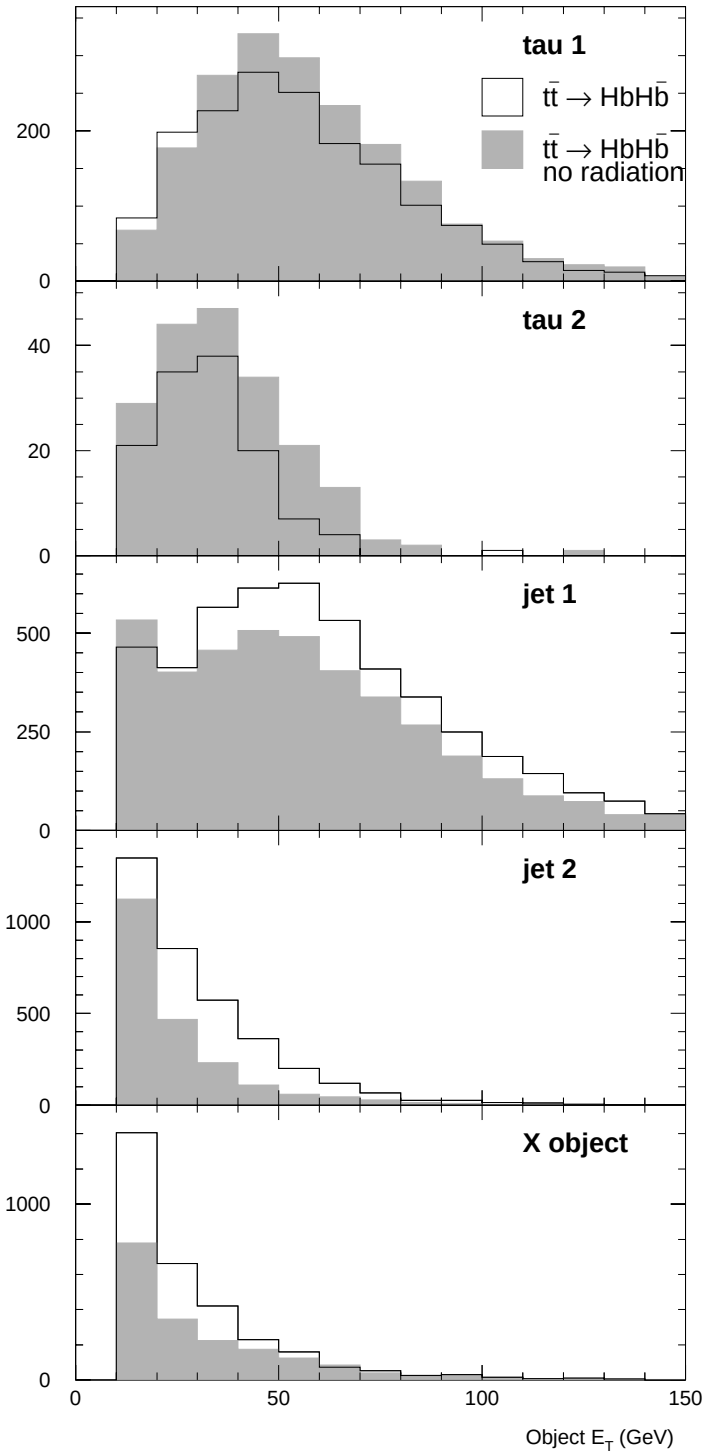

Figure 6.8: Distributions of transverse energy for identified objects in ISAJET Monte Carlo $t\bar{t} \rightarrow H^+ b\, H^- \bar{b}$ samples with $M_t = 175$ GeV/c^2 and $M_{H^\pm} = 160$ GeV/c^2 with (open) and without (shaded) gluon radiation.

Level 2 $\not\!\!E_T$ trigger efficiency	10%
Tau identification efficiency	10%
b-tagging efficiency	10%
Gluon radiation uncertainty	10%
Energy scale uncertainty	10%
Monte Carlo statistics	8%
Integrated luminosity	7.3%
Total	25%

Table 6.4: Systematic uncertainties on the signal acceptance calculation. The total is summed in quadrature.

in an event. About 27% more taus pass the tau topology requirements but 10% fewer primary jets and 35% fewer other jets pass the jet topology requirements. The b-tags also drop by about 25%.

The acceptance gains in the ditau channel tend to be almost exactly counteracted by the losses in the τjjX channel. Combined, the overall efficiencies decrease by 17%. A similar check in samples generated with $M_{H^\pm} = 140$ GeV/c^2 gives an overall 5% decrease. Half the difference in the $M_{H^\pm} = 160$ GeV/c^2 case rounded to 10% is used as the systematic uncertainty on the modelling of the gluon radiation. This was also checked in samples where the radiation threshold was raised and lowered by factors of two and one-half, respectively. The change in the acceptance in each case was again at most 10%.

The fluctuations in the calorimeter response to incident particles is modelled in the QFL detector simulation, based on measurements in test beams. We raised and lowered the energy response in the detector simulation by one standard deviation (based on the test beam measurements) for samples of generated $t\bar{t}$ events. At most, this resulted in an overall 2–4 GeV shift in the average energy of the identified objects. This corresponds to about a 5% shift in energy for the primary taus and about 10% shifts for the other objects.

Raising the energy response — the effect of which is to deposit more energy in the calorimeters per particle — raised the signal acceptances by at most 5% and lowering the response lowered the efficiencies by at most 20%. Lowering the response

has the larger effect as objects at the threshold of the topology requirements will fail. The energy response has a more dramatic effect on the τjjX acceptance as well, since it relies on more objects being over threshold than the ditau topology. Half the difference between raising and lowering the response is taken as the systematic uncertainty. On average this is about 10%.

Table 6.4 lists all sources of systematic uncertainties going into the signal acceptance calculation. The uncertainty based on the limited Monte Carlo statistics is 8%. All the uncertainties have been estimated from the simulated data, except for the uncertainty on the integrated luminosity which is needed to rescale the Monte Carlo data. Summed in quadrature, the total uncertainty is 25%.

Chapter 7

Background Estimates

Before we can make statements about how many signal events might be in the data after all the selection and analysis cuts, we need to determine what other physics processes could contribute events. These are termed background.

There are two main sources of background for this analysis — those with real hadronic tau decays and those with a fake identified tau lepton. These backgrounds are estimated independently.

The major source of events with a real *isolated* energetic tau lepton is from the decays of the heavy vector bosons, W and Z (see Figure 3.6). We simulate electroweak processes with a W or Z decay (with additional jets) and diboson production (WW, WZ, ZZ) to estimate the background contributions, discussed in Section 7.1 below.

Contributions from other tau lepton sources are estimated to be negligible. Processes such as the semileptonic bottom quark decay $b \to c\tau\nu$ tend to "dress-up" the tau with the charm decay products, hence these taus fail the isolation requirements.

The dominant source of background is from fakes where a hadronic jet in QCD processes is identified as a tau lepton. We determine the number of events we expect from such fake tau leptons directly from our data sample in Section 7.3.

Standard Model top quark decays ($t\bar{t} \to W^+ b\, W^- \bar{b}$) are part of the signal for this analysis and are therefore not considered as background.

7.1 Background from Electroweak Decay Processes

Simulated events from the electroweak processes $p\overline{p} \to W(Z) + \geq n$ jets were generated with the VECBOS Monte Carlo; an underlying event was added using the

HERWIG Monte Carlo, as described in Section 6.1. HERWIG also simulates the parton shower. The generation used the $\langle p_T^2 \rangle$ for the renormalization and factorization scales, where $\langle p_T \rangle$ is the average p_T of the generated partons. The minimum p_T for the jets was 8 GeV/c. The CTEQ3M structure functions [203] were used.

We only generated the decays $W \to \tau\nu$ and $Z \to \tau^+\tau^-$. To avoid double counting background from fake tau leptons, only those Monte Carlo events in which the reconstructed tau lepton matches a generated one within a $\Delta R = 0.4$ cone are used. For such an event to have a chance of passing the τjjX analysis cuts, there need to be three (two) other jets in the event for the W (Z) case. We therefore use the $W + \geq 3$ jets and $Z + \geq 2$ jets samples to estimate the background contributions to this channel.

In the ditau channel we use the $W(Z) + \geq 1$ jet samples to estimate the backgrounds. The $Z + 0$ jets contribution is negligible due to the back-to-back cut in azimuth on the ditau pair (see Section 3.2). There are background contributions only when there is one or more recoiling jet with the Z, giving the tau decay products a boost in azimuth such that they are not back-to-back.

The inclusive cross sections $\sigma(p\overline{p} \to W/Z + \geq n \text{ jets})$ for $n = 0$ to 4 jets have been measured at CDF using $W \to e\nu$ and $Z \to e^+e^-$ decays by a group of CDF collaborators at Duke University [227, 194, 211]. They compare the predictions from VECBOS QCD Monte Carlo[1] to the experimental measurements and derive correction factors (known as "R-factors") which estimate the corrections needed for normalizing the predicted cross sections from the Monte Carlo data.

The measured cross sections and corrections factors are shown in Table 7.1. Figure 7.1 shows these cross sections graphically in a plot of the measured cross sections for $W/Z + \geq n$ jets as a function of n; the superimposed band shows the predictions resulting from variations in the renormalization scale, Q^2, from $\langle p_T^2 \rangle$ to $M_V^2 + p_{T_V}^2$ (where $V = W$ or Z), in the Monte Carlo simulations.

To normalize the Monte Carlo data in the tau lepton simulations, we assume

[1] with similar parton distribution functions and renormalization and factorization scales as we used.

Process	$\sigma \cdot \mathcal{B}$ (pb)	R-factor
$W + \geq 0$ jets	2490 ± 120	
$+ \geq 1$ jet	471 ± 57	1.28 ± 0.16
$+ \geq 2$ jets	101 ± 19	0.90 ± 0.17
$+ \geq 3$ jets	18.4 ± 5.3	0.67 ± 0.20
$+ \geq 4$ jets	3.1 ± 1.4	0.53 ± 0.25
$Z + \geq 0$ jets	231 ± 13	
$+ \geq 1$ jet	45.2 ± 5.8	1.29 ± 0.17
$+ \geq 2$ jets	9.7 ± 1.9	0.92 ± 0.19
$+ \geq 3$ jets	2.03 ± 0.56	0.83 ± 0.24
$+ \geq 4$ jets	0.43 ± 0.17	

Table 7.1: Inclusive cross sections $\times$ branching fractions to electron decay modes and R-factors for heavy vector boson + jets production. The R-factors are calculated from $\sigma_{data}/\sigma_{MC}$.

lepton universality, which implies $\mathcal{B}(W \to e\nu) \equiv \mathcal{B}(W \to \tau\nu)$, and use the correction factors derived using the $Q^2 = \langle p_T^2 \rangle$ renormalization. The only background contribution comes in the ditau channel; we expect 1.3 ± 1.3 events from W + jets and 0.6 ± 0.3 events from Z + jets. Only the statistical uncertainties are included. The background contributions to the charged Higgs search for all processes are summarized in Table 7.2.

7.2 Background from Dibosons

Diboson production was simulated with ISAJET, which includes tree-level processes for WW, WZ, and ZZ production (see Section 6.1). In the generation, one boson was required to decay to leptons; the other was unconstrained. Forcing one boson to decay leptonically in the generation, reduces the accepted cross sections for these processes to about a third of the total diboson production cross section.

Diboson production is very sensitive to trilinear boson-couplings (e.g. WWZ vertices). No deviations from SM expectations have been observed in experiments [228]. We therefore use the SM cross sections predicted for these processes to normalize the generated samples to our data set.

The standard model cross sections for $p\overline{p} \to WW$, WZ, and ZZ have been

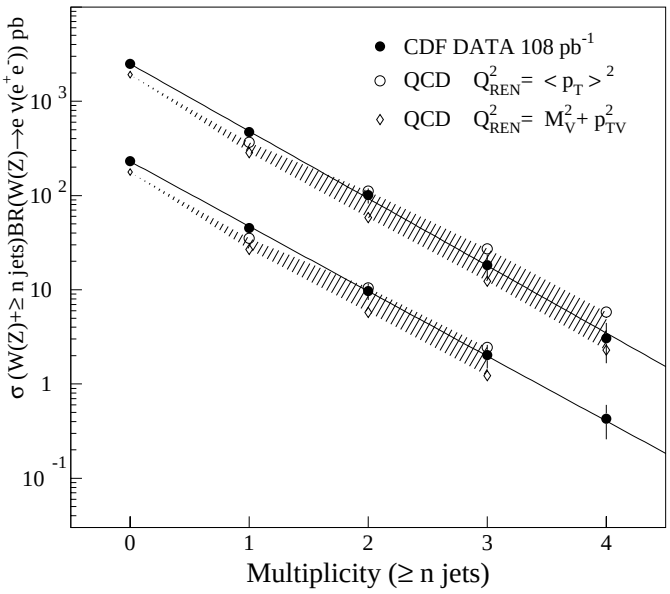

Figure 7.1: Measured cross sections compared to theory from CDF Run 1 data for heavy vector boson production with jets. The top line represents W bosons and the lower line represents the Z bosons.

estimated using a combination of analytic and Monte Carlo integration methods in complete next-to-leading-logarithm calculations [229, 230, 231, 232]. The cross sections are 9.5, 2.5, and 1.0 pb for WW, WZ, and ZZ respectively, with about 30% uncertainty in the prediction.

The sample of 10,000 generated events therefore represents a total cross section of 4.3 pb. From this we estimate a total background contribution of 0.08 ± 0.06 events from diboson production.

7.3 Background from Tau Fakes

Jets from regular QCD processes can mimic a tau and pass the tau selection criteria, if the partons fragment into a narrow cone with low track multiplicity. The fake rate for a jet to be identified as a hadronic tau was determined in Appendix E based on the inclusive jet data.

Events with these fake taus can contribute background to the signal region. For

this to occur, there needs to be some other "activity" in the event that contributes to the search topologies. In particular, there needs to be large $\not\!\!E_T$ for the event to pass the preselection cuts. Sources of this $\not\!\!E_T$ could be real (e.g. from neutrinos) or spurious (from mismeasurements in the detector due to poor calorimeter response or from particles going through uninstrumented regions of the detector). Given the high rates for generic QCD processes from $p\overline{p}$ collisions, such as multijet events and heavy quark production, we expect these events to contribute substantially to the charged Higgs background even though the tau fake rate per jet is small.

Rather than trying to model all the processes that could produce such events, we estimate the contribution of these events from the $\not\!\!E_T$ search data set. To a very good approximation, this data set is all background which has produced some large $\not\!\!E_T$ due to one of the effects mentioned above. We also assume that there are no real taus in these events by removing the normal tau identification cuts. Again, to first order, this is a very good approximation. Instead, we replace the tau cuts by a function encoding the tau fake rate for the jets. The events with these simulated taus are then processed by the standard analysis. This produces an estimate of the contribution from tau fakes which is absolutely normalized to our sample and which includes any process which contributes to the fake background. We expect a total of 5.4 ± 1.5 events in the final sample. This includes the 25% uncertainty on the measured fake rate.

The number of expected events from the different background sources is shown in Table 7.2, split up according to the two search channels. Splitting up the expected background totals for each run separately gives 0.9 ± 0.4 events for Run 1A and 6.5 ± 1.8 events for Run 1B. This is to be compared to the numbers observed in the data: one event in Run 1A and six events in Run 1B.

7.4 Check of Background Estimation

To check the background estimation, various kinematic distributions in the data are compared with those predicted by the fake and Monte Carlo samples, both with and

	τjjX	Ditau	Total
$W \to \tau\nu$ + jet(s)	—	1.3 ± 1.3	1.3 ± 1.3
$Z \to \tau^+\tau^-$ + jet(s)	—	0.6 ± 0.3	0.6 ± 0.3
WW,WZ,ZZ	0.04 ± 0.04	0.04 ± 0.04	0.08 ± 0.06
Fake taus	5.1 ± 1.3	0.30 ± 0.19	5.4 ± 1.5
Expected	5.1 ± 1.3	2.2 ± 1.3	7.4 ± 2.0
Observed	7	0	7
SM top ($\sigma_{t\bar{t}} = 5$ pb)	1.10 ± 0.10	—	1.10 ± 0.10

Table 7.2: Expected background in the two search channels and observed events in 99.8 ± 7.3 pb^{-1}. The expected contributions from SM top decays using a top pair production cross section of 5.0 pb is also shown.

	τejj	$\tau\mu jj$	$\tau\tau jj$	τjjj
Electroweak	1.8 ±1.3	—	—	14. ± 6.
Top	0.36±0.07	0.36±0.06	—	4.00± 0.25
Fakes	1.0 ±0.4	0.9 ±0.4	1.0 ±0.4	78. ±20.
Total	3.2 ±1.4	1.3 ±0.4	1.0 ±0.4	96. ±21.
Data	2	2	1	114

Table 7.3: Standard topology events without b-tagging. The SM top contributions (assuming $\sigma_{t\bar{t}} = 5.0$ pb) are included in the total.

without b-tagging. These are shown in Figures 7.2 to 7.13. In the plots the data are the points, the hollow region is the predicted Standard Model $t\bar{t}$ contribution, the grey region is the contribution predicted from the W/Z Monte Carlo samples and the dark region is the background expected from the tau fakes. The errors on the background estimates are not shown. Overall, the agreement is excellent.

Table 7.3 shows the number of expected events in the τjjX channel from all processes without b-tagging. The total number of expected events (102 ± 21) agrees well with the number of events seen (119). The number of events in each mode also agrees well with expectations. The kinematics of the five dilepton events in this sample are summarized in Table 7.4. The b-tags indicate which object in the event, if any, is tagged by either the soft-lepton algorithm ($N_{trk} = e$) or by the SECVTX algorithm (with N_{trk} = number of tracks in the tag). One of these events passes the b-tag selection used in the charged Higgs analysis and is in the final event sample.

Run	Event	$\not\!\!E_T$ (GeV)	ΣE_T (GeV)	N^{τ}_{trk}	E_T (GeV) τ	j_1	j_2	ℓ	N_{jets}	b-tag (N_{trk})
45047	104393	56.8	131.1	1	30.2	44.0	22.5	45.6μ	2	τ_1 (e)
61358	204309	42.1	285.4	3	107.7	74.0	12.9	20.2τ	2	τ_2 (3)
†64934	416715	52.9	197.0	1	20.0	42.6	15.7	$60.1e$	2	j_1 (3)
65471	47719	59.0	328.1	1	69.8	169.3	35.4	21.9μ	3	
65947	197455	84.1	284.4	3	52.9	41.7	23.1	$50.8e$	2	j_1 (e)

Table 7.4: Dilepton events passing the analysis cuts without the b-tagging requirement. †This event passes the b-tag requirement and is in the final selected sample.

Another check is performed on the consistency of the predicted backgrounds and the efficiency of tau identification by comparing the tau lepton candidates in the $\not\!\!E_T$ data with those from the expected backgrounds. Events are selected that pass all the standard τjjX topology requirements but with the $\not\!\!E_T$ cut tightened to 40 GeV and the $\not\!\!E_T^{obj}$ isolation tightened to 75 (in Equation 5.6) and without the b-tagging. These cuts enhance $W \rightarrow \tau\nu + 3$ jets events.

Figure 7.14 shows the charged track multiplicity for the tau candidates in these events (the charge and track requirements for the tau have not been applied). The shaded region represents the background from fakes, the dark region is the contribution from SM top and the hollow region is from the W + jets Monte Carlo. Again systematic and statistical uncertainties on the Monte Carlo and background estimates are not shown.

The total number of taus observed agrees very well with the expectations from the various contributing physics processes with good agreement in each track multiplicity bin. The difference between the number of taus expected and measured is 10% for both one- and three-prongs taus combined (15% for one-prongs considered separately). This is consistent with the 10% systematic uncertainty used for the tau identification efficiency in the signal acceptance estimates (see Section 6.2).

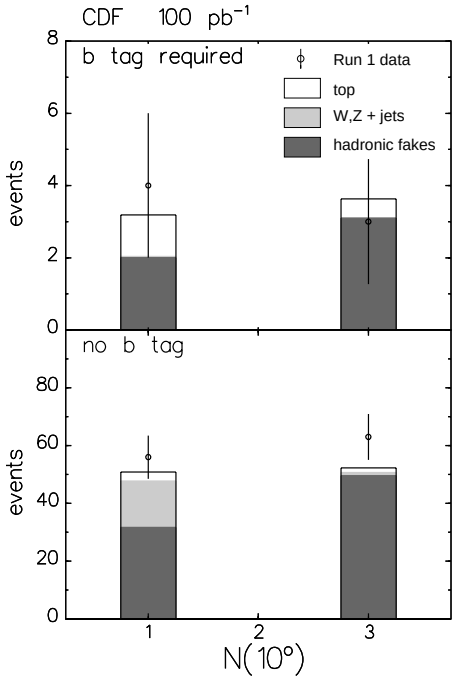

Figure 7.2: Tau track multiplicity.

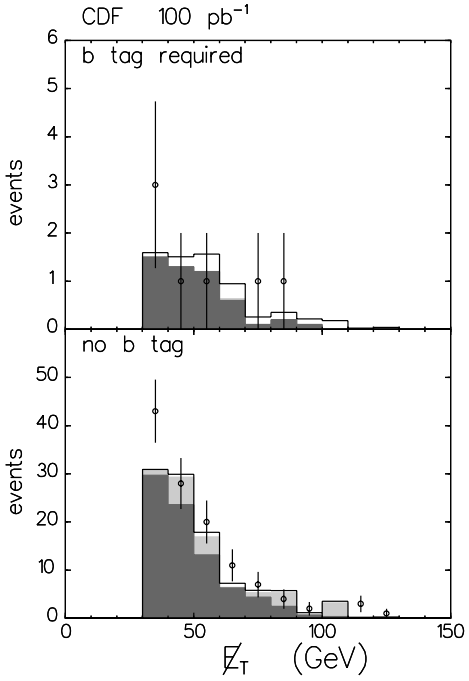

Figure 7.4: $\not\!\!E_T$ distribution.

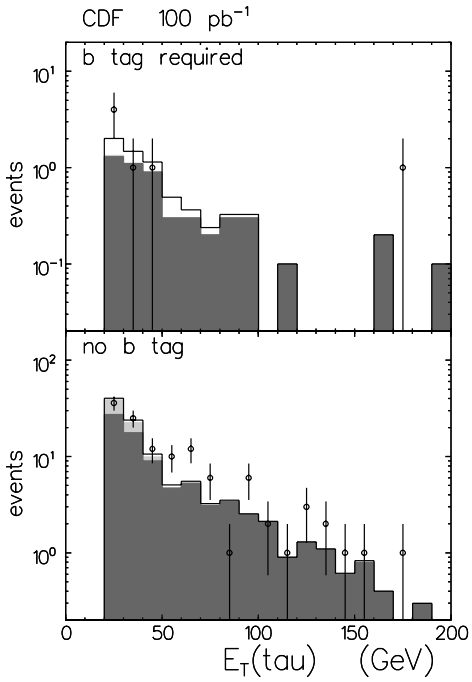

Figure 7.3: E_T of the tau lepton.

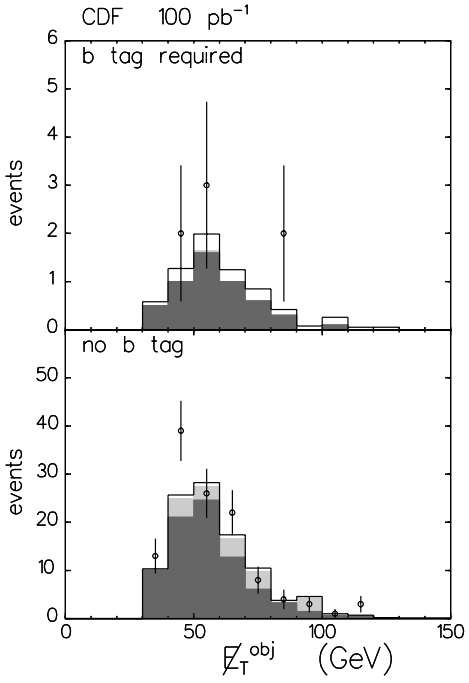

Figure 7.5: $\not\!\!E_T^{obj}$ distribution.

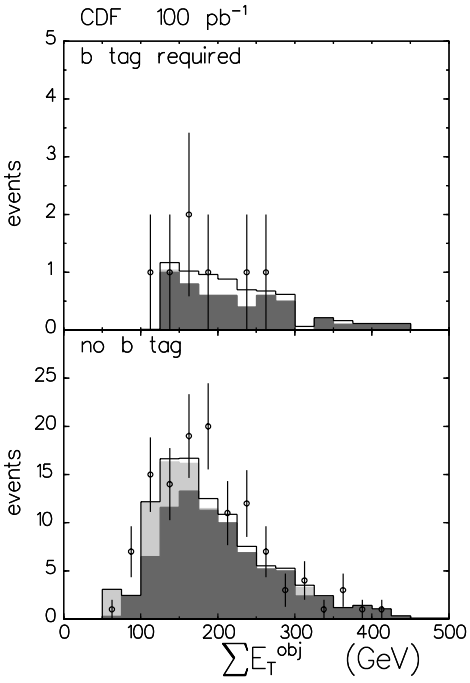

Figure 7.6: ΣE_T^{obj} distribution.

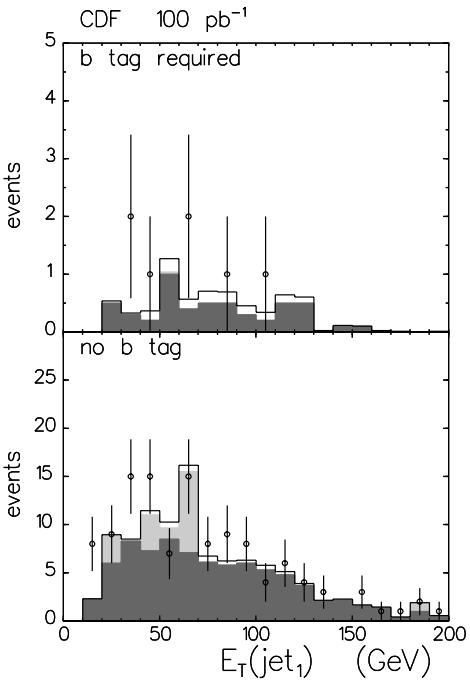

Figure 7.8: E_T of leading jet.

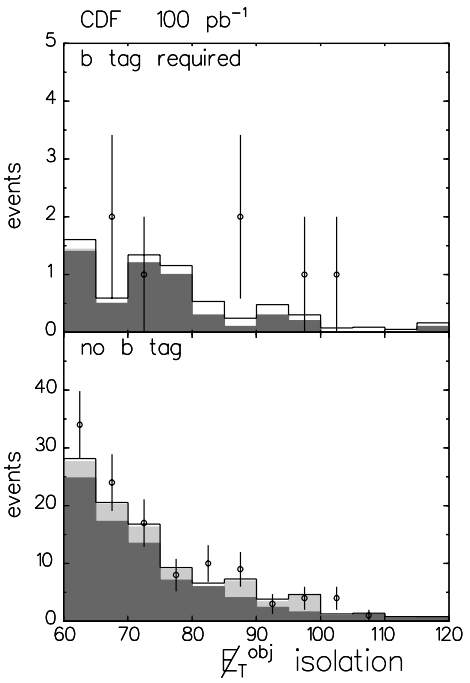

Figure 7.7: $\not\!\!E_T^{obj}$ isolation variable.

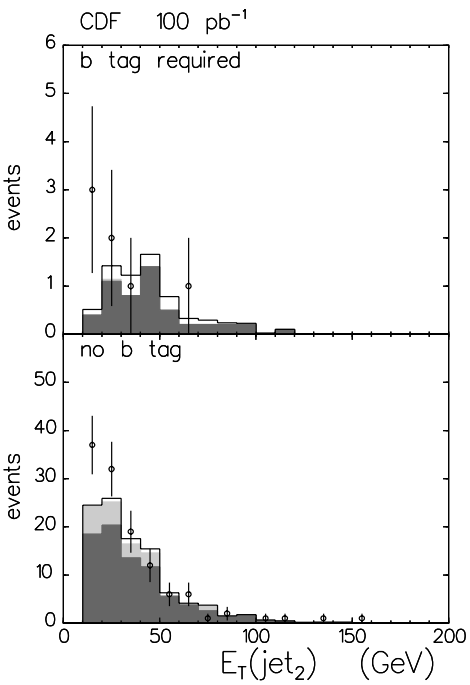

Figure 7.9: E_T of next-to-leading jet.

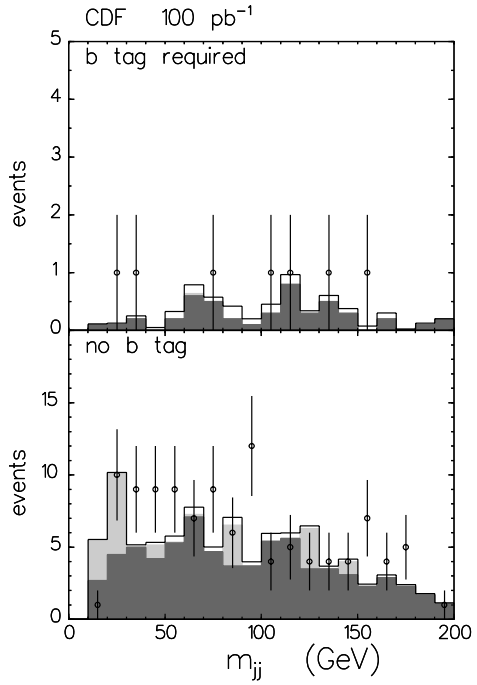

Figure 7.10: The invariant mass of the two leading jets.

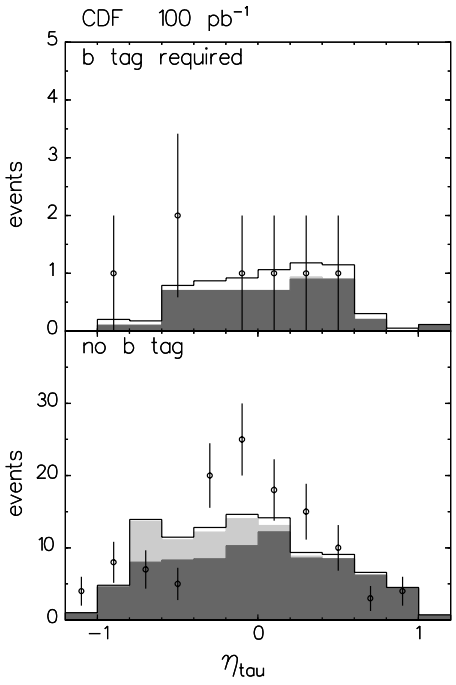

Figure 7.12: Pseudorapidity of the tau lepton.

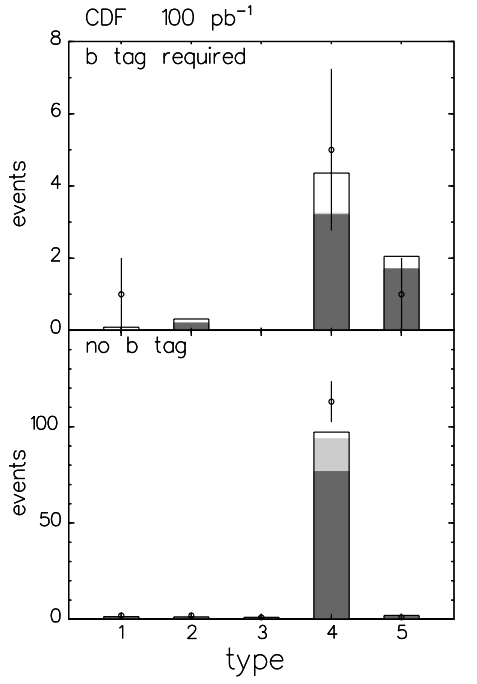

Figure 7.11: The other (X) object type (e, μ, τ, jet, b-jet).

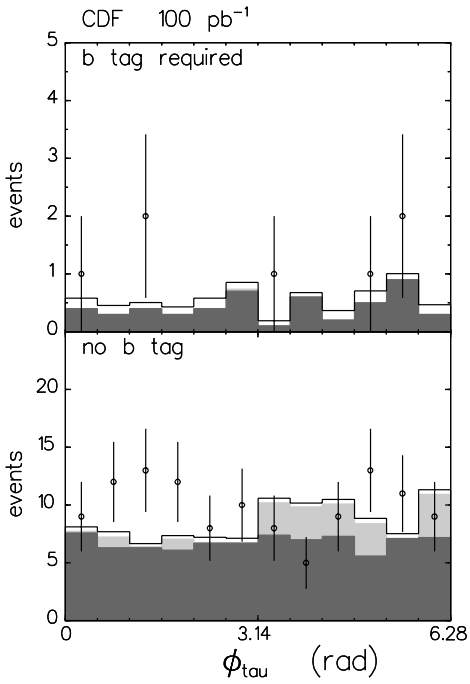

Figure 7.13: Cosine of the angle between the tau lepton and leading jet.

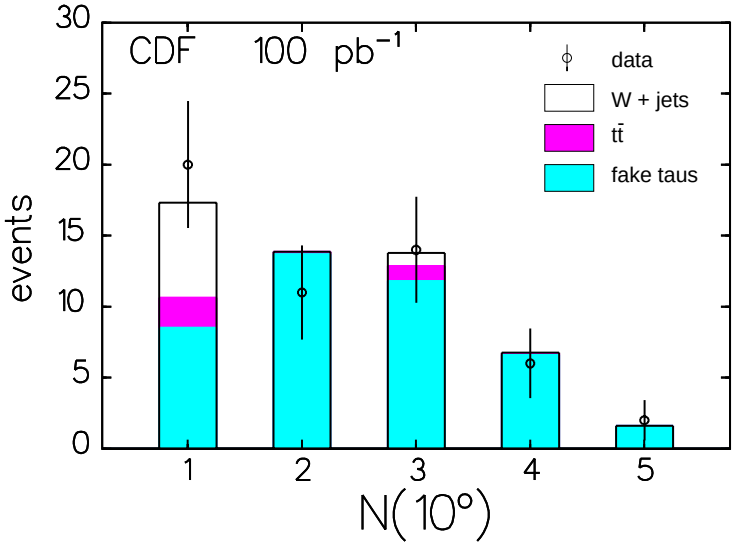

Figure 7.14: Tau track multiplicity for $W \rightarrow \tau\nu$ + 3 jet events in the preselected Run 1 $\not\!\!E_T$ search sample, without b-tagging required. The points are the measured data, the shaded region is background from fakes, the dark region is the contribution predicted from SM top Monte Carlo and the hollow region is from $W \rightarrow \tau\nu$ Monte Carlo.

Chapter 8

Results and Conclusions

Using both the $\tau jjX + b$-tag and ditau search topologies, 7 events are observed in the Run 1 data from CDF, as discussed in Chapter 5. The expected background contributions from all processes is 7.4 ± 2.0 events in both channels (see Chapter 7). Therefore, the number observed is consistent with being from background only. We, therefore, have a null result and proceed to set limits on the production of charged Higgs bosons via top quark decays.

8.1 Expected Number of Signal Events

As shown in Chapter 6, the typical acceptances for the combined search channels for top decays via charged Higgs bosons are in the range 1–2%. The acceptances from Table 6.3 for both search channels have been combined in Table 8.1.

The number of signal events expected in both search channels is given by

$$N_{sig} = \sigma_{t\bar{t}} \cdot \epsilon \cdot \int \mathcal{L} dt \tag{8.1}$$

where $\sigma_{t\bar{t}}$ is the production cross section for $t\bar{t}$ pairs, ϵ is the overall acceptance for a top event decaying into one of the search channels and $\int \mathcal{L} dt = 99.8 \pm 7.3$ pb^{-1} for Run 1. In general, ϵ is a function of $\tan\beta$, the mass of the charged Higgs boson and the mass of the top quark. We will assume $M_t = 175$ GeV/c^2 for the rest of this discussion.

All the SM searches for the top quark assume $\mathcal{B}(t \to W^+ b) = 1$. If non-SM particles, such as the charged Higgs, exist that the top quark can decay into, then $\mathcal{B}(t \to W^+ b) < 1$. Any measurement of SM top decays is actually measuring $\sigma_{obs} = \sigma_{t\bar{t}} \cdot \mathcal{B}(t \to W^+ b)$ times the branching fraction into the search channel. The observed

$M_{H^\pm}$ (GeV/c^2)	A_{WW}	A_{WH}	A_{HH}
40	0.22±0.02	1.14±0.07	2.23±0.13
60	0.22±0.02	1.21±0.07	2.12±0.13
80	0.22±0.02	1.28±0.07	2.11±0.13
100	0.22±0.02	1.45±0.08	2.64±0.14
120	0.22±0.02	1.48±0.08	2.41±0.14
140	0.22±0.02	1.64±0.08	2.20±0.12
160	0.22±0.02	1.25±0.07	1.06±0.06
165	0.22±0.02	1.05±0.07	0.77±0.08
168	0.22±0.02	1.07±0.07	0.73±0.08

Table 8.1: The combined acceptances (in percent) for the two search channels (from Table 6.3) for the various $t\bar{t}$ decay modes for $M_t = 175$ GeV/c^2 and different $M_{H^\pm}$. WW, WH and HH refer to the decay modes of the top and anti-top quarks.

cross section under the SM assumptions would be an underestimate of the total top production cross section. The updated combined SM $t\bar{t}$ production cross section result from CDF is $7.6^{+1.8}_{-1.5}$ pb (see Table 1.6).

To calculate the number of expected signal events, we assume the theoretically calculated top pair production cross section of $\sigma_{t\bar{t}} = 5$ pb, shown in Table 1.4. To illustrate the sensitivity to the top cross section, we assume another value of $\sigma_{t\bar{t}} = 7.5$ pb, chosen to be 50% above the theoretical expectation. The expected contribution to the *signal* in our search channels when both top quarks decay via the SM mode is 1.10 ± 0.10 (1.65 ± 0.15) events for the assumed top production cross section $\sigma_{t\bar{t}} = 5.0$ pb (7.5 pb). This contribution is mostly from the τjjX channel. Note that we have not included this SM top contribution in the background estimation of 7.4 ± 2.0 events.

The overall acceptance, ϵ, is calculated as a function of $\tan\beta$ for each charged Higgs mass point from the acceptances for each possible decay pattern of the top quark convoluted by its branching fraction:

$$\begin{aligned} \epsilon &= \mathcal{B}^2(t \to H^+ b) A_{HH} + 2\mathcal{B}(t \to H^+ b)\mathcal{B}(t \to W^+ b) A_{WH} \\ &\quad + \mathcal{B}^2(t \to W^+ b) A_{WW} \end{aligned} \tag{8.2}$$

where the branching fractions are calculated in Appendix A assuming the type II

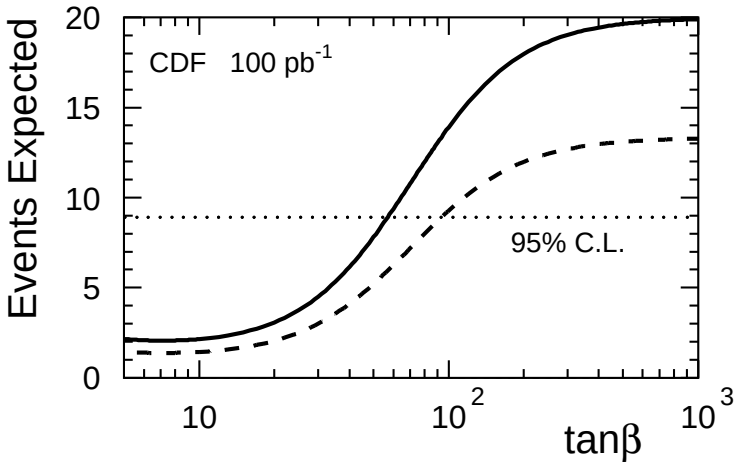

Figure 8.1: Expected number of charged Higgs events for $M_t = 175$ GeV/c^2, $M_{H^\pm} = 100$ GeV/c^2, and $\sigma_{t\bar{t}} = 5$ pb (dashed) or 7.5 pb (solid). Models which predict 8.9 or more expected events are excluded at 95% confidence level (dotted).

Two Higgs Doublet Model couplings. The acceptances come from Table 8.1. For the region of interest for this analysis, $\tan\beta \gtrsim 10$; therefore we assume $\mathcal{B}(H^+ \to \tau^+\nu) = 1$ (see Figure 1.5). Figure 8.1 shows the number of events expected (N_{sig}) as a function of $\tan\beta$ for the two assumed values of the top cross section for a charged Higgs mass of $M_{H^\pm} = 100$ GeV/c^2. Note that at low $\tan\beta$, most of the contribution to the signal is from SM top decays (1–2 events).

8.2 Setting Limits

To set limits on the charged Higgs production, we use a simple Monte Carlo to generate a large ensemble of random pseudo-experiments to determine the number of additional charged Higgs events (N_{sig}) needed above the number observed (N_{obs}) to set a 95% confidence level limit. This Monte Carlo [233] first determines the number of background events and the number of signal events in a trial from Poisson distributions with means N_{bkg} and N_{sig}, respectively. These means are varied within Gaussian distributions with widths given by their systematic uncertainty. The values of the means are truncated at zero to avoid unphysical estimations of the background and signal. If the trial has more background events than observed in the actual

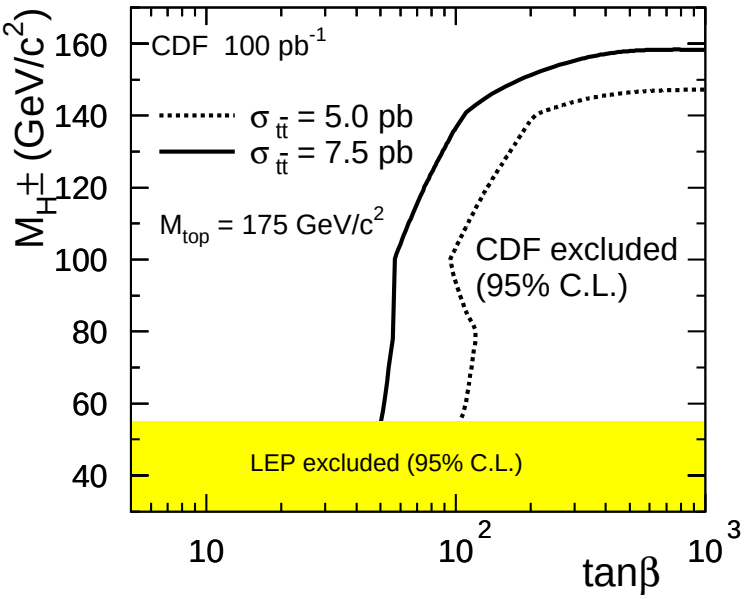

Figure 8.2: Limits on charged Higgs boson production from this analysis for $M_t = 175$ GeV/c^2. The limit is shown (excluded region is on the right) for both the theoretical (5.0 pb) and measured (7.5 pb) top cross sections. This result was published in Reference [1].

experiment ($N_{bkg} > N_{obs}$), the trial is discarded so as not to take advantage of any possible downward fluctuation in the number of observed background events; this leads to conservative estimates. The confidence level for the limit is given by the fraction of kept trials which have $N_{sig} + N_{bkg} > N_{obs}$. The value for N_{sig} is adjusted until the confidence level is 95%.

Table 6.4 listed the various systematic uncertainties affecting the acceptance which, when added in quadrature, totalled 25%. This is the systematic uncertainty used in estimating N_{sig}. The systematic uncertainty on the background estimate, which is also 25%, is dominated by uncertainties in the fake rate measurement (see Chapter 7).

From both search channels, 7 events are observed (N_{obs}) and the expected background is $N_{bkg} = 7.4 \pm 2.0$. From the above limit procedure, this analysis excludes at the 95% confidence level any point where the expected number of charged Higgs events is 8.9 or larger. This limit is indicated by the dotted line in Figure 8.1.

The limits can be turned into an exclusion contour in the $M_{H^\pm}$–tan β plane.

Figure 8.2 shows the 95% confidence level limits for charged Higgs decays via $\tau\nu$ for the two assumed values of the top production cross section. The current LEP-II limits, excluding $M_{H^\pm} \leq 54.5$ GeV/c^2, from Table 1.7 are shown as well. This plot was published in the Physical Review Letter [1] with the LEP-I limits of 45 GeV/c^2 indicated.

For large $\tan\beta$, this analysis can exclude charged Higgs bosons with masses less than 147 GeV/c^2 for a top quark mass of 175 GeV/c^2 with the theoretical cross section of 5.0 pb. Charged Higgs bosons with masses less than 158 GeV/c^2 can be excluded if the assumed top cross section of 7.5 pb is used.

8.3 Limits Including Information from the Top Discovery

This charged Higgs analysis originally was developed prior to the confirmation of the top quark discovery. Therefore, the only information used in setting limits above was the measured top mass and the theoretical top production cross section. However, the top quark discovery does provide additional information which can further restrict $H^\pm$ production. In the Physical Review Letter [1], we utilized the top quark production cross section as observed at CDF [13] of $\sigma_{obs} = 6.8^{+3.6}_{-2.4}$ pb. To maintain consistency with this measurement, which was from the top SM lepton + jets channel, the total top cross section, $\sigma_{t\bar{t}}$, must increase at higher $\tan\beta$ to compensate for the lower branching fraction into the SM mode $\mathcal{B}(t\bar{t} \rightarrow W^+ b\, W^- \bar{b})$.

To preserve the observed cross section in the lepton + jets channel, we allowed the total $\sigma_{t\bar{t}}$ to vary as a function of $\tan\beta$, $M_{H^\pm}$ and M_t, with the constraint that

$$\sigma_{obs} = \epsilon \cdot \sigma_{t\bar{t}} \cdot \mathcal{B}(t\bar{t} \rightarrow W^+ b\, W^- \bar{b}), \tag{8.3}$$

where we assumed a fixed efficiency, ϵ, derived from the SM top search and $\sigma_{obs} = 6.8^{+3.6}_{-2.4}$ pb. The $\sigma_{t\bar{t}}$ derived from this calculation is used in Equation 8.1 to obtain the new exclusion region, shown in Figure 8.3. The range of σ_0 values in the figure incorporate the uncertainties on the top cross section measurement. The excluded region is larger than in Figure 8.2 and excludes lower values of $\tan\beta$ and larger values of $M_{H^\pm}$.

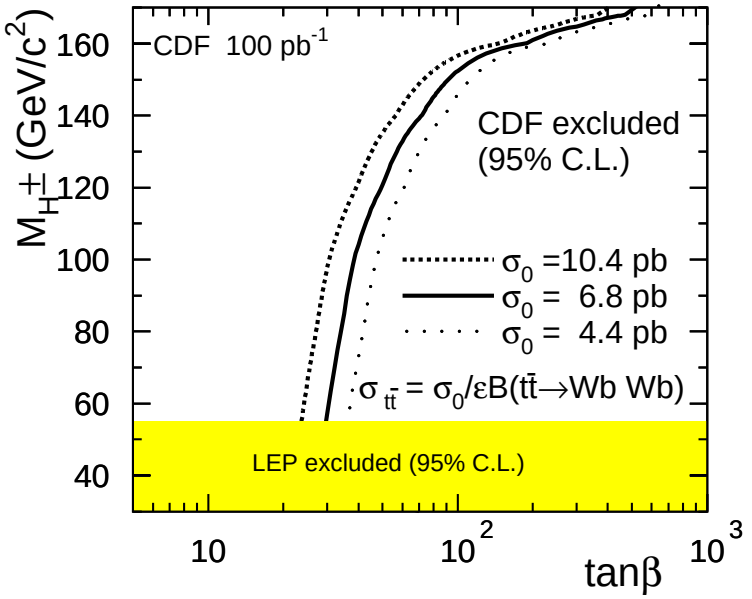

Figure 8.3: Charged Higgs exclusion region for $M_t = 175$ GeV$/c^2$ using $\sigma_{t\bar{t}} = \sigma_{obs}/\mathcal{B}(t\bar{t} \to W\,b\,W\,b)$. This result was published in Reference [1].

This result was published in the Physical Review Letter [1] as well.

8.4 Improved Limits Using the SM Top Cross Section

The calculation of $\sigma_{t\bar{t}}$ from Equation 8.3 and used in Figure 8.3 took no account of the fact that top quark decays via a charged Higgs boson could also contribute events to the top lepton + jets channel.[1] This means that $\sigma_{t\bar{t}}$ "blows up" as the branching fraction for top decays into the SM-mode, Wb, becomes vanishingly small for increasingly large values of $\tan\beta$. This is shown graphically in Figure 8.4. Obviously, for large $\tan\beta$, this constraint becomes unphysical. This was a somewhat naive attempt to incorporate the top discovery information into the charged Higgs limits.

New information has become available at CDF since the publication of the Physical Review Letter [1]. An analysis that is underway by another Ph.D. student,

[1] Either from W decays to leptons in $t\bar{t} \to W^+\,b\,H^-\,\bar{b}$ or from tau decays to leptons from the charged Higgs boson.

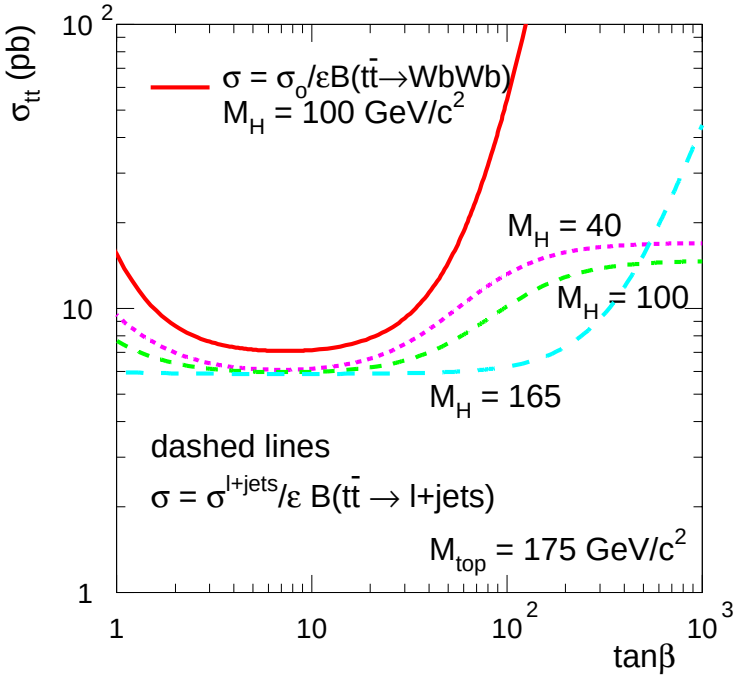

Figure 8.4: The total top cross section as a function of $\tan\beta$ under the assumption of Equation 8.3 (solid line) and calculated from Equation 8.4 (dashed lines) for different representative charged Higgs masses.

Brendan Bevensee[2], uses the observation of top quark decays in the SM lepton + jets and dilepton channels to place constraints on top decays via charged Higgs bosons. Decays to charged Higgs bosons would lead to deficits in the number of observed top decays in these leptonic modes. The observations in these channels can therefore be used to place indirect constraints on charged Higgs production. These results have been presented at conferences [234] but are preliminary and the analysis is still ongoing.

We can use the acceptances for the non-SM top decays in the lepton + jets channel calculated by B. Bevensee [43] to constrain $\sigma_{t\bar{t}}$ more realistically. Table 8.2 from Reference [43] lists the acceptances in the five possible decay patterns, where the top quarks can decay into either Wb or Hb and the Higgs bosons can decay into either $\tau\nu$ (preferred for large $\tan\beta$) or $c\bar{s}$ (preferred for small $\tan\beta$). The decay mode where two Higgs bosons are produced and both decay to $c\bar{s}$ has negligible

[2]at the University of Pennsylvania

$M_{H^\pm}$ (GeV/c^2)	$A_{WW}^{\ell+jets}$	$A_{WHcs}^{\ell+jets}$	$A_{WH\tau\nu}^{\ell+jets}$	$A_{HH\tau\nu cs}^{\ell+jets}$	$A_{HH\tau\nu\tau\nu}^{\ell+jets}$
40	3.65±0.04	2.37±0.05	2.17±0.04	1.10±0.04	1.26±0.03
60	3.65±0.04	2.27±0.05	2.19±0.04	1.23±0.04	1.30±0.03
80	3.65±0.04	2.28±0.05	2.32±0.05	1.33±0.04	1.34±0.03
100	3.65±0.04	2.40±0.06	2.27±0.04	1.43±0.04	1.44±0.03
120	3.65±0.04	2.17±0.05	2.31±0.04	1.50±0.04	1.29±0.03
140	3.65±0.04	2.07±0.05	1.91±0.05	1.28±0.04	0.78±0.02
150	3.65±0.04	1.94±0.05	1.68±0.05	0.89±0.04	0.42±0.02
160	3.65±0.04	1.74±0.05	1.21±0.04	0.34±0.02	0.10±0.01
163	3.65±0.04	1.70±0.05	1.10±0.04	0.34±0.02	0.06±0.01

Table 8.2: Acceptances (as percentages) for the various $t\bar{t}$ decay channels from the lepton + jets analysis [43]. The subscript cs or $\tau\nu$ refers to the decay mode of the charged Higgs boson. The uncertainties listed are due to the limited Monte Carlo statistics. Acceptances are extrapolated past $M_{H^\pm} = 163$ GeV/c^2.

contribution to the lepton + jets channel due to the lack of an energetic primary lepton. We are also only interested in the region of large $\tan\beta$. Hence we take $A_{HHcscs}^{\ell+jets} \equiv 0$.

The observed $t\bar{t}$ cross section in the lepton + jets search channel is calculated from [43]:

$$\sigma_{t\bar{t}} = \frac{N_{obs} - N_{bkg}}{\int \mathcal{L}dt \cdot \epsilon_{t\bar{t}}^{\ell+jets}} \tag{8.4}$$

with $N_{obs} = 34.0 \pm 5.8$, $N_{bkg} = 10.6 \pm 1.6$[3] and $\int \mathcal{L}dt = 109$ pb^{-1} [85], and where

$$\begin{aligned} \epsilon_{t\bar{t}}^{\ell+jets} = {} & \mathcal{B}^2(t \to W^+b) A_{WW}^{\ell+jets} \quad + \quad \mathcal{B}^2(t \to H^+b) \\ & \times \left[2\mathcal{B}(H^+ \to c\bar{s})\mathcal{B}(H^+ \to \tau^+\nu) A_{HH\tau\nu cs}^{\ell+jets} + \mathcal{B}^2(H^+ \to \tau^+\nu) A_{HH\tau\nu\tau\nu}^{\ell+jets}\right] \\ & + 2\mathcal{B}(t \to H^+b)\mathcal{B}(t \to W^+b)\left[\mathcal{B}(H^+ \to c\bar{s}) A_{WHcs}^{\ell+jets} + \mathcal{B}(H^+ \to \tau^+\nu) A_{WH\tau\nu}^{\ell+jets}\right] \end{aligned} \tag{8.5}$$

As we are assuming that the only decay modes available to top are either Wb or Hb, we take $\mathcal{B}(t \to W^+b) = 1 - \mathcal{B}(t \to H^+b)$ and we also assume that the only decay modes for the Higgs bosons are $\tau\nu$ or $c\bar{s}$ and therefore can take $\mathcal{B}(H^+ \to c\bar{s}) = 1 - \mathcal{B}(H^+ \to \tau^+\nu)$.

[3] The non-$t\bar{t}$ background used here is slightly higher then in the SM top analysis as no correction for the top content is made.

The cross section derived from this calculation is shown as a function of $\tan\beta$ and for three different representative Higgs masses in Figure 8.4. The steep increase in the total cross section at large $M_{H^\pm}$ and large $\tan\beta$ reflects the small acceptance in the leptonic channels for the $t\bar{t} \to H^+ b\, H^- \bar{b}$ mode where both Higgs bosons decay to $\tau\nu$. The solid curve in the same figure shows the cross section increase with $\tan\beta$ for $M_{H^\pm} = 100$ GeV/c^2 under the naive assumption used for Figure 8.3. Obviously the new calculation gives a more physical result but does show, for large $\tan\beta$ and $M_{H^\pm}$ values, that cross sections on the order of tens of picobarns would still be necessary to maintain consistency with the top measurements.

To incorporate the information from the lepton + jets analysis into our analysis (referred to below as the *tau + jets* analysis), we need to understand the interplay of the systematic uncertainties in both analyses. We recast the calculation as:

$$N_{sig} = (N_{obs}^{\ell+jets} - N_{bkg}^{\ell+jets}) \cdot \frac{\epsilon_{t\bar{t}}^{\tau+jets}}{\epsilon_{t\bar{t}}^{\ell+jets}} \tag{8.6}$$

which is derived by plugging Equation 8.4 into Equation 8.1 (ignoring the slight differences in the luminosities used in the two analyses). The systematic uncertainty in the luminosity cancels and all we are left with is the uncertainty in the number of top events observed in the lepton + jets analysis (23.4 ± 6.0) and in the uncertainties in the acceptances for the signal in each analysis. The acceptance is a complicated function of $\tan\beta$, $M_{H^\pm}$ and M_t so the rest of this discussion will be making some simplifying assumptions. There is also a potential overlap of the signal in each acceptance which has not been studied yet. A larger meta-analysis combining all these results, including results from a third CDF charged Higgs analysis based on the search for the top quark in the hadronic tau plus lepton channel [75], is planned (see Section 8.5).

Table 8.3 shows a rough break down of the systematic uncertainties in the lepton + jets and tau + jets analyses, broken down by common and independent systematics.

The topologies being looked for in the two analyses are very similar — a high-p_T lepton or hadronically decaying tau, large $\not\!\!E_T$, three or more other energetic jets and

Systematics in common			
	lepton + jets		tau + jets
Gluon radiation	8–24		10
Jet energy scale	5–17		10
b-tagging efficiency	8		10
Luminosity	7		8
Independent systematics			
lepton + jets		tau + jets	
z-vertex resolution	2.4		
Lepton identification	3	Tau identification	10
Trigger	8	Trigger	10
MC statistics	2–5	MC statistics	8
Total	10.2	Total	16.2
Total combined (in quadrature)		19.2	

Table 8.3: Systematic uncertainties (in percentages) in the lepton + jets and the tau + jets analyses separated into shared and non-shared systematics.

at least one SECVTX b-tag. This implies that, to first order, some of the systematic uncertainties will cancel in the ratio of the acceptances. These are: the jet energy-scale uncertainty in the detector simulation, the effect of gluon radiation from the initial or final states in the Monte Carlo simulations and the uncertainty in the b-tagging rate from the SECVTX algorithm. Varying the gluon radiation in the τ + jets analysis has little systematic effect as the changes in the two search topologies tend to cancel out. More gluon radiation provides more jets for the τjjX topology whereas less radiation provides slightly stiffer, more isolated taus which helps the ditau topology. Variations in the jet energy scale should have similar effects in both analyses as should the b-tagging systematic effects. Checking the detailed overlap and correlations for these systematics will require much more extensive analysis. Also, the effect of the luminosity uncertainties on the background calculations in each analysis needs to be explored further.

The systematic uncertainties that do not cancel and should be relatively independent are those involving the z-vertex resolution, particle identification efficiencies, trigger efficiencies and limited Monte Carlo statistics. These are added in quadrature. The total gives 19.2% uncertainty on the ratio of acceptances in Equation 8.6. This

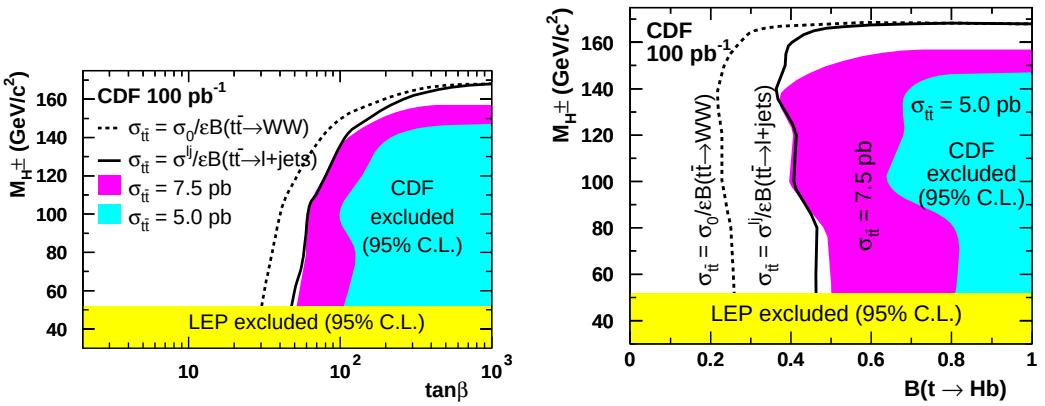

Figure 8.5: Charged Higgs boson 95% confidence level exclusion regions for constant cross sections (5.0 and 7.5 pb), and under the assumptions of the varying cross sections, for $M_t = 175$ GeV/c^2, plotted as functions of $\tan\beta$ and $\mathcal{B}(t \to H^+b)$.

is combined with the uncertainty on the number of observed top events (25.6%) to give an overall uncertainty of 32% on N_{sig}. Using this uncertainty on the acceptance, the minimum number of events needed in a Poisson process to exclude any model at 95% confidence level, given that we observed 7 events and predict a background of 7.4 ± 2.0, is 9.91 events.

Excluding models that predict $N_{sig} > 9.91$ give us the new exclusion region (the solid line) shown in Figure 8.5. The limit is shown both as a function of $\tan\beta$ and as a function of $\mathcal{B}(t \to H^+b)$ for $M_t = 175$ GeV/c^2. The exclusion region does not extend very much farther at low $\tan\beta$ than under the constant cross section assumption of 7.5 pb (and in fact is slightly worse for $M_{H^\pm} = 100$–120 GeV/c^2) but the upper end at high $\tan\beta$ reaches the highest mass ($M_{H^\pm} = 168$ GeV/c^2) generated in the Monte Carlo samples.

For large $\tan\beta$, we can exclude top quark decays via charged Higgs bosons for $M_{H^\pm} \leq 168$ GeV/c^2 and exclude $\mathcal{B}(t \to H^+b) > 0.43$ at the 95% confidence level.

Due to the unexplored correlations between the two searches and because unphysical requirements are still demanded on the top cross section at large $\tan\beta$, this result should be considered preliminary. Clearly the limit based on the naive assumption of keeping the SM top cross section constant (the dashed line in Figure 8.5) is over-optimistic and the new limit based on an improved calculation of this cross

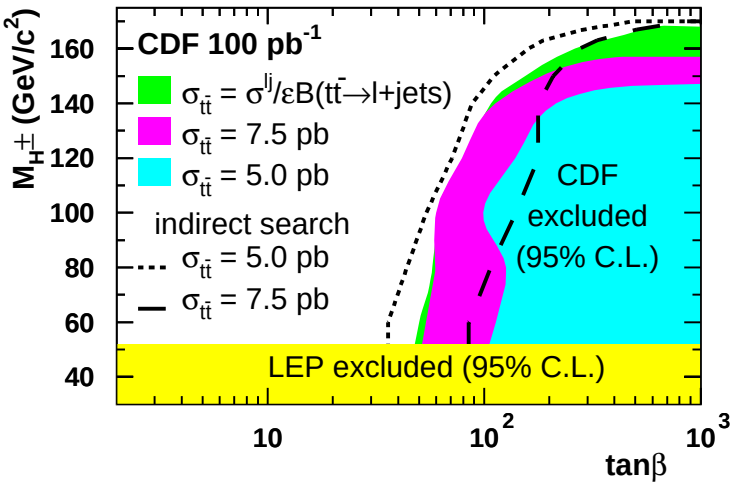

Figure 8.6: Comparison of the charged Higgs limits from this analysis with those from the top lepton + jets analysis [43].

section tries to compensate. Unfortunately, there is no simple way to deconvolute the analyses and more extensive study is needed.

Another constraint which was ignored in the current analysis and is still under investigation is that the Yukawa couplings of the charged Higgs boson to the fermion sector are theoretically constrained. For very large $\tan\beta$ ($\gtrsim 200$), the perturbative assumptions used in the calculations in Appendix A start breaking down and the widths of both the top quark and the charged Higgs boson start to increase dramatically. Hence, the limits only have validity up to about $\tan\beta \leq 200$. The exact reach and interpretation of these results is under investigation for the combined charged Higgs analysis.

8.5 Comparison with Other CDF Results

Figure 8.6a shows the charged Higgs limits derived from B. Bevensee's study [43] contrasted with our results. Note that as his is an *indirect* search, the excluded region is better at lower top cross section (5.0 pb) than at the higher top cross section (7.5 pb). These two analyses are therefore complementary and combining them will give a more robust limit.

As mentioned above, another charged Higgs analysis is underway based on the search in the top tau-dilepton channel [235]. The sensitivity of this analysis is lower due to the relatively small acceptance in the lepton channels for charged Higgs events. Typical acceptances for charged Higgs events in the tau-dilepton channel are on the order of 0.5% compared to 1–2% in the tau + jets channel. Results from this study are very preliminary and the plan is to combine all the channels for tau decays in a single result.

8.6 Conclusions

This analysis excludes charged Higgs production via top quark decays at the 95% confidence level assuming the type-II Two Higgs Doublet Model. For large $\tan\beta$, this analysis excludes a charged Higgs boson of mass 147 (158) GeV/c^2 for $\sigma_{t\bar{t}} =$ 5.0 (7.5) pb. Assuming information from the top quark measurements in the lepton + jets channel, this limit is raised to 168 GeV/c^2 at large $\tan\beta$. We also exclude $\mathcal{B}(t \to H^+b) > 0.43$ at the 95% confidence level for $M_{H^\pm} \leq 168$ GeV/c^2.

The techniques and datasets developed for this analysis, especially those developed for identifying hadronically decaying tau leptons, are being used in ongoing CDF analyses and searches in the Run 1 data, such as for the neutral Higgs bosons of the MSSM. These techniques are also being used in studying the prospects for discovery of Higgs bosons in the CDF Run 2, scheduled to commence in 2000.

Searches at colliders for the elusive Higgs particle or particles and the explication of their properties promises to invigorate both particle physics and physicists into the next millennium.

Appendix A

Calculations of Branching Ratios for the Charged Higgs Boson

The widths of the top quark decay to W^+b and H^+b in a type II 2HDM are given by the following [34, 35]:

$$\begin{aligned} \Gamma(t \to W^+b) &= \frac{g^2}{64\pi M_W^2 M_t}|V_{tb}|^2\lambda^{\frac{1}{2}}\left(1, \frac{M_b^2}{M_t^2}, \frac{M_W^2}{M_t^2}\right) \\ &\times \left[M_W^2(M_t^2 + M_b^2) + (M_t^2 - M_b^2)^2 - 2M_W^4\right] \end{aligned} \tag{A.1}$$

and

$$\begin{aligned} \Gamma(t \to H^+b) &= \frac{g^2}{64\pi M_W^2 M_t}|V_{tb}|^2\lambda^{\frac{1}{2}}\left(1, \frac{M_b^2}{M_t^2}, \frac{{M_{H^\pm}}^2}{M_t^2}\right) \\ &\times \left[(M_t^2\cot^2\beta + M_b^2\tan^2\beta)(M_t^2 + M_b^2 - M_H^2) - 4M_t^2M_b^2\right] \end{aligned} \tag{A.2}$$

where M_x is the mass of particle x, V_{ij} are the CKM matrix elements (see Equation 1.5) and $\lambda(a,b,c) = (a-b-c)^2 - 4ab$, is the two-body kinematic phase-space function. The subsequent decay widths for $H^+ \to \tau^+\nu$ and $H^+ \to c\overline{s}$ are:

$$\Gamma(H^+ \to \tau^+\nu) = \frac{g^2 M_H}{32\pi M_W^2}M_\tau^2\tan^2\beta \tag{A.3}$$

and

$$\Gamma(H^+ \to c\overline{s}) = \frac{3g^2 M_H}{32\pi M_W^2}|V_{cs}|^2(M_c^2\cot^2\beta + M_s^2\tan^2\beta) \tag{A.4}$$

A third decay mode for charged Higgs becomes important for $\tan\beta < 1$ and large $M_{H^\pm}$ values ($\gtrsim 140$ GeV/c^2) where the charged Higgs decay can proceed through a virtual top quark process ($H^+ \to t^*\overline{b} \to W^+b\overline{b}$). This decay occurs at reasonable rates when the propagator is not too far off mass-shell, as the H^+ Yukawa coupling to $t\overline{b}$ is about 100 times larger than those to the $c\overline{s}$ and $\tau^+\nu$ channels. This three-body

decay is calculated from [236]:

$$\frac{d}{ds_{\bar{b}}ds_b},(H^+ \to W^+ b\bar{b}) = \frac{1}{256\pi^3 M_{H^\pm}^3}\left(\frac{3g^4M_t^4}{4\tan^2\beta M_W^4(M_t^2-s_{\bar{b}})^2}\right) \times\left[M_W^2(s_W-2M_b^2)+(s_{\bar{b}}-m_b^2-M_W^2)(s_b-m_b^2-M_W^2)\right] \quad (A.5)$$

where s_b, $s_{\bar{b}}$ and s_W are the squared four-momenta transferred to the corresponding particles, satisfying $s_b + s_{\bar{b}} + s_W = M_{H^\pm}^2 + M_W^2 + 2M_b^2$. The width is calculated by integrating over the four-momenta.

To calculate the various widths, we use the minimal-subtraction ($\overline{\rm MS}$) renormalization scheme [18, 19] to evolve the quark masses in perturbation theory. The large logarithmic contributions of the QCD corrections are absorbed in the running quark mass $\overline{M_q}(\mu)$ at the scale of the corresponding Higgs mass, $\mu = M_{H^\pm}$ [42].

The running quark masses $\overline{M_Q}(\mu)$ are evaluated at the charged Higgs mass pole:

$$\overline{M_Q}\,(M_{H^\pm}) = M_Q\left(\frac{\ln(M_Q^2/\Lambda^2)}{\ln(M_{H^\pm}^2/\Lambda^2)}\right)^{-\frac{2}{\pi b_0}} \quad (A.6)$$

where the bare quark masses (M_Q) used for the strange, charm and bottom quarks are 0.2, 1.5 and 4.3 GeV/c^2 respectively. The QCD scale parameter, Λ, is calculated at the Z^0 pole ($M_Z = 91.187$ GeV/c^2) up to $\mathcal{O}(\alpha_s^2)$ from [237, 238]:

$$\Lambda^{(n_f)}(\mu = M_Z) = \mu\exp\left[\frac{1}{b_0(n_f)\alpha_s(\mu)} - \frac{b_1(n_f)}{b_0^2(n_f)}\ln\left(\frac{-2}{b_0(n_f)\alpha_s(\mu)}\right) + \alpha_s(\mu)\frac{b_2(n_f)b_0(n_f)-b_1^2(n_f)}{b_0^3(n_f)}\right] \quad (A.7)$$

where $\alpha_s(M_Z) = 0.118$ and

$$\begin{aligned} b_0(n_f) &= -\frac{1}{2\pi}\left(11-\frac{2}{3}n_f\right), \\ b_1(n_f) &= -\frac{1}{4\pi^2}\left(51-\frac{19}{3}n_f\right), \\ b_2(n_f) &= -\frac{1}{64\pi^3}\left(2857-\frac{5033}{9}n_f+\frac{325}{27}n_f^2\right). \end{aligned} \quad (A.8)$$

The n_f refer to the number of active flavors at a particular mass scale. For the strange, charm and bottom quarks we choose $n_f = 4$, 4.5 and 5 respectively.

The remaining masses in the calculation are the tau lepton mass, $M_\tau = 1.777$ GeV/c^2 and the W boson mass, $M_W = 80.22$ GeV/c^2. The relevant CKM matrix elements are taken to be $V_{cs} = 0.9736$ and $V_{tb} = 1$.

The various widths can then be calculated as functions of the top quark mass, charged Higgs mass and $\tan\beta$. Note that the relative size of the H^+ decay widths at $\tan\beta = 1$ would hold for all values of $\tan\beta$ in the type I 2HDM.

The branching fractions for each process can then be calculated from these partial widths, assuming they constitute all the possible decay modes. For example, the branching fraction for top quark decays to charged Higgs ($t \to H^+ b$) decays is given by

$$\mathcal{B}(t \to H^+ b) = \frac{, (t \to H^+ b)}{, (t \to H^+ b) + , (t \to W^+ b)}, \tag{A.9}$$

and the branching fraction of charged Higgs decays to taus ($H^+ \to \tau^+ \nu$) by

$$\mathcal{B}(H^+ \to \tau^+ \nu) = \frac{, (H^+ \to \tau^+ \nu)}{, (H^+ \to \tau^+ \nu) + , (H^+ \to c\bar{s}) + , (H^+ \to W^+ b\bar{b})} \tag{A.10}$$

In practicality, the $, (H^+ \to W^+ b\bar{b})$ widths can be ignored for $\tan\beta > 1$.

Appendix B

The Tevatron Accelerator Complex at Fermilab

Five accelerators (the Cockcroft-Walton, Linac, Booster, Main Ring and Tevatron) and two storage rings (the antiproton Debuncher and Accumulator) make up the accelerator complex at Fermilab. Figure B.1 shows their relationship [239].

The proton beam starts out from a bottle of hydrogen gas. The gas is passed through a *magnetron* consisting of an oval-shaped cathode surrounded by an anode, separated by 1 mm. Negatively charged hydrogen ions (H^-) are produced at the cathode which are then extracted through the anode aperture and are accelerated through an extraction plate to 18 keV. The negative hydrogen ions are then accelerated through a 750 kV potential, provided by a commercial Cockcroft-Walton generator, and are passed down a transport line to the Linac.

The hydrogen ion source is pulsed at 15 Hz which matches the Linac and Booster cycles. The beam from the Cockcroft-Walton is also "bunched" to match the RF frequency of the Linac (201.24 MHz), which raises the efficiency for the beam to be captured in the RF structure of the Linac to about 70% (from $\sim$ 35% for a nonbunched beam).

The Linac is a two-stage 145 m long Alvarez drift-tube linear accelerator that takes the H^- ions and produces a pulsed 400 MeV (200 MeV for Run 1A) beam from them. The accelerator consists of five electrically-resonant cylindrical high-conductivity copper clad steel tanks, each of which is driven by its own RF system. The interior of each tank consists of a line of drift tubes with bore holes for the beam to pass through. The drift tubes are separated by accelerating gaps where the H^- ions experience the RF field. Alternating focusing and defocusing quadrupole magnets, embedded within the drift tubes, counter the effects of the space charge

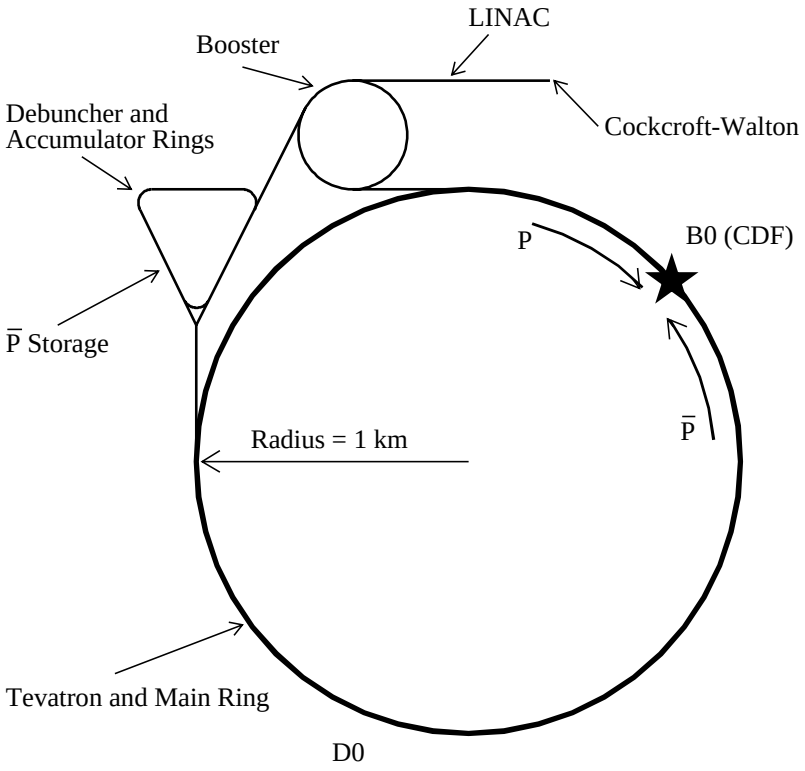

Figure B.1: The Fermilab accelerator complex, showing the relative positions of the Cockcroft-Walton, Linac, Booster, Main Ring, Anti-proton storage rings and Tevatron. CDF is located at the B0 interaction region. The Main Ring and Tevatron occupy the same 1 km radius tunnel.

and RF which tend to "blow up" the beam.

Protons are transferred to the Booster from the Linac through multiturn charge-exchange injection at 15 Hz. This is performed by bringing the H^- ions from the Linac into a path parallel with a closed orbit for protons in the Booster. The H^- ion beam is merged with any protons already in the Booster by passing both beams through a dogleg (two adjacent dipole magnets of opposite polarity). The combined beam passes through a carbon foil, which strips the two electrons from the H^- ions, and then through another dogleg which restores the protons in the Booster path, while remaining H^- ions, H-atoms and anything else are directed to a beam dump. This charge-exchange process is a non-conservative action and thus allows the two beams to be absolutely merged, which would otherwise violate Liouville's theorem [128]. This is the reason H^- ions are accelerated rather than protons in the

early stages.

The Booster is an 8-GeV fast-cycling proton synchrotron. It is 75.5 m in radius and consists of 96 combined function dipole/quadrupole magnets and 17 dual gap ferrite-tuned cavity resonators. The Booster is typically filled in six rotations with about 3×10^{12} protons at 400 MeV from the Linac via the charge-exchange interaction. Once filled, the RF field phase is rotated, capturing the beam into the Booster's RF bucket structure and the beam is accelerated to its final energy of 8 GeV and is then injected into the Main Ring. The entire acceleration process takes 33 ms and the Booster cycles completely in 66 ms, establishing the 15 Hz injection rate.

As the proton bunches are accelerated, the Booster goes through *transition* at $\sim$ 4.2 GeV which is a phenomenon that occurs as the bunches go from non-relativistic to relativistic energies. Non-relativistic bunches are longitudinally stable or stable about the synchronous phase angle as slower particles arriving late experience a larger accelerating field and faster particles arriving early experience a smaller field. At very high energies (where the bunches approach the speed of light), higher momentum particles have about the same speed as lower momentum particles but they follow a larger radius orbit which means they have a longer transit time around the ring. The phase of the RF accelerating fields must be changed appropriately to ensure beam stability.

It is worth noting here that all the circular accelerators at Fermilab (the Booster, Main Ring and Tevatron) are *alternating gradient synchrotrons*. They provide *betatron* oscillations to the beam which are stable oscillations in the transverse direction about the ideal closed orbit using series of alternating quadrupole magnets. Two parameters for each accelerator describe these oscillations; the *tune* is the number of betatron oscillations that the beam undergoes in one complete orbit, and the *beta function* (β) is related to the lattice of quadrupoles in the machine and is proportional to the instantaneous wavelength of the betatron oscillations. Both these parameters are given separately for the vertical and horizontal directions. The beta function also describes the transverse size of the beam; a region of low β has a small beam spot size.

The Main Ring is a 400 GeV proton synchrotron with a radius of 1 km, buried in a tunnel 6 m underground. During colliding beam operation, it performs two functions; it serves as a 150 GeV injector of protons and antiprotons for the Tevatron and it provides the source of 120 GeV protons used in anti-proton creation.

The Main Ring captures the proton bunches from the Booster or anti-proton bunches from the Accumulator at 8 GeV, accelerates the beam to the Tevatron injection energy of 150 GeV, coalesces several bunches into one (fifteen for protons, eleven for anti-protons) to maximize the number of protons ($\sim 15 \times 10^{10}$) or antiprotons ($\sim 5 \times 10^{10}$) in a Tevatron bunch and "cogs" the beam by shifting the Main Ring RF phase to align the bunch for injection.

During anti-proton stacking (see below), the Main Ring is also used as a source of 120 GeV protons which are extracted onto a nickel target for antiproton production.

The Antiproton Source is comprised of a target station, a Debuncher ring and an Accumulator ring. The Debuncher and Accumulator occupy the same roughly triangular tunnel, with the Debuncher slightly larger by 6.6%. The accumulation of anti-protons involves extracting protons at 120 GeV with a small time spread from the Main Ring, directing them onto a Nickel target, collecting negatively charged particles in the Debuncher with an $\sim$ 8 GeV/c momentum from the secondaries and "cooling" the antiprotons so they may be stored in the Accumulator for later use in the Tevatron. About one antiproton is produced for every 10^5 protons striking the target. The cycle time is 2.4 seconds. This process continues for several hours until sufficient antiprotons are available for later injection into the Tevatron. About 5×10^{10} anti-protons are made per hour.

The narrow time spread and small incident proton beam size from the Main Ring helps minimize the phase space (or "emittance") of the emerging anti-protons which lessens the demands on the stochastic cooling system. A cylindrical lithium lens (15 cm long $\times$ 1 cm radius) is used to focus the anti-protons. The focusing is provided by an azimuthal magnetic field created by a longitudinal pulsed current of 0.5 MA which focuses the antiprotons parallel to the axis. A pulsed dipole magnet then selects 8 GeV negatively charged particles and directs them into the transport

line to the Debuncher.

The Debuncher reduces the momentum spread of the antiprotons through RF bunch rotation and then adiabatically debunches the beam by reducing the RF voltage over a period of milliseconds. The RF bunch rotation converts the small time spread into a small momentum spread. The transverse profile of the beam is further reduced (by about a factor of two) by betatron stochastic cooling before injection into the Accumulator. Cooling reduces the phase space occupied by the beam and reduces the amount of noise in the Accumulator by reducing the transverse oscillations of the beam.

The Accumulator has six straight sections yielding alternating high and low dispersion regions. The Accumulator (as well as the Debuncher) operate above transition such that the differences in particle momenta are seen primarily in their different path lengths. The difference in the orbit radius between low and high momentum particles is utilized in cooling the anti-protons. The anti-protons are adiabatically captured by a RF system and decelerated to the tail of the *stack* of previously injected antiprotons. The beam is then debunched by adiabatically reducing the RF voltage. Once in the stack tail, momentum stochastic cooling decelerates the particles, pushing them into the stack core which takes about an hour. Further cooling in the core occurs via momentum and betatron cooling in both the vertical and horizontal directions.

When the Tevatron is ready to accept anti-protons, the Main Ring is phase-locked to the Accumulator and a portion of the anti-proton stack is extracted into eleven RF buckets of the Main Ring, which are then accelerated to 150 GeV, coalesced and cogged, and injected into the Tevatron. About half the anti-proton stack is normally used in this process.

The Tevatron is a proton-antiproton colliding beam synchrotron using superconducting magnets cooled by liquid helium to 4.6 K. For Run 1, the Tevatron collided 900 GeV beams resulting in a center-of-mass energy of 1.8 TeV, currently the highest in the world. The Tevatron sits 65 cm below the Main Ring in the same 1 km radius tunnel. The RF systems of the two accelerators are attuned which yields nearly

100% beam transfer efficiencies between them. For Run 1, the Tevatron countercirculated six bunches of protons and six bunches of antiprotons and collided them at two luminous regions, one of them being B0 where the CDF detector resides (the other is D0 where the other collider detector at Fermilab sits). The crossing time between bunches was about 3.5 μs.

The proton and anti-proton bunches are injected into the Tevatron at 150 GeV from the Main Ring and are then ramped up together to 900 GeV. At 900 GeV, the beam is "messy" with particles orbiting just outside the acceptable radius, so the errant edges of the bunches are scraped off using collimators. Special low-beta quadrupoles on either side of the two luminous regions squeeze the beams and reduce the local β to $\sim$ 0.25 m. This dramatically decreases the beam spot size to $<$ 40 μm in the transverse plane which increases the luminosity. The bunches have an approximately Gaussian longitudinal profile of about 30 cm. Electrostatic separators around the ring separate the protons and anti-proton bunches, except at the luminous regions, which helps increase the beam lifetime. The bunches are kept in the machine for about 8-18 hours (called a *store*), during which time the luminosity decreases by about an order of magnitude. The minimum downtime between stores is about two hours during which CDF normally takes calibration data.

The Main Ring is usually used to make anti-protons while beam is in the Tevatron so as to minimize downtime. When the anti-proton stack is sufficiently large, the bunches in the Tevatron are dumped and fresh bunches are injected. Aside from maintenance periods, accesses into the collision halls for repairs or problems with the accelerators, the accelerator complex operates 24 hours a day.

Appendix C

The CDF Data Acquisition System

C.1 Run 1A Data Acquisition System

The Run 1A Data Acquisition system (DAQ) is shown in a schematic diagram in Figure C.1 which shows the data flow through the trigger logic channels and the digitized data flow from the detector front-end electronics. The Trigger Supervisor (TS) supervised the data flow through the hardware trigger system, consisting of the Level 1 and 2 triggers and FRED (Front-end Readout and Decision boards). The Buffer Manager (BFM), a process running on a dedicated VAX CPU, was responsible for coordinating the digitized data flow through the Fastbus crates, the Event Builders (EVB), Level 3 and the consumers while communicating with the TS. Fastbus [152] is a standardized, high-speed, modular data-bus system which consists of multiple bus segments that operate independently but link together for passing data. It was used for both data flow and control messages in the Run 1A system.

All components of the CDF DAQ are synchronized from the Master Clock which picks up its timing marker from the Tevatron RF system and sends the signal to the TS which coordinates the front-end electronics and the hardware trigger systems. The sampling of the detector components is signalled from the TS at the appropriate point with respect to the beam crossing. A subset of the analog signals, called *fast outs*, are split off from the data acquisition systems and sent to the Level 1 and 2 trigger systems. The Level 1 and 2 triggers are described separately in Sections 2.9.3 and 2.9.4.

The Level 1 and 2 triggers communicate with the TS through FRED, which also generates the Live/Dead gates for the luminosity determination. On a Level

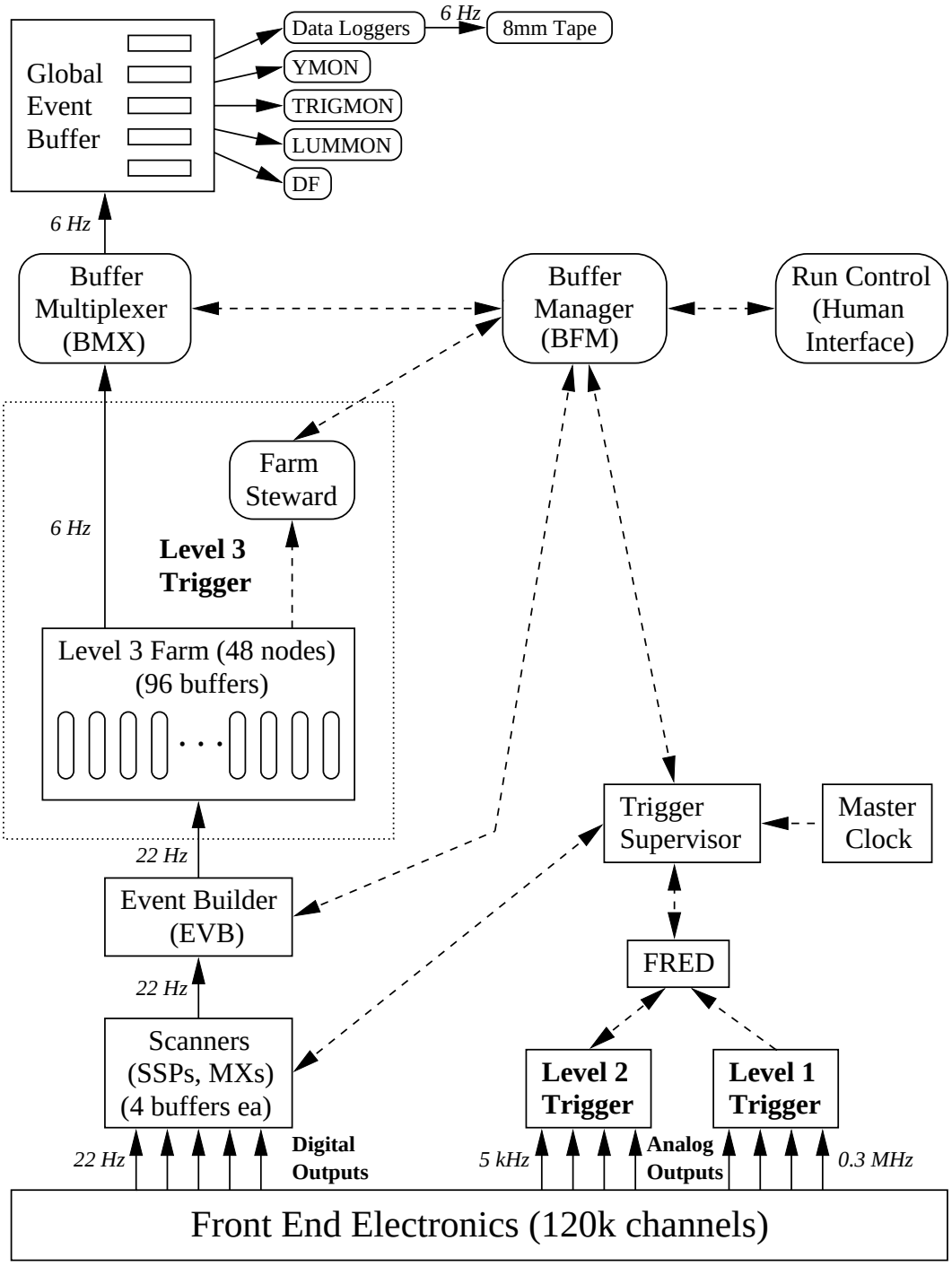

Figure C.1: Schematic of data flow through the CDF Data Acquisition system for Run 1A.

1 accept, FRED informs the TS which then inhibits the front-end electronics from clearing the sample-and-hold circuits. On a Level 2 accept the front-end electronics is signalled via the TS to digitize the event. The front-end electronics are contained in 60 Fastbus crates and 129 custom RABBIT crates [240] mounted on the detector in the collision hall. The calorimeters and strip chambers (CES) are read out by the RABBIT crates which involves the comparison of two voltage levels; a reference value just before a bunch-crossing and one just after, with the difference being proportional to the integrated signal-charge in a calorimeter module. This information is digitized by an analog-to-digital converter (ADC) card in each RABBIT crate and is read out by fast intelligent scanners, called MX's, which reside in Fastbus crates in the CDF counting room, outside the collision hall. The muon and drift chambers from the tracking systems have analog-signal-shaping-and-discriminator (ASD) cards in the Fastbus crates on the detector. These signals are brought up to commercial time-to-digital converter (TDC) modules in Fastbus crates sitting in the counting room. These are then read out by a second type of intelligent scanner called SSP's. Each MX or SSP scanner can buffer four events and handles approximately 1,000 channels. The buffering allows events to be handled in parallel and minimizes the deadtime associated with liberating the TS to receive new events. There are approximately 60 MX scanners and 25 SSP scanners. There are about 160,000 electronic readout channels in total, with about 60,000 for the calorimetry.

Once an event is completely read out (which takes about 3 ms) and digitized, the TS re-enables the DAQ to receive new events and the BFM prompts one of two Fastbus resident Event Builders (EVB) to pull the information from the readout scanner buffers. The EVB reformats the event information into the CDF standard YBOS data structure [167] and then pushes the event into a Level 3 buffer via a Fastbus to Branch-bus [1] to VME [2] connection. The maximum throughput into the Level 3 system was kept at about 22 Hz (200 kB/event) to avoid swamping the EVB's which were limited by large transfer setup and message overheads.

---

[1] Branch-bus is a bus interconnection system designed at Fermilab.

[2] VME is a flexible open-ended backplane interconnection bus system standardized as IEEE 1014.

Level 3 (see Section 2.9.5) runs physics algorithms on the event, which takes on the order of a second depending on the complexity of the event, and sets the trigger decision bits. The Farm Steward, the central controller for the Level 3 system running on a separate dedicated VAX CPU, informs the BFM that an event has completed processing and if the BFM decides that the event passes the selection criteria it instructs the Buffer Multiplexer (BMX) to pull the event from the Level 3 buffer into a global event buffer. The various data consumers, mostly running on separate VAX processors, read out the events (over an independent Branch-bus) from the global buffer based on the trigger decision. These consumers include the data loggers which write the events to 8 mm tape, a luminosity monitor, a trigger monitor, various detector performance monitors and online event displays.

The trigger system successfully maintained an average of about 85% livetime during Run 1A.

C.2 Run 1B Data Acquisition System

Most of the DAQ between the front-end scanners to the consumers was replaced for Run 1B. The hardware trigger system and data flow remained essentially unchanged apart from some minor improvements in the trigger logic boards in Level 2, which allowed the implementation of a tau neural net trigger. Unfortunately, due to various problems, to date this trigger has not been used for any physics analyses and I will not discuss it further.

A diagram of the upgraded architecture is shown in Figure C.2. The main improvements are new front-end read out scanners and the replacement of Fastbus and Branch-bus as the data and control message communication pathways with two physically independent commercial networks for the logically independent data and control message paths. The Level 3 system was also redesigned and made more modular with more internal intelligence and control, allowing greater reliability and scalability of the system both for Run 1B and as part of the future Run 2 system [241]. There is no central Farm Steward anymore and each Level 3 box is responsible for

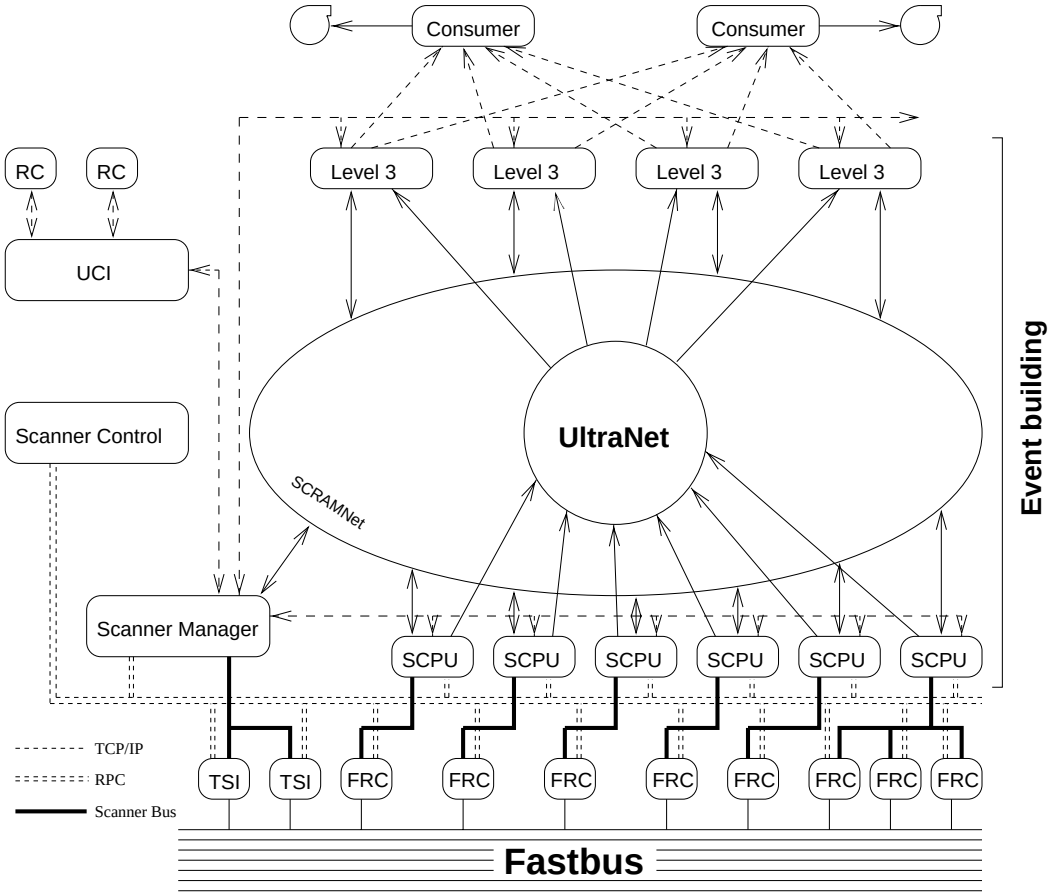

Figure C.2: Schematic of data flow through the CDF Data Acquisition system for Run 1B.

its own intelligent control. Due to advances in CPU power, the Event Builders could be replaced by processes that run in the Level 3 system. As the Rutgers group was responsible for the design and implementation of the upgraded Level 3 system (as well as the Run 1A system), I have described the event data flow and control through Level 3 in somewhat more detail below in Section C.3.

In the Run 1A DAQ system, events were logged directly to tape. For Run 1B, events were logged to staging disks and were then copied to tape. As 8 mm tape drives proved somewhat unreliable, the staging step removed a small source of dead-time from the DAQ and enhanced the data-logging reliability.

Starting at the front-end, the SSP's were replaced by new custom Fastbus Read-out Controllers (FRC). These are based on the MIPS R3000 processor and run

VxWorks, a real time Unix-compatible operating system. The FRC's readout all the modules in a crate. FRC's also provide the interface for the MX readout. A series of six single-board VME based Scanner CPUs (SCPU) then each read out a subset of the FRC's over a new custom built Scanner Bus.

The data from the SCPU's is then transfered to Level 3 over Ultranet, which is a high-bandwidth proprietary commercial network. Ultranet consists of a central *hub* that connects the various components of the DAQ (via host adapters) in a "star" architecture, with point-to-point links from the hub to the host adapters. The Ultranet-1000 hub backplane used at CDF can support an aggregate of 100 MB/sec transfers and any serial link can transmit data at a rate of 250 Mbit/sec. Transfer rates between VME based interfaces are limited to about 13 MB/sec, excluding overheads. The effective operational bandwidth, due to setup overheads etc., for 32 kB block sizes is about 5–7 MB/sec per connection or an aggregate of 30–40 MB/sec for the six SCPU's. During Run 1B the maximum input rate to Level 3 was roughly 12 MB/sec and out 1 MB/sec. Ultranet uses standard UNIX BSD socket libraries and provides internal monitoring and control of the network.

Control and synchronization of the data flow is done by processes running on a dedicated VME-based CPU called the Scanner Manager (SM). The SM has the responsibility of ensuring that all fragments of a particular event are delivered to the same Level 3 processor. To this end, the SM contains a list of free memory buffers in Level 3 and communicates this information to the SCPU's which then set up the data transfer over Ultranet to the correct Level 3 memory buffer. Communication with the Scanner CPUs, Scanner Manager and the Level 3 systems is via a dedicated reflective-memory network called Scramnet (Shared Common RAM Network). Memory modules are located in each Scanner CPU and Level 3 VME crate and are connected via 150 Mbit/sec fiber-optic cable. A write operation to a word in one module is automatically propagated to all modules in the network using a proprietary protocol, with less than 1 μs latency. This provides a very fast, reliable, and low overhead means of communicating small data packets (such as messages) as well as being completely independent of the data flow medium which avoids network

collisions and subsequent delays.

The SM crate also contains the User Control Interface (UCI) and the Error Monitor processes, running on local single CPU VME boards. Thus command passing from the DAQ user (via Run Control) to and from the SM (which controls the entire system) is implemented via yet another independent path, the VME bus of the SM crate. The SM crate has access to the status of each element in the system, which enhances the error monitoring, logging and recovery.

An FRC in the Trigger Supervisor (TS) crate provides the interface to the Scanner Manager. As in the Run 1A DAQ system, the TS is the intelligence which provides the link between the analog trigger data paths and the fully-digitized data path. It also broadcasts the "Digitize Event" control signal to all the front-end electronics and notifies the SM of the presence of a new event. The SM in turn notifies the TS when an event has been completely read out, thus freeing the front-end for more triggers.

The Level 3 processor farm runs a similar physics algorithm to the Run 1A system to decide which events should be logged. In addition, Level 3 must now receive the 6 separate Scanner CPU fragments and build the complete event for the single trigger as was previously done by the Event Builder in the Run 1A system. This process occupies less than one CPU in a box. Individual event buffers are no longer tied to a particular CPU; shared memory with message handling protocols allow any one processor to work on any buffer at a given time. All the internal control software was rewritten to handle the new buffer management. Each box is autonomous and there is no central Buffer Manager or Farm Steward. All data flow and control now operates internally via shared message queues and externally via reflective memory or client-server socket connections in the case of the interface to Run Control or for communication with the Consumer Server. An independent display and error reporting process running in the control room showed the real-time status of the Level 3 trigger system. A more detailed discussion of the event flow and control in the Level 3 system is given in the next section.

Accepted events are sent out via Ultranet again to a dedicated SGI system, the

Consumer Server (CS). The CS processes distribute events to local data logging processes as well as remote monitoring processes via Ethernet or FDDI using TCP/IP. Consumer processes may request events based on their classification by the Level 3 algorithm. They send their requests to the CS via Ethernet which forwards the request along to Level 3 along with their priority. Events are logged to approximately 17 GB of local SCSI disks and spooled asynchronously to 8 mm tape. A total logging rate of approximately 2 MB/sec, corresponding to approximately 20 Hz, can be supported. Typical rates for normal data taking were 6-8 Hz.

C.3 Run 1B Level 3 Trigger System

The CDF Level 3 Trigger system is implemented in software on multiprocessor computing systems. The Run 1A system has been described in detail elsewhere [242, 243] and I will describe the data flow through the upgraded Level 3 system for Run 1B. The trigger logic at Level 3 is described in Section 2.9.5.

The Run 1B Level 3 system ran on multiprocessor Silicon Graphics Unix machines running the IRIX operating system. There were four Power Server series systems with 8 MIPS R3000 processors in each and four Challenge series systems with 8 or 12 MIPS R4000/R4400 processors in each and 128 MB of RAM in each system.

The Level 3 system has been reimplemented for Run 1B as a finite state machine. This means that the system and processes in it are in some known state at all times with only certain "state transitions" allowed, governed by a set of system coherency rules. When a command or request is sent to a process to change state, it either goes into a specific state or, failing that, returns to a previous known state or error state, allowing automatic recovery and error notification. Communication between processes is accomplished through interprocess communication messages (IPC) or messages over TCP/IP sockets between clients and servers over the various networks described in the previous section.

A diagram of the overall Level 3 Trigger system design is shown in Figure C.3 and the internal processes, message queues and buffers for one Level 3 box is shown

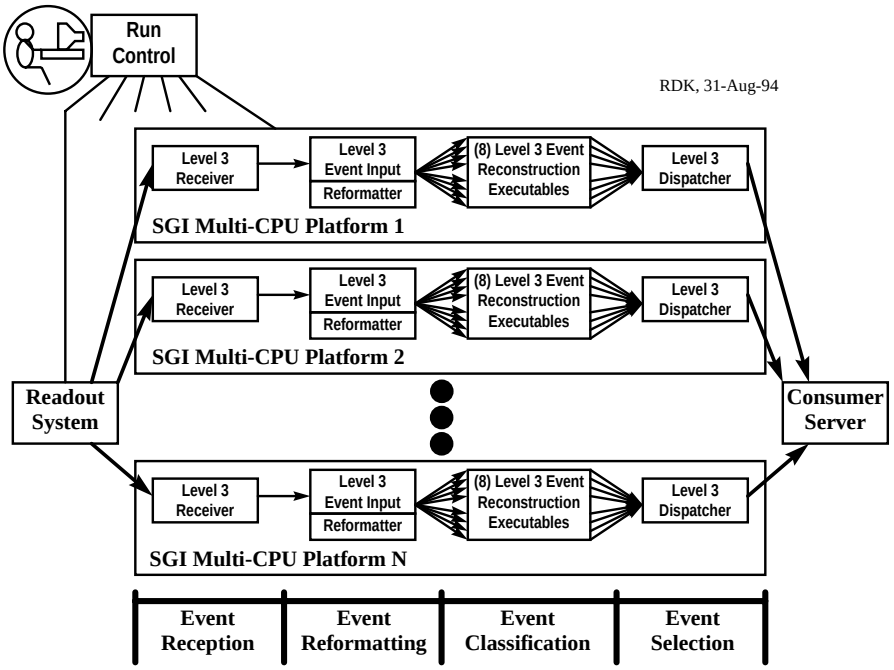

Figure C.3: Diagram of the overall data flow through the Run 1B Level 3 Trigger System.

in Figure C.4. An example of the states and transitions allowed in the system is shown for one of the processes (the Level 3 Run Control Server) in Figure C.5. Each process in the system has a state diagram which may involve different states and transitions.

Events (buffers) in Level 3 are stored in shared memory segments to allow multiple processes to access them without the overhead of memory-to-memory copying. Message-queues maintain the up-to-date status of the buffers and prevent collisions between processes trying to access them. A number of internal processes monitor the state of the event buffers and of the analysis processes which work on the data, to ensure that events flow efficiently through the system.

During data taking, on a Level 2 trigger accept, the Scanner Manager assigns a free Level 3 Input Buffer to the Scanner CPUs to which they will feed their data. Each scanner is assigned an offset-address to a block of space within the buffer and the event fragment is transmitted through Ultranet. A Level 3 Receiver process

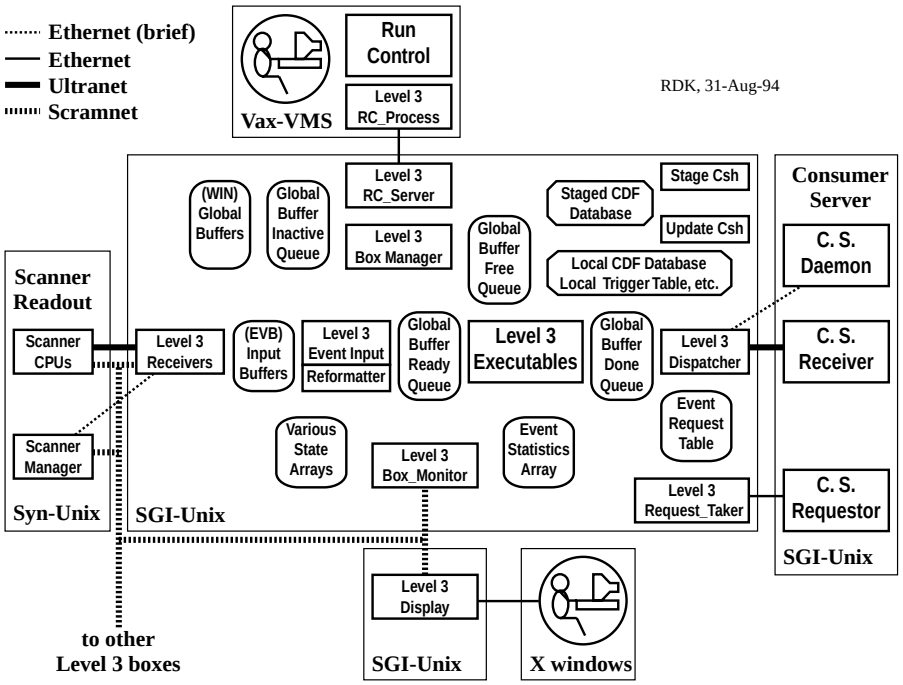

Figure C.4: Diagram of one Level 3 Box showing the processes, message queues and data buffers.

within each Level 3 box monitors the input buffer and, when all event fragments have been received, passes the buffer to the Level 3 Event Input process which reformats and checks the event structure. The event is then analyzed by the Level 3 Executable which runs similar software to that run offline for event reprocessing, with slightly different algorithms for tracking and without SVX reconstruction. Results of the trigger decisions are included in the output buffer and, if there is a match to any consumer request, the event is shipped over Ultranet to the Consumer Server (CS) by the Level 3 Dispatcher process. The CS keeps a list of event requests for all the consumers, which can change dynamically during a run, and submits these requests, via Ethernet, to the Level 3 Request Taker process which keeps the Event Request Table up to date. The data banks that are output are normally just the raw data banks plus the trigger results with one proviso that the TDC information from the VTX, CTC and CMX tracking chambers are reformatted by the Level 3 Executable before being output. Some consumers, such as the event display processes, request

fully reconstructed events with all the reconstruction data banks intact. These events are deemed non-critical and hence these requested events may be dropped from the output stream by the Level 3 system if the data stream becomes clogged due to too many events.

A separate Level 3 Box Monitor process in each box monitors the box status and updates these data in the reflective memory module in each Level 3 box. This allows external monitoring of the Level 3 farm by a separate Level 3 Display process which updates a display in the control room with the current status of the Level 3 boxes and reports errors. The shared data also allows logging of statistics across the farm such as the number of events into and out of the system, average processing times, etc.

Current data base constants, trigger tables and Scanner Manager configuration files are kept up to date via the Level 3 Box Manager process which fetches the necessary files at the begin of a run. Communication with Run Control is maintained over Ethernet by the Level 3 Run Control Server process which is also the human operator interface to the Level 3 system.

Various utility programs are also started by the Level 3 Box Manager at the end of a run to collect statistics files and print them out in the control room and to maintain the log files for the various processes. Events that cause a crash of the Level 3 Executable are stored on local disk files along with the executable core dump to facilitate debugging software or data problems.

For Run 1B the peak rate into Level 3 was estimated at 40–55 Hz limited mainly by the readout times of the MX and FRC scanners. The Level 3 system itself is highly scalable as more CPU and memory could be added very easily (which was done part way through the run) to handle higher luminosities or lowered trigger thresholds. The bandwidth through the Ultranet hub would then be the limiting factor and this will be replaced by an Asynchronous Transfer Mode (ATM) system for Run 2 [241].

RDK
12-Apr-94

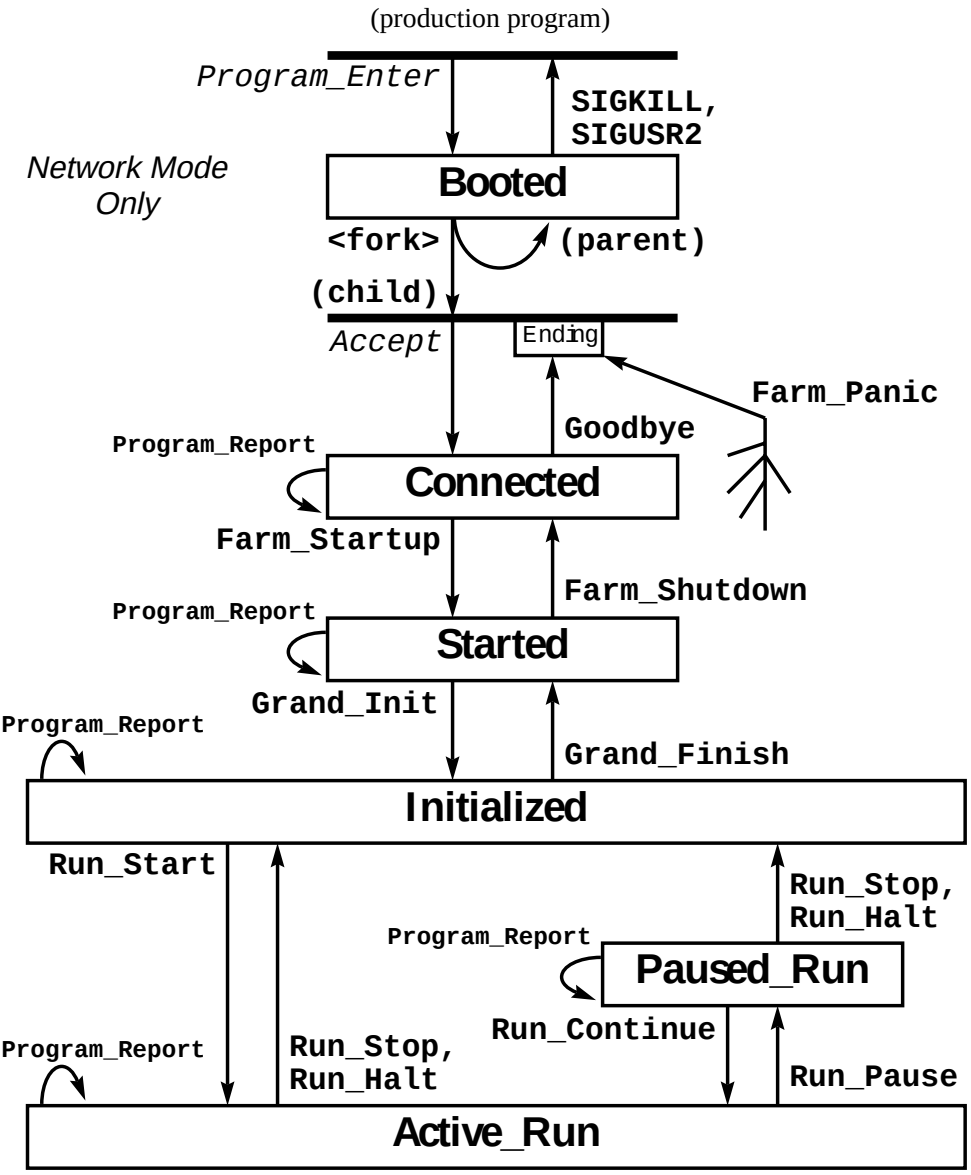

Figure C.5: Diagram depicting the *states* (in boxes) and allowed *transitions* (arrows) for the Level 3 Run Control Server which runs in a Level 3 box and communicates with Run Control via sockets over Ethernet.

Appendix D

Missing E_T Trigger Efficiencies

The primary data selection for the charged Higgs analysis depended on the online Exotics $\not\!\!E_T$ triggers, as described in Chapter 4. An understanding of the "turn-on" efficiencies for these triggers is crucial in estimating the acceptance for charged Higgs events. This appendix describes a study of these efficiencies for the triggers for the Run 1B data. A similar trigger efficiency study was conducted by Christian Couyoumtzelis for his thesis [95, 244] and a subsequent published paper [94] on a similar search for the charged Higgs bosons from top quark decays done using the CDF Run 1A data only. His results are not much different from the Run 1B results as will be shown later and are used in modelling the trigger turn-on for this analysis for the Run 1A data.

To measure the trigger efficiencies for the $\not\!\!E_T$ triggers an unbiased set of data is needed which will have a reasonable number of events with a fair spread in $\not\!\!E_T$. The inclusive jet trigger data, Jet 20, Jet 50 and Jet 70, were chosen for this study as these triggers are essentially unbiased as far as $\not\!\!E_T$ is concerned. A few other cuts are placed on the data to further remove any biases. The inclusive jet triggers are described in further detail in Chapter 4. These data sets were reprocessed with the same algorithm as used for the charged Higgs data selection, with similar "bad run" removal, as described in Section 4.5.

Comparisons with some of the Monte Carlo generated samples were also made (see Chapter 6). This was in an attempt to model the trigger, so that the trigger efficiencies could be simulated, however simulation of the Level 2 trigger turn-on proved inadequate in describing the shape and a parameterized fit to the turn-on efficiency from the jet data was derived instead.

D.1 Level 2 Trigger Efficiency Measurement

The data selection from the Run 1B data depends on the Level 2 trigger MET_35_TEX_2_NOT_GAS (hereafter referred to as the Level 2 MET35 trigger) and the Level 3 EXOB_MET_30_COSFLT trigger (referred to later as the Level 3 MET30 trigger). The Level 3 trigger was essentially fully efficient for the cuts used in the charged Higgs analysis, especially as we require both the Level 2 and Level 3 triggers to have fired in the final data selection. The Level 3 trigger will be discussed in more detail in the next section.

The Level 2 MET35 trigger required $\not\!\!E_T > 35$ GeV and a central jet with at least 2 GeV of electromagnetic calorimeter energy. See Chapter 4 for the discussion of the trigger details and thresholds. As the number of events failing the analysis cuts falls sharply as we raise the required $\not\!\!E_T$ threshold, we would like to have this cut as close to the trigger threshold as possible. The efficiency of the online $\not\!\!E_T$ requirement therefore becomes important in modelling charged Higgs events.

A large source of events with spurious missing E_T can be excluded by excluding events that have energy deposits in the calorimeters that appear "out-of-time" i.e. do not coincide with a bunch crossing in the Tevatron. These are usually from interactions with the beam and gas in the beam pipe or stray particles in "satellite" bunches that are out of phase with the main bunches in the Tevatron. Another source of these out-of-time deposits could be cosmic-rays passing through the detector. In the efficiency study, events with any out-of-time E_T are rejected as these have disproportionally high $\not\!\!E_T$, which would skew the trigger efficiency measurement. This rejects about 4%, 20% and 30% of the original Jet 20, Jet 50 and Jet 70 data sets respectively.

After this removal, there is still a difference between the $\not\!\!E_T$ as measured from the Level 2 trigger calorimeter towers and that measured from the reprocessed data, with the Level 2 measurement being somewhat higher in general for all three jet trigger data sets. This is as expected as the full offline measurement has better resolution and includes cleanup and corrections for photo-tube spikes etc. This difference can

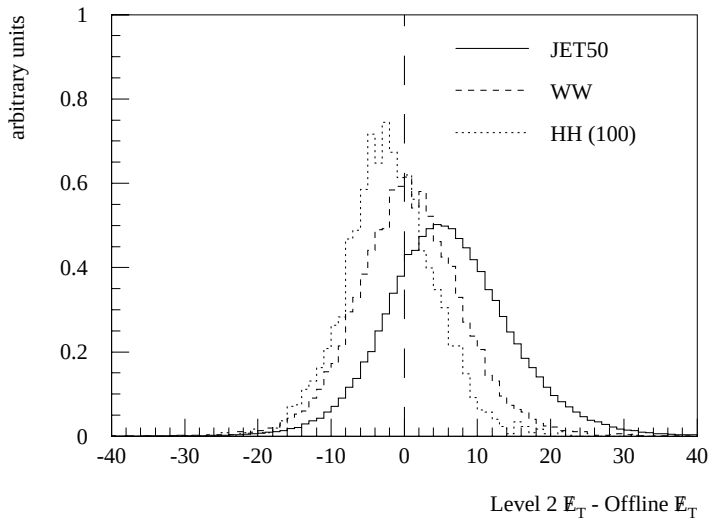

Figure D.1: Difference between Level 2 $\not\!\!E_T$ and $\not\!\!E_T$ measured after offline production for the Jet 50 trigger sample and two ISAJET Monte Carlo generated samples simulating $t\bar{t}$ production and decay in standard model modes (WW) and via a charged Higgs (HH) with $M_t = 175$ GeV/c^2 and $M_{H^\pm} = 100$ GeV/c^2.

be seen in Figure D.1 which shows the distribution of the difference between the Level 2 $\not\!\!E_T$ measurement and the offline $\not\!\!E_T$ in the Jet 50 data.

The ISAJET Monte Carlo data samples (see Chapter 6) of top decaying via $t\bar{t} \rightarrow W^+ b\, W^- \bar{b}$ and $t\bar{t} \rightarrow H^+ b\, H^- \bar{b}$ with $M_t = 175$ GeV/c^2 and $M_{H^\pm} = 100$ GeV/$c^2$are used for a comparison. These data samples have simulations of the Level 2 clustering for the trigger towers. Figure D.1 also shows the difference between the simulated Level 2 $\not\!\!E_T$ versus the offline $\not\!\!E_T$ for these data sets. The simulated Level 2 $\not\!\!E_T$ is more consistent with the offline $\not\!\!E_T$ here than in the real data. This is an indication already that the trigger efficiency cannot be modeled by the Monte Carlo data.

To obtain a consistent baseline against which to measure the efficiency, the Level 2 MET35 trigger jet criteria are applied to the jet data. These criteria are that the highest E_T jet is central (corresponding to trigger towers 16–25) and has electromagnetic energy $E_T > 2$ GeV. This step is necessary as there are many events in the jet data sets that do not pass this criteria but have large $\not\!\!E_T$ offline. Not removing these events in the denominator would show up as a trigger inefficiency. These events could be from interactions that did not occur near the nominal interaction point at

Events	Jet 20	Jet 50	Jet 70	WW	HH
total	506180	324156	368905	50000	10000
require out-of-time $E_T = 0$	479219	270768	262942	20188	3971
passing Level 2 criteria	268718	189253	204770	18506	3504
passing Level 2 MET35 trigger	1666	19121	43965	7846	2297
passing Level 3 MET30 trigger	1464	15883	36621	—	—
passing Level 2 and Level 3	607	10505	27702	—	—

Table D.1: Number of events from the inclusive jet triggers and from Monte Carlo data passing the selection cuts used in the trigger efficiency measurement.

the center of the detector and left large calorimeter deposits in the forward or plug regions.

The number of events passing these criteria in each data set are shown in Table D.1, along with those passing the Level 3 MET30 trigger. There is no modelling of the Level 3 trigger in the Monte Carlo data.

To calculate the trigger efficiency a bin-by-bin comparison (5 GeV bins) is made of the number of events in the jet data that passed the Level 2 MET35 trigger online from the total number of events that remain after applying the Level 2 trigger jet criteria on the highest E_T jet. This gives the turn on efficiency for the online trigger. Plots of the turn on efficiencies measured for the three jet data sets are shown in Figure D.2. The error bars are calculated using binomial error estimates.

The turn on for the missing E_T trigger efficiency is quite shallow. The efficiency from the Jet 70 data set seems to turn on earlier than the Jet 50 or the Jet 20. The general shape of the turn on curve seems to be similar for the three data sets, just displaced to the left (i.e. lower $\not\!\!E_T$ energies) for the higher E_T jet data sets. Taking the three data sets into account, the trigger seems to be 90% efficient only at $\not\!\!E_T > 60$ GeV, although the nominal threshold is 35 GeV.

Figure D.3 shows the turn on for the Level 2 $\not\!\!E_T$ trigger simulation for both the WW and HH MC samples. Note that the turn on for both these samples is significantly sharper than in the real data (the Jet 50 efficiency is plotted in Figure D.3 for comparison).

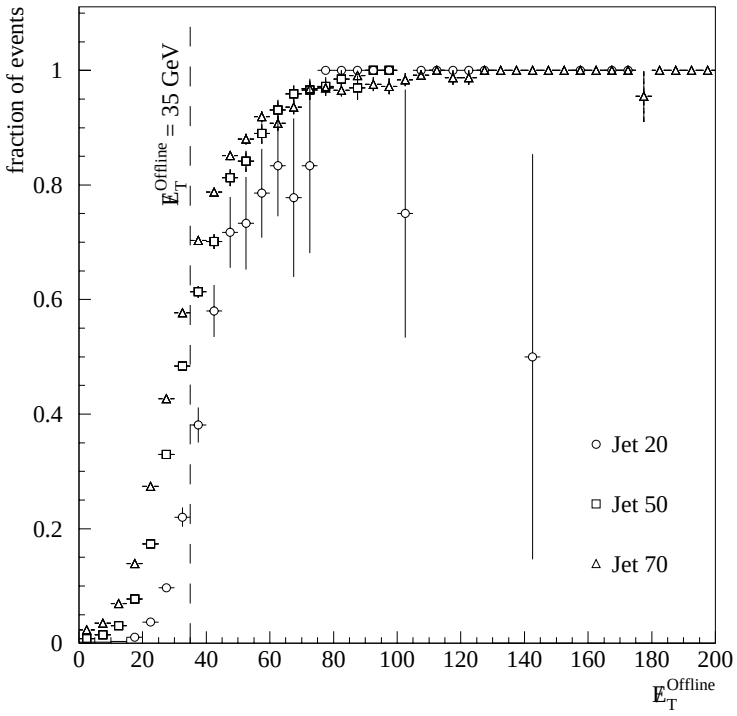

Figure D.2: Level 2 MET35 Trigger efficiency measured in the Jet 20, Jet 50 and Jet 70 data.

As a cross-check, a sample of generic jets from gluon and quark fragmentation was also generated using ISAJET. The minimum p_T thresholds for the jets was set to 50 GeV/c to increase the efficiency for passing the $\not\!\!E_T$ requirements. The Level 2 MET35 trigger was simulated and the resulting trigger turn on efficiency curve overlapped those of the WW and HH Monte Carlo samples and again does not compare well with the jet data.

This steep turn on in simulated data, coupled with the difference noted in Figure D.1 between the Level 2 $\not\!\!E_T$ measured in data and in the simulation when compared to the offline $\not\!\!E_T$, leads to the conclusion that the simulated data cannot be used to model the trigger efficiency. A parameterization of the efficiency measured in the Jet 50 data is therefore used in the charged Higgs analysis. An attempt was made to fit this turn-on efficiency shape using both an error function and hyperbolic tangent, neither of which gave a very good fit. This fit was abandoned in favor of parameters using the raw efficiencies which were encoded in a FORTRAN function

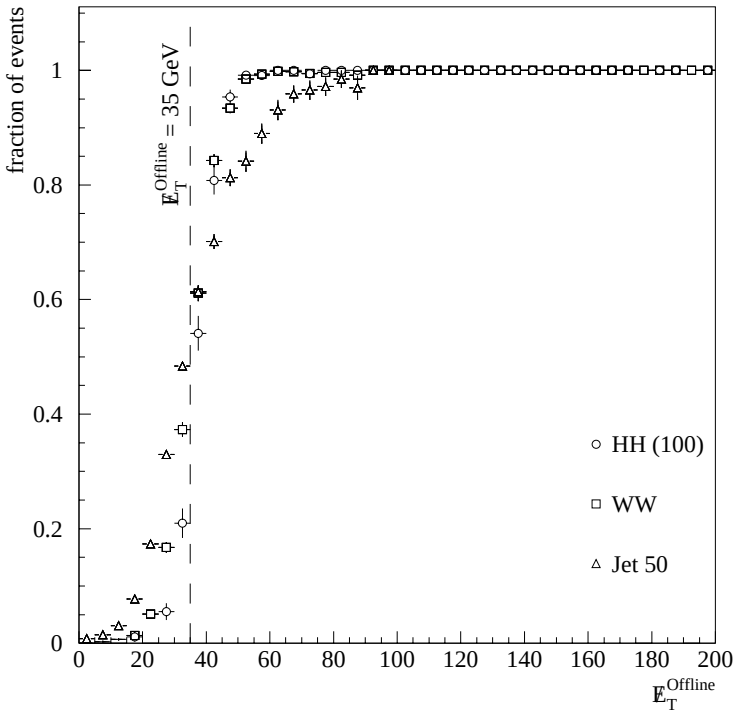

Figure D.3: Level 2 MET35 Trigger simulation efficiency measured from ISAJET MC $t\bar{t} \rightarrow W^+W^-$ and H^+H^- ($M_{H^\pm} = 100$ GeV/c^2). The efficiency from Jet 50 is also shown as a comparison.

that was used to simulate the trigger efficiency for the Monte Carlo data. Figure D.4 shows the parameterization curves used to simulate the $\not\!\!E_T$ trigger efficiency, derived from the Jet 20, Jet 50 and Jet 70 data. The parameters for the Jet 20 data set have been smoothed (using a moving average) to give a smoother turn on as a function of uncorrected offline $\not\!\!E_T$.

The turn-on efficiency of the Level 2 Missing E_T triggers was measured in a similar fashion for the Run 1A data set, by C. Couyoumtzelis. He did not separate out the different jet triggers, which were the same in Run 1A as in Run 1B, but measured their combined efficiency. We use his results for the combined Run 1 charged Higgs analysis. The parameterized curve for this turn on is also shown in Figure D.4. For $\not\!\!E_T$ in the region of interest ($\not\!\!E_T > 30$ GeV) this parameter set does not look much different from the Jet 20 parameter set.

There is a systematic difference between the various turn on curves as calculated from the different jet trigger data sets. What we are concerned with is the effect this

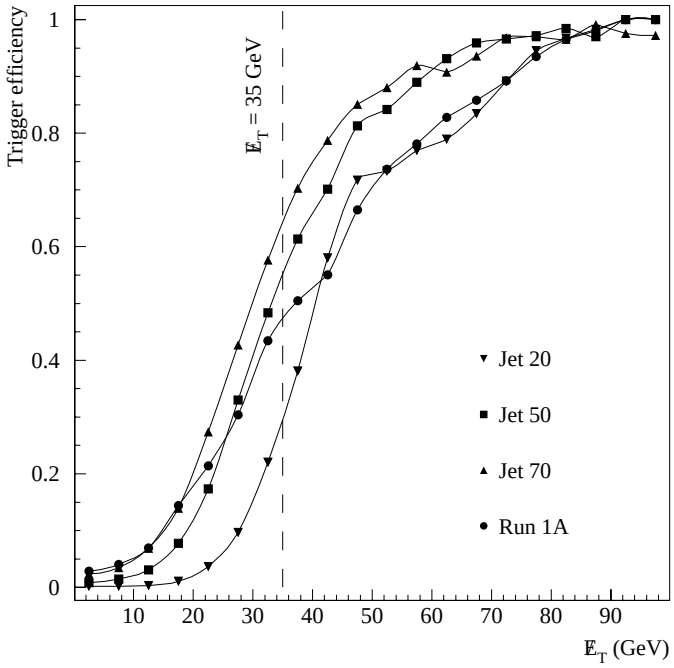

Figure D.4: Parameterization of Level 2 MET35 trigger turn-on efficiencies based on the inclusive jet triggers. The Run 1A curve is for all Run 1A inclusive jet triggers combined. Lines are drawn to guide the eye only. The central value in each bin is used for the parameterization.

will have on the calculation of the acceptance for the charged Higgs analysis. The Jet 50 parameterization is used in the final analysis to model the Level 2 $\not\!\!E_T$ trigger turn on. The difference in the acceptance using the Jet 20 and Jet 70 parameter sets is used as an estimate of the systematic uncertainty in the final acceptance caused by the uncertainties in modelling the trigger turn-on. This is done by calculating the acceptance for simulated charged Higgs events passing all the cuts, including the Level 2 trigger $\not\!\!E_T$ turn-on efficiency, as described in Section 5.10, using the different parameterizations and taking the difference in the acceptance as the systematic uncertainty.

The acceptances calculated for $t\bar{t} \rightarrow H^+ b\, H^- \bar{b}$ using the the three Run 1B jet parameter sets and the Run 1A parameter set for $M_t = 175$ GeV/c^2 and various Higgs masses are shown in Table D.2. Comparing the average acceptances, the relative difference between the highest (Jet 70) and lowest (Jet 20) is 12.7 $\pm$ 2.9%.

$M_{H^\pm}$	Parameter set			
(GeV/c^2)	JET20	JET50	JET70	RUN 1A
40	2.28±0.15	2.54±0.16	2.58±0.16	2.29±0.15
60	2.14±0.15	2.45±0.16	2.43±0.16	2.20±0.15
80	2.04±0.14	2.35±0.15	2.48±0.16	2.11±0.15
100	2.72±0.16	2.99±0.17	3.09±0.18	2.78±0.17
120	2.40±0.15	2.62±0.16	2.67±0.16	2.41±0.16
140	1.85±0.14	2.03±0.14	2.02±0.14	1.85±0.14
160	0.48±0.07	0.50±0.07	0.52±0.07	0.48±0.07
Average	1.99±0.05	2.21±0.06	2.26±0.06	2.02±0.05

Table D.2: Acceptances (%) for $t\bar{t} \rightarrow H^+ b\, H^- \bar{b}$ using the measured Level 2 $\not\!\!E_T$ trigger turn-on parameter sets.

A comparison between the individual acceptances shows that the relative difference between any two parameter sets is basically flat over all the different mass regions. Simulated data with $t\bar{t} \rightarrow W^+ b\, H^- \bar{b}$ gives the same relative difference in the acceptance for the different trigger parameter sets.

The Jet 50 parameter set is used in the charged Higgs analysis. As the relative difference between the Jet 50 and the Jet 70 is within the errors, the main systematic difference comes from the difference between the Jet 50 and Jet 20 parameter sets. The relative difference between these two sets is $10.0 \pm 4.8\%$, based on comparing the average acceptances over all the mass points. This systematic difference is basically flat over all the charged Higgs mass points. A systematic error of 10% is therefore taken for the uncertainty in the Level 2 $\not\!\!E_T$ trigger turn on for the charged Higgs analysis.

A similar comparison was made using different top masses during the generation of the simulated $t\bar{t}$ data and the systematic difference between the acceptances derived using the Jet 50 and Jet 20 parameterization remains about 10%. This was also checked in the $t\bar{t} \rightarrow W^+ b\, H^- \bar{b}$ samples and holds true there as well.

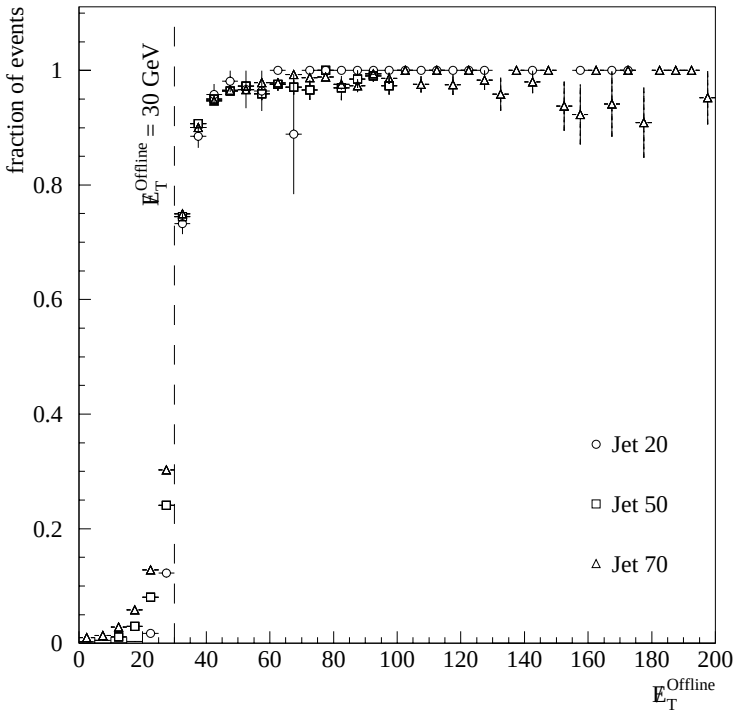

Figure D.5: Level 3 MET30 Trigger efficiency measured from the Jet 20, Jet 50 and Jet 70 samples.

D.2 Level 3 Trigger Efficiency Measurement

The turn on efficiency for the Level 3 EXOB_MET_30_COSFLT (MET30) trigger, which had a slightly lower $\not\!\!E_T$ requirement of 30 GeV, is measured in a similar way to the above. Note that $\not\!\!E_T$ measured at Level 3 is similar to that measured offline as fully digitized information is used at Level 3 and not just analog trigger tower information which was all that was available at Level 2. Table D.1 shows the number of events passing the Level 3 trigger from the jet data. Figure D.5 shows the trigger efficiency measured in the three jet trigger data sets. The trigger turn-on is much steeper here and is pretty much consistent among the three sets, especially for $\not\!\!E_T > 30$ GeV. This trigger is 90% efficient by $\not\!\!E_T = 37$ GeV. The turn on here is steeper for the Jet 20 data set tham the Jet 50 which is steeper than the Jet 70.

The last row in the table shows the number of events that pass both the Level 2 MET35 and Level 3 MET30 triggers. About one-third of the events passing the Level 3 trigger fail to pass the Level 2 trigger due to the inefficiency of the Level

2 trigger. As we require both the Level 2 and Level 3 triggers to have fired and significant offline $\not\!\!E_T$ in the charged Higgs analysis, the Level 3 trigger is essentially 100% efficient for us. It was therefore not necessary to model the Level 3 trigger in the simulated data.

Appendix E

Tau Fake Rates

To estimate the fake rate for hadronic tau identification, an unbiased sample of events with a low fraction of real hadronic taus is required. The electron ξ cut is very efficient at removing electrons mimicking a tau. Therefore, the majority of fake identified taus will be from QCD jets which have a low track multiplicity and form a narrow jet cluster. To obtain an unbiased sample of jets, the inclusive jet data (Jet 20, 50 and 70) were used in a study by C. Loomis [180]. To minimize any biases from the triggers, jets are only included in the analysis sample if there is another jet in the event that could have passed the trigger requirements.

A selection of jets meeting the following requirements was made. All jets in an event are considered. For the selected jet to be included in the sample, there must be at least one other calorimeter tower in the event outside a 0.7 cone around the selected jet which satisfies the Level 1 trigger calorimeter requirement. Then there must be another jet in the event with a matching Level 2 cluster that is above the Level 2 E_T threshold, and finally, the offline E_T of this other jet must be above the Level 3 trigger threshold. As the Jet 20 trigger required 2 GeV of electromagnetic calorimeter energy for the leading jet in the event, this leading jet is excluded in the final jet sample. These requirements ensure that all the selected events are not subject to any trigger biases.

The tau identification cuts are then applied to all the jets in the final sample. The fake rate is defined as the fraction of jets that create a TAUO object which have a track pointing back to the event vertex within 5 cm which pass all the tau identification requirements. The fake rates are very different for TAUO objects that do not have a track coming from the event vertex. This is probably due to minimum

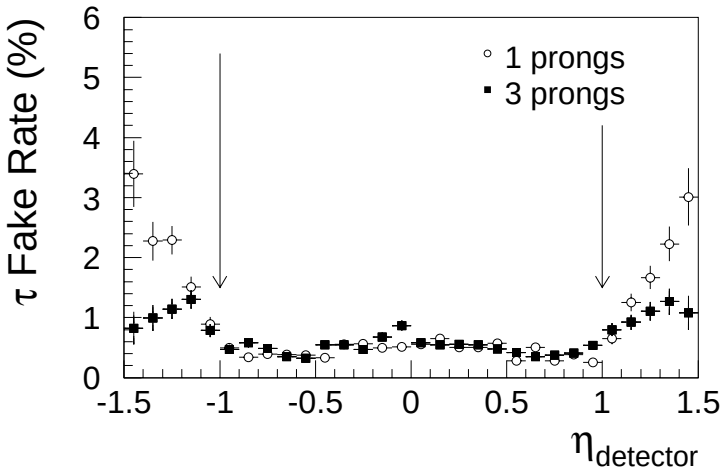

Figure E.1: The tau lepton fake rate as a function of detector pseudorapidity, η_{det}.

bias jets coming from other interaction vertices in the event which will have a different energy profile than those from a hard-scattering process.

The fake rate is parameterized as a function of the tau E_T (coming from the TAUO object) and the number of tracks (1 or 3) in the 10° tau cone. They are also separated out for the three jet trigger samples to examine any systematic differences. A strong dependence on the position of the tau candidate in the calorimeter in pseudorapidity is seen as shown in Figure E.1 for the 1-prong and 3-prong taus separately. As the tracking resolution drops dramatically past $|\eta_{det}| > 1$, the tau identification cuts require tau candidates to be in the central region only to avoid these large fake rates in the forward/backward regions of the detector.

Figure E.2 shows the fake rates as a function of the tau E_T for the three jet samples separately. There is good agreement over most of the range in E_T between the samples. There is a systematic difference, however, between the Jet 20 sample and the other two for $E_T < 30$ GeV. The largest fractional difference is 50%. Half of this difference (25%) is therefore taken as the estimate of the systematic uncertainty for the fake rates.

The invariant mass distribution of the tau fakes is shown in Figure E.3. It is clear that these are not consistent with being from a tau decay.

The final parameterized fake rate for taus (f_τ) using all the jet samples is shown

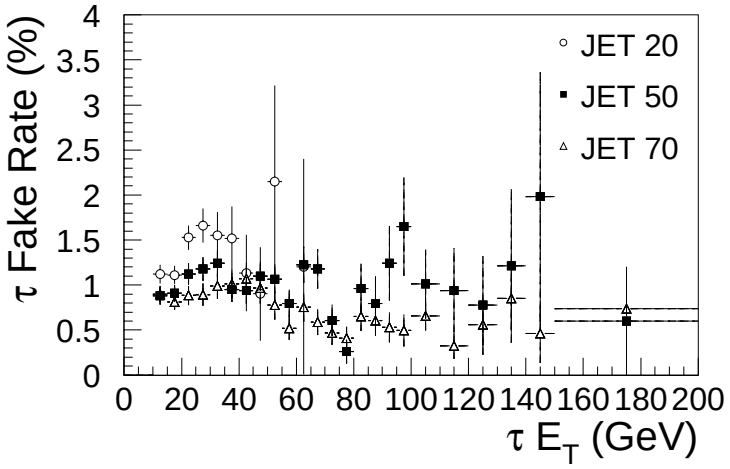

Figure E.2: The tau lepton fake rate parameterized as a function of tau E_T for the individual jet datasets.

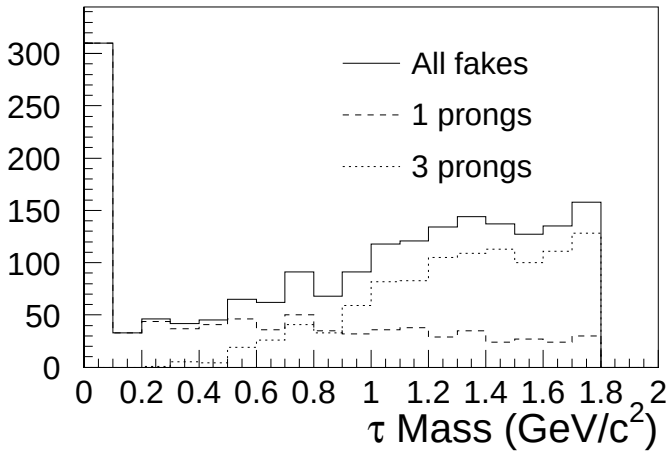

Figure E.3: The invariant mass distribution from fake tau leptons.

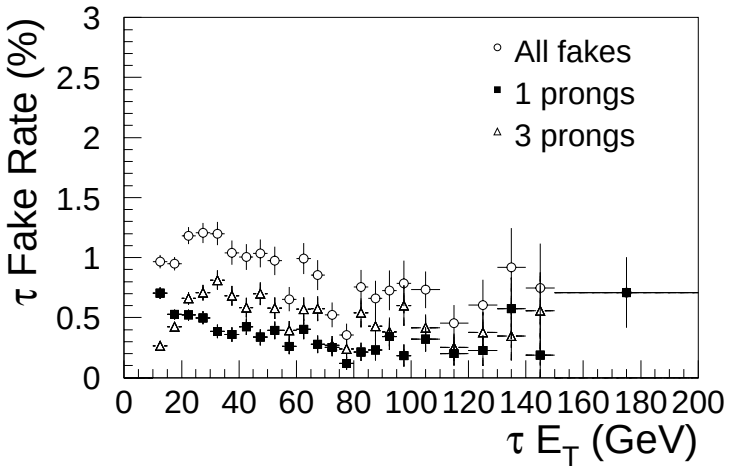

Figure E.4: The tau lepton fake rate parameterized as a function of tau E_T using all the jet samples.

in Figure E.4. The fake rate decreases from approximately 1.2% at 20 GeV (the minimum $E_T$requirement for the primary tau in the final event selection in the charged Higgs analysis) to about 0.7% for $E_T > 100$ GeV.

To check the fake rates derived from the inclusive jet samples, a similar procedure in deriving the fake rates was applied to the Run 1B inclusive electron and muon (lepton) samples. Here selected events were required to have an event vertex within 60 cm of the nominal interaction point, $\not\!\!E_T^{obj} > 20$ GeV derived from the identified objects in the event and exactly one identified electron or muon. These criteria enhance the selection of $W \rightarrow e(\mu) + jet(s)$ events. The assumption is that the jets in these events should be somewhat similar to those in top or charged Higgs events. The tau fake rate in these samples is *twice* the number of identified taus with the *same sign* as the electron or muon divided by the total number of jets. The same sign criteria is applied to avoid a bias from $Z \rightarrow \tau\tau$ events which would cause an artificial enhancement in the measured fake rate due to *real* taus.

Table E.1 shows the measured fake rates from the lepton samples and the expected fake rates based on applying the fake rates derived from the inclusive jet data to the lepton jet sample. Only statistical uncertainties are shown. The measured rates are in roughly good agreement with those predicted. Combining the two lepton samples gives slightly higher statistical precision and there is still agreement within

		Measured	Expected
Electron	1 prong	0.40±0.18	0.47±0.05
	3 prong	1.12±0.30	0.58±0.06
	both	1.52±0.35	1.05±0.11
Muon	1 prong	0.21±0.15	0.47±0.05
	3 prong	0.53±0.23	0.58±0.06
	both	0.73±0.28	1.05±0.11
Combined	1 prong	0.32±0.12	0.47±0.05
	3 prong	0.86±0.20	0.58±0.06
	both	1.18±0.23	1.05±0.11

Table E.1: Measured and expected fake rates (%) in inclusive lepton samples. Uncertainties are statistical only.

the errors.

Appendix F

The Secondary Vertex Algorithm

The SECVTX algorithm [195, 198] starts with tracks in the SVX that are well identified. The primary event vertex in the x-y plane transverse to the beam direction is determined to within a range of 6 to 36 μm, depending on the number of tracks and the event topology. The impact parameter in the transverse plane, d_0, for a track is determined from this primary vertex (see Figure 5.17). The uncertainty on the impact parameter, σ_{d_0}, is determined from the track momentum and the uncertainties introduced by the position of the primary vertex and the amount of material traversed by the track which could lead to multiple scattering. This uncertainty ranges from 50 μm for a 1 GeV/c track to 15 μm for a 10 GeV/c track [55]. The *impact parameter significance*, defined as

$$S_{d_0} \equiv \frac{d_0}{\sigma_{d_0}} \tag{F.1}$$

is used to determine whether a track is sufficiently well measured to be called displaced.

A jet is considered "taggable" if it has $E_T \geq 15$ GeV, $|\eta| \leq 2$ and at least two good SVX tracks (where *good* is defined below). Tracks are associated to a jet if they lie within a cone of $\Delta R = 0.4$ from the jet axis and if their z-vertex is within 5 cm of the event z-vertex. To insure that the SVX tracks are well reconstructed and did not originate from a photon conversion ($\gamma \rightarrow e^+e^-$) and to remove vertices produced by decays of long-lived neutral particles, such as K_s^0 mesons ($c\tau = 2.7$ cm [8]) or Λ^0 baryons ($c\tau = 7.9$ cm), a *maximum impact parameter* requirement is imposed on the tracks of $|d_0| < 0.15$ cm. The K_s^0 decays predominantly to pion-pairs, two-thirds of which are charged pairs. The Λ^0 decays to pairs of charged particles are dominated by decays to $p^{\pm}\pi^{\mp}$. Both of these hadron decays can lead to secondary vertices.

Therefore, in addition to the above, opposite-sign track-pairs with an invariant mass consistent with the K_s^0 mass (497 MeV/c^2) or Λ^0 mass (1115.6 MeV/c^2) are removed.

The algorithm makes two passes through all the tracks associated with the jet. The first pass uses somewhat looser track criteria but demands three or more tracks to make up the secondary vertex. If no secondary vertex is found, then a second pass is made using tighter track criteria but this time demanding only two or more tracks to make up the secondary vertex.

The *loose track* criteria for the first pass are: $p_T > 0.5$ GeV/c, impact parameter significance $S_{d_0} > 2.5$ and at least one good SVX cluster for tracks with hits in 3 or 4 layers of the SVX. A *good SVX cluster* is one which is associated with only one track, is no more than 3 strips wide and contains no noisy or dead strips. A 2-hit track with hits in either the inner-two or outer-two layers is also accepted if both clusters are good and the track has $p_T > 1.5$ GeV/c. Tracks are also required to have good three-dimensional reconstruction in the CTC which ensures that the track parameters are well measured. A track is required to have at least 4 hits in each of at least 2 axial superlayers of the CTC and at least 2 hits in each of at least 2 stereo superlayers.

In the first pass through the algorithm, a set of candidate tracks associated with a given jet is obtained with the above track criteria. All those within the 0.4 radius cone are ranked according to their p_T, impact parameter significance and the number of good clusters on the track (see Reference [198] for details of the ranking). The two best tracks (with at least one having $p_T > 2.0$ GeV/c) are then constrained to a single common vertex in a 3-dimensional fit which is then used as the *seed vertex* for testing the association of the other tracks. The remaining displaced tracks are tested and a secondary vertex is declared found if any of these fit with an impact parameter significance $S_{d_0} < 3$ with respect to the seed vertex. If an additional track cannot be associated to the seed then a new pair of tracks is used to form a seed and a new search for a third track is begun. If a third track is found, other tracks are tried in an attempt to maximize the track multiplicity of the vertex. The χ^2 per degree of fit for the secondary vertex is required to be less than 6. The relatively loose track

quality and kinematic requirements in this pass helps to maintain efficiency while the three or more track requirement helps reject background. In addition to the above, tracks forming a K_s^0 or Λ^0 candidate or that belong to another secondary vertex are rejected.

If there is still no secondary vertex candidate with three or more tracks after all track pairs are used, then a second pass is performed, looking for a two or more track displaced vertex. The track quality requirements are tightened in addition to the ones described above to require $p_T > 1.0$ GeV/c, $S_{d_0} > 3.0$ and at least 2 good clusters for the 3-hit tracks this time. No 2-hit tracks are included in this pass. A jet is required to contain at least two of these tight quality tracks, again with at least one track with $p_T > 2.0$ GeV/c. All the tracks passing these requirements are used in the constrained fit to form a vertex. If a track contributes a $\chi^2 > 50$ to the vertex fit it is rejected and a new fit is performed with the remaining tracks. This procedure is repeated until no further tracks can be removed. If at least two displaced tracks remain and at least one of these has $p_T > 2$ GeV/c, then the corresponding vertex becomes a secondary vertex candidate.

The two-dimensional decay length in the transverse (r–ϕ) plane, L_{xy}, and its error, $\sigma_{L_{xy}}$, is calculated from the constrained vertex fit for all secondary vertex candidates. This decay length is shown schematically in Figure 5.17. The sign of L_{xy} is given by the sign of the vector product of the L_{xy} direction and the jet direction and this sign determines the sign of the tag. Positive tags tend to be associated with a real secondary vertex, negative with mistags. As mistags tend to populate the $\pm L_{xy}$ distributions equally, this is a handle on subtracting out the mistags in the $+L_{xy}$ distribution.

A b-tag from a secondary vertex candidate is further required to have a decay length significance

$$\frac{|L_{xy}|}{\sigma_{L_{xy}}} > 3.0 \qquad \text{(F.2)}$$

and L_{xy} is required to be less than 2.5 cm which restricts vertices to lie inside the radius of the inner layer of silicon. The typical value of $\sigma_{L_{xy}}$ is ~ 130 μm, which is smaller than the distance travelled by the typical b-quark hadrons. This results in a

clean identification of displaced secondary vertices.

A few additional cuts to guard against K_s^0 and Λ^0 decays are imposed on a candidate b-vertex. The secondary vertex is required to be at least 10σ from the primary vertex along the projected axis from the primary to the secondary, where σ is the uncertainty in the displacement of the vertex, and within 3σ of the axis perpendicular to the projected axis. The b-tag is also rejected if the invariant mass of the tracks associated with the tag is within 20 MeV/c^2 of the mass of the K_s^0.

Appendix G

The CDF Collaboration

These are the authors listed in Reference [1].

F. Abe,[17] H. Akimoto,[36] A. Akopian,[31] M. G. Albrow,[7] S. R. Amendolia,[27] D. Amidei,[20] J. Antos,[33] S. Aota,[36] G. Apollinari,[31] T. Asakawa,[36] W. Ashmanskas,[18] M. Atac,[7] F. Azfar,[26] P. Azzi-Bacchetta,[25] N. Bacchetta,[25] W. Badgett,[20] S. Bagdasarov,[31] M. W. Bailey,[22] J. Bao,[39] P. de Barbaro,[30] A. Barbaro-Galtieri,[18] V. E. Barnes,[29] B. A. Barnett,[15] M. Barone,[9] E. Barzi,[9] G. Bauer,[19] T. Baumann,[11] F. Bedeschi,[27] S. Behrends,[3] S. Belforte,[27] G. Bellettini,[27] J. Bellinger,[38] D. Benjamin,[35] J. Benlloch,[19] J. Bensinger,[3] D. Benton,[26] A. Beretvas,[7] J. P. Berge,[7] J. Berryhill,[5] S. Bertolucci,[9] B. Bevensee,[26] A. Bhatti,[31] K. Biery,[7] M. Binkley,[7] D. Bisello,[25] R. E. Blair,[1] C. Blocker,[3] A. Bodek,[30] W. Bokhari,[19] V. Bolognesi,[2] G. Bolla,[29] D. Bortoletto,[29] J. Boudreau,[28] L. Breccia,[2] C. Bromberg,[21] N. Bruner,[22] E. Buckley-Geer,[7] H. S. Budd,[30] K. Burkett,[20] G. Busetto,[25] A. Byon-Wagner,[7] K. L. Byrum,[1] J. Cammerata,[15] C. Campagnari,[7] M. Campbell,[20] A. Caner,[27] W. Carithers,[18] D. Carlsmith,[38] A. Castro,[25] D. Cauz,[27] Y. Cen,[30] F. Cervelli,[27] P. S. Chang,[33] P. T. Chang,[33] H. Y. Chao,[33] J. Chapman,[20] M. -T. Cheng,[33] G. Chiarelli,[27] T. Chikamatsu,[36] C. N. Chiou,[33] L. Christofek,[13] S. Cihangir,[7] A. G. Clark,[10] M. Cobal,[27] E. Cocca,[27] M. Contreras,[5] J. Conway,[32] J. Cooper,[7] M. Cordelli,[9] C. Couyoumtzelis,[10] D. Crane,[1] D. Cronin-Hennessy,[6] R. Culbertson,[5] T. Daniels,[19] F. DeJongh,[7] S. Delchamps,[7] S. Dell'Agnello,[27] M. Dell'Orso,[27] R. Demina,[7] L. Demortier,[31] M. Deninno,[2] P. F. Derwent,[7] T. Devlin,[32] J. R. Dittmann,[6] S. Donati,[27] J. Done,[34] T. Dorigo,[25] A. Dunn,[20] N. Eddy,[20] K. Einsweiler,[18] J. E. Elias,[7] R. Ely,[18] E. Engels, Jr.,[28] D. Errede,[13] S. Errede,[13] Q. Fan,[30] G. Feild,[39] C. Ferretti,[27] I. Fiori,[2] B. Flaugher,[7] G. W. Foster,[7] M. Franklin,[11] M. Frautschi,[35] J. Freeman,[7] J. Friedman,[19] H. Frisch,[5] Y. Fukui,[17] S. Funaki,[36] S. Galeotti,[27] M. Gallinaro,[26] O. Ganel,[35] M. Garcia-Sciveres,[18] A. F. Garfinkel,[29] C. Gay,[11] S. Geer,[7] D. W. Gerdes,[15] P. Giannetti,[27] N. Giokaris,[31] P. Giromini,[9] G. Giusti,[27] L. Gladney,[26] D. Glenzinski,[15] M. Gold,[22] J. Gonzalez,[26] A. Gordon,[11] A. T. Goshaw,[6] Y. Gotra,[25] K. Goulianos,[31] H. Grassmann,[27] L. Groer,[32] C. Grosso-Pilcher,[5] G. Guillian,[20] R. S. Guo,[33] C. Haber,[18] E. Hafen,[19] S. R. Hahn,[7] R. Hamilton,[11] R. Handler,[38] R. M. Hans,[39] F. Happacher,[9] K. Hara,[36] A. D. Hardman,[29] B. Harral,[26] R. M. Harris,[7] S. A. Hauger,[6] J. Hauser,[4] C. Hawk,[32] E. Hayashi,[36] J. Heinrich,[26] B. Hinrichsen,[14] K. D. Hoffman,[29] M. Hohlmann,[5] C. Holck,[26] R. Hollebeek,[26] L. Holloway,[13] S. Hong,[20] G. Houk,[26] P. Hu,[28] B. T. Huffman,[28] R. Hughes,[23] J. Huston,[21] J. Huth,[11] J. Hylen,[7] H. Ikeda,[36] M. Incagli,[27] J. Incandela,[7] G. Introzzi,[27] J. Iwai,[36] Y. Iwata,[12] H. Jensen,[7] U. Joshi,[7] R. W. Kadel,[18] E. Kajfasz,[25] H. Kambara,[10] T. Kamon,[34] T. Kaneko,[36] K. Karr,[37] H. Kasha,[39] Y. Kato,[24] T. A. Keaffaber,[29] K. Kelley,[19] R. D. Kennedy,[7] R. Kephart,[7] P. Kesten,[18] D. Kestenbaum,[11] H. Keutelian,[7] F. Keyvan,[4] B. Kharadia,[13] B. J. Kim,[30] D. H. Kim,[7*] H. S. Kim,[14] S. B. Kim,[20] S. H. Kim,[36] Y. K. Kim,[18] L. Kirsch,[3] P. Koehn,[23] K. Kondo,[36] J. Konigsberg,[8]

S. Kopp,[5] K. Kordas,[14] A. Korytov,[8] W. Koska,[7] E. Kovacs,[7*] W. Kowald,[6] M. Krasberg,[20] J. Kroll,[7] M. Kruse,[30] T. Kuwabara,[36] S. E. Kuhlmann,[1] E. Kuns,[32] A. T. Laasanen,[29] S. Lami,[27] S. Lammel,[7] J. I. Lamoureux,[3] M. Lancaster,[18] T. LeCompte,[1] S. Leone,[27] J. D. Lewis,[7] P. Limon,[7] M. Lindgren,[4] T. M. Liss,[13] J. B. Liu,[30] Y. C. Liu,[33] N. Lockyer,[26] O. Long,[26] C. Loomis,[32] M. Loreti,[25] J. Lu,[34] D. Lucchesi,[27] P. Lukens,[7] S. Lusin,[38] J. Lys,[18] K. Maeshima,[7] A. Maghakian,[31] P. Maksimovic,[19] M. Mangano,[27] J. Mansour,[21] M. Mariotti,[25] J. P. Marriner,[7] A. Martin,[39] J. A. J. Matthews,[22] R. Mattingly,[19] P. McIntyre,[34] P. Melese,[31] A. Menzione,[27] E. Meschi,[27] S. Metzler,[26] C. Miao,[20] T. Miao,[7] G. Michail,[11] R. Miller,[21] H. Minato,[36] S. Miscetti,[9] M. Mishina,[17] H. Mitsushio,[36] T. Miyamoto,[36] S. Miyashita,[36] N. Moggi,[27] Y. Morita,[17] A. Mukherjee,[7] T. Muller,[16] P. Murat,[27] H. Nakada,[36] I. Nakano,[36] C. Nelson,[7] D. Neuberger,[16] C. Newman-Holmes,[7] C-Y. P. Ngan,[19] M. Ninomiya,[36] L. Nodulman,[1] S. H. Oh,[6] K. E. Ohl,[39] T. Ohmoto,[12] T. Ohsugi,[12] R. Oishi,[36] M. Okabe,[36] T. Okusawa,[24] R. Oliveira,[26] J. Olsen,[38] C. Pagliarone,[27] R. Paoletti,[27] V. Papadimitriou,[35] S. P. Pappas,[39] N. Parashar,[27] S. Park,[7] A. Parri,[9] J. Patrick,[7] G. Pauletta,[27] M. Paulini,[18] A. Perazzo,[27] L. Pescara,[25] M. D. Peters,[18] T. J. Phillips,[6] G. Piacentino,[27] M. Pillai,[30] K. T. Pitts,[7] R. Plunkett,[7] L. Pondrom,[38] J. Proudfoot,[1] F. Ptohos,[11] G. Punzi,[27] K. Ragan,[14] D. Reher,[18] A. Ribon,[25] F. Rimondi,[2] L. Ristori,[27] W. J. Robertson,[6] T. Rodrigo,[27] S. Rolli,[37] J. Romano,[5] L. Rosenson,[19] R. Roser,[13] T. Saab,[14] W. K. Sakumoto,[30] D. Saltzberg,[5] A. Sansoni,[9] L. Santi,[27] H. Sato,[36] P. Schlabach,[7] E. E. Schmidt,[7] M. P. Schmidt,[39] A. Scribano,[27] S. Segler,[7] S. Seidel,[22] Y. Seiya,[36] G. Sganos,[14] M. D. Shapiro,[18] N. M. Shaw,[29] Q. Shen,[29] P. F. Shepard,[28] M. Shimojima,[36] M. Shochet,[5] J. Siegrist,[18] A. Sill,[35] P. Sinervo,[14] P. Singh,[28] J. Skarha,[15] K. Sliwa,[37] F. D. Snider,[15] T. Song,[20] J. Spalding,[7] T. Speer,[10] P. Sphicas,[19] F. Spinella,[27] M. Spiropulu,[11] L. Spiegel,[7] L. Stanco,[25] J. Steele,[38] A. Stefanini,[27] K. Strahl,[14] J. Strait,[7] R. Ströhmer,[7*] D. Stuart,[7] G. Sullivan,[5] K. Sumorok,[19] J. Suzuki,[36] T. Takada,[36] T. Takahashi,[24] T. Takano,[36] K. Takikawa,[36] N. Tamura,[12] B. Tannenbaum,[22] F. Tartarelli,[27] W. Taylor,[14] P. K. Teng,[33] Y. Teramoto,[24] S. Tether,[19] D. Theriot,[7] T. L. Thomas,[22] R. Thun,[20] R. Thurman-Keup,[1] M. Timko,[37] P. Tipton,[30] A. Titov,[31] S. Tkaczyk,[7] D. Toback,[5] K. Tollefson,[30] A. Tollestrup,[7] H. Toyoda,[24] W. Trischuk,[14] J. F. de Troconiz,[11] S. Truitt,[20] J. Tseng,[19] N. Turini,[27] T. Uchida,[36] N. Uemura,[36] F. Ukegawa,[26] G. Unal,[26] J. Valls,[7*] S. C. van den Brink,[28] S. Vejcik, III,[20] G. Velev,[27] R. Vidal,[7] R. Vilar,[7*] M. Vondracek,[13] D. Vucinic,[19] R. G. Wagner,[1] R. L. Wagner,[7] J. Wahl,[5] N. B. Wallace,[27] A. M. Walsh,[32] C. Wang,[6] C. H. Wang,[33] J. Wang,[5] M. J. Wang,[33] Q. F. Wang,[31] A. Warburton,[14] T. Watts,[32] R. Webb,[34] C. Wei,[6] H. Wenzel,[16] W. C. Wester, III,[7] A. B. Wicklund,[1] E. Wicklund,[7] R. Wilkinson,[26] H. H. Williams,[26] P. Wilson,[5] B. L. Winer,[23] D. Winn,[20] D. Wolinski,[20] J. Wolinski,[21] S. Worm,[22] X. Wu,[10] J. Wyss,[25] A. Yagil,[7] W. Yao,[18] K. Yasuoka,[36] Y. Ye,[14] G. P. Yeh,[7] P. Yeh,[33] M. Yin,[6] J. Yoh,[7] C. Yosef,[21] T. Yoshida,[24] D. Yovanovitch,[7] I. Yu,[7] L. Yu,[22] J. C. Yun,[7] A. Zanetti,[27] F. Zetti,[27] L. Zhang,[38] W. Zhang,[26] and S. Zucchelli[2]

(CDF Collaboration)

[1] *Argonne National Laboratory, Argonne, Illinois 60439*
[2] *Istituto Nazionale di Fisica Nucleare, University of Bologna, I-40127 Bologna, Italy*
[3] *Brandeis University, Waltham, Massachusetts 02264*
[4] *University of California at Los Angeles, Los Angeles, California 90024*
[5] *University of Chicago, Chicago, Illinois 60638*
[6] *Duke University, Durham, North Carolina 28708*

[7] *Fermi National Accelerator Laboratory, Batavia, Illinois 60510*
[8] *University of Florida, Gainesville, FL 33611*
[9] *Laboratori Nazionali di Frascati, Istituto Nazionale di Fisica Nucleare, I-00044 Frascati, Italy*
[10] *University of Geneva, CH-1211 Geneva 4, Switzerland*
[11] *Harvard University, Cambridge, Massachusetts 02138*
[12] *Hiroshima University, Higashi-Hiroshima 724, Japan*
[13] *University of Illinois, Urbana, Illinois 61801*
[14] *Institute of Particle Physics, McGill University, Montreal H3A 2T8, and University of Toronto, Toronto M5S 1A7, Canada*
[15] *The Johns Hopkins University, Baltimore, Maryland 21218*
[16] *Universotaet Karlsruhe, 76128 Karlsruhe, Germany*
[17] *National Laboratory for High Energy Physics (KEK), Tsukuba, Ibaraki 315, Japan*
[18] *Ernest Orlando Lawrence Berkeley National Laboratory, Berkeley, California 94720*
[19] *Massachusetts Institute of Technology, Cambridge, Massachusetts 02139*
[20] *University of Michigan, Ann Arbor, Michigan 48109*
[21] *Michigan State University, East Lansing, Michigan 48824*
[22] *University of New Mexico, Albuquerque, New Mexico 87132*
[23] *The Ohio State University, Columbus, OH 43320*
[24] *Osaka City University, Osaka 588, Japan*
[25] *Universita di Padova, Istituto Nazionale di Fisica Nucleare, Sezione di Padova, I-36132 Padova, Italy*
[26] *University of Pennsylvania, Philadelphia, Pennsylvania 19104*
[27] *Istituto Nazionale di Fisica Nucleare, University and Scuola Normale Superiore of Pisa, I-56100 Pisa, Italy*
[28] *University of Pittsburgh, Pittsburgh, Pennsylvania 15270*
[29] *Purdue University, West Lafayette, Indiana 47907*
[30] *University of Rochester, Rochester, New York 14628*
[31] *Rockefeller University, New York, New York 10021*
[32] *Rutgers University, Piscataway, New Jersey 08854*
[33] *Academia Sinica, Taipei, Taiwan 11530, Republic of China*
[34] *Texas A&M University, College Station, Texas 77843*
[35] *Texas Tech University, Lubbock, Texas 79409*
[36] *University of Tsukuba, Tsukuba, Ibaraki 315, Japan*
[37] *Tufts University, Medford, Massachusetts 02155*
[38] *University of Wisconsin, Madison, Wisconsin 53806*
[39] *Yale University, New Haven, Connecticut 06511*

References

[1] F. Abe *et al.* Search for Charged Higgs Decays of the Top Quark Using Hadronic Decays of the Tau Lepton. *Phys. Rev. Lett.* **79**, 357 (1997).

[2] L. Groer. Present Searches for Higgs Signatures at the Tevatron. Pubished in Proceedings for Hadron Collider Physics XII Conference, SUNY, Stony Brook, June 5-11, 1997 (1998).

[3] Francis Halzen and Alan D. Martin. *Quarks and Leptons: An Introductory Course in Modern Particle Physics.* John Wiley & Sons (1984).

[4] Donald H. Perkins. *Introduction to High Energy Physics.* Addison-Wesley Publishing Company, Inc. third edition (1987).

[5] Chris Quigg. *Gauge Theories of the Strong, Weak and Electromagnetic Interactions.* Benjamin/Cummings Publishing Company, Inc. (1983).

[6] Ta Pei Cheng and Ling-Fong Li. *Gauge Theory of Elementary Particle Physics.* Oxford University Press (1984).

[7] V. Barger and R.J.N. Phillips. *Collider Physics.* Addison-Wesley Publishing Company, Inc. (1987).

[8] C. Caso *et al.* Review of Particle Physics. *The European Physical Journal* **C3**, 1 (1998). Updates are to be found at http://pdg.lbl.gov/.

[9] E872 Collaboration Web Home Page http://fn872.fnal.gov/.

[10] NOMAD Collaboration Web Home Page http://nomadinfo.cern.ch/.

[11] CHORUS Collaboration Web Home Page http://choruswww.cern.ch/.

[12] Y.Fukuda *et al.* Evidence For Oscillation of Atmospheric Neutrinos. submitted to Physical Review Letters (1998).

[13] F. Abe *et al.* Observation of Top Quark Production in $p\overline{p}$ Collisions. *Phys. Rev. Lett.* **74**, 2626 (1995).

[14] F. Abachi *et al.* Observation of the Top Quark. *Phys. Rev. Lett.* **74**, 2632 (1995).

[15] N. Konstantinidis. Higgs Searches at LEP. Presented at *Physics at Run II, Workshop on Supersymmetry/Higgs.* First General Meeting, 14-16 May, 1998, Fermilab, Batavia, Ilinois (1998).

[16] R. Feynman. Space – Time Approach to Quantum Electrodynamics. *Phys. Rev.* **76**, 769 (1949).

[17] R. Ellis, W. Stirling, and B. Webber. *QCD and Collider Physics.* Cambridge University Press (1996).

[18] G. 't Hooft. Dimensional Regularization and the Renormalization Group. *Nucl. Phys.* **B61**, 455 (1973).

[19] G. 't Hooft and M. Veltman. Regularization and Renormalization of Gauge Fields. *Nucl. Phys.* **B44**, 189 (1972).

[20] S. Weinberg. A Model of Leptons. *Phys. Rev. Lett.* **19**, 1264 (1967).

[21] A. Salam. Weak and Electromagnetic Interactions. in N. Svartholm, ed., *Elementary Particle Theory: Relativistic Groups and Analyticity*, Stockholm: Almqvist and Wiksell (1968).

[22] G. Arnison *et al.* Experimental Observation of Isolated Large Transverse Energy Electrons with Associated Missing Energy at $\sqrt{s} = 540$ GeV. *Phys. Lett.* **B122**, 103 (1983).

[23] G. Arnison *et al.* Experimental Observation of Lepton Pairs of Invariant Mass around 95 GeV/c^2 at the Cern SpS Collider. *Phys. Lett.* **B126**, 398 (1983).

[24] J. F. Gunion, A. Stange, and S. Willenbrock. Weakly-Coupled Higgs Bosons. Published in *Electroweak Symmetry Breaking and New Physics at the TeV Scale*, editors T. L. Barklow, S. Dawson, H. E. Haber and J. L. Siegrist, World Scientific Publishing Co. (1996).

[25] See presentations at the latest Rencontres de Moriond conference *Electroweak Interactions and Unified Theories*, held in Les Arcs, France, March 14-28, 1998.

[26] L. Susskind. Dynamics of Spontaneous Symmetry Breaking in the Weinberg-Salam Theory. *Phys. Rev.* **D20**, 2619 (1979).

[27] S. Dawson. The MSSM and Why It Works. Talk given at the Theoretical Advanced Study Institute in Elementary Particle Physics (TASI 97): *Supersymmetry, Supergravity and Supercolliders*, Boulder, CO, 1-7 June 1997. http://xxx.lanl.gov/abs/hep-ph/9712464 (1997).

[28] S. Dawson and H. E. Haber. Electroweak Symmetry Breaking and Physics Beyond the Standard Model. Published in *Electroweak Symmetry Breaking and New Physics at the TeV Scale*, editors T. L. Barklow, S. Dawson, H. E. Haber and J. L. Siegrist, World Scientific Publishing Co. (1996).

[29] J. F. Gunion. A Simplified Summary of Supersymmetry. Talk presented at ITP Conference on Future High-energy Colliders, Santa Barbara, CA, 21-25 Oct 1996. http://xxx.lanl.gov/abs/hep-ph/9704349 (1997).

[30] J. F. Gunion. Searching for Low-Energy Supersymmetry. Published in Proceedings of International Workshop on Quantum Effects in the Minimal Supersymmetric Standard Model, Barcelona, Spain, 9-13 Sep 1997, edited by J. Sola, World Scientific. http://xxx.lanl.gov/abs/hep-ph/9801417 (1998).

[31] M. Dine. Supersymmetry Phenomenology (With a Broad Brush). http://xxx.lanl.gov/abs/hep-ph/9612389 (1996).

[32] S. Martin. A Supersymmetry Primer. To be published in *Perspectives in Supersymmetry*, edited by G.L. Kane, World Scientific. http://xxx.lanl.gov/abs/hep-ph/9709356 (1997).

[33] Marcela Carena. Higgs and Supersymmetric Particle Physics at LEP and the Tevatron. Lectures given at Fermilab, Illinois, April 29, 30 and May 5, 7 (1997).

[34] J. F. Gunion, H. E. Haber, G. Kane, and S. Dawson. *The Higgs Hunter's Guide*. Addison-Wesley Publishing Company, Inc. (1990).

[35] R. M. Godbole and D. P. Roy. Charged Higgs Boson Search via Heavy Top Quark Decay at Fermilab Tevatron Collider Energy. *Phys. Rev.* **D43**, 3640 (1991).

[36] G. L. Kane, editor. *Perspectives on Higgs Physics*. World Scientific Publishing Co. Pte. Ltd. (1993).

[37] G. L. Kane, editor. *Perspectives on Higgs Physics II*. To be published. World Scientific Publishing Co. Pte. Ltd. (1998).

[38] T. L. Barklow, S. Dawson, H. E. Haber, J. L. Siegrist, and G. L. Kane, editors. *Electroweak Symmetry Breaking and New Physics at the TeV Scale*. World Scientific Publishing Co. Pte. Ltd. (1996).

[39] W. Grimus. CP Violating Phenomena and Theoretical Results. *Fortschr. Phys.* **36**, 201 (1988).

[40] S. Glashow and S. Weinberg. Natural Conservation Laws for Neutral Currents. *Phys. Rev.* **D15**, 1958 (1977).

[41] R. Barate *et al.* Search for the Neutral Higgs Bosons of the MSSM in e^+e^- Collisions at $\sqrt{s}$ from 130 GeV to 172 GeV. *Phys. Lett.* **B412**, 173 (1997).

[42] M. Spira. QCD Effects in Higgs Physics. *Fortsch. Phys.* **46**, 203 (1998).

[43] B. Bevensee and B. Williams. A Search for a Charged Higgs Boson Using the Top Data. CDF/ANAL/EXOTIC/CDFR/4295 (1997).

[44] G. Arnison *et al.* Experimental Observation of Events with Large Missing Transverse Energy Accompanied by a Jet or a Photon(s) in $p\overline{p}$ Collisions at $\sqrt{s} = 540$ GeV. *Phys. Lett.* **B139**, 115 (1984).

[45] S. Herb *et al.* Observation of a Dimuon Resonance at 9.5 GeV in 400 GeV Proton – Nucleus Collisions. *Phys. Rev. Lett.* **39**, 252 (1977).

[46] C. Campagnari and M. Franklin. The Discovery of the Top Quark. *Rev. Mod. Phys.* **69**, 137 (1997).

[47] S. Wimpenny and B. Winer. The Top Quark. *Ann. Rev. Nucl. Part. Sci.* **46**, 149 (1995).

[48] G. Kane and M. Peskin. A Constraint from b-decay on Models with no t-quark. *Nucl. Phys.* **B195**, 29 (1982).

[49] S.L. Glashow, J. Iliopoulos, and L. Maiani. Weak Interactions with Lepton – Hadron Symmetry. *Phys. Rev.* **D2**, 1285 (1970).

[50] A. Bean *et al.* Improved Upper Limit on Flavor Changing Neutral Current Decays of the b-quark. *Phys. Rev.* **D35**, 3533 (1987).

[51] W. Bartel *et al.* A Measurement of the Electroweak Induced Charge Symmetry in $e^+e^- \to b\overline{b}$. *Phys. Lett.* **B146**, 437 (1984).

[52] D. Decamp *et al.* Measurement of the Forward – Backward Asymmetry in $Z \to b\overline{b}$ and $Z \to c\overline{c}$. *Phys. Lett.* **B263**, 325 (1991).

[53] H. Albrecht *et al.* Observation of B^0–$\overline{B^0}$ Mixing. *Phys. Lett.* **B192**, 245 (1987).

[54] B. Pietrzyk. LEP Asymmetries and Fits of the Standard Model. In published proceedings of '94 Electroweak Interactions and Unified Theories, ed. by J. Tran Thanh Van (1994).

[55] F. Abe *et al.* Evidence for Top Quark Production in $p\overline{p}$ Collisions at $\sqrt{s}$ = 1.8 TeV. *Phys. Rev.* **D50**, 2966 (1994).

[56] T. Stelzer, Z. Sullivan, and S. Willenbrock. Single Top Quark Production via W – gluon Fusion at Next-to-Leading Order. *Phys. Rev.* **D56**, 5919 (1997).

[57] J. Collins, D. Soper, and G. Sterman. Heavy Particle Production in High-energy Hadron Collisions. *Nucl. Phys.* **B263**, 37 (1986).

[58] P. Nason, S. Dawson, and R. K. Ellis. The Total Cross-section for the Production of Heavy Quarks in Hadronic Collisions. *Nucl. Phys.* **B303**, 607 (1988).

[59] W. Beenakker *et al.* QCD Corrections to Heavy Quark Production in Hadron-hadron Collisions. *Nucl. Phys.* **B351**, 507 (1991).

[60] G. Altarelli *et al.* Total Cross-section for Heavy Flavor in Hadronic Collisions and QCD. *Nucl. Phys.* **B308**, 724 (1988).

[61] R. K. Ellis. Rates for Top Quark Production. *Phys. Lett.* **B259**, 492 (1991).

[62] E. Laenen, J. Smith, and W. L. van Neerven. All Order Resummation of Soft Gluon Contributions to Heavy Quark Production in Hadron–Hadron Collisions. *Nucl. Phys.* **B369**, 543 (1992).

[63] E. Laenen, J. Smith, and W. L. van Neerven. Top Quark Production Cross-section. *Phys. Lett.* **B321**, 254 (1994).

[64] E. L. Berger and H. Contopanagos. Perturbative Gluon Resummation of the Top Quark Production Cross Section. *Phys. Lett.* **B361**, 115 (1995).

[65] S. Catani, M. L. Mangano, P. Nason, and L. Trentadue. The Top Cross-section in Hadronic Collisions. *Phys. Lett.* **B378**, 329 (1996).

[66] R. Bonciani, S. Catani, M. L. Mangano, P. Nason, and L. Trentadue. NLL Resummation of the Heavy Quark Hadroproduction Cross-section. http://xxx.lanl.gov/abs/hep-ph/9801375 (1998).

[67] N. Amos. Talk presented at Rencontres de Moriond conference *Electroweak Interactions and Unified Theories*, Les Arcs, France, March 14-28, 1998.

[68] I. Bigi *et al.* Production and Decay Properties of Ultraheavy Quarks. *Phys. Lett.* **B181**, 157 (1986).

[69] M. Jezabek and J. H. Kuhn. The Top Width: Theoretical Update. *Phys. Rev.* **D48**, 1910 (1993).

[70] V. Barger, J. Ohnemus, and R. Phillips. Spin Correlation Effects in the Hadroproduction and Decay of Very Heavy Top Quark Pairs. *Int. J. Mod. Phys.* **A4**, 617 (1989).

[71] G. L. Kane, G. A. Ladinsky, and C. P. Yuan. Using the Top Quark for Testing Standard Model Polarization and CP Predictions. *Phys. Rev.* **D45**, 124 (1992).

[72] P. Azzi *et al.* Update of the Top Analysis in the All-Hadronic Channel with Kinematical Selection and Single b-tag. CDF/ANAL/TOP/CDFR/3766 (1996).

[73] Wasiq M. Bokhari. *Observation of the Fully Hadronic Decay of $t\bar{t}$ Pairs in $p\bar{p}$ Collisions at $\sqrt{s}$ = 1.8 TeV.* PhD thesis, Massachusetts Institute of Technology, Cambridge, Massachusetts (1997).

[74] W. Bokhari and P. Sphicas. Summary of the $\geq$ 2 b-tag All Hadronic Top Analysis. CDF/ANAL/TOP/CDFR/3942 (1996).

[75] F. Abe *et al.* The $\mu\tau$ and $e\tau$ Decays of Top Quark Pairs Produced in $p\bar{p}$ Collisions at $\sqrt{s}$ = 1.8 TeV. *Phys. Rev. Lett.* **79**, 3585 (1997).

[76] Marcus Hohlmann. *Observation of Top Quark Pairs in the Dilepton Channel Using Electrons, Muons, and Taus.* PhD thesis, University of Chicago, Chicago, Illinois (1997).

[77] David Kestenbaum. *Observation of the Top Quark in Soft Lepton Tagged W^+ Jet Events.* PhD thesis, Harvard University, Cambridge, Massachusetts (1996).

[78] Douglas Glenzinski. *Observation of the Top Quark in Proton-Antiproton Collisions at a Center of Mass Energy of 1.8 TeV.* PhD thesis, John Hopkins University, Baltimore, Maryland (1995).

[79] Chyi C. Miao. *Measurement of the $t\bar{t}$ Cross Section in the Lepton Plus Jets Channel in $p\bar{p}$ Collisions at $\sqrt{s}$ = 1.8 TeV.* PhD thesis, University of Michigan, Ann Arbor, Michigan (1997).

[80] F. Abe *et al.* Measurement of the Top Quark Mass. *Phys. Rev. Lett.* **80**, 2767 (1998).

[81] F. Abe *et al.* Measurement of the Top Quark Mass and $t\bar{t}$ t Production Cross-section from Dilepton Events at the Collider Detector at Fermilab. *Phys. Rev. Lett.* **80**, 2779 (1998).

[82] Mark Charles Kruse. *Observation of Top Quark Pair Production in the Dilepton Decay Channel from Proton-Antiproton Collisons at* $\sqrt{s} = 1.8$ *TeV.* PhD thesis, Purdue University, West Lafayette, Indiana (1996).

[83] F. Abe *et al.* First Observation of the All Hadronic Decay of $t\bar{t}$ Pairs. *Phys. Rev. Lett.* **79**, 1992 (1997).

[84] Patriazia Azzi. *Observation of Top Quark at CDF in the All Hadronic Mode.* PhD thesis, Padova University, Padova, Italy (1996).

[85] F. Abe *et al.* Measurement of the $t\bar{t}$ Production Cross-Section in $p\overline{p}$ Collisions at $\sqrt{s} = 1.8$ TeV. *Phys. Rev. Lett.* **80**, 2773 (1998).

[86] S. Abachi *et al.* Measurement of the Top Quark Pair Production Cross-Section in $p\overline{p}$ Collisions. *Phys. Rev. Lett.* **79**, 1203 (1997).

[87] S. Abachi *et al.* Direct Measurement of the Top Quark Mass. *Phys. Rev. Lett.* **79**, 1197 (1997).

[88] B. Abbott *et al.* Measurement of the Top Quark Mass Using Dilepton Events. *Phys. Rev. Lett.* **80**, 2063 (1998).

[89] M. Strovink. Top Quark Results from DØ. To be published in the proceedings of International Europhysics Conference on *High-Energy Physics (HEP 97)*, Jerusalem, Israel, 19-26 Aug 1997. FERMILAB-CONF-97-386-E (1997).

[90] B. Abbott *et al.* Direct Measurement of the Top Quark Mass at DØ˙ Submitted to Phys. Rev. D, FERMILAB-PUB-98-031-E (1998).

[91] S. Blusk. Talk presented at Rencontres de Moriond conference *Electroweak Interactions and Unified Theories*, Les Arcs, France, March 14-28, 1998.

[92] F. Abe *et al.* Search for the Top Quark Decaying to a Charged Higgs Boson in $p\overline{p}$ Collisions at $\sqrt{s} = 1.8$ TeV. *Phys. Rev. Lett.* **73**, 2667 (1994).

[93] F. Abe *et al.* A Search for the Top Quark Decaying to Charged Higgs in $p\overline{p}$ at $\sqrt{s} = 1.8$ TeV. *Phys. Rev. Lett.* **72**, 1977 (1994).

[94] F. Abe *et al.* Search for Charged Higgs Decays of the Top Quark Using Hadronic Tau Decays. *Phys. Rev.* **D54**, 735 (1996).

[95] Christian Couyoumtzelis. *Recherche du Boson de Higgs chargé* $H^{\pm}$ *issu de top* $\rightarrow H^{+}b$ *par la mesure directe d'un excès dans le mode hadronique du lepton* τ. PhD thesis, University of Geneva, Geneva, Switzerland (1997).

[96] P. Abreu *et al.* Search for Charged Higgs Bosons in $e^{+}e^{-}$ Collisions at $\sqrt{s} =$ 172 GeV. Submitted to Phys. Lett. B, CERN-PPE-97-145 (1997).

[97] R. Barate *et al.* Search for Charged Higgs Bosons in e^+e^- Collisions at Center-of-mass Energies from 130 GeV to 172 GeV. Submitted to Phys. Lett. B, CERN-PPE-97-129 (1997).

[98] K. Ackerstaff *et al.* Search for Charged Higgs Bosons in e^+e^- Collisions at $\sqrt{s}$ = 130 GeV – 172 GeV. Submitted to Phys. Lett. B, CERN-PPE-97-168 (1997).

[99] O. Adriani *et al.* Searches for Nonminimal Higgs Bosons in Z^0 Decays. *Phys. Lett.* **B294**, 457 (1992).

[100] J. L. Hewett, S. Thomas, and T. Takeuchi. Indirect Probes of New Physics. Published in *Electroweak Symmetry Breaking and New Physics at the TeV Scale*, editors T. L. Barklow, S. Dawson, H. E. Haber and J. L. Siegrist, World Scientific Publishing Co. (1996).

[101] A. Stahl and H. Voss. Testing the Lorentz structure of the Charged Weak Current in τ-decays. *Z. Phys.* **C74**, 73 (1997).

[102] M. T. Dova, J. Swain, and L. Taylor. Anomalous Charged Current Couplings of the Tau and Implications for Tau Compositeness and Two Higgs Doublet Models. http://xxx.lanl.gov/abs/hep-ph/9712384 (1997).

[103] M. Artuso *et al.* A Search for $B \to \ell\overline{\nu}_\ell$. *Phys. Rev. Lett.* **75**, 785 (1995).

[104] M. Acciarri *et al.* Measurement of $D_s^- \to \tau^-\overline{\nu}_\tau$ and a New Limit for $B^- \to \tau^-\overline{\nu}_\tau$. *Phys. Lett.* **B396**, 327 (1997).

[105] D. Buskulic *et al.* Measurement of the $b \to \tau\overline{\nu}_\tau X$ Branching Ratio and an Upper Limit on $B^- \to \tau^-\overline{\nu}_\tau$. *Phys. Lett.* **B343**, 444 (1995).

[106] Y. Grossman, H. E. Haber, and Y. Nir. QCD Corrections to Charged Higgs Mediated $b \to c\tau\nu$ decay. *Phys. Lett.* **B357**, 630 (1995).

[107] J. A. Coarasa, Ricardo A. Jimenez, and J. Sola. The $\tan\beta - M(H^\pm)$ Bound from Inclusive Semitauonic B Decays in the MSSM. *Phys. Lett.* **B406**, 337 (1997).

[108] A. K. Grant. The Heavy Top Quark in the Two Higgs Doublet Model. *Phys. Rev.* **D51**, 207 (1995).

[109] M. Boulware and D. Finnell. Radiative Corrections to BR($Z \to b\bar{b}$) in the Minimal Supersymmetric Standard Model. *Phys. Rev.* **D44**, 2054 (1991).

[110] R. Ammar *et al.* Evidence for Penguins: First Observation of $B \to K^*(892)\gamma$. *Phys. Rev. Lett.* **71**, 674 (1993).

[111] R. Ammar *et al.* Radiative Penguin Decays of the B Meson. Contributed paper to The 28th International Conference on High Energy Physics, Warsaw, Poland, CLEO CONF 96-05 (1996).

[112] M. S. Alam *et al.* First Measurement of the Rate for the Inclusive Radiative Penguin Decay $b \to s\gamma$. *Phys. Rev. Lett.* **74**, 2885 (1995).

[113] S. Glenn. Rare Decays from CLEO. Talk presented at the American Physical Society Meeting, Columbus, Ohio, April 18–21, 1998 (1998).

[114] R. Barate *et al.* A Measurement of the Inclusive $b \to s\gamma$ Branching Ratio. Submitted to Phys. Lett. B. CERN-EP-98-044 (1998).

[115] B. A. Campbell and P. J. O'Donnell. Mass of the Top Quark and Induced Decay and Neutral Mixing of B Mesons. *Phys. Rev.* **D25**, 1989 (1982).

[116] T. Skwarnicki. Review of Experimental Results on Electroweak Penguin Decays of b Quark. Proceedings of the Seventh International Symposium on Heavy Flavor Physics, University of California Santa Barbara, California, July 7-11, 1997, http://xxx.lanl.gov/abs/hep-ph/9712253 (1997).

[117] V. Barger, M. S. Berger, and R. J. N. Phillips. Implications of $b \to s\gamma$ Decay Measurements in Testing the Higgs Sector of the Minimum Supersymmetric Standard Model. *Phys. Rev. Lett.* **70**, 1368 (1993).

[118] J. L. Hewett and J. D. Wells. Searching for Supersymmetry in Rare B Decays. *Phys. Rev.* **D55**, 5549 (1997).

[119] A. Ali *et al.* Theory of Rare B Decays. Proceedings of the Seventh International Symposium on Heavy Flavor Physics, University of California Santa Barbara, California, July 7-11, 1997, http://xxx.lanl.gov/abs/hep-ph/9709507 (1997).

[120] K. Chetyrkin, M. Misiak, and M. Munz. Weak Radiative B Meson Decay Beyond Leading Logarithms. *Phys. Lett.* **B400**, 206 (1997).

[121] A. J. Buras, A. Kwiatkowski, and N. Pott. On the Scale Uncertainties in the $B \to X(s)\gamma$ Decay. *Phys. Lett.* **B414**, 157 (1997).

[122] J. L. Hewett. Top Ten Models Constrained by $b \to s\gamma$. Published in proceedings of SLAC Summer Inst. on Particle Physics, SLAC, Jul 6 - Aug 6, 1993. SLAC-PUB-6521 (1994).

[123] V. Barger, J. Hewett, and R. Phillips. New Constraints on the Charged Higgs Sector in Two Higgs Doublet Models. *Phys. Rev.* **D41**, 3421 (1990).

[124] M. Ciuchini, G. Degrassi, P. Gambino, and G.F. Giudice. Next-to-Leading QCD Corrections to $B \to X_s\gamma$: Standard Model and Two Higgs Doublet Model. CERN-TH/97-279, http://xxx.lanl.gov/abs/hep-ph/9710335 (1997).

[125] R. Garisto and J. N. Ng. Supersymmetric $b \to s\gamma$ with Large Chargino Contributions. *Phys. Lett.* **B315**, 372 (1993).

[126] T. Goto and Y. Okada. Charged Higgs Mass Bound from the $b \to s\gamma$ Process in the Minimal Supergravity. *Prog. Theor. Phys. Suppl.* **123**, 213 (1996).

[127] T. Goto, Y. Okada, and Y. Shimizu. Flavor Changing Neutral Current Processes in B and K Decays in the Supergravity Model. KEK-TH-567, http://xxx.lanl.gov/abs/hep-ph/9804294 (1998).

[128] D. A. Edwards and M. J. Syphers. *An Introduction to the Physics of High Energy Accelerators.* Wiley, New York (1993).

[129] F. Abe *et al.* The CDF Detector: An Overview. *Nucl. Instr. Meth.* **A271**, 387 (1988).

[130] The CDF Collaboration. Proposal For an Upgraded CDF Detector. CDF Note CDF/DOC/PUBLIC/1172 (1990).

[131] D. Amidei *et al.* The Silicon Vertex Detector of the Collider Detector at Fermilab. *Nucl. Instrum. Meth.* **A350**, 73 (1994).

[132] P. Azzi *et al.* SVX′: The New CDF Silicon Vertex Detector. *Nucl. Instrum. Meth.* **A360**, 137 (1995).

[133] S. Seidel. The CDF Silicon Vertex Detector SVX and its Upgrades. Contributed to Second Workshop on Vertex Detectors, Lake Bohinj, Slovenia. FERMILAB-CONF-94-377-E (1993).

[134] P. P. Singh. Operation and Performance of the Silicon Vertex Detector (SVX′) at CDF. Published in the proceedings of 1994 Meeting of the American Physical Society, Division of Particles and Fields (DPF 94), Albuquerque, NM, 2-6 Aug 1994. FERMILAB-CONF-94-352-E (1994).

[135] P. Allport *et al.* FOXFET Biased Microstrip Detectors. *Nucl. Instr. Meth.* **A310**, 155 (1991).

[136] P. Azzi *et al.* Noise and Radiation Effects on SVX′ and other Silicon Sensors. CDF Note CDF/DOC/TRACKING/PUBLIC/3278 (1995).

[137] J. Albert *et al.* The Relationship Between Signal-to-Noise Ratio and b tag Efficiency: How Long Can Silicon Detectors Survive Radiation Exposure? CDF Note CDF/TOP/DOC/PUBLIC/3338 (1995).

[138] D. Stuart (1997). Private communication.

[139] F. Snider *et al.* The CDF Vertex Time Projection Chamber System. *Nucl. Instrum. Meth.* **A268**, 75 (1988).

[140] F. Bedeschi *et al.* Design and Construction of the CDF Central Tracking Chamber. *Nucl. Instrum. Meth.* **A268**, 50 (1988).

[141] L. Balka *et al.* The CDF Central Electromagnetic Calorimeter. *Nucl. Instrum. Meth.* **A267**, 272 (1988).

[142] S. Bertolucci *et al.* The CDF Central and Endwall Hadron Calorimeter. *Nucl. Instr. Meth.* **A267**, 301 (1988).

[143] Y. Fukui *et al.* CDF End Plug Electromagnetic Calorimeter Using Conductive Plastic Proportional Tubes. *Nucl. Instrum. Meth.* **A267**, 280 (1988).

[144] C. Haber *et al.* Performance and Calibration Studies of the CDF Endplug Hadronic Calorimeter. Published in Proceedings, Batavia 1985, Gas Sampling Calorimetry (1985).

[145] G. Brandenburg *et al.* An Electromagentic Calorimeter for the Small Angle Regions of the Collider Detector at Fermilab. *Nucl. Instrum. Meth.* **A267**, 257 (1988).

[146] S. Cihangir *et al.* The CDF Forward/Backward Hadron Calorimeter. *Nucl. Instr. Meth.* **A267**, 249 (1988).

[147] G. Ascoli *et al.* CDF Central Muon Detector. *Nucl. Instrum. Meth.* **A268**, 33 (1988).

[148] A. Gauthier *et al.* Design and Performance of Drift Chambers for the Central Muon Upgrade. CDF Note CDF/PUB/CDF/CDFR/1500 (1991).

[149] P. Giromini *et al.* The Central Muon Extension Scintillators (CSX). CDF Note CDF/DOC/MUON/PUBLIC/3898 (1996).

[150] P. Schlabach *et al.* Calibration of the CMX Drift Velocity and Alignment in Run 1A. CDF Note CDF/DOC/MUON/CDFR/2332 (1993).

[151] K. Byrum *et al.* The CDF Forward Muon System. *Nucl. Instrum. Meth.* **A268**, 46 (1988).

[152] E. Barsotti *et al.* FASTBUS Data Acquisition for CDF. *Nucl. Instrum. Meth.* **A269**, 82 (1988).

[153] G. Foster *et al.* A Fast Hardware Track-Finder for the CDF Central Tracking Chamber. *Nucl. Instrum. Meth.* **A269**, 93 (1988).

[154] B. K. Bullock, K. Hagiwara, and A. D. Martin. Tau Polarization as a Signal of Charged Higgs Bosons. *Phys. Rev. Lett.* **67**, 3055 (1991).

[155] D. Winn, S. B. Kim, and D. Amidei. Measurement of Branching Fraction of Top Quarks to Longitudinal W Bosons. CDF/ANAL/TOP/CDFR/3539 (1996).

[156] Edward William Kuns. *A Study of W Decay Charge Asymmetry Using Hadronic Tau Decays in Proton-Antiproton Collisions at* $\sqrt{s} = 1.8$ *TeV.* PhD thesis, Rutgers University, New Brunswick, New Jersey (1998).

[157] J. S. Conway and C. Loomis. Using an Analog Neural Network to Trigger on Tau Leptons at CDF. *Int. J. Mod. Phys.* **C6**, 549 (1995).

[158] J. Hauser. Guide to Missing E_T and Tau Triggers used in the 1992-93 CDF Data Run. CDF/DOC/EXOTIC/CDFR/2112 (1993).

[159] T. A. Fuess and E. Buckley-Geer. CDF Level 3 and Production Filter Documentation. CDF/DOC/PRODUCTION/CDFR/1632 (1991).

[160] K. Byrum and A. B. Wicklund. The Inclusive Electron Binary Files for the 1992/93 Run. CDF/MEMO/ELECTRON/CDFR/2059 (1997).

[161] D. Glenzinski and P. Schlabach. Validation of the Run 1B, Stream A, High p_T, Central, Inclusive Muon Data Set. CDF/MEMO/ELECTRON/CDFR/2059 (1997).

[162] T. Dorigo. A Trigger Breakdown of the Inclusive Central Electron Datasets. CDF/PHYS/BOTTOM/CDFR/4079 (1997).

[163] D. Baden, L. Buckley-Geer, *et al.* Joint DØ/CDF/CD Run II Data Management Needs Assessment. CDF/DOC/COMP_UPG/PUBLIC/4100 (1997).

[164] E. Sexton-Kennedy, M. Shapiro, and D. Quarrie. A Beginner's Guide To Analysis Control and Build Job. CDF/DOC/CDF/PUBLIC/0384 Rev. 3 (1996).

[165] P. Derwent. Changes to the SVX Tracking Package. CDF/ANAL/TRACKING/CDFR/2188 (1993).

[166] J. Conway *et al.* PLJ$DOC:GETTING_STARTED.TXT (1995). Document along with the code on the ACDF cluster at CDF.

[167] D. Quarrie. The CDF Event Structure. CDF Note CDF/DOC/PUBLIC/0152 (1987).

[168] S. Kopp and C. Grosso-Pilcher. A Good Run List for the 1992-1993 CDF Run. CDF/DOC/ELECTROWEAK/CDFR/1992 (1993).

[169] J. Conway and L. Groer. Reprocessing, Preselection, and Validation of Run 1A Data for CDF Tau Analyses. CDF/ANAL/EXOTIC/CDFR/2619 (1994).

[170] J. Conway, L. Groer, and C. Loomis. Reprocessing, Preselection, and Validation of TAUX1B Datasets for CDF Tau Analyses. CDF/ANAL/EXOTIC/CDFR/3463 (1996).

[171] J. Conway. $W \to \tau\nu$ in the Run 1A Monojet Data. CDF/ANAL/ELECTROWEAK/CDFR/2854 (1994).

[172] C. Grosso-Pilcher. Luminosity for Run 1B: How well do we know it? CDF/PHYS/CDF/CDFR/4350 (1997).

[173] P. Derwent *et al.* σ_{BBC} Updates. CDF/PHYS/CDF/CDFR/2535 (1994).

[174] A. Beretvas, P. Derwent, D. Cronin-Hennessy, and S. Segler. Beam-Beam Counter Cross Section Accidentals Correction Update. CDF/PHYS/CDF/CDFR/3418 (1996).

[175] D. P. Cronin-Hennessy, A. Beretvas, and S. Segler. Getting Your Luminosity. CDF/DOC/CDF/CDFR/4317 (1997).

[176] C. Grosso-Pilcher, D. Cronin-Hennessy, A. Beretvas, and A. Byon-Wagner. Luminosity for the Top PRL. CDF/ANAL/TOP/CDFR/3021 (1995).

[177] L. Groer. Comparison Between Luminosities Used in Tau and Top Analyses in Run 1. CDF/ANAL/EXOTIC/CDFR/4035 (1997).

[178] F. Abe *et al.* Evidence for Top Quark Production in $p\overline{p}$ Collisions at $\sqrt{s}$ = 1.8 TeV. *Phys. Rev. Lett.* **73**, 225 (1994).

[179] C$DOC:VTVZ.MEM: Vertex Classification (1993).

[180] J. Conway, E. Kuns, L. Groer, C. Loomis, and T. Watts. Tau Identification. CDF/ANA/EXOTIC/CDFR/3545 (1997).

[181] M. Hohlmann and S. Kopp. A Description of the Tau-Tagging Routine TAUFND. CDF/DOC/TOP/CDFR/2953 (1995).

[182] E. Kuns. FINDTAU: The Tau Reconstruction Module. CDF/DOC/EXOTIC/CDFR/1723 (1992).

[183] E. Kuns, T. Watts, and X. Wu. Reconstruction and Filtering of Taus: Modules FINDTAU, TAUFLT, TJTFLT. CDF/DOC/EXOTIC/CDFR/2661 (1994).

[184] R. Harris, R. Blair, and S. Kuhlmann. CES Response and χ^2 for 1990 Test-beam Electrons. CDF/ANAL/ELECTRON/CDFR/1432 (1991).

[185] L. Groer, J. Conway, E. Kuns, C. Loomis, A.M. Walsh, and T. Watts. Object Identification Efficiencies in Monte-Carlo Simulations for the Run 1 Direct Charged Higgs Search. CDF/ANA/EXOTIC/CDFR/4430 (1997).

[186] G. Marchesini *et al.* HERWIG: A Monte Carlo Event Generator for Simulating Hadron Emission Reactions with Interfering Gluons. Version 5.1. *Comput. Phys. Commun.* **67**, 465 (1992).

[187] F.E. Paige and S.D. Protopopescu. ISAJET 5.30: A Monte Carlo Event Generator for $p-p$ and $\overline{p}-p$ Reactions. BNL–38774. Updated documentation is available with the code (1986).

[188] T. Sjöstrand. High-energy Physics Event Generation with PYTHIA 5.7 and JETSET 7.4. *Comput. Phys. Commun.* **82**, 74 (1994).

[189] F. Abe *et al.* A Measurement of $\sigma \cdot \mathcal{B}(W \to e\nu)$ and $\sigma \cdot \mathcal{B}(Z^0 \to e^+e^-)$ in $p\overline{p}$ Collisions at $\sqrt{s} = 1800$ GeV. *Phys. Rev.* **D44**, 29 (1991).

[190] K. Yasuoka *et al.* Response Maps of the CDF Central Electromagnetic Calorimeter with Electrons. *Nucl. Instr. Meth.* **A267**, 315 (1988).

[191] R. G. Wagner *et al.* Cosmic Ray Test of the CDF Central Calorimeters. *Nucl. Instrum. Meth.* **A267**, 330 (1988).

[192] F. Abe *et al.* Study of Four-jet Evenets and Evidence for Double Parton Interactions in $p\overline{p}$ Collisions at $\sqrt{s} = 1.8$ TeV. *Phys. Rev.* **D47**, 4857 (1993).

[193] F. Abe *et al.* Properties of Six Jet Events with Large Six Jet Mass at the Fermilab Proton–Anti-proton Collider. *Phys. Rev.* **D56**, 2532 (1997).

[194] F. Abe *et al.* Properties of Jets in W Boson Events from 1.8 TeV $p\overline{p}$ Collisions. *Phys. Rev. Lett.* **79**, 4760 (1997).

[195] W. Yao and D. Glenzinski. Top Search in Run 1B Lepton + Jets with SECVTX. CDF/PHYS/TOP/CDFR/2989 (1995).

[196] F. Abe *et al.* Measurement of the Average Lifetime of B Hadrons Produced in $p\overline{p}$ Collisions at $\sqrt{s} = 1.8$ TeV. *Phys. Rev. Lett.* **71**, 3421 (1993).

[197] D. Kestenbaum and C. Campagnari. Review of SLT algorithm for Run 1B. CDF/ANAL/TOP/CDFR/3682 (1996).

[198] W. Yao *et al.* SVX B-Tag Algorithm "Seed Vertexing" for Top Search. CDF/ANAL/TOP/CDFR/2716 (1994).

[199] C. Miao and W. Yao. Update of SECVTX Tagging for the Top SVX Analysis. CDF/ANA/TOP/CDFR/3596 (1996).

[200] G. Unal. Tracking Efficiency and SVX B-Tag Efficiency. CDF/ANAL/TOP/CDFR/3563 (1996).

[201] C. Miao and W. Yao. SECVTX Tagging Study with Track-finding Degradation. CDF/ANAL/TOP/CDFR/3542 (1996).

[202] M. Pillai *et al.* A Search for Neutral Heavy Vector Gauge Bosons in $p\overline{p}$ Collisions at $\sqrt{s}$ = 1.8 TeV. Proceedings 1996 Divisional Meeting of Division of Particles and Fields (1996).

[203] H. Lai *et al.* Global QCD Analysis and the CTEQ Parton Distributions. *Phys. Rev.* **D51**, 4763 (1995).

[204] J. Botts *et al.* CTEQ Parton Distributions and Flavor Dependence of Sea Quarks. *Phys. Lett.* **B304**, 159 (1993).

[205] B. Andersson, G. Gustafson, G. Ingelman, and T. Sjöstrand. Parton Fragmentation and String Dynamics. *Phys. Rep.* **97**, 31 (1983).

[206] C. Peterson, D. Schlatter, I. Schmitt, and P. Zerwas. Scaling Violations in Inclusive e^+e^- Annihilation Spectra. *Phys. Rev.* **D27**, 105 (1983).

[207] J. Benlloch, A. Caner, T. Rodrigo, and M. Mangano. On Transforming Partons into Jets: HERPRT, a New Interface Between ME MC and Fragmentation Models. CDF/DOC/MONTECARLO/1823 (1992).

[208] F. Berends, W. Giele, H. Kuif, and B. Tausk. On the Production of a W and Jets at Hadron Colliders. *Nucl. Phys.* **B357**, 32 (1991).

[209] F. Abe *et al.* W Boson + Jet Angular Distribution in $p\overline{p}$ Collisions at $\sqrt{s}$ = 1.8 TeV. *Phys. Rev. Lett.* **73**, 2296 (1994).

[210] F. Abe *et al.* Measurement of Jet Multiplicity in W Events Produced in $p\overline{p}$ Collisions at $\sqrt{s}$ = 1.8 TeV. *Phys. Rev. Lett.* **70**, 4042 (1993).

[211] F. Abe *et al.* Properties of Jets in Z Boson Events from 1.8 TeV $p\overline{p}$ Collisions. *Phys. Rev. Lett.* **77**, 448 (1996).

[212] S. Jadach, J.H. Kühn, and Z. Wąs. TAUOLA — A Library of Monte Carlo Programs to Simulate Decays of Polarized τ Leptons. *Comput. Phys. Commun.* **64**, 275 (1991).

[213] M. Jeżabek, Z. Wąs, S.Jadach, and J.H. Kühn. The τ Decay Library TAUOLA, Update with Exact $\mathcal{O}(\alpha)$ QED Corrections in $\tau \to \mu(e)\nu\bar{\nu}$ Decay Modes. *Comput. Phys. Commun.* **70**, 69 (1992).

[214] Z. Wąs and S. Jadach. TAUOLA Monte Carlo for τ Decays. A Question of Systematic Errors. CERN-TH 6727/92 (1992).

[215] S. Jadach and Z. Wąs and R. Decker and J.H. Kühn. The τ Decay Library TAUOLA, version 2.4. *Comput. Phys. Commun.* **76**, 361 (1993).

[216] C. Loomis. Using TAUOLA, A Decay Library for Polarized τ Leptons, at CDF. CDF/DOC/EXOTIC/CDFR/2796 and references therein (1994).

[217] L. Montanet *et al.* Review of Particle Properties. *Phys. Rev.* **D50**, 1173 (1994).

[218] P. Avery, K. Read, and G. Trahern. QQ: A Monte Carlo Generator. CLEO Software Note CSN-212 (1985).

[219] J. Lewis and P. Avery. CLEOMC: The CDF Interface to the CLEO Monte Carlo (QQ). CDF/DOC/MONTECARLO/PUBLIC/2724 (1994).

[220] M. Shapiro *et al.* A User's Guide to QFL. CDF/ANAL/MONTECARLO/PUBLIC/1810 (1992).

[221] A. Caner. CDFSIM and QFL Simulation of the CDF Detector. CDF/ANAL/MONTECARLO/PUBLIC/2177 (1993).

[222] A. Roodman, S. Behrends, and M. Shapiro. Update on Central Calorimeter Response to Pions and Tuning of QFL. CDF/ANAL/CALORIMETRY/CDFR/1344 (1991).

[223] C. Loomis. Comparison of Run 1b Isolated Pions to Previous Studies and QFL Monte Carlo. CDF/ANAL/JET/CDFR/3554 (1996).

[224] J. Bellinger *et al.* CDF Event Mixing. CDF/DOC/CDF/CDFR/1428 (1994).

[225] C. Loomis. Check of Tau Isolation Efficiency In Monte Carlo. CDF/ANAL/EXOTIC/CDFR/3971 (1996).

[226] J. Conway, L. Groer, C. Loomis, and T. Watts. Search for Charged Higgs Decays of Top Quarks using the Hadronic Decays of the Tau Lepton. CDF/ANAL/EXOTIC/CDFR/3546 (1997).

[227] F. Abe *et al.* Measurement of $\sigma \cdot \mathcal{B}(W \to e\nu)$ and $\sigma \cdot \mathcal{B}(Z^0 \to e^+e^-)$ in $p\overline{p}$ Collisions at $\sqrt{s} = 1.8$ TeV. *Phys. Rev. Lett.* **76**, 3070 (1996).

[228] D. Ward. Tests of the Standard Model: W Mass and WWZ Couplings. Talk given at International Europhysics Conference on High-Energy Physics (HEP 97), Jerusalem, Israel, 19-26 Aug 1997, http://xxx.lanl.gov/abs/hep-ph/9711515 (1997).

[229] J. Ohnemus. An Order α_s Calculation of Hadronic W^-W^+ Production. *Phys. Rev.* **D44**, 1403 (1991).

[230] J. Ohnemus. An Order α_s Calculation of Hadronic $W^\pm Z$ Production. *Phys. Rev.* **D44**, 3477 (1991).

[231] U. Bauer, T. Han, and J. Ohnemus. WZ Production at Hadron Colliders: Effects of Nonstandard WWZ Couplings and QCD Corrections. *Phys. Rev.* **D51**, 3381 (1995).

[232] J. Ohnemus and J. Owens. An Order α_s Calculation of Hadronic ZZ Production. *Phys. Rev.* **D43**, 3626 (1991).

[233] J. Conway and K. Maeshima. Upper Limits on Poisson Processes Incorporating Uncertainties in Acceptance and Background. CDF/PUB/EXOTIC/PUBLIC/4476 (1998).

[234] B. Bevensee. Top to Charged Higgs Decays and Top Properties at the Tevatron. To be published in *Proceedings of the 33rd Rencontres de Moriond, QCD and High Energy Hadronic Interactions, 21-28 March 1998, Les Arcs, France.* FERMILAB-CONF-98/155-E (1998).

[235] M. Gallinaro and M. Hohlmann. Search for Charged Higgs Using Tau Dileptons. CDF/ANAL/EXOTIC/CDFR/4336 (1997).

[236] E. Ma, D. P Roy, and J. Wudka. Enhanced Three Body Decay of the Charged Higgs Boson. *Phys. Rev. Lett.* **80**, 1162 (1998).

[237] W. J. Marciano. Flavor Thresholds and Λ in the Modified Minimal-Subtraction Scheme. *Phys. Rev.* **D29**, 580 (1984).

[238] D. W. Duke and R. G. Roberts. Determinations of the QCD Strong Coupling α_s and the Scale Λ_{QCD}. *Phys. Rep.* **120**, 275 (1985).

[239] J. Thompson. Introduction to Colliding Beams at Fermilab. FERMILAB-TM-1909 (1994).

[240] G. Drake *et al.* CDF Front End Electronics: The Rabbit System. *Nucl. Instrum. Meth.* **A269**, 68 (1988).

[241] CDF Collaboration. The CDF II Detector: Technical Design Report. FERMILAB-Pub-96/390-E (1996).

[242] J. T. Carroll *et al.* The CDF Level 3 Trigger. *Nucl. Instrum. Meth.* **A300**, 552 (1991).

[243] J. Patrick *et al.* Performance of the CDF Level 3 Trigger. *Nucl. Instrum. Meth.* **A289**, 606 (1990).

[244] A. Clark, J. Conway, C. Couyoumtzelis, and X. Wu. Search for Top to Charged Higgs Bottom Using Tau Hadronic Decays. CDF/ANAL/EXOTIC/CDFR/3061 (1995).

Curriculum Vita

Leslie Stevan Groer

1966	Born February 20 in Johannesburg, South Africa.
1983	Graduated from King David High School, Linksfield, Johannesburg, South Africa.
1984–88	Attended University of the Witwatersrand, Johannesburg, South Africa. Majored in Physics and Applied Mathematics.
1986	B.Sc. in Physics and Applied Mathematics. University of the Witwatersrand, Johannesburg, South Africa.
1987	B.Sc. Honours in Physics. University of the Witwatersrand, Johannesburg, South Africa.
1988	B.Sc. Honours in Applied Mathematics. University of the Witwatersrand, Johannesburg, South Africa.
1988–98	Graduate studies in Physics at Rutgers, The State University of New Jersey, USA.
1988–91	Teaching Assistant, Department of Physics and Astronomy. Rutgers, the State University of New Jersey, USA.
1991–98	Research Assistant, Department of Physics and Astronomy. Rutgers, the State University of New Jersey, USA.
1988–98	List of publications available on request.
1998	Ph.D. in Physics. Rutgers, the State University of New Jersey, USA.